Tectonic evolution of continental rifts. Inference from numerical modelling and fission track thermochronology

Pieter van Der Beek

▶ **To cite this version:**

Pieter van Der Beek. Tectonic evolution of continental rifts. Inference from numerical modelling and fission track thermochronology. Other. Vrije Universiteit, 1995. English. NNT : . tel-00785951

HAL Id: tel-00785951
https://theses.hal.science/tel-00785951

Submitted on 7 Feb 2013

HAL is a multi-disciplinary open access archive for the deposit and dissemination of scientific research documents, whether they are published or not. The documents may come from teaching and research institutions in France or abroad, or from public or private research centers.

L'archive ouverte pluridisciplinaire **HAL**, est destinée au dépôt et à la diffusion de documents scientifiques de niveau recherche, publiés ou non, émanant des établissements d'enseignement et de recherche français ou étrangers, des laboratoires publics ou privés.

M.GEOSCIENCES.GRENOBLE UJF
D 050 036366 2

VAN DER BEEK, P.

TECTONIC EVOLUTION OF CONTINENTAL RIFTS

inferences from numerical modelling and fission track thermochronology

0 8 NOV. 1999
UNIVERSITE DE GRENOBLE 1
INSTITUT DE GÉOLOGIE
DOCUMENTATION
15, RUE MAURICE GIGNOUX
F 38031 GRENOBLE CEDEX
TÉL. (33) 76 63 59 66
FAX. (33) 76 87 82 43

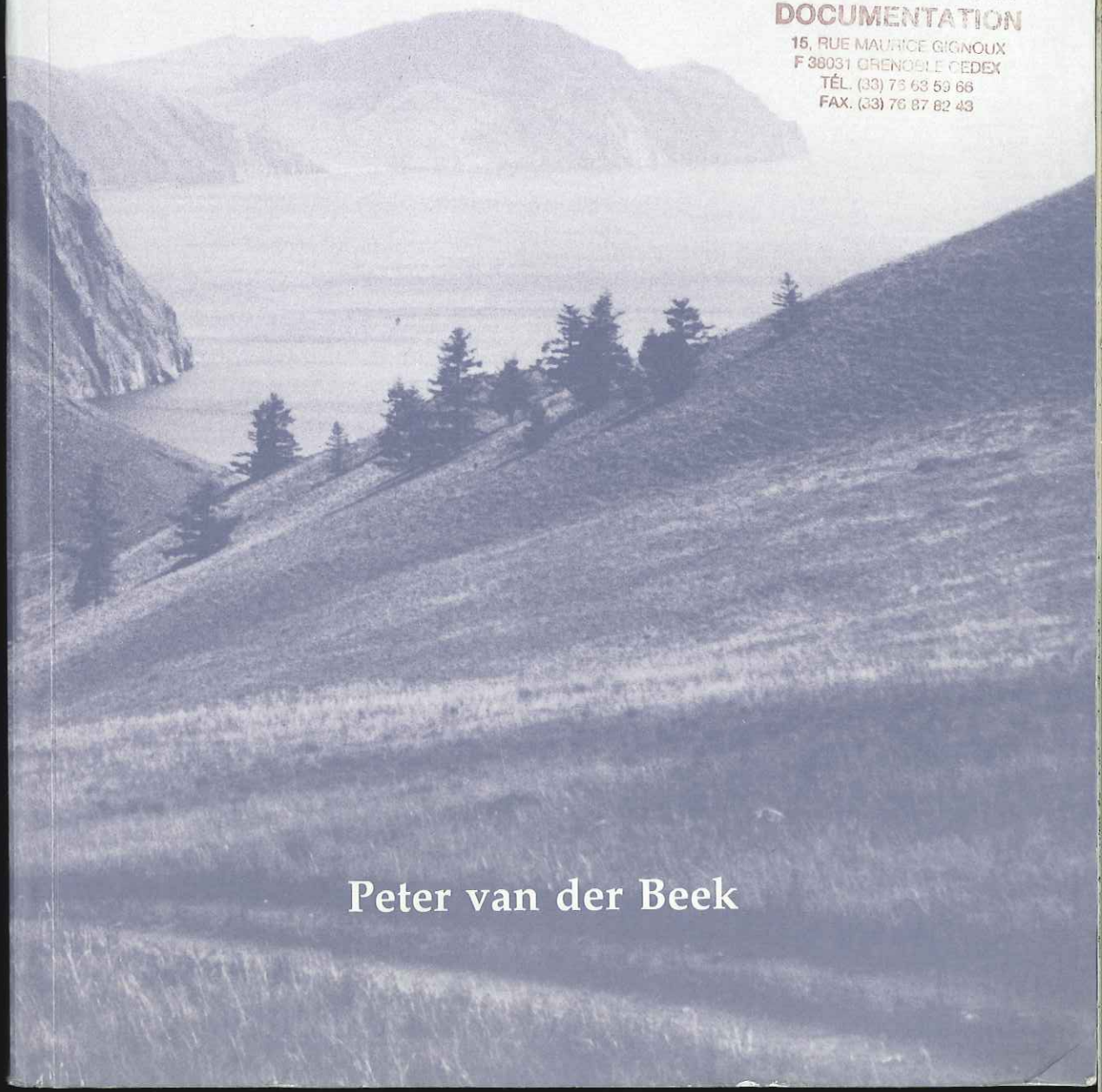

Peter van der Beek

UNIVERSITE DE GRENOBLE
INSTITUT DE GEOLOGIE
DOCUMENTATION
15, RUE MAURICE GIGNOUX
F 38031 GRENOBLE CEDEX
TÉL. (33) 76 63 59 66
FAX. (33) 76 87 82 43

VRIJE UNIVERSITEIT

TECTONIC EVOLUTION OF CONTINENTAL RIFTS

0 8 NOV. 1999

inferences from numerical modelling and fission track thermochronology

ACADEMISCH PROEFSCHRIFT

ter verkrijging van de graad van doctor aan
de Vrije Universiteit te Amsterdam,
op gezag van de rector magnificus
prof.dr E. Boeker,
in het openbaar te verdedigen
ten overstaan van de promotiecommissie
van de faculteit der aardwetenschappen
op woensdag 24 mei 1995 te 15.45 uur
in het hoofdgebouw van de universiteit, De Boelelaan 1105

door

PIETER ALBERT VAN DER BEEK

geboren te Voorburg

10249621

Promotor : prof.dr S.A.P.L. Cloetingh
Copromotor : dr P.A.M. Andriessen
Referenten : dr R.A. Stephenson
dr B.T. Larsen

Cover illustration: The Primorsky range, which forms the western flank of lake Baikal. The Primorsky fault, the main border fault of the central Baikal rift, runs along the lake shore. See Chapter 3.

The research reported in this thesis was carried out at the

Tectonics/Structural Geology Group
and the
Deparment of Petrology and Isotope Geology

Faculty of Earth Sciences, Vrije Universiteit
De Boelelaan 1085, 1081 HV Amsterdam
The Netherlands

Netherlands Research School of Sedimentary Geology (NSG)
contribution no. 950326

CIP-GEGEVENS KONINKLIJKE BIBLIOTHEEK, DEN HAAG

Beek, Pieter Albert van der

Tectonic evolution of continental rifts: inferences from
numerical modelling and fission track thermochronology /
Pieter Albert van der Beek. - [S.l : s.n.]. - Ill.
Proefschrift Vrije Universiteit Amsterdam. - Met lit. opg.
ISBN 90-9008076-7
NUGI 816
Trefw.: geologie / tektoniek / geochronologie

CONTENTS

Univ. J. Fourier - O.S.U.G.
MAISON DES GEOSCIENCES
DOCUMENTATION
B.P. 53
F. 38041 GRENOBLE CEDEX
Tél. 04 76 63 54 27 - Fax 04 76 51 40 58
Mail : ptalour@ujf-grenoble.fr
25 AOUT 2003

DANKWOORD IX

SAMENVATTING XI

BIBLIOGRAPHY XV

CHAPTER 1
INTRODUCTION 1
1.1 HISTORICAL PERSPECTIVE 1
1.2 MECHANISMS OF RIFT FORMATION 4
1.3 APATITE FISSION TRACK THERMOCHRONOLOGY 9
1.3.1 Annealing of fission tracks and confined track length distributions 10
1.3.2 Fission track profiles: constraints on tectono-thermal histories and vertical motions 13
1.4 SCOPE AND OUTLINE OF THE THESIS 15

CHAPTER 2
TECTONIC UPLIFT, EROSION, AND ISOSTATIC REBOUND AT RIFTED CONTINENTAL MARGINS 19
2.1 INTRODUCTION 19
2.2 REGIONAL EXAMPLES; TECTONIC SETTING 24
2.2.1 The Saudi Arabian Red Sea margin 24
2.2.2 The Transantarctic Mountains 24
2.2.3 The southeastern Australian margin 25
2.2.4 The Namibian Atlantic margin 26
2.3 VERTICAL MOTIONS AT RIFTED MARGINS 27
2.3.1 Mechanisms of rift margin uplift 27
2.3.2 Estimates of rift margin uplift from fission track data 31
2.3.3 Flexural strength of the lithosphere during extension 33
2.3.4 Backstacking rifted margin uplifts 35
2.3.5 Forward modelling of rift margin uplift 39
2.4 MORPHOTECTONIC EVOLUTION OF RIFTED MARGINS 44
2.4.1 Surface processes model 45
2.4.2 Controls on margin evolution; general modelling results 48
2.4.3 Modelling regional examples 52
2.5 DISCUSSION 60

CHAPTER 3
MECHANISMS OF SYN-RIFT FLANK UPLIFT: A STUDY OF THE BAIKAL RIFT (SE SIBERIA) AND A COMPARISON WITH THE MALAWI RIFT (EAST AFRICA) 67
3.1 INTRODUCTION 67
3.2 UPLIFT OF THE BAIKAL RIFT FLANKS 68
3.2.1 Tectonic setting 68
3.2.2 Exhumation history of the Baikal region from fission track thermochronology 75
3.2.3 Modelling rift flank uplift adjacent to the central Baikal basin 80
3.3 A COMPARISON WITH THE MALAWI RIFT, E. AFRICA 86
3.3.1 Introduction and tectonic setting 86
3.3.2 Fission track data 88
3.3.3 Modelling uplift and erosion of the Malawi rift flanks ... 93
3.4 3D MODELLING OF UPLIFT PATTERNS AROUND THE BAIKAL RIFT ... 96
3.5 DISCUSSION AND CONCLUSIONS 102

CHAPTER 4
MECHANISMS OF POST-RIFT MARGIN UPLIFT: THE CASE OF SOUTHERN NORWAY 107
4.1 INTRODUCTION 107
4.2 TECTONIC AND PALEOGEOGRAPHIC EVOLUTION OF SOUTHERN NORWAY 109
4.3 MESO-CENOZOIC MORPHOTECTONIC EVOLUTION OF SOUTHERN NORWAY FROM APATITE FISSION TRACK THERMOCHRONOLOGY ... 114
4.3.1 Fission track data 114
4.3.2 Paleogeographic implications 124
4.4 MECHANISMS OF NEOGENE TECTONIC UPLIFT IN SOUTHERN NORWAY 127
4.4.1 Quantification of uplift and erosion patterns 127
4.4.2 A comparison with other North Atlantic margins 133
4.4.3 Models for uplift 134

CHAPTER 5
THERMAL AND MAGMATIC EVOLUTION OF A FAILED CONTINENTAL RIFT: THE OSLO GRABEN, SE NORWAY 141
5.1 INTRODUCTION 141
5.2 TECTONIC SETTING 142
5.3 A MODEL FOR EXTENSION AND MAGMATISM IN THE OSLO GRABEN 147
5.3.1 Introduction and modelling approach 147
5.3.2 Modelling results 149
5.4 THERMAL EVOLUTION OF THE OSLO GRABEN FROM FISSION TRACK THERMOCHRONOLOGY 153
5.3.1 Fission track results 153
5.3.2 Interpretation of fission track data 160
5.5 DISCUSSION - IMPLICATIONS FOR RIFT MODELS 164

CHAPTER 6
SYNTHESIS 169
6.1 WHAT IS THE PHYSICAL MEANING OF THE 'LEVEL OF NECKING'? .. 170
6.2 WHAT CONTROLS THE (A)SYMMETRY OF RIFTING? 176
6.3 SOME REMARKS ON 'ACTIVE' AND 'PASSIVE' RIFTING 178

APPENDIX 1
THERMAL MODELLING OF APATITE FISSION TRACK DATA 183
A1.1 FORWARD MODEL 183
A1.2 INVERSE MODEL 189

APPENDIX 2
SAMPLE DETAILS 197

APPENDIX 3
FISSION TRACK ANALYTICAL DATA 203

REFERENCES 209

DANKWOORD

Dit proefschrift had niet tot stand kunnen komen zonder de bijdragen, in velerlei vorm, van velen om mij heen. Ten eerste ben ik dank verschuldigd aan mijn promotor, Sierd Cloetingh, die de mogelijkheid schiep om dit onderzoek te doen en een zeer enthousiasmerende werkomgeving tot stand heeft doen komen. Mijn co-promotor, Paul Andriessen, was met zijn kenmerkende gevoel voor humor en relativeringsvermogen een goede aanvulling. Bovendien bepaalde Paul de ouderdommen voor de monsters van hoofdstuk 3.

I would like to thank my referees, Randell Stephenson and Bjørn Larsen, for their critical reading and constructive comments on the manuscript. Both have seen the study grow from close by, from 'bush-bashing' on Jeløya island in the summer of '91, to the present finalisation. I thank Tom Pedersen for the more than pleasant cooperation on melt modelling in the Oslo Graben, and Else-Raghnild Neumann for her interest and stimulating discussions.

The expedition to the Baikal rift in the summer of '93 was organised by Jean Klerkx of the Royal Museum for Central Africa in Tervuren, Belgium, and Kiril Levi (Institute of Physics of the Earth's Crust, Irkutsk, Russia). I thank them, as well as Damien Delvaux, Sergei Kuzmin and Vladimir Sankov, amonst many others, for the succesful trip and good company. Evgeni Burov supplied me with gravity and topography data for the Baikal rift.

A significant part of this thesis has been published in scientific journals or is in press. I thank the reviewers Chris Beaumont, Cynthia Ebinger, Kerry Gallagher and Dale Sawyer (Chapter 2), Paul Fitzgerald and Roy Gabrielsen (Chapter 4), and Tony Hurford, Stig Pallesen and Tom Pedersen (Chapter 5) for their constructive comments. Damien Delvaux read an early version of Chapter 3, and Jan Inge Faleide did so for part of Chapter 4. Gianna Bassi and Henk Kooi also read large parts of the thesis and gave very useful comments.

Ik dank Lodewijk IJlst, Tineke Vogel en de medewerkers van het laboratorium voor isotopen geologie voor het vele werk dat ze verzet hebben in de monster-voorbereiding en voor de goede sfeer. De computer groep van de faculteit, en met name Arie Bikker, zorgde voor een adequate ondersteuning.

Max Rohrman wil ik bedanken voor zijn gezellige gemopper tijdens de vele weken in Noorwegen en in de isotopen-kelder. Ik zal het missen. Ik heb erg veel gehad aan mijn collega's in de tektoniek/structurele geologie groep. Ten eerste mijn kamergenoten Paul Reemst en Marlies ter Voorde, voor de gezelligheid en het doorstaan van de laatste weken promotie-stress. Paul was bovendien prima gezelschap tijdens congressen en reizen naar Noorwegen. De discussies met Henk Kooi, J.D. van Wees, Reini Zoetemeijer, Marjel Janssen en Ronald van Balen waren erg stimulerend. Fred Beekman gaf mij vele technische en tactische computer-tips. Michel Heeremans, Harry Stel, Tim Peper, Menno de Ruig, Ritske Huismans, Gerco Stapel, Carlo Sanders, Cees Bierman, Giovanni Bertotti, Yuri Podladchikov, Bertrand Daudré, Paul Johnston, Tore Skar en Maaike den Houting droegen op vele manieren bij aan een prettig vierjarig verblijf in 'paviljoen E1'. Harm Rondeel, Eric Zwart, Marjel Janssen, Kay Beets, Jeroen Kenter, Hubert Vonhof en Taco den Bezemer maakten de jaarlijkse veldwerken in zuid Spanje tot ontspannende en leerzame ervaringen. I would like to thank

the 'visitors' Laszlo Lenkey, Nihal Okaya, Daniel Ciulavii, Tore Odinsen, Ivar Grunaleite and Matthias Gölke for good times. Giacomo Spadini and Deirdre O'Leary stayed longer and have become good friends.

Tenslotte, en vooral, bedank ik mijn ouders en Kees, Marianne en Heleen. Ik dank Nienke voor de steun die zij de eerste jaren kon geven, en voor de vriendschap daarna. Mijn vrienden Leo, Paul en Daniëlla, Rick en Andrea, Anco en Arjette, Daniël, Marjel, Caroline, Michel, Josine, Ron, Jeroen en Jan-Henk zorgden ervoor dat de wereld uit meer dan keien en computers bestond. Et surtout, je remercie Gianna pour sa tendresse, sa gentillesse et sa compréhension.

SAMENVATTING

Continentale rifts (slenken) zijn enige tientallen kilometers brede, door afschuivingen begrensde valleien waar de aardkorst onder invloed van rekspanningen uit elkaar getrokken wordt. Voorbeelden zijn het Oost Afrikaanse riftsysteem en de Baikal-rift. Bij doorgaande extensie ontwikkelen rifts zich tot brede continentale extensiebekkens, zoals bijvoorbeeld het Noordzeebekken. Het uitrekkingsproces veroorzaakt uiteindelijk het opbreken van een continent en leidt tot de vorming van een oceanisch bekken met passieve continentale marges, zoals wordt waargenomen aan beide zijden van de Atlantische oceaan. De ontwikkeling van het uitrekkingsproces kan echter ook onvolledig zijn, met als gevolg de vorming van een fossiel riftsysteem, zoals bijvoorbeeld de Oslo-rift. Er zijn twee belangrijke redenen om de processen die leiden tot continentale riftvorming te bestuderen: ten eerste spelen rifts, als eerste expressie van het mechanisme dat leidt tot opbreken van continenten, een fundamentele rol in de plaattektoniek; ten tweede worden in de sedimentaire bekkens die door extensie ontstaan zijn grote hoeveelheden olie en gas gevonden.

Continentale rifts zijn gedurende de laatste eeuw uitgebreid bestudeerd en er zijn vele theorieën ontwikkeld over hun ontstaan en ontwikkeling. Met name de drijvende kracht achter continentale extensie is onderwerp van discussie geweest. In 'aktieve' riftvormings-modellen wordt deze drijvende kracht geleverd door opwellend warm mantelmateriaal, terwijl in 'passieve' modellen horizontale intra-plaatspanningen, veroorzaakt door krachten die aan de plaatranden aangrijpen, de uitrekking veroorzaken. Ook de vraag of continentale extensie een fundamenteel symmetrisch of asymmetrisch proces is, is een belangrijk onderwerp van studie geweest maar is nog niet beantwoord.

Continentale rifts worden in veel gevallen begrensd door hoog opgeheven schouders of flanken. De oorzaken van deze schouderopheffingen, en hiermee samenhangend de wijze van isostatische kompensatie en de sterkte van de lithosfeer in extensie, zijn omstreden. De eerste modellen voor shouderopheffing, die begin jaren '80 ontwikkeld zijn, verklaarden flankopheffingen als een gevolg van opwarming of verdunning van de mantel onder de schouders. De laatste jaren zijn echter modellen ontwikkeld waarin regionale (flexurale) isostatische kompensatie van opwaartse krachten, die het gevolg zijn van riftvorming, de schouders omhoog houden.

De diverse gepostuleerde modellen leiden tot verschillende voorspellingen voor de met extensiebekkens geassocieerde korststruktuur en zwaartekrachts-anomalieën, de relatieve opeenvolging van rift-daling, schouderopheffing en magmatisme, en de grootte van de vertikale bewegingen. Door deze voorspellingen met observaties te vergelijken kunnen we de modellen toetsen en zo een beter begrip krijgen van de processen die leiden tot continentale extensie. Over de daling van extensiebekkens zijn we de laatste jaren veel te weten gekomen aan de hand van de sedimentaire opvulling van deze bekkens, waarbij met name door de olie-industrie verzamelde gegevens een belangrijke rol gespeeld hebben. De opheffing van riftschouders leidt echter tot erosie, en is daarom niet direkt waarneembaar.

De vertikale bewegingen van de schouders zijn te achterhalen met behulp van

thermochronologische methoden, zoals splijtingssporen-analyse. Splijtingssporen zijn de, onder een optische microscoop waarneembare, schadezones die ontstaan door natuurlijke splijting van ^{238}U in bepaalde mineralen - met name apatiet, zirkoon en titaniet. De sporendichtheid in een mineraal is een maat voor het Uranium-gehalte en de geologische ouderdom. De stabiliteit van splijtingssporen is tijds- en temperatuurs-afhankelijk; ten gevolge van verhoogde temperaturen verkorten splijtingssporen en uiteindelijk verdwijnen ze. Van dit proces wordt gebruikt gemaakt in splijtingssporen-analyses: door de dichtheid en lengteverdeling van splijtingssporen te meten wordt informatie verkregen over de thermische geschiedenis van gesteenten bij lage temperaturen (≤120°C voor het mineraal apatiet), en daarmee over hun opheffings en erosie (denudatie) geschiedenis.

Het doel van deze studie is om tektonische modellen voor riftvorming te toetsen aan de hand van de thermische evolutie van extensiebekkens en hun marges, zoals deze wordt vastgelegd door splijtingssporen-analyses. Hiertoe heb ik numerieke modelstudies uitgevoerd, gebaseerd op zowel gepubliceerde (hoofstuk 2) als nieuw verworven (hoofstukken 3 t/m 5) gegevens. De verworven inzichten uit de kinematische modelleringen in deze studies worden vergeleken met resultaten van dynamische modellen voor riftvorming.

De inleiding (hoofdstuk 1) geeft een historisch overzicht, behandelt de verschillende modellen voor riftvorming en beschrijft de techniek van splijtingssporen analyse. Hierna wordt in hoofdstuk 2 de rol besproken van verschillende opheffingsmechanismen, bij het creëren van de huidige topografie en erosiepatronen van passieve marges. Thermochronologische studies van een aantal passieve marges (bv. de marges van de Rode Zee, zuidelijk Afrika, zuidoost Australië, het Transantarctisch gebergte) hebben laten zien dat daar, tijdens en na het opbreken, de bovenste 2 à 3 km van de aardkorst zijn geërodeerd. In hoofstuk 2 wordt aangetoond dat deze hoeveelheden erosie alleen mogelijk zijn als de marges tijdens het opbreken ook meerdere kilometers zijn opgeheven. Een tektonische modelstudie voorspelt dat opheffingen die het gevolg zijn van thermische mechanismen, veel kleiner zijn; de observaties worden dan ook beter verklaard door het mechanisme van flexurele schouderopheffing. Om de opheffings-geschiedenis van passieve marges te bepalen aan de hand van hun denudatie geschiedenis, is een erosiemodel ontwikkeld dat de gevormde topografie relateert aan denudatiesnelheden. Toepassing van dit model leidt tot twee belangrijke voorspellingen. Ten eerste zal een opgeheven schouder binnen 50 tot 100 miljoen jaar eroderen; hoge continentranden en kustgebergten die ouder zijn (bv. de kustgebergten van zuidelijk Afrika en Brazilië) zijn dus op zichzelf geen indicatie voor tektonische schouderopheffing. Deze kustgebergten zijn het resultaat van een drastische verlaging van de erosiebasis na opbreking en regionale isostatische compensatie van de erosie. Ten tweede blijkt dat, met behulp van splijtingssporen-analyse, de fase van snelle erosie die samenhangt met het opbreken gedateerd wordt; splijtingssporen-ouderdommen die jonger zijn dan de ouderdom van opbreken, geven op zichzelf geen uitsluitsel over het al of niet bestaan van oudere opheffingsfasen.

In hoofdstuk 3 worden de mechanismen van schouderopheffing meer in detail

bestudeerd, door te kijken naar topografie en erosie bij twee recent gevormde intracontinentale rifts: de Baikal-rift in zuidoost Siberië en de Malawi-rift in oostelijk Afrika. Splijtingssporen-analyse toont aan, dat in het Baikal-gebied een belangrijke erosiefase plaatsgevonden heeft tijdens het vroeg-Krijt, met nauwelijks erosie van de huidige schouders. De flanken van de Malawi-rift zijn wel door recente erosie aangetast. Ik heb een aantal verschillende modellen voor flexurele schouderopheffing getest, waaronder symmetrische 'necking' modellen en modellen die symmetrische en asymmetrische deformatie combineren. In dit hoofdstuk wordt aangetoond dat voorspellingen van het zogenaamde 'flexurele hefboom-model', waarin schouders gedragen worden door de dunne (<10 km) elastische bovenkorst, niet in overeenstemming zijn met de topografie en hoeveelheden erosie die bij deze twee riftsystemen worden geobserveerd. De schouders worden gedragen door de sterke sub-crustale lithosfeer, die een elastische dikte van meerdere tientallen kilometers heeft. De modellen voorspellen een necking-niveau in de middenkorst en/of décollements in de onderkorst. Deze voorspellingen zijn in overeenstemming met de rheologie van de lithosfeer onder deze riftsystemen, zoals bekend uit zwaartekrachts- en seismologische gegevens, en uit zijn thermische en petrologische (seismische) struktuur. Een drie-dimensionale modellering van de topografie bij de Baikal-rift laat zien dat flexurele mechanismen niet het totaalbeeld van de geobserveerde schouderopheffing kunnen verklaren; een aanvullende opwaartse kracht is nodig om de anomaal hoge flanken en het ondiepe bekken in het noorden van de riftzone te verklaren. Dit kan betekenen dat aan de noordkant van de rift de mantel sterker verdund is dan de korst.

Mechanismen voor latere reactivatie van passieve marges komen in hoofstuk 4 aan de orde, met de morfologisch-tektonische evolutie van zuid-Noorwegen als voorbeeld. Door splijtingssporen-analyse te combineren met geomorfologische gegevens op het land en de (seismische) stratigrafie van de noordelijke Noordzee-bekkens, worden twee belangrijke Meso-Cenozoïsche erosiefasen in kaart gebracht: één gedurende de Trias en Jura; de ander beginnend in het Neogeen. Denudatie tijdens de Trias en Jura kan worden toegeschreven aan erosie van de marge als gevolg van verlaging van de erosiebasis en schouderopheffing. Een bewijs hiervoor wordt geleverd door de dikke klastische sequenties die in de gelijktijdig aktieve rifts van de Noordzee werden afgezet. Ik toon aan dat Neogene erosie het gevolg is van een koepelvormige opheffing, die een maximale amplitude van ~1.5 km heeft en gecentreerd is onder de hoogste gebergtepieken van zuid-Noorwegen. Ik bespreek de correlatie met de tektonische evolutie van de noordelijke Atlantische oceaan en vergelijk de hier verkregen resultaten met andere studies van recente opheffingen in het noord-Atlantische gebied (o.a. in oost-Groenland en de Barents-zee). Tenslotte worden mogelijke mechanismen voor Neogene koepelvormige opheffing geëvalueerd. Het blijkt dat geen van de mechanismen die eerder zijn gepostuleerd alle geologische en geofysische observaties tegelijkertijd kunnen verklaren. Een model dat thermische erosie van de lithosfeer combineert met de opbouw van compressieve intraplaatspanningen benadert de waarnemingen het beste, maar verklaart nog steeds niet alle opheffing die wordt waargenomen.

In hoofdstuk 5 wordt de thermo-tektonische ontwikkeling van een magmatische continentale rift behandeld. De magmatische ontwikkeling van de Oslo-rift, die aktief was tijdens het laat-Carboon en Perm, wordt bestudeerd met behulp van een numeriek model voor decompressie-smeltvorming. De modelresultaten suggereren dat de mantel ter plaatse, vergeleken met droge peridotiet, een sterk verlaagde solidus moet hebben gehad. Bovendien moet de verdunning van de mantel beduidend sterker zijn geweest dan de uitrekking van de korst, willen de geobserveerde hoeveelheden magmatisme verklaard kunnen worden. Aangezien de magmas afkomstig lijken te zijn uit de lithosfeer, er geen opheffing vóór riftvorming heeft plaatsgevonden en de produktie-snelheid van de magmas tamelijk laag is, kunnen riftvorming en magmatisme in Oslo niet geassocieerd geweest zijn met een gebied van heet opwellend mantelmateriaal. De lithosfeer onder de Oslo-rift was eerder abnormaal 'nat' dan 'heet' en magmatisme werd voornamelijk veroorzaakt door passieve uitrekking en 'necking' van de lithosfeer. De thermische evolutie van de Oslo-rift heb ik bestudeerd aan de hand van splijtingssporen-analyse van zirkonen, titanieten en apatieten. Het blijkt dat de thermische struktuur van de rift sterk beïnvloed is geweest door magmatische en hydrothermale warmtestromen. De flanken van de rift vertonen, in tegenstelling hiermee, geen thermisch signaal dat met riftvorming geassocieerd is. Dit houdt in dat de verhoogde warmtestroom die het gevolg was van lithosfeerverdunning en magmatisme, vrijwel geheel in de riftzone zelf geconcentreerd werd, analoog aan de situatie in moderne magmatische rifts (bv. de Kenya-rift). De splijtingssporen-ouderdommen van de apatieten laten zien dat de rift tijdens het Trias en de vroege Jura, vrij kort na de laatste fase van rift-activiteit, geërodeerd is en dat er weinig tot geen post-rift daling heeft plaatsgevonden.

Tenslotte worden, in hoofdstuk 6, de belangrijkste conclusies van deze studie samengebracht, en hun implicaties voor rheologische modellen van de lithosfeer en dynamische modellen voor extensie besproken. Dit proefschrift toont de sterke koppeling tussen processen in de diepe lithosfeer en die aan de oppervlakte aan. Aan het aardoppervlak waarneembare processen, zoals vertikale bewegingen, sedimentatie en erosie, worden beïnvloedt door grootschalige tektoniek. Dit tektonische signaal is uit de waarnemingen te destilleren en hieruit kunnen we iets leren over de dynamiek van de lithosfeer.

BIBLIOGRAPHY

A list of publications by the author follows below. Those marked with an asterisk have been included in this thesis.

van der Beek, P.A. and Cloetingh, S. 1992. Lithospheric flexure and the tectonic evolution of the Betic Cordilleras (SE Spain). *Tectonophysics* **203**, 325-344.

*van der Beek, P.A., Cloetingh, S. and Andriessen, P.A.M. 1994. Mechanisms of extensional basin formation and vertical motions at rift flanks: Constraints from tectonic modelling and fission-track thermochronology. *Earth Plan. Sci. Lett.* **121**, 417-433.

*van der Beek, P.A., Andriessen, P.A.M. and Cloetingh, S. 1995. Morphotectonic evolution of rifted continental margins: Inferences from a coupled tectonic-surface processes model and fission track thermochronology. *Tectonics*, in press.

Cloetingh, S., van der Beek, P.A., van Rees, D., Roep, Th. B., Biermann, C. and Stephenson, R.A. 1992. Flexural interaction and the dynamics of Neogene extensional basin formation in the Alboran-Betic region. *Geo-Marine Lett.* **12**, 66-75.

Cloetingh, S., van Wees, J.D., van der Beek, P.A. and Spadini, G. 1995. Role of pre-rift rheology in kinematics of extensional basin formation: Constraints from thermomechanical models of meditterranean and intracratonic basins. *Mar. Petrol. Geol.*, in press.

Heeremans, M.M.H., Stel, H., van der Beek, P.A. and Lankreijer, A.C. 1995. Tectono-magmatic control on vertical dip-slip basement faulting: the example of southern Finland. submitted to *Terra Nova*.

Jelsma, H.A., van der Beek, P.A. and Vinyu, M.L. 1993. Tectonic evolution of the Bindura-Shamva greenstone belt (northern Zimbabwe): progressive deformation around diapiric batholiths. *J. Struct. Geol.* **15**, 163-176.

*Pedersen, T. and van der Beek, P.A. 1994. Extension and magmatism in the Oslo Rift, SE Norway: no sign of a mantle plume. *Earth Plan. Sci. Lett.* **123**, 317-330.

*Rohrman, M., van der Beek, P.A. and Andriessen, P.A.M. 1994. Syn-rift thermal structure and post-rift evolution of the Oslo Rift (SE Norway): New constraints from fission-track thermochronology. *Earth Plan. Sci. Lett.* **127**, 39-54.

Rohrman, M., Andriessen, P.A.M. and van der Beek, P.A. 1995. The relationship between basin and margin thermal evolution assessed by fission track thermochronology: an application to offshore southern Norway. submitted to *Basin Res.*

*Rohrman, M., van der Beek, P.A., Andriessen, P.A.M. and Cloetingh, S. 1995. Meso-Cenozoic morphotectonic evolution of southern Norway: Neogene domal uplift inferred from apatite fission-track thermochronology. *Tectonics*, in press.

Stel, H., Cloetingh, S., Heeremans, M.M.H. and van der Beek, P.A. 1993. Anorogenic granites, magmatic underplating and the origin of intracratonic basins in a non-extensional setting. *Tectonophysics* **226**, 285-299.

van Balen, R.T., van der Beek, P.A. and Cloetingh, S. 1995. The effect of rift shoulder erosion on stratigraphic patterns at passive margins: Implications for sequence stratigraphy. submitted to *Earth Plan. Sci. Lett.*

CHAPTER 1

INTRODUCTION

1.1 HISTORICAL PERSPECTIVE

The term 'rift valley' was introduced by Gregory (1896) to describe the morphological feature in central Kenya that nowadays bears his name. He used the term to define a long strip of country that had subsided between (sets of) normal faults, bordered by broad arches. A similar morphotectonic setting had been described previously in the Rhinegraben (e.g., de Beaumont, 1847; Suess, 1880, 1909). Although the areal extent of continental rifts is rather limited, they have received considerable attention for two reasons: (1) continental rifts constitute the initial stages in the evolutionary cycle that finally leads to continental break-up and ocean basin formation (Wilson, 1966); (2) they provide particularly suitable environments for hydrocarbon accumulation. The discovery of hydrocarbons associated with continental rifts and extensional basins, around the turn of this century, has sparked an extensive and worldwide interest in rifted basin evolution (e.g., Bally, 1982; Sclater and Célerier, 1987; Landon, 1994).

Tectonically active continental rifts possess a number of characteristic features (Holmes, 1965; Morgan and Baker, 1983): (1) they are rather narrow, with a typical width of some 50 km (Figure 1-1); this is close to the thickness of the rifted continental crust (Allemand and Brun, 1991); (2) they are generally bounded by large normal faults of opposing polarity that are not necessarily continuous but often aligned *en echelon*; (3) there is usually extensive shallow level (≤15 km) seismicity, although deeper earthquakes also occur (Shudofsky et al., 1987; Déverchère et al., 1991); (4) seismic and gravity data indicate that most rifts are underlain by anomalously light mantle at shallow depths; (5) they are zones of relatively high heat flow, as well as volcanic and geothermal activity; (6) they are often associated with extensive and chemically distinctive alkaline magmatism. Whereas most experimental models of rift formation (cf. Rosendahl, 1987 for a review) predict a symmetrical full graben form (and this also seems to be the traditional picture of a continental rift that comes to mind), extensive seismic reflection profiling has shown that most rifts are in fact asymmetric (Rosendahl, 1987; Figure 1-1). Individual grabens are usually bounded on one side by a steeply dipping border fault; on the opposing side the basement gradually rises along smaller faults or flexures. Rift zones are composed of a number of half grabens linked together, often with opposing polarities.

Continental rifts constitute one of the surface expressions of lithospheric extension. They represent a specific extensional tectonic style, evolving as narrow linear zones of extension as opposed to wider, more diffuse extensional terrains such as the Basin and Range province in western North America (e.g., Coney, 1987) or the Mediterranean 'back arc' basins (Horváth and Berkhemer, 1982). Primary controls on the style of continental extension are

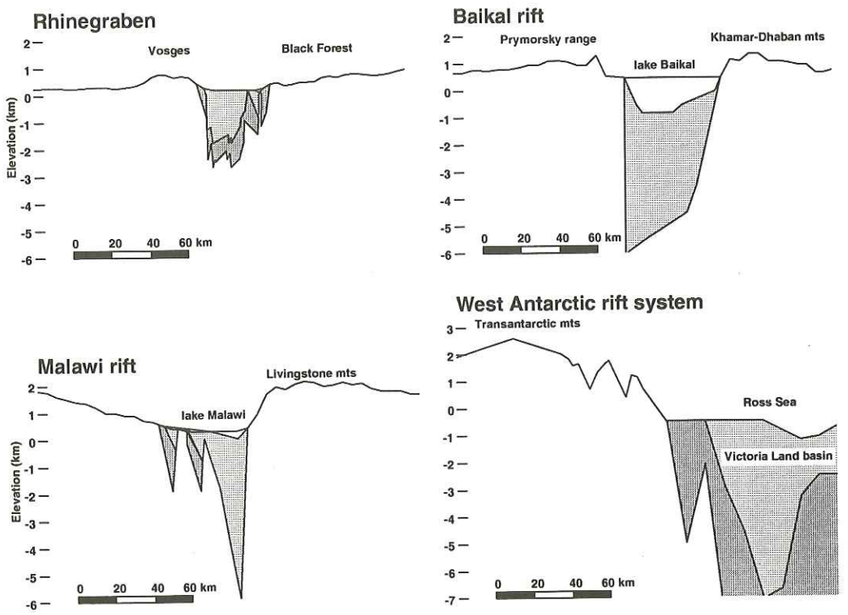

Figure 1-1. Simplified topographic and structural profiles through four intracontinental rifts and their flanks. Light shading in rift basin denotes syn-rift sediments, darker shading pre-rift sediments. Topography is from the ETOPO-5 database, except for the Transantarctic Mountains where it is compiled from Stern and Ten Brink (1989); structural cross sections after Brun et al. (1991; Rhinegraben), Scholz et al. (1993; Baikal Rift), Specht and Rosendahl (1989; Malawi Rift) and Davey and Cooper (1991a, west Antarctic rift system). Scale is the same for all profiles.

exerted by the pre-rift rheology of the lithosphere, as well as the magnitude of the extensional forces to which it is subjected (England, 1983; Buck, 1991; Bassi, 1991, 1995). Several attempts have been made to classify extensional basins according to geodynamic setting or structural characteristics (e.g., Bally, 1982; Reading, 1982; Sclater and Célerier, 1987; Ingersoll, 1988; Ziegler, 1995). The theory of plate tectonics has provided a framework to link continental rifts in a genetic sense with extensional basins and rifted margins (Wilson, 1966; Salveson, 1978; Bally, 1982; such a link was already proposed by Wegener, 1912). With increasing amounts of extension, continental rifts develop into wide extensional basins and eventually rifted continental margins (Figure 1-2). This development is particularly clear, and was first described, in the East African - Ethiopian - Red Sea rift system (Girdler et al., 1969; Baker et al., 1972). The duration of the rifting stage varies widely from one rift to another (Ziegler, 1995), the evolution from initial extension to continental break-up taking anything from ~5 My (e.g., Red Sea) to >250 My (Norwegian margin). The evolution of a rift may stop

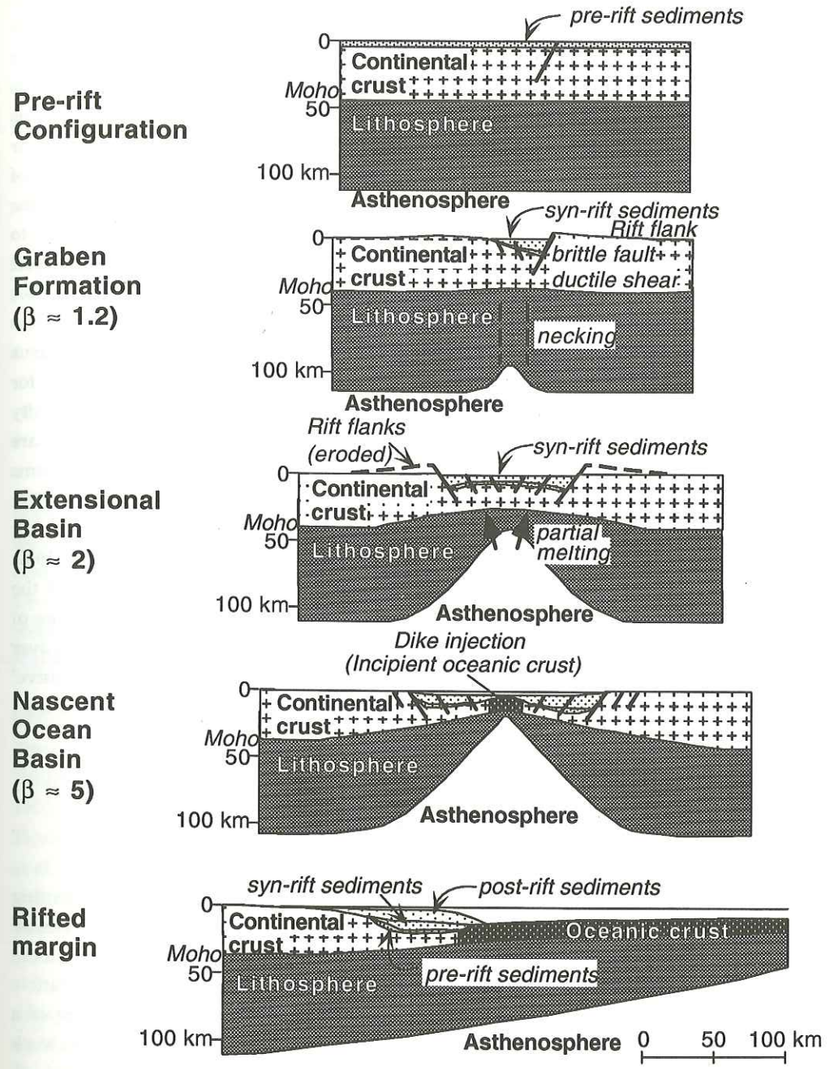

Figure 1-2. Diagramatic model of the evolution of a continental rift to an extensional basin and eventually a rifted margin (modified from Salveson, 1978).

during any phase, leaving a failed or paleo-rift.

The processes causing continental rift formation have been debated since rifts were first described in the last century (cf. Suess, 1909 for an early overview). Cloos (1939) is generally credited for establishing the extensional nature of rifts, although some of his ideas were probably based on pioneering work by de Beaumont, Gregory and Suess. Cloos envisaged crustal doming and the resulting extensional stresses as the main driving force for rifting. Vening-Meinesz (1950) provided a mechanical basis for the coincident subsidence of grabens and uplift of their flanks across a border fault in an extensional setting. Since the early seventies, the recognition of the role of continental rifting in plate tectonics has led to an increased interest in rifts, reflected in a large number of publications related to the subject (e.g., Ramberg and Neumann, 1978; Illies, 1981; Morgan and Baker, 1983; Coward et al., 1987; Ramberg et al., 1987; Gangi, 1991; Ziegler, 1992; Landon, 1994). Much of the attention has been focused on the controversy concerning the driving forces of extension, i.e. 'active' versus 'passive' rifting (Şengör and Burke, 1978). In active rifting models, the driving force for extension is uplift or doming of the crust as a result of impingement of hot, low density mantle material (Burke and Dewey, 1973). In passive rifting models, extensional stresses are created by horizontal forces in the lithosphere, which result from plate driving mechanisms and are transmitted from plate boundaries (Turcotte and Oxburgh, 1973; McKenzie, 1978; Salveson, 1978). Before the advent of plate tectonics, the static view of the earth implied that active rifting was generally accepted as the mechanism driving extension (e.g., Cloos, 1939; Holmes, 1965). However, during the last twenty years it has become apparent that the initiation and evolution of most continental rifts can be explained as being a consequence of plate driving forces (e.g., Ziegler, 1995), which cause consistently oriented stress patterns over large regions (Zoback et al., 1989). As most continental rifts display both 'active' and 'passive' features, one can question whether this fundamental genetic distinction is still justified (e.g., Bois, 1993; Wilson, 1993).

1.2 Mechanisms of rift formation

The last twenty years have seen the advent of a large variety of hypotheses concerning continental rift formation and evolution. In a landmark paper, Artemjev and Artyushkov (1971) showed that previous models of rift formation by subsidence of wedge shaped blocks along crustal scale normal faults (e.g., Cloos, 1939; Vening-Meinesz, 1950) were incompatible with seismic and gravity data for the Baikal rift, and suggested extensional necking of a brittle-ductile lithosphere as the main mechanism of rift formation. Some aspects of this work only resurfaced 18 years later (e.g., Braun and Beaumont, 1989a).

McKenzie (1978) provided an elegant mathematical formulation for the local isostatic response of the lithosphere to extension induced thinning and heating (Figure 1-3). This model explains the first order patterns of extensional basin subsidence and has become very

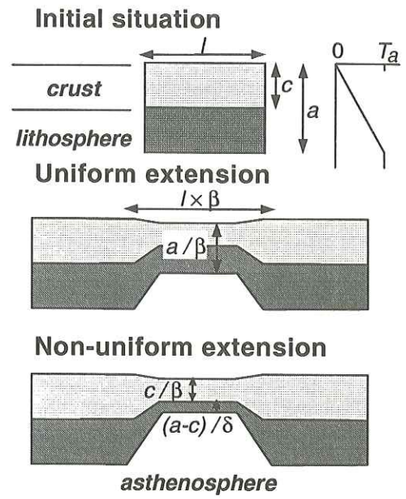

Figure 1-3. Instantaneous stretching models. The pre-rift (top) and immediate post-rift crustal and lithospheric thicknesses are shown for uniform (McKenzie, 1978; centre) and non-uniform (Royden and Keen, 1980; bottom) extension, along with a simplified thermal structure. Modified from Keen (1987).

popular (e.g., Sclater and Christie, 1980; Le Pichon and Sibuet, 1981; Barton and Wood, 1984; see Sclater and Célerier (1987) for a review). Early refinements of the model included the effects of finite duration (instead of instantaneous) rifting (Jarvis and McKenzie, 1980; Cochran, 1983) and the incorporation of two-dimensionality by introducing a flexural response of the lithosphere to sediment loading (Watts et al., 1982) and lateral heat transport (Cochran, 1983).

The main aspect of continental rift formation that remains unexplained by the uniform thinning model of McKenzie (1978) is the intimate association of uplift and subsidence. Practically all continental rifts are associated with uplifted regions; broad domal swells (Holmes, 1965; Fuchs et al., 1981) and/or more linear rift flanks (Vening-Meinesz, 1950; Bott, 1976; cf. Figure 1-1). Rift flank uplift can produce rather spectacular topography: the Ruwenzori massif of East Africa (Holmes, 1965) and the Transantarctic Mountains (Fitzgerald et al., 1987) both rise >3 km over the surface of the rifts adjoining them, the latter also being over 3000 km in length. A number of rifted margins around the world also show prominent escarpment systems, associated with a step in elevation of more than a km (cf. Figure 2-2). A number of mechanisms have been proposed to explain these uplifts.

An adaptation of the uniform stretching model involved heterogeneous (depth dependent) thinning of the lithosphere, in order to provide a thermal support for rift flank uplifts (Royden and Keen, 1980; Beaumont et al., 1982; Hellinger and Sclater, 1983; Figure 1-3). Depth-dependent stretching requires large strain gradients within the sub-crustal lithosphere and is not compatible with the condition of volume conservation (e.g., Rowley and Sahagian, 1986). An alternative thermal model suggested that small scale convection in the sub-lithospheric mantle is induced by extension, producing excess lithospheric thinning

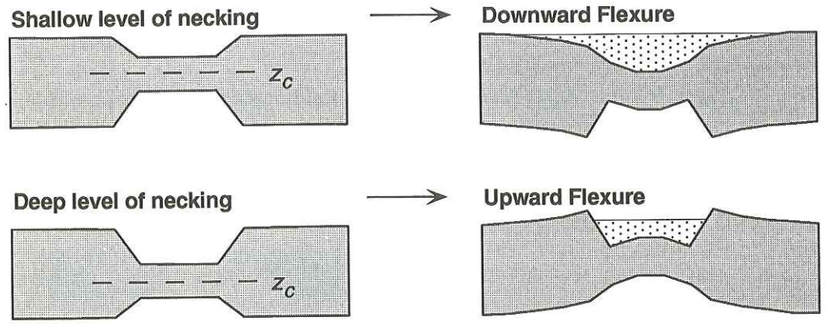

Figure 1-4. Concept of lithospheric necking (after Kooi, 1991; modified from Braun and Beaumont, 1989a). The level of necking z_c is defined as the level of no vertical motion, in the absence of isostatic forces. A shallow level of necking (top) creates a surface depression which is shallower than the isostatically compensated basin depth and results in a downward state of flexure. Conversely, for a deep level of necking (bottom) an upward load acts on the lithosphere, resulting in flexurally supported rift flanks.

by thermal erosion (Keen, 1985; Steckler, 1985; Buck, 1986; Fleitout et al., 1986).

A number of observations, however, raise doubts on the concept of thermal support of rift flank uplifts. For instance, thermal uplift is by its nature transient and thermally supported rift flanks should subside within the thermal time constant of the lithosphere (~60 My). In reality, however, rift flank uplifts may exist for substantially longer times than this (cf. Weissel and Karner, 1989). Strongly negative Bouguer gravity anomalies under rift flanks, which would be expected if large amounts of hot, low density material are present, are not generally observed. Instead, the pattern of residual anomalies over continental rifts suggests that the lithosphere retains finite strength during rifting and that rift flanks are mechanically supported by upward flexure (Bullard, 1936; Vening-Meinesz, 1950; Artemjev and Artyushkov, 1971; Bott, 1976; Weissel and Karner, 1989; Ebinger et al., 1991; Kooi et al., 1992). Braun and Beaumont (1989a,b) provided a dynamic explanation for this behaviour, by suggesting that upon extension, a rheologically layered lithosphere necks around its strongest layer. If this level of necking is sufficiently deep, a surface depression which is deeper than the isostatically compensated basin depth (i.e. the basin depth predicted by the McKenzie (1978) model) is created, and an upward state of flexure is induced (Figure 1-4; cf. Section 2.3.1).

An entirely different approach was taken by Wernicke (1985) who explained uplift adjacent to subsiding basins by large scale simple shear along a shear zone cutting the entire lithosphere (Figure 1-5). His model was based on observations in the Basin and Range province of western North America. Subsequent dynamic modelling suggested that lithospheric simple shear can only be initiated under the very specific condition of a thick hot crust (Braun and Beaumont, 1989b, Buck, 1991; Govers, 1993) and this style of extension

Figure 1-5. Models for lithospheric pure shear (McKenzie, 1978; top), simple shear (Wernicke, 1985; centre) and combined shear (Lister et al., 1986; bottom) extension. Modified from Ziegler (1988).

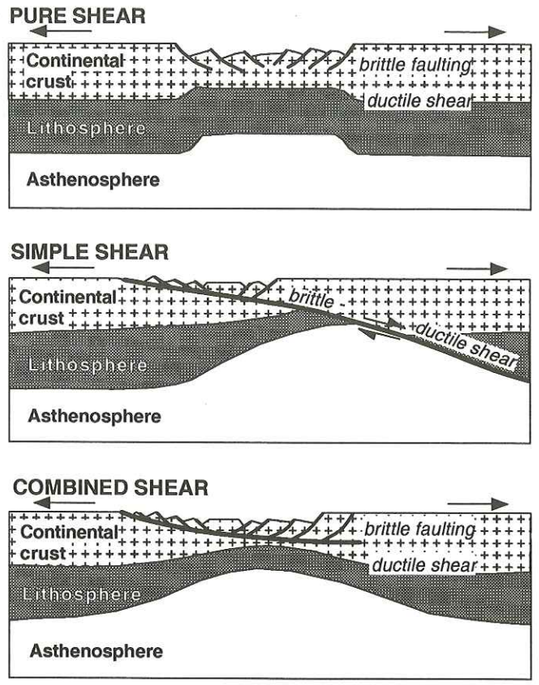

would thus be limited to post-orogenic extensional collapse (Dewey, 1988). Alternatively, intra-crustal detachments could accommodate shear strain between the upper crust and mantle, enabling an offset between the loci of crustal and sub-crustal extension (Ussami et al., 1986; Lister et al., 1986, 1991). In such a model thermal and mechanical processes may interact to produce uplifted rift flanks (Kusznir et al., 1987; Weissel and Karner, 1989).

In contrast to the linear and relatively narrow (<200 km) rift flanks adjoining continental rifts, the broad (~1000 km wavelength) domal swells that are associated with, for instance, the East African rift system, the Rhinegraben and the Baikal rift, are characterised by long wavelength negative Bouguer anomalies (e.g., Bullard, 1936; Girdler et al., 1969; Fairhead, 1976; Ebinger et al., 1989; Zorin et al., 1989). Such large radius domes are probably dynamically compensated by hot and partially molten upwelling asthenosphere (Crough, 1978; Houseman and England, 1986; Neugebauer, 1987; Ebinger et al., 1989; Westaway, 1993). Finally, crustal thickening by underplating, due to partial melting of the upwelling mantle, can cause permanent uplift of large regions bordering volcanically active rifts (Cox, 1980, 1989; McKenzie, 1984; White and McKenzie, 1989; Gallagher et al., 1994a).

Verification of models

The hypotheses listed above have nearly all been expressed as quantitative models. The main goal of tectonic modelling is to study the interaction of different geodynamic processes and to illustrate how these might result in particular geological features. To this end, numerous experimental or 'physical' models have been designed, using a wide variety of scaled down analogues of earth materials. The rapid increase of computing power during the 1980's has allowed the advent of a 'dynamic' modelling approach, in which the deformation of a model lithosphere with a specified rheology, subjected to specified forces and boundary conditions, is calculated. In a 'kinematic' modelling approach, the deformation of the lithosphere itself is prescribed and it is the expression of this deformation, in terms of vertical motions and thermal history, which is calculated. As the choice of input parameters is usually less limited in kinematic than in dynamic models, internal consistency is less guaranteed, and conclusions regarding the deformation scenario may be non-unique. On the other hand, a free search of input parameters and deformation scenarios, in order to provide a best fit to certain observed features, is more easily achieved using kinematic models; the predictions of dynamic models can usually only be compared to observations in a qualitative manner (e.g, Sawyer and Harry, 1991; Bassi et al., 1993). In this sense, dynamic and kinematic models can be viewed as working from two ends towards a common goal; in dynamic modelling the response of the lithosphere to specific processes is predicted, whereas in kinematic modelling the aim is to extract these processes from the observable geological record.

Geological and geophysical data which have been used as constraints on kinematic models of rifting comprise crustal structure, as inferred from deep seismic reflection and refraction data, gravity and heat flow (e.g., Burrus et al., 1987; Ebinger et al., 1991; Kooi et al., 1992; Janssen et al., 1993; Spadini et al., 1995a). Basin subsidence is recorded by its sedimentary infill, and the stratigraphy and paleo-bathymetry of extensional basins may be used to reconstruct the stretching history (e.g., Keen and Beaumont, 1990; Kooi, 1991; Cloetingh et al., 1992a; Reemst et al., 1994; Spadini et al., 1995b). Thermal maturation of basin sediments constrains the thermal history of a basin (e.g., Issler and Beaumont, 1989). However, whereas the subsidence history of extensional basins has been extensively studied from the stratigraphic record, the uplift and erosion of rift flanks leave, by their nature, no easily recoverable record. Where a known pre-rift stratigraphy has been eroded from the flanks, recognisable erosion fragments in the basin fill may provide some clues (Garfunkel, 1988) but most rift flanks expose laterally homogeneous crystalline basement. In this case, practically the only record of rift flank uplift is provided by low temperature thermochronological techniques, of which apatite fission track thermochronology is, at present, the most valuable.

1.3 APATITE FISSION TRACK THERMOCHRONOLOGY

Over the past decade, apatite fission track thermochronology has become a well established and widely used technique to constrain the low temperature (≤125°C) thermal histories of rocks. Excellent reviews of the technique have been provided by Green et al. (1989a), Hurford (1991), Dumitru et al. (1991), Ravenhurst and Donelick (1992), Brown et al. (1994) and Andriessen (1995), while an in-depth discussion of the theory can be found in Fleischer et al. (1975) and Wagner and Van den haute (1992).

Fission tracks are damage zones in the crystal lattice that have been formed by spontaneous fission of ^{238}U. Upon fission, two positively charged high-energy fragments are created that are propelled away from each other, creating a single linear ionisation trail. The tracks are originally 15-20 µm long and only 25-50 Å wide, their length depending on the crystal density. They become visible under an optical microscope (500-1000× magnification) when an internal surface of the crystal is polished and chemically etched (Figure 1-6). As each spontaneous fission event creates one fission track, the track density is determined by the rate of fission decay, the concentration of ^{238}U and the 'age' of the sample. The half life for spontaneous fission of ^{238}U is ~9.9×10^{15} y (Fleischer et al., 1975). A simple and accurate way to determine the uranium concentration is to irradiate the sample with thermal neutrons, in a nuclear reactor. This causes the isotope ^{235}U to fission, inducing a new set of tracks. The $^{235}U/^{238}U$ isotope abundance ratio is constant, so that the ^{238}U abundance can be calculated from the induced track density. The fission track age equation then becomes:

$$t = \frac{1}{\lambda_D} \ln\left[1 + \frac{\lambda_D \phi \sigma c I \rho_s}{\lambda_f \rho_i}\right] \qquad (1.1)$$

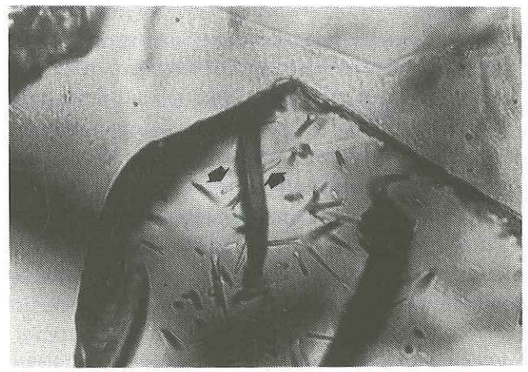

Figure 1-6. Photomicrograph of a polished and etched section through an apatite crystal. Etched fission tracks intersecting the surface are clearly visible as cones. Arrows point to a horizontal confined track. Length of confined track is ~15 µm.

in which λ_D = total decay constant for ^{238}U (1.551×10^{-10} y^{-1}); λ_f = spontaneous fission decay constant for ^{238}U (~1×10^{-16} y^{-1}); $c = 2\pi/4\pi$ geometry factor; $I = {}^{235}U/{}^{238}U$ isotope abundance ratio (7.253×10^{-3}); σ = thermal neutron fission cross section for ^{235}U (580.2×10^{-24} cm^{-2}); ϕ = thermal neutron fluence ($cm^{-2}s^{-1}$); ρ_s = spontaneous track density and ρ_i = induced track density in the sample (Hurford, 1990).

There are a number of parameters in the equation which are either poorly known (λ_f) or difficult to determine accurately (ϕ). This problem is circumvented if a ζ-calibration approach (Hurford and Green, 1983) is adopted. The constants in the equation are then taken together in a ζ factor:

$$\zeta = \frac{\phi \sigma I}{\lambda_f \rho_d} \qquad (1.2)$$

with ρ_d = the induced track density in a dosimeter glass with known U content that has been irradiated with the sample. ζ is calibrated against age standards of known age (Hurford, 1990).

Two fission track dating techniques are commonly used. In the population method, the sample is split into two portions, one of which is etched to reveal spontaneous tracks, the other one is completely annealed and irradiated to count induced tracks. A method which has become more popular during recent years is the external detector method, where induced tracks are counted in a thin sheet of muscovite (the external detector) secured against the polished mineral surface during irradiation. This approach has the advantage that inter-grain variability in track densities is revealed, so that statistical tests of the significance of the fission track age can be performed.

1.3.1 Annealing of fission tracks and confined track length distributions

The damage in the crystal lattice composed by a fission track is not stable but will tend to be repaired by a process called annealing. Annealing is a diffusive process which takes place at strongly temperature dependent rates. As a result of annealing, the etchable length of a track, which is similar for all tracks upon their formation, will be shortened (Green et al., 1986; Carlson, 1990). Because the mean length of the tracks in a sample determines the probability that they intersect an internal surface, the track density (and thus the fission track age) are also reduced during annealing (Green, 1988).

Annealing under geological conditions has been studied in apatites recovered from drill cores (Naeser, 1979, 1981; Gleadow and Duddy, 1981). These studies have shown that the temperature of total annealing is 120±10°C for apatite. Above these temperatures, annealing takes place at a faster rate than track production, so that the fission track age becomes zero. Although temperature is the most important factor controlling annealing, additional controls are exerted by the duration of heating (Naeser, 1981; Gleadow and Duddy, 1981), the chemistry of the apatites (most important is the Cl/(F + Cl) ratio; Green

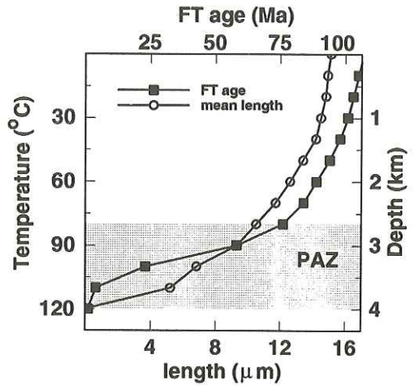

Figure 1-7. Variation of fission track age and mean track length with temperature, calculated using the annealing model of Laslett et al. (1987; cf. Appendix 1), for a 100 Ma stable thermal regime. A depth scale is added assuming a 30°C/km geotherm. Both fission track age and mean track length decrease rapidly between 80-120°C in the partial annealing zone (PAZ).

et al., 1986, 1989a) and the crystallographic orientation of the tracks (Green et al., 1986; Donelick et al., 1990). The amount of annealing increases non-linearly with temperature (Figure 1-7). Below ~60°C annealing rates are very slow, they increase rapidly in the temperature range of 60-120°C; this interval has been termed the partial annealing zone (Naeser, 1979; Wagner, 1979). For the higher temperature zircon and sphene fission track systems, the annealing temperatures are known with much less certainty, primarily because of sparsity of data, as the annealing temperatures for zircon and sphene are only encountered in ultra deep drill holes (e.g., Jacobs et al., 1993; Rohrman, manuscript in prep.).

The process of annealing can be quantified by measuring the lengths of horizontal confined tracks (Gleadow et al., 1986), i.e. tracks which do not cut the surface but have been etched because they intersect cracks or other tracks (cf. Figure 1-6). Because tracks are formed continuously, each track experiences a different portion of the thermal history of the sample. Thus, the track length distribution, obtained by measuring the lengths of a sufficient number of confined tracks (preferably ≥100), bears information on the thermal history experienced by the sample. The kinetics of fission track annealing have been established by laboratory experiments (Green et al., 1986; Crowley et al., 1991), enabling a quantitative determination of the relationship between thermal history and track length distribution (Laslett et al., 1987; Duddy et al., 1988; Green et al., 1989b; Crowley et al., 1991; Corrigan, 1991; Lutz and Omar, 1991). The mathematical description of a model that relates track length distribution to thermal history is presented in Appendix 1. Although such models, at present, probably still contain systematic errors because of the limited amount of experimental data on which they depend (e.g., Corrigan, 1993; Ravenhurst et al., 1994; Wagner et al., 1994), they are extremely useful in delimiting possible ranges of thermal histories.

Figure 1-7 shows how fission track age and mean track length decrease with increasing temperature under thermally stable conditions. Because of the chemical and crystallographic dependence of annealing rates, track length distributions (measured as the standard deviation σ) become wider with increasing annealing, as does the distribution of

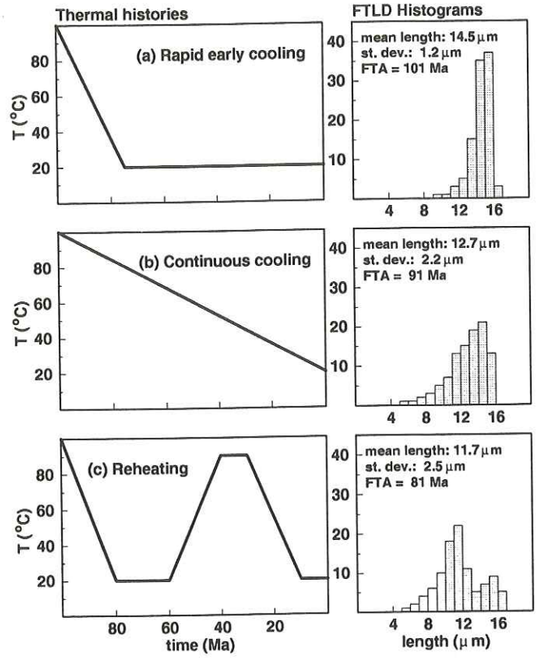

Figure 1-8. Three model thermal histories with their corresponding predicted fission track age and track length distributions. All three histories start at 100 Ma at 100°C: (a) rapid cooling; (b) slow, continuous cooling; (c) reheating.

single grain ages. An example of samples which have experienced different thermal histories is given in Figure 1-8. In samples which have cooled rapidly from temperatures >120°C, for instance volcanics which were never reheated after extrusion, little annealing has occurred; as a result, track length distributions are long and narrow and the fission track age faithfully records the time at which the sample cooled through 120°C (Figure 1-8(a)). On the other hand, samples which have cooled more slowly, for instance basement rocks which were slowly exhumed, have shorter mean track lengths, wider track length distributions and a fission track age which is not simply related to a cooling 'event' (Figure 1-8(b)). The situation becomes even more complicated in samples which were reheated, for instance after deposition and burial in a sedimentary basin. Such a thermal history gives rise to complicated bimodal track length distributions, with one population of tracks formed before and the other one after reheating, and a fission track age that is difficult to interpret (Figure 1-8(c)). These examples indicate that track length information is essential in order to meaningfully interpret a fission track age (Gleadow et al., 1986; Green et al., 1989a).

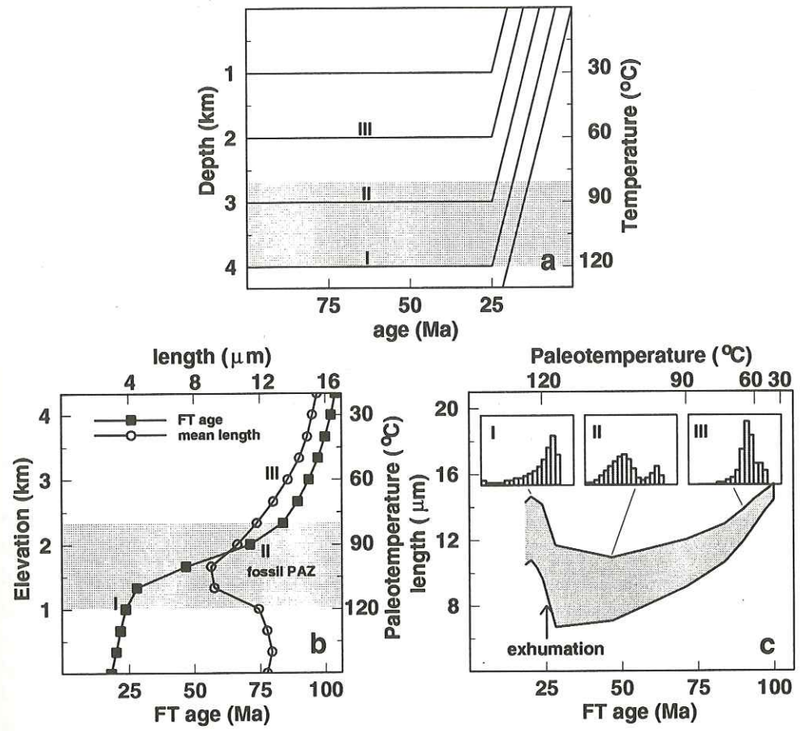

Figure 1-9. (a) Exhumation paths of rocks from different structural levels for a history of 5 km exhumation from 25 Ma onwards; labels I, II and III indicate rocks exhumed from below, within and above the partial annealing zone (shaded) these are also indicated in (b) and (c). (b) Resulting pattern of fission track ages and mean track lengths, the base of the fossil PAZ is characterized by a break in slope in the age-elevation plot and records the amount of exhumation as well as the timing of its onset. (c) Resulting age-length plot; shaded area represents mean length ± standard deviation for samples from different paleotemperatures (scale on top). Samples from the base of the fossil PAZ produce the low-age peak in the diagram and date the onset of exhumation. Insets show modelled fission track length distributions for 'samples' I, II and III.

1.3.2 Fission track profiles: constraints on tectono-thermal histories and vertical motions

Under tectonically stable conditions, fission track age and mean track length decrease with temperature, and hence depth (Figure 1-7). When a tectonic block cools as a result of exhumation, remnants of this characteristic pattern may be retained, producing a trend of increasing fission track ages with elevation (Wagner and Reimer, 1972; Figure 1-9). The base

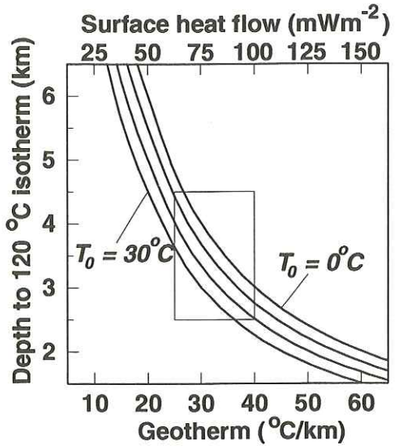

Figure 1-10. Relationship between geothermal gradient and depth to the 120°C isotherm (= total annealing temperature for apatite fission tracks) for surface temperatures T_0 = 0, 10, 20 and 30°C. Box indicates conditions most commonly encountered.

of the fossil (exhumed) partial annealing zone, when exposed, will produce a characteristic break in slope in the age-elevation plot, the age of which approximates the initiation of cooling/exhumation. Samples from below the break in slope were exhumed from temperatures ≥120°C, and contain only tracks formed during and after cooling. In contrast, samples above the break in slope contain two generations of tracks, one from before and one from after the onset of cooling (Figure 1-9(b)). The amount of exhumation can thus be derived from the elevation of the break in slope (Gleadow and Fitzgerald, 1987). The actual shape of the age-elevation plot, and the trend of track length distributions with elevation, will depend on the amount and rate of exhumation (Brown et al., 1994).

The characteristic relationship between track length distributions and thermal history can also be used to constrain the amount and timing of exhumation (e.g., Green, 1986; Omar et al., 1989). A plot of fission track age against mean track length of an area that has undergone cooling will show a characteristic 'boomerang' shape (Figure 1-9(c)); the length peak at young ages corresponds to samples which were exhumed from the base of the partial annealing zone, and thus retain only tracks formed after the onset of cooling.

It should be noted that fission tracks strictly record cooling of a sample only. Where fission track data show the characteristic relationship to elevation described above, or when additional geological data are available (e.g., absence of contemporaneous magmatic or geothermal activity, correspondence of cooling intervals with periods of sediment deposition in nearby sedimentary basins, presence of planation surfaces of corresponding age), cooling can be interpreted to result from exhumation. The amount of exhumation can be quantified if the geothermal gradient is known (Figure 1-10). In most cases, cooling from 120°C represents 3.5±1 km of exhumation. In the past, there has been considerable confusion concerning the difference between (tectonic) uplift, exhumation, and cooling (e.g., England and Molnar, 1990; Molnar and England, 1990). This was caused partly by the practice of

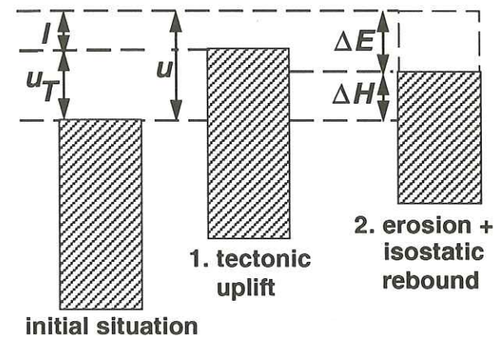

Figure 1-11. Cartoon to show the relationships between surface uplift (u), tectonic uplift (u_T), isostatic rebound (I), change in elevation (ΔH) and exhumation or denudation (ΔE).

reporting thermochronologically derived cooling rates as 'uplift' rates (e.g., Hurford, 1991). In this thesis, I will use the terminology that has been devised in the last few years (Brown, 1991; Kamp and Tippett, 1993; Brown et al., 1994; cf. Figure 1-11). *Uplift* is the (positive) vertical movement of a reference surface with respect to a fixed level (for instance sea level corrected for eustatic movements). Note that (surface) uplift is not the same as change in regional elevation, and can only be determined if the position of a marker horizon and/or the amount of erosion are known. Surface uplift has two components: *tectonic uplift* which has an internal (tectonic) cause and *isostatic rebound* as a response to erosion. *Erosion* is the physical removal of material from (a part of) the earth's surface, and leads to *denudation* (the movement of the surface downward with respect to a rock sample) or *exhumation* (the upward movement of a rock sample towards the surface). The quantitative relationships between exhumation, tectonic uplift and isostatic rebound are treated in Section 2.3.2. The amount of denudation or exhumation is measured by fission track thermochronology, if the geothermal gradient is known. Exhumation may, in itself, disturb the geothermal gradient by compressing isotherms in the upper crust, but this only influences thermochronological data for extremely high (>500 m/My) exhumation rates (Stüwe et al., 1994).

1.4 Scope and outline of the thesis

The primary goal of the studies reported in this thesis was to incorporate the thermo-tectonic evolution of rifted basins and their margins, as recorded by fission track thermochronological data, into numerical models for rifted basin formation and evolution. Such data provide an additional constraint on these models, enabling a further discrimination between geologically feasible and unrealistic hypotheses. To this end, numerical modelling studies were performed, based on published (Chapter 2) as well as newly collected (Chapters 3-5) fission track data. As the objective of these studies is to incorporate observations on vertical motions into tectonic models, a kinematic modelling approach is employed throughout. The kinematic

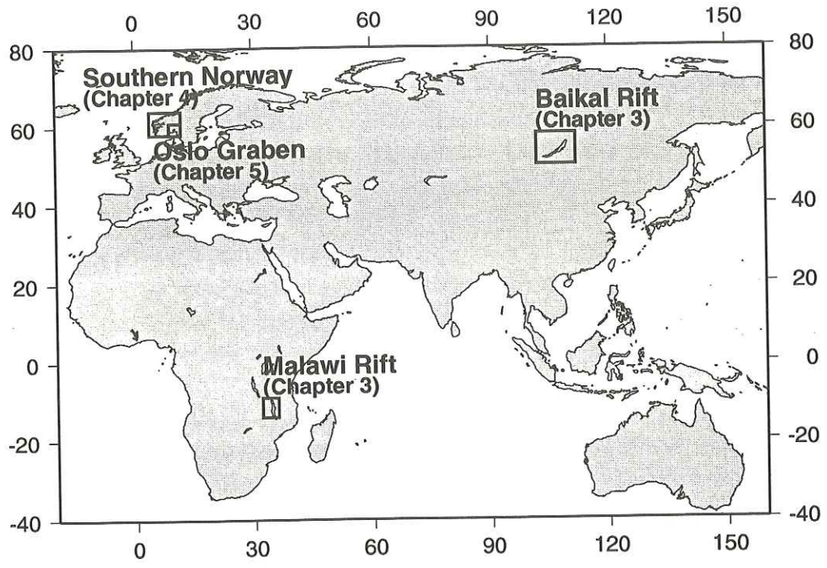

Figure 1-12. Location of study areas described in this thesis.

modelling results are interpreted by comparing them with predictions of rheological and dynamic models of extension.

Chapter 2 introduces the role of different uplift mechanisms in creating the currently observed topography and erosion patterns at rifted continental margins. A number of fission track studies have concluded that significant amounts (≥3 km) of syn- and post-rift erosion have affected the seaward areas of rifted margins (e.g., Moore et al., 1986; Bohannon et al., 1989; Omar et al., 1989; Dumitru et al., 1991; Gallagher et al., 1994a). It is shown in Chapter 2 that, for reasonable lithospheric strength values, such amounts of erosion require several kilometres of tectonic rift flank uplift. Forward thermo-mechanical modelling suggests that thermal mechanisms fail to explain the inferred tectonic uplift patterns; flexural uplift as a result of lithospheric necking appears to be a much more plausible mechanism. In order to reconstruct the uplift history from the exhumation paths recorded by fission track data, a surface processes model is developed which relates erosion rates to topography. Two important results are obtained: (1) an uplifted rift flank should degrade by erosion within 50-100 My; the development of an escarpment at rifted continental margins is, thus, in itself not an indication of tectonic rift flank uplift but results from the existence of a high elevation interior plateau, erosional base level lowering as a consequence of rifting and regional isostatic response to erosion of the margin; (2) fission track thermochronology dates the onset

of rapid erosion which coincides with the initiation of strong relief; fission track ages which are younger than the age of rifting can thus not be unambiguously interpreted as excluding pre-rift uplift. The timing of margin uplift can only be established by careful track length analysis and integration with regional stratigraphic data.

In Chapter 3 mechanisms of rift flank uplift are studied in more detail by looking at topography and erosion adjacent to two young intracontinental rifts: the Baikal rift (SE Siberia) and the Malawi rift (East Africa). Several models of mechanical rift flank uplift are tested, including pure shear necking as well as combined shear detachment and flexural cantilever models. It is shown that a flexural cantilever model, in which rift flanks are supported by the low rigidity upper crust, is incompatible with the topography and amounts of erosion observed at these two rift systems. In contrast, rift flanks are supported by the strong sub-crustal lithosphere. The models generally predict mid-crustal levels of necking and/or detachment levels within the lower crust. These predictions are found to be in good agreement with the rheology of the lithosphere below these rift systems, inferred from seismology and gravity data as well as from its thermal and petrological (seismic) structure. Three dimensional modelling of flank uplift adjacent to the Baikal rift indicates that flexural mechanisms can not explain all of the observed topography; an additional source of buoyancy is required to support the anomalously high flanks and shallow basin in northern Baikal.

Chapter 4 discusses mechanism of post-rift 'passive' margin uplift, as exemplified by the morphotectonic evolution of southern Norway. Fission track thermochronology, together with the onshore geomorphological and offshore seismic-stratigraphic record, reveals two major Meso-Cenozoic erosional phases: one during the Triassic-Jurassic and the other one from the Neogene onwards. Triassic-Jurassic denudation is attributed to rift margin erosion as a result of base level lowering and flank uplift, as evidenced by thick continental clastic sequences deposited in the contemporaneously active half grabens of the North Sea basins. Neogene exhumation is shown to be the result of domal uplift with a maximum of ~1.5 km, centred below the high peaks of southern Norway. The correlation with the evolution of the North Atlantic region is discussed and a comparison is made with other studies of uplift around the North Atlantic. Possible mechanisms creating Neogene domal uplift are evaluated: it appears that no single proposed mechanism can explain all the geological and geophysical observations pertaining to Neogene uplift. A model that combines sub-lithospheric thermal erosion and build-up of compressional intraplate stresses comes closest.

In Chapter 5 the focus is turned towards the thermo-tectonic evolution of a magmatic continental rift. The magmatic evolution of the Permo-Carboniferous Oslo Graben is studied using a decompression melting model developed by Pedersen and Ro (1992) and Pedersen and van der Beek (1994). Modelling results suggest that the lithospheric solidus must have been reduced relative to anhydrous peridotite and that mantle thinning must have been significantly larger than crustal extension, in order to explain the observed amounts of melt. The lithospheric affinity of the mafic rocks, evidence against pre-rift uplift and low magma production rates indicate that Oslo Graben magmatism was not associated with a thermal

mantle plume. The lithosphere beneath the Oslo Graben was more 'wet' than 'hot' and magmatism was primarily caused by passive necking of the lithosphere. The syn- to post-rift thermal evolution of the Oslo Graben is studied employing zircon, sphene and apatite fission track thermochronology. It appears that the syn-rift thermal structure of the Oslo Graben was strongly influenced by magmatic and hydrothermal activity. In contrast, rifting left no thermal imprint onto the flank regions, suggesting that heating associated with rifting and magmatism was focussed into the currently exposed rift zone.

Finally, in Chapter 6 the main conclusions of this study are brought together and their implications for rheological models of the lithosphere and dynamic models of extension are discussed.

CHAPTER 2

TECTONIC UPLIFT, EROSION, AND ISOSTATIC REBOUND AT RIFTED CONTINENTAL MARGINS

2.1 INTRODUCTION

Rifted margins around the world can be divided into two archetypes according to their morphology: those which show a conspicuous escarpment separating a high-elevation interior plateau from a strongly dissected and low-lying exterior area, versus those with relatively subdued topography (Ollier, 1985; Summerfield, 1991a; Figures 2-1, 2-2). Escarpments at rifted continental margins constitute some of the larger morphological features on earth. Their existence affects drainage patterns on a sub-continental scale (Cox, 1989; Gilchrist et al., 1994) and exerts a first order control on the stratigraphy of the adjacent rifted basin (van Balen and Cloetingh, 1994). Escarpment systems direct sediment supply towards and away from rifted basins, supplying coarse clastics directly to the basin but diverting a large proportion of the sediments away from the rift, except where river systems breach the escarpment and become major point sources of sediment. The development of topography at rifted margins may play an important role in the evolution of climate, at least on a continental scale (Behrendt and Cooper, 1991; Raymo and Ruddiman, 1992). The hydraulic head provided by rift margin topography is critical in driving hydrothermal circulation in rifted basins (Steckler et al., 1993; van Balen and Cloetingh, 1994) and thus influences the distribution of petroleum and mineral deposits. Therefore, the generation and evolution of topography at rifted continental margins is an important tectonic and geomorphological problem.

Topography generation at rifted continental margins results from the interplay between tectonics, erosion and isostatic rebound (e.g., Stephenson and Lambeck, 1985; Gilchrist and Summerfield, 1990). The exact mechanism of escarpment formation remains, however, controversial. Escarpment systems have generally been interpreted in terms of tectonic rift margin uplift, as a result of thermal (e.g., Beaumont et al., 1982; Steckler, 1985), dynamic (Houseman and England, 1986; Westaway, 1993), or flexural (Braun and Beaumont, 1989; Weissel and Karner, 1989, Kooi et al., 1992) forces (see Section 1.2). The fact that a number of high-elevation rifted margins are associated with large continental flood basalt provinces (Figure 2-1), whose age broadly coincides with the age of rifting, could suggest that decompression melting and underplating play a role in creating the observed topography (Cox, 1980, 1989; McKenzie, 1984; White and McKenzie, 1989). Topographic asymmetry between conjugate continental margins have led some authors to stress the role of simple shear in continental breakup (Ussami et al., 1986; Lister et al., 1986, 1991). The long lived

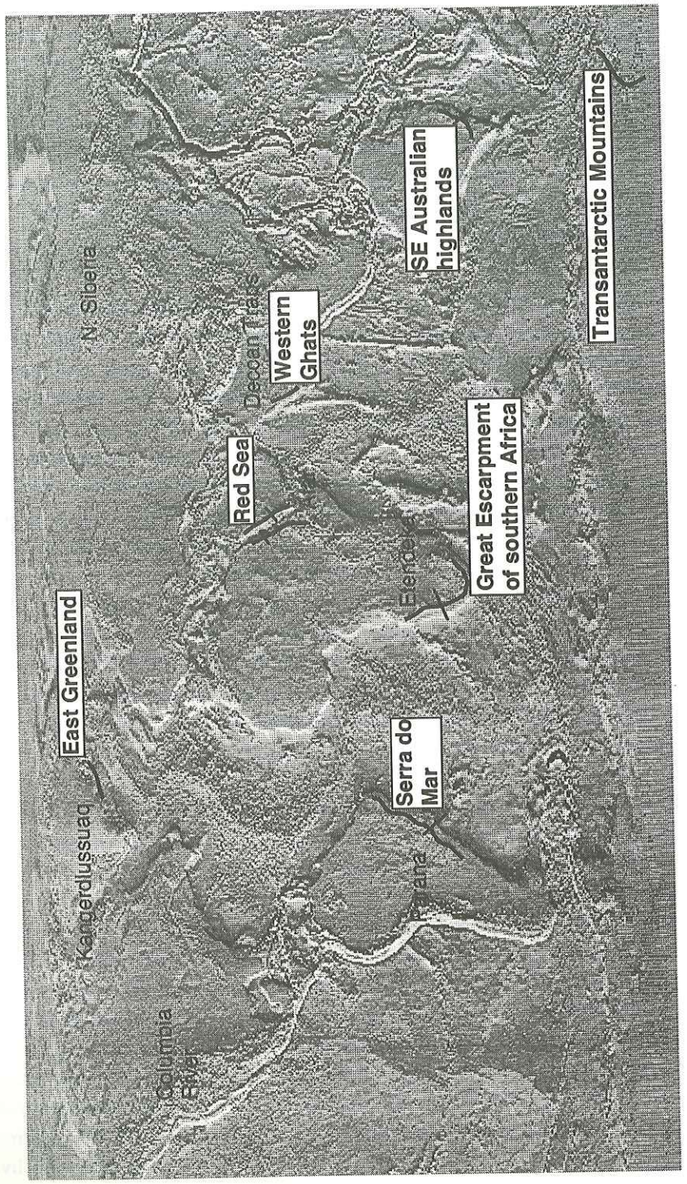

Figure 2-1. Map of continental topography and oceanic bathymetry, showing the locations of major erosional escarpments on rifted continental margins (bold names in boxes). Major continental flood basalt areas are also indicated (names in italics). Thin lines indicate locations of profiles shown in Figure 2-2.

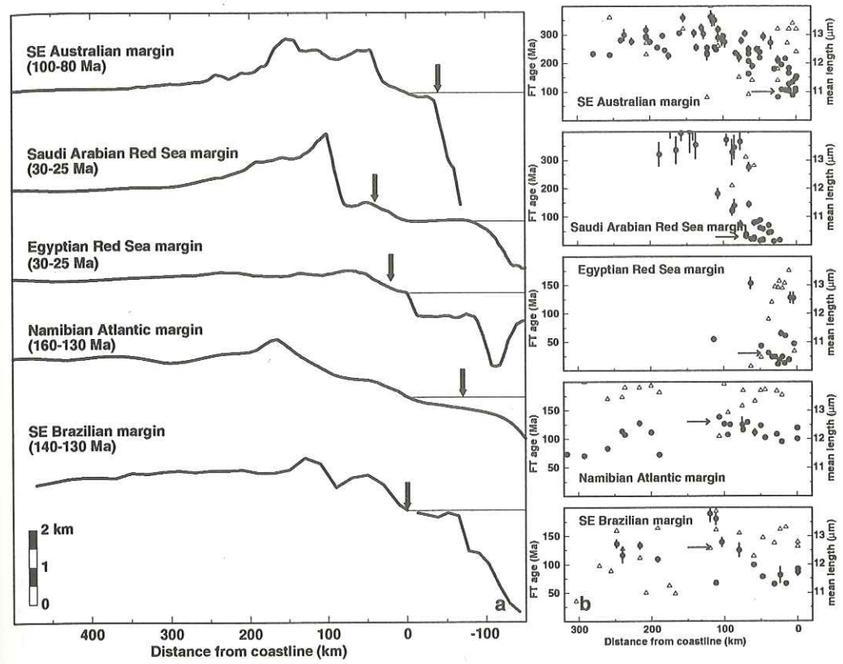

Figure 2-2. (a) Topographic profiles of selected rifted continental margins, showing the characteristic morphology of an escarpment separating an elevated interior plateau from a low lying exterior area, as well as the morphological variations between margins. The profiles are aligned at the coastline, arrows indicate the approximate location of the master fault bounding the rifted basin; the distance between this and the top of the escarpment represents the amount of erosional retreat. Numbers in parentheses indicate timing of rift phase. (b) Patterns of apatite fission track ages (dots with error bars) and mean track lengths (open triangles) across these margins. Arrows denote timing of initiation of rifting. Data from Moore et al. (1986) and Dumitru et al. (1991) for southeastern Australia, Bohannon et al. (1989) for Saudi Arabia, Omar et al. (1989) for Egypt, Brown et al. (1990) for Namibia, and Gallagher et al (1994a) for southeastern Brazil.

nature of a number of elevated margins, e.g. those bordering former Gondwanaland, has been used as an argument to rule out thermal or dynamic effects as the major force driving uplift because the thermal time constant of the lithosphere (~60 My) is too small to support rift shoulders existing since the Mesozoic (Weissel and Karner, 1989). For mechanisms resulting in permanent uplift (e.g. flexure, underplating) the life span of a rift shoulder should be controlled by an erosional time constant. Such a quantity is, however, poorly understood and may vary strongly according to non-tectonic factors such as climate and lithology.

The timing of topography generation with respect to rifting has important implications for geodynamic models of rift initiation and evolution. Whereas 'active' rifting models, involving mantle plume activity, predict regional plateau uplift preceding the main rifting phase by some 30-60 My (White and McKenzie, 1989), most 'passive' models predict rift flank uplift coinciding with extension (e.g. Steckler, 1985; Braun and Beaumont, 1989). Recently, a number of authors have suggested that regional uplift may also post-date the main rifting phase by 10-20 My (Menzies et al., 1992; Bois, 1993; Ziegler, 1995), suggesting a change in rift mode from 'passive' to 'active' during the evolution of the rift. Models of passive rifting that include a heat flow boundary condition at the base of the lithosphere and the effects of partial melting, predict that thermal uplift may peak as long as 50 My after the onset of rifting (e.g., Keen, 1987; Stephenson et al., 1989).

However, according to some authors (e.g., Gilchrist and Summerfield, 1990; Brown, 1991; Gallagher et al., 1994a; Tucker and Slingerland, 1994), escarpments flanking rifted margins are primarily maintained by a high-elevation interior plateau and regional isostatic response to denudation, as a result of base level lowering during rifting. Therefore, regional plateau uplift (acting on a subcontinental scale) might be the main tectonic mechanism responsible for the existence of escarpments, with rift flank uplift (affecting only the margin itself) playing a secondary role.

The erosional development of elevated rifted margins has been a subject of debate since the first models were developed more than 40 years ago (e.g., King, 1955). A currently widely held view is that the characteristic concave morphology of escarpment systems evolves by parallel erosional retreat (e.g., Ollier, 1985; Weissel, 1990; Summerfield, 1991b). Erosion rates are highest along the edge of the escarpment because of high relief. Intermediate erosion rates are recorded in the exterior areas where fluvial systems carry the debris of escarpment erosion away. Inland of the escarpment, erosion rates, with transport of material towards the hinterland, are generally low. High-elevation rifted margins generally expose crystalline basement rocks and the absence of a sedimentary record of flank evolution has long hampered comparison of models with data. During the last decade, apatite fission track thermochronology has made a large contribution in understanding the erosional evolution of rifted margins (cf. Brown et al., 1994).

Several fission track studies (e.g., Moore et al., 1986; Bohannon et al., 1989, Omar et al., 1989; Brown et al., 1990; Dumitru et al., 1991; Gallagher et al., 1994a) have revealed a typical pattern of fission track ages and track length distributions at rifted continental margins (Figure 2-2(b)). Samples from close to the basin edge typically have fission track ages younger than the age of rifting and relatively high mean track lengths, indicating that they experienced temperatures >120°C prior to rifting. Fission track ages usually increase rapidly over the escarpment, while mean lengths first decrease and then increase again inland, indicative of samples exhumed from subsequently lower temperature ranges (Figure 2-3). The observed patterns suggest that rocks exposed in the area seaward of the escarpment have been exhumed from depths of 3-4 km since the onset of rifting. These studies thus support the conceptual models of escarpment evolution and suggest a 'passive' origin for rift margin

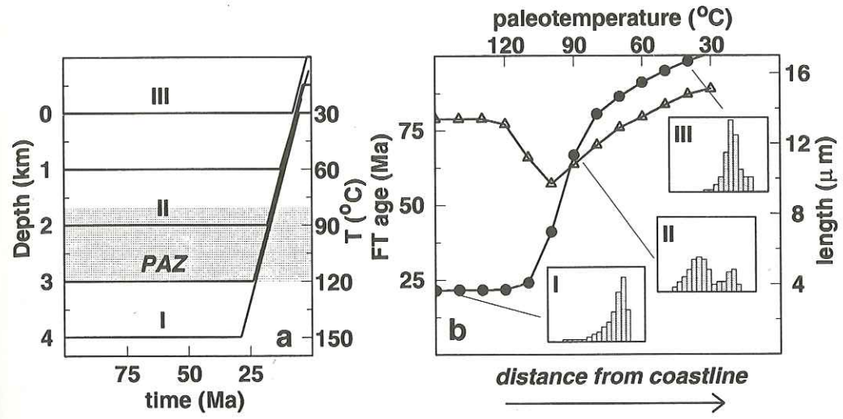

Figure 2-3. Conceptual model for interpreting fission track data across escarpments at rifted continental margins. (a) Simplified exhumation paths for a model of exhumation by escarpment retreat: samples from closest to the shoreline were exhumed from greatest depths. (b) Expected pattern of fission track ages (filled dots) and mean track lengths (open triangles). Fission track parameters were calculated using the quantitative annealing model of Laslett et al. (1987). Insets show modelled fission track length distributions for samples from close to the shoreline (I), the base (II) and top (III) of the escarpment, which have experienced the exhumation paths depicted in (a).

uplift.

In this chapter, I will first explore the roles of different mechanisms in creating rifted margin topography and derive a method to compare predicted uplift values with observations. Brown (1991) proposed a method to quantify tectonic uplift using apatite fission track data, analogous to backstripping of sedimentary basin strata. I extend this technique to the two-dimensional case, including a flexural response of the lithosphere. The results are compared to predictions of a thermo-mechanical forward model (Kooi, 1991; Kooi et al., 1992) with the purpose to determine the mechanisms causing rifted margin uplift and the kinematics of extension. I will then continue by focusing on the temporal evolution of rifted continental margins, combining the tectonic uplift patterns predicted by the forward model of rifted margin evolution with a surface processes model developed by Beaumont et al. (1992) and Kooi and Beaumont (1994), in order to predict the morphological evolution and erosional history of rifted continental margins. I will concentrate on questions such as: (1) the relative importance of regional elevation (plateau uplift) versus rift flank uplift; (2) the timing of uplift with respect to rifting; (3) the role of different tectonic (thermal/flexural) mechanisms in driving rift margin uplift.

Using this approach, I will present both general modelling results, to obtain an insight into how different assumptions and parameters affect model predictions, and apply the model to several case studies. For this purpose, a number of margins were selected where

sufficient data are available to test the model predictions. Specifically, the model is constrained by present-day topography and published fission track data, as well as by seismic and gravity data which image the crustal structure underlying the margins.

2.2 Regional examples; tectonic setting

2.2.1 The Saudi Arabian Red Sea Margin

Rifting in the central and southern Red Sea was initiated at approximately 30 Ma, lasted for about 5 My and led to continental break-up at 25 Ma (Bohannon, 1986; Bohannon and Eittreim, 1991). The Saudi Arabian Red Sea margin is characterized by a prominent escarpment which is located 100-150 km inland from the shoreline; the escarpment peaks rise up to 2000-2500 m while the interior Arabian platform lies at an elevation of around 1000 m. Major normal faults bounding the highly extended and intensively intruded Red Sea basement are encountered up to 40 km inland (Bohannon, 1986); the escarpment thus retreated approximately 100 km.

Apatite fission track ages for the Saudi Arabian Red Sea margin decrease from ~400 Ma inland of the escarpment to <30 Ma near the shoreline (Bohannon et al., 1989; Figure 2-2(b)), providing evidence for 3-4 km of erosion seaward of the escarpment since the onset of rifting. The high elevation of the Arabian platform indicates that continental-scale plateau uplift has also taken place. Late Eocene-Oligocene shallow marine sediments occur on the Arabian platform (Garfunkel, 1988; Bohannon et al., 1989), indicating that this uplift occurred simultaneously with or post-dated rifting. Camp and Roobol (1992) and Menzies et al. (1992) suggest that regional plateau uplift is the result of active mantle upwelling beneath the Arabian subcontinent which may have commenced as late as 15 Ma. In the northern Red Sea, conglomerates dated at 16-17 Ma seem to indicate increased uplift and erosion around that time (Garfunkel, 1988). However, fission track data from the Egyptian margin provide evidence for an onset of rift-related exhumation at, at least, 21 Ma (Omar et al., 1989; Steckler and Omar, 1994).

2.2.2 The Transantarctic Mountains

The Transantarctic Mountains transect the Antarctic continent from the Ross to the Weddell Seas and form the geographic, as well as tectonic, boundary between eastern and western Antarctica. They form the most impressive rift flank topography in the world today, with the highest peaks reaching >3000 m. (cf. Figure 1.1). The eastern Transantarctic Mountain front consists of a major fault-controlled escarpment with several intermediate steps (Fitzgerald, 1992, 1994). The mountain range does not show the common morphology of an elevated rifted margin. Instead, the (subglacial) basement lies below sea level inland of the mountain

range, so that the morphology of the range can be considered as that of a typical rift flank. The Transantarctic Mountains expose Precambrian basement and a Paleozoic sedimentary sequence (the Beacon Supergroup), capped by a thick Jurassic mafic sill (the Ferrar dolerite). The area inland of the highest peaks is covered by the Antarctic ice sheet, which reaches a thickness of approximately 3 km.

Gleadow and Fitzgerald (1987) and Fitzgerald (1992) presented results of extensive fission track surveys of the mountain range, mostly in the form of vertical profiles. Their data suggest that uplift and exhumation of the Transantarctic Mountains commenced at around 60 Ma, coeval with extension in the west Antarctic rift system (Cooper et al., 1991a). Maximum uplift and erosion seems to have occurred between the present-day locus of maximum elevation and the mountain front, approximately 20 km inland. More recent fission track data indicate that substantial Mesozoic uplift and erosion may have preceded the Cenozoic phase (Fitzgerald, 1994). The Victoria Land basin in the Ross Sea is underlain by a (probably) Mesozoic basin under which the basement reaches nearly 15 km depth (Cooper et al., 1991a). The Ross Sea covers the west Antarctic rift system, a wide area of probably highly extended continental crust; there is no evidence for oceanic crust underlying the sea (Cooper et al., 1991b). Several arguments (e.g., the geomorphology of the mountain range, stratigraphic patterns within the sediments of the west Antarctic rift system and the age of volcanics within the rift) suggest that rifting activity has been ongoing during the Cenozoic and is still active today (cf. Cooper et al., 1991a,b; Fitzgerald, 1992). There has been a vigorous debate concerning the most recent (<3.5 Ma) evolution of the mountain range, with some authors (e.g., Behrendt and Cooper, 1991) claiming major surface uplift during this time interval, while others (e.g., Wilch et al., 1993) maintain that the relief of the range has not changed dramatically during the late Cenozoic.

2.2.3 The southeastern Australian margin

The continental margin of (south) eastern Australia is characterised by the eastern highlands belt running along its length. The highest peaks of the eastern highlands are located approximately 100-150 km from the coastline, approximately 100 km inland from a major escarpment (Figure 2-2(a)). Maximum elevation is over 1500 m, while the Australian interior lies at an altitude below 200 m. The timing and origin of the uplift of the eastern highlands has been a subject of debate for nearly a century, with estimates for the initiation of uplift varying between the Paleozoic and Late Tertiary (e.g., Veevers, 1984; Lambeck and Stephenson, 1986; Wellman, 1987; cf. review by Bishop, 1988). The highlands expose rocks of the Tasman fold belt, which record extensive compressional deformation and widespread magmatism dating from late Paleozoic active margin orogenesis. This was presumably associated with the generation of high elevation and relief. Late Paleozoic-Mesozoic clastic sediments occur in the basins surrounding the eastern highlands, indicating that they were a source of sediments, and thus a topographic high, during this time (e.g. Lambeck and Stephenson,

1986). However, by the late Jurassic, the area could have developed into a platform region with little relief (Gallagher et al., 1994b).

Moore et al. (1986) and Dumitru et al. (1991) present apatite fission track data from southeastern Australia that indicate a thermal pulse between 100-80 Ma and significant (~2-3 km) erosion since then. Heating of the margin is suggested by strongly bimodal track length distributions in samples with intermediate ages, erosion by samples with young ages (≤80 Ma) and high mean lengths (Figure 2-2(b)). The inferred timing immediately precedes continental break-up in the Tasman Sea (79-72 Ma; Veevers, 1984), supporting a model in which the highlands were uplifted during rifting, with subsequent erosional retreat taking place (Ollier, 1982; Veevers, 1984). Fission track data from wells in the Mesozoic basins of eastern Australia (Gallagher et al., 1994b) support this interpretation; the eastern basins record ~2.5 km of erosion since the late Cretaceous - early Tertiary, while in the west erosion amounts to ≤1 km and commenced in the mid Tertiary.

The strong asymmetry between the uplifted southeastern Australian margin and the conjugate Lord Howe Rise, which subsided below sea level, led Etheridge et al. (1989) to propose that simple shear played an important role during breakup, with Australia constituting the upper-plate margin of the system. The more recent history of the highlands is also debated. Veevers (1984) and Wellman (1987) suggest that accelerated uplift and erosion may have occurred during the Cenozoic, coinciding with basaltic volcanism within the range, whereas Lambeck and Stephenson (1986) emphasize the role of passive erosion and isostatic rebound in the evolution of the highlands since the late Paleozoic.

2.2.4 The Namibian Atlantic Margin

The morphology of southern Africa is dominated by the 'Great Escarpment' (King, 1955, 1963) which separates the low-lying, high-relief coastal zones of Namibia and South Africa from the high-elevation (~1000 m) interior Kalahari plateau. The Great Escarpment lies 100 km or more inland in most areas, and is bordered by a topographic upwarp that directs drainage toward the interior (Gilchrist and Summerfield, 1990; Gilchrist et al., 1994).

The Great Escarpment is generally believed to have originated during breakup of Gondwanaland and opening of the South Atlantic (cf. Ollier, 1985). Rifting in the South Atlantic took place in the Late Jurassic - Early Cretaceous (~160-130 Ma; Gerrard and Smith, 1982). The major basin-bounding faults occur approximately 50 km offshore (Gerrard and Smith, 1982), so that escarpment retreat amounts to some 150 km.

The elevation of southern Africa prior to rifting is poorly constrained (Gilchrist et al. 1994); the last time that the area was close to sea level, as recorded by marine sediments, was during the late Paleozoic. The amount of post-rift erosion has been estimated from several geological markers to amount to 0.5-3.5 km over most of the region (Gilchrist et al., 1994), with the exterior area recording more denudation than the interior. Apatite fission track data (Brown et al., 1990) show a remarkably consistent pattern across the area (Figure 2-2(b)). In

contrast to other rifted margins, fission track ages do not increase significantly inland. Instead, both sea- and landward of the escarpment most samples have ages of 70-130 Ma, with pre-Cretaceous ages confined to the highest elevations. Brown et al. (1990) interpreted this pattern as indicating significant (~3 km) erosion over most of southern Africa during the Cretaceous. Unconsolidated late Mesozoic sediments encountered in the Kalahari and Namib deserts suggest that most denudation occurred prior to the Cenozoic (Gilchrist et al., 1994).

The inferred high rates of denudation during the Cretaceous are consistent with the offshore sedimentary record (Gerrard and Smith, 1982; Brown et al., 1990). The Orange River basin accumulated large amounts of sediment during the late Cretaceous. The sudden surge in sediment supply can be explained by breaching of the escarpment and capture of the continental interior drainage basin by the Orange River during this time (Gilchrist et al., 1994).

2.3 Vertical motions at rifted margins*

2.3.1 Mechanisms of rift margin uplift

In this section I explore the consequences of various models of rift flank uplift for vertical motions and crustal structure at rifted margins, using a thermo-mechanical model developed by Kooi (1991). The model proceeds from a kinematic formulation of lithospheric extension, by defining crustal and subcrustal stretching values (β and δ, respectively) along a profile. The imposed lithospheric thinning leads to a perturbation of the thermal structure which subsequently relaxes; the resulting temperature evolution is governed by the conductive heat equation:

$$\frac{\partial T(x,z)}{\partial t} = \kappa\left(\frac{\partial^2 T}{\partial z^2} + \frac{\partial^2 T}{\partial x^2}\right) \qquad (2.1)$$

with T = temperature, t = time, x = distance along the profile, z = depth and κ = thermal diffusivity of the lithosphere ($\kappa = K/\rho c_v$; K = thermal conductivity, ρ = density and c_v = specific heat). Subsequently, all loads (i.e. both thermal and isostatic) acting on the extended lithosphere are integrated and regionally compensated (cf. Stephenson et al., 1989) resulting in an isostatic compensation (in the absence of in-plane stresses):

---

* This section has been published as: van der Beek, P.A., Cloetingh, S. and Andriessen, P.A.M. 1994. Mechanisms of extensional basin formation and vertical motions at rift flanks: Constraints from tectonic modelling and fission track thermochronology. *Earth Planet. Sci. Lett.* **121**, 417-433.

$$\frac{\partial^2}{\partial x^2}\left(D(x)\frac{\partial^2 W(x)}{\partial x^2}\right)+(\rho_a-\rho_s)g\,W(x) = F(x) \qquad (2.2)$$

where W = flexural deflection, ρ_a = asthenospheric density, ρ_s = density of material infilling the basin, g = acceleration of gravity and D = flexural rigidity; $D = (E\,T_e^3 / 12\,(1 - \nu^2))$, E = Young's modulus, T_e = equivalent elastic thickness of the lithosphere, ν = Poisson's ratio, F = the vertically integrated force:

$$F(x) = \int(\Delta\rho\,(x,z)\,[1-\alpha\,T(x,z)])\,g\,dz \qquad (2.3)$$

where $\Delta\rho$ = density contrast caused by thinning and α = thermal expansion coefficient. Values for these parameters are given in Table 2-1.

By varying the stretching distributions and the mechanism of isostatic compensation (incorporating either local isostasy or a lithosphere which retains finite strength during extension, with T_e defined by the depth to a specific isotherm), the various conceptual models for rift flank uplift can be quantified. This should be considered as a parameter study to obtain an insight into the effects of different assumptions. The dynamical implications of these assumptions will be discussed later.

Figure 2-4 shows predicted tectonic uplift/subsidence patterns and crustal structure for a model of thermal uplift, mechanical uplift (induced by lithospheric necking) and a detachment model. Crustal extension factors (β) are the same in all model runs. Thermal uplift is modelled by 2-layer extension with lithospheric stretching (δ) 5 times as large as β and extending twice as far inland as it, in order to maximize the resulting uplift. Dynamical models of sub-lithospheric small scale convection suggest that it can thin the lithosphere by a factor 2 to 3 more than the crust and widens the zone of lithospheric extension with respect to that of crustal extension (Keen, 1985; Buck, 1986).

Table 2-1. Parameters employed in thermo-mechanical model

Symbol	description	value
T_a	asthenosphere temperature	1300°C
κ	thermal diffusivity	1×10^{-6} m^{2}s^{-1}
ρ_c	crustal density at 0°C	2800 kgm^{-3}
ρ_a	mantle density at 0°C	3300 kgm^{-3}
ρ_s	sediment density	2400 kgm^{-3}
α	thermal expansion coefficient	3×10^{-5} °C^{-1}
g	acceleration of gravity	9.8 ms^{-2}
E	Young's modulus	1×10^{11} Nm^2
ν	Poisson's ratio	0.25

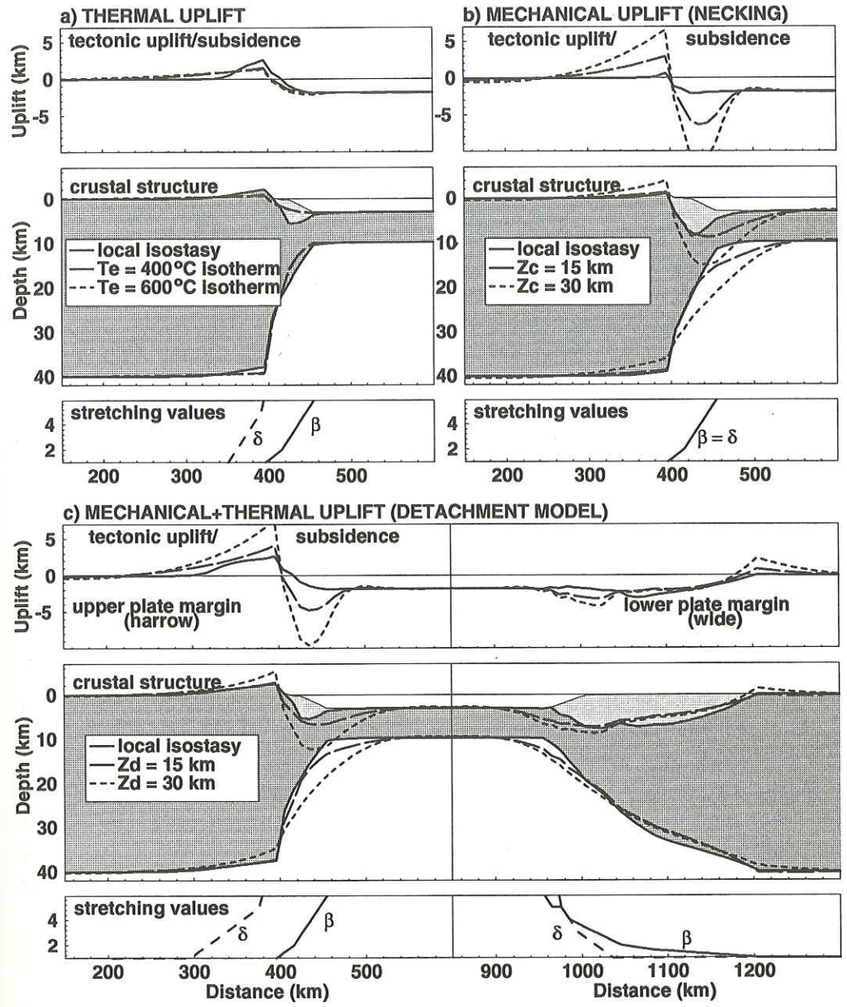

Figure 2-4. Predictions of forward models of rift flank uplift for vertical motions and crustal structure at rifted margins. (a) Thermal uplift of rift flanks adopting local isostasy and different isotherm-defined flexural rigidities; (b) pure shear mechanical (flexural) uplift as a result of lithospheric necking for different necking depths z_c; (c) simple shear detachment model for local isostasy (thermal uplift only) and a lithosphere that maintains finite strength (thermal and mechanical uplift) for different detachment depths z_d. The tectonic uplift/subsidence and crustal structure at the end of rifting is shown; β factors are similar for all models.

The kinematics of extension in the mechanical uplift model are controlled by a kinematic reference level or 'depth of necking' z_c; upon extension a kinematic surface depression S is produced (Weissel and Karner, 1989; Kooi et al., 1992):

$$S = \left(1 - \frac{1}{\beta}\right) z_c \qquad (2.4)$$

When z_c is sufficiently deep a surface depression which is deeper than the locally compensated basin depth is created and a regionally upward state of flexure develops, creating rift flank uplift (cf. Figure 1-4).

Finally, a detachment model is defined by an offset between δ and β, with δ concentrated below the upper plate margin (cf. Lister et al., 1991). In this model z_c is interpreted as the depth to the detachment (Kusznir et al., 1987; Weissel and Karner, 1989). In the case of local isostasy, uplift will be thermally supported (e.g., Buck et al., 1988; Lister et al., 1991); if the lithosphere retains strength the uplift will be supported flexurally as well as thermally, with the two mechanisms reinforcing each other at the upper plate margin and counteracting at the lower plate margin.

Figure 2-5 shows the dependence of model results on (1) width of the rifted margin (a narrow margin where the transition from unextended continental crust to oceanic crust takes place within 50 km, and a wide one where this transition zone is 200 km wide), (2) thermo-tectonic 'age' of the lithosphere (a 'young' continental setting with crustal thickness of 30 km and a lithospheric thickness of 125 km vs. an 'old' or 'cratonic' setting with 40 km crust and 200 km lithosphere) and the (3) rifting velocity (5 My rifting time vs 50 My rifting time).

The results indicate that flexural uplift of rift flanks is much more effective than thermal uplift. Maximum thermal uplift reaches 2.5 km for local isostasy, a thick lithosphere and short rifting times, but also in this extreme case it is <1.5 km when a strong lithosphere is employed. If mantle thinning is spread out over a much wider area than crustal thinning (as in the 'wide margin' case) the difference between the local and regional isostasy models becomes much smaller. Such a widespread zone of excessive lithospheric thinning cannot be explained by secondary convection models and would require regional thermal doming or widespread underplating.

Mechanical uplift can reach more than 6 km for relatively deep levels of z_c at narrow margins and even more at upper plate margins, where it is aided by thermal uplift. The strongest control on the amount of mechanical uplift is exerted by the depth of z_c. Both lithospheric 'age' (thickness) and rifting duration have a more significant effect on thermal uplift patterns (lithospheric thickness has a positive effect, the duration of rifting a negative one) than on mechanical uplift. Finally, the results suggest that the width of the rifted margin exerts a major control on the predicted amount of flank uplift, with maximum uplift taking place at narrow margins. For wide margins the difference in uplift patterns and crustal structure between the various models is much smaller than for narrow margins.

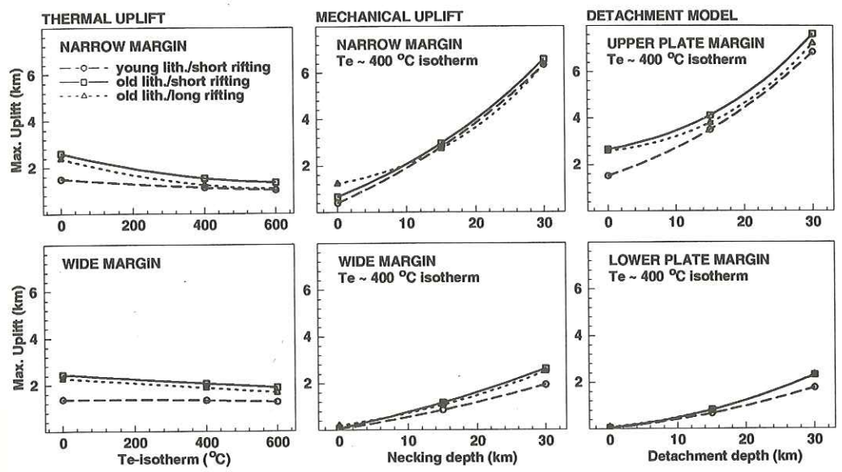

Figure 2-5. Dependence of model results on adopted parameter values. Upper panels show maximum tectonic uplift for narrow margins (50 km transition from unextended continental to oceanic lithosphere) and lower panels for wide margins (200 km transition zone). 'Young' lithosphere denotes a model with 30 km crustal thickness and 125 km lithospheric thickness; 'old' lithosphere: 40 km crustal thickness and 200 km lithospheric thickness. 'Short' rifting time is 5 My from onset of extension to crustal separation; 'long' rifting time: 50 My. Complete uplift/subsidence patterns and crustal structure for the model with old lithosphere and short rifting time are shown in Figure 2-4.

2.3.2 Estimates of rift margin uplift from fission track data

In Section 1.3 it was shown how apatite fission track data (fission track age, FTA, and track length distributions, FTLD) can be used to quantify the low temperature cooling history of a rock sample. In order to translate this thermal history into an exhumation (or erosion) path the geothermal gradient must be either known, estimated, or assumed (cf. Figure 1-10). Some authors have interpreted fission track data from rifted margins in terms of rift related heating (e.g., Moore et al., 1986). However, both observational data (e.g., Section 5.3) and modelling results (Buck et al., 1988; Gallagher et al., 1994a) suggest that, for pure-shear extension, heating of the upper crust adjacent to the rifted basin is of very little importance. Figure 2-6(a) shows the evolution of surface heat flow at a typical rifted margin, as predicted by the extension model adopted here. There is only a very slight (<10%) increase in surface heat flow, and thus in upper crustal geothermal gradient, immediately adjacent to the rifted basin, as a result of lateral heat flow. Also, exhumation rates at rifted margins are sufficiently slow (in the order of 10-100 m/My; Leeder, 1991; Section 2.4) for isotherms in the upper crust not to be significantly perturbed (cf. Stüwe et al., 1994). Thus, the assumption of a constant

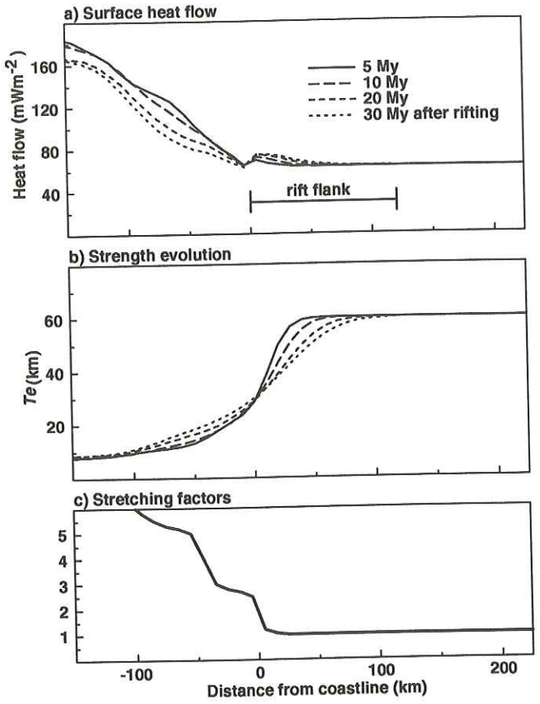

Figure 2-6. (a) Predicted pattern of surface heat flow and (b) predicted evolution of elastic thickness T_e (tracked by the 400°C isotherm) at a rifted continental margin. Adopted β-values (c) and duration of rifting (5 My) are chosen to approximate situation at Saudi Arabian Red Sea margin. Surface heat flow is calculated for an initially 200 km thick lithosphere and a 40 km thick crust with a heat production of 1 mWm^{-3}. Sediment blanketing effects are not taken into account.

geotherm at the rift margin does not introduce serious errors into the model. Although continental heat flow varies widely, a generally accepted mean value for geothermal gradients in the upper crust is 30°C/km and I will use this value in modelling fission track data throughout this chapter.

Present-day topography is the integrated result of pre-tectonic elevation, tectonic uplift, erosion and isostatic rebound as a response to erosion (e.g., Stephenson and Lambeck, 1985; Garfunkel, 1988; England and Molnar, 1990; Brown, 1991; Figure 1-11). Brown (1991), in particular, suggested a method to resolve between tectonic uplift and isostatic rebound in shaping topography. By analogy with the backstripping technique in sedimentary basins (Steckler and Watts, 1978), where:

$$u_T = w + s\frac{(\rho_s - \rho_a)}{(\rho_w - \rho_a)} \qquad (2.5)$$

with u_T = tectonic subsidence, w = present-day water depth, s = sediment thickness and ρ_w, ρ_s and ρ_a = the densities of seawater, sediments and sub-lithospheric mantle, respectively; the backstacked tectonic uplift of an eroded area is:

$$u_T = (H_0 + \Delta E) - \frac{\Delta E \rho_c}{\rho_a} - H_i \qquad (2.6)$$

with H_0 and H_i = present-day and initial elevation, respectively, ΔE = amount of erosion/exhumation as derived, for instance, from apatite fission track data, and ρ_c and ρ_a = densities of eroded crustal material and sub-lithospheric mantle, respectively.

2.3.3 Flexural strength of the lithosphere during extension

Backstripping or backstacking analyses are extremely sensitive to assumptions on the isostatic compensation of sedimentation or erosion. The estimated amount of isostatic readjustment is inversely proportional to the adopted lithospheric strength and, therefore, the amount of inferred tectonic uplift/subsidence is proportional to it. This is because, in a flexural backstripping or backstacking scheme with constant flexural rigidity, the amount of isostatic compensation is filtered by a flexural response function $\Psi_{(k)}$, which depends on the wavelength (wavenumber k) of the load and the flexural rigidity (D) of the lithosphere (Watts et al., 1982; Stephenson and Lambeck, 1985):

$$\Psi_{(k)} = \left[1 + \frac{Dk^4}{\Delta\rho g}\right]^{-1} \qquad (2.7)$$

with $\Delta\rho$ = density contrast between eroded/deposited material and the buoyant asthenosphere.

Because of the relatively small density contrast between crustal and asthenospheric material, isostatic rebound after erosion will be substantial (approximately 5/6 of the amount of erosion) for local isostatic equilibrium, low flexural rigidities or long erosional wavelengths. To derive a consistent tectonic uplift pattern it is, therefore, essential to have a reliable estimate of lithospheric strength. Previous models of flexural uplift of the rifted margins studied here found best fits for equivalent elastic thicknesses (T_e) greater than 40 km (corresponding flexural rigidity $D = 5.7\times10^{23}$ Nm) for the Saudi Arabian Red Sea margin (Le Pichon and Chamot-Rooke, 1991) and up to 110 km ($D = 1.2\times10^{25}$ Nm) for the Transantarctic Mountains and Namibian Atlantic margin (Ten Brink and Stern, 1992). The latter study, however, seems biased towards high values because tectonic uplift was modelled as being the result of a line load acting at the coastline. Most studies infer that flexural rigidities decrease towards the rift basin; T_e within the west Antarctic rift system is only 20-24 km ($D = 7.1\text{-}12.0\times10^{22}$ Nm; Stern and Ten Brink, 1989; Stern et al., 1991). Figure 2-6(b) shows how

T_e, which is tracked by the 400°C isotherm in the model adopted here, is strongly reduced below the rifted basin, as a result of the thermal perturbation associated with rifting.

Other studies (e.g., Barton and Wood, 1984; Fowler and McKenzie, 1989; Kusznir et al., 1991) arrived at much lower T_e's of <5 km ($D < 2.5\times10^{21}$ Nm) for extensional basins and margins. However, these studies may seriously underestimate the strength of the lithosphere because of their kinematic assumptions. The traditional 'sediment loading' model (Watts et al., 1982) employed in the earlier analyses (Barton and Wood, 1984; Fowler and McKenzie, 1989) implicitly assumes near-zero strength during the syn-rift phase (cf. Kooi et al., 1992) whereas the 'flexural cantilever' model (Kusznir et al., 1991) directly translates upper crustal deformation (block faulting) to lithospheric strength, while these are probably decoupled (cf. Section 3.5).

An independent estimate of lithospheric flexural rigidity can be made from coherence analyses of Bouguer gravity anomalies and topography (for a discussion of coherence analyses, see Section 4.4.1). Several of these studies have been performed in similar tectonic settings (i.e. cratonic areas adjacent to rifts or rifted margins) and they come up with relatively large values: $D \approx 1.0\times10^{23}$ Nm (T_e = 22 km) for southeastern Australia (Stephenson and Lambeck, 1985); $D \approx 2.8\times10^{23}$ Nm (T_e = 32 km) for the Baikal Rift area (Diament and Kogan, 1990) and D varying from 1.7×10^{23} Nm to 4.4×10^{24} Nm (T_e = 27-79 km) for East Africa (Ebinger et al., 1989). These values are consistent with the results of flexure in these areas (Ebinger et al., 1991; Ruppel et al., 1993). I conclude that flexural rigidity is maintained at rifted continental margins, with T_e ranging from around 20 km ($D \approx 7.1\times10^{22}$ Nm) within the basin to >40 km ($D > 5.7\times10^{23}$ Nm) inland; compatible with models in which T_e is tracked by the 400-450°C isotherm. These values are substantially higher than T_e values ≤ 15 km ($D \leq 3.0\times10^{22}$ Nm) inferred by models where the topography is solely the result of differential erosion and isostatic rebound (Gilchrist and Summerfield, 1990; Gallagher et al., 1994a).

Furthermore, in a rifted margin setting, there will be an interplay of upward isostatic compensation as a result of erosion of the rift flank and downward isostatic compensation of the sedimentary infill of the basin, which will also influence the derived tectonic uplift and subsidence patterns. In order to arrive at a consistent tectonic uplift/subsidence section across a rifted basin and its margins using a flexural model, it is thus necessary to simultaneously backstrip the basin sediments and backstack the eroded rift flank. In the next section, I will demonstrate this for the four selected areas, using seismic reflection profiles for 2-dimensional backstripping and denudation estimates from fission track data for backstacking. Flexural backstacking is done using a 2-dimensional finite difference algorithm originally developed for modelling of foreland basins (cf. Zoetemeijer, 1993). While, in principle, the temporal evolution of tectonic subsidence and uplift can be calculated if well data and fission track length distributions are available, I will restrict myself here to the total subsidence and uplift since rifting. In section 2.4, I will extend the analysis to the morphotectonic evolution of rifted margins through time.

2.3.4 Backstacking rifted margin uplifts

Saudi Arabian Red Sea margin

Apatite fission track data for the Saudi Arabian Red Sea margin are shown in Figure 2-2(b). I have converted the fission track ages to pre-erosion paleo-temperatures assuming exhumation of a 400 Ma old crustal block, at a constant rate, from 30 Ma onward (Figure 2-7(a)). Samples that have experienced temperatures >90°C (FTA <152 Ma according to this scenario) are confined to the western side of the escarpment, and samples that were at

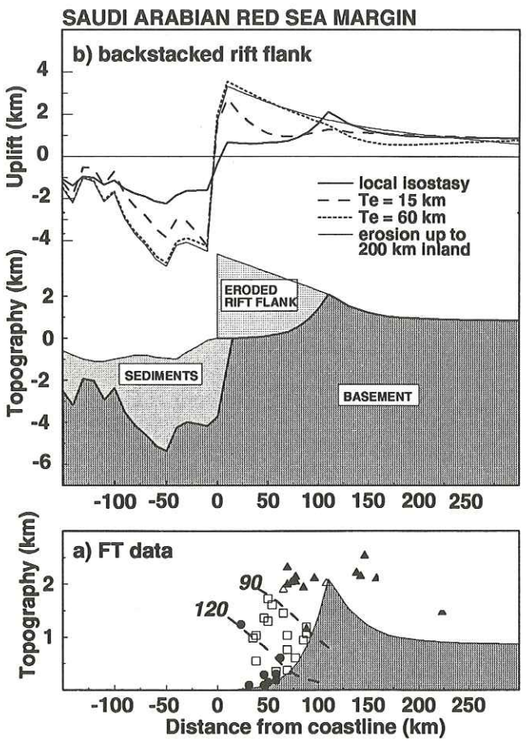

Figure 2-7. (a) Apatite fission track data from the Saudi Arabian Red Sea margin (from Bohannon et al., 1989). Samples are plotted at their true elevations and labelled according to inferred paleo- (pre-exhumation) temperature adopting an idealized exhumation model (exhumation of 400 Ma old crust at a constant rate since 30 Ma) and the annealing model of Laslett et al. (1987; cf. Appendix 1). • = Samples exhumed from temperatures > 120°C; □: 90-120°C; △: 60-90°C; ▲: < 60°C. Shaded area indicates present-day topography, dashed lines labelled 90 and 120 are paleo-isotherms. Because samples are projected onto profile line they do not all fall on the observed topography. (b) Results of backstripping/backstacking for different models of lithospheric strength. Lower panel shows sediment fill of the basin determined from seismic data (from Izzeldin, 1987) and estimated amount of erosion on the flanks. Upper panel shows reconstructed tectonic uplift/-subsidence patterns for different isostatic compensation models. A model with erosion up to 200 km inland is also shown (thin line).

Univ. J. Fourier - O.S.U.G.
MAISON DES GEOSCIENCES
DOCUMENTATION
B.P. 53
F. 38041 GRENOBLE CEDEX
Tél. 04 76 63 54 27 - Fax 04 76 51 40 58
Mail : ptalour@ujf-grenoble.fr

temperatures >120°C (FTA < 22 Ma) are found only at localities ≤50 km from the shoreline, at elevations <1 km. The pattern of paleo-isotherms indicates that the geothermal gradient prior to rifting was around 30°C/km and that maximum erosion of around 4 km (assuming a surface temperature of 30°C) has occurred in the area seaward of the escarpment. Paleo-isotherms dip inland, indicating that maximum erosion took place at the present-day shoreline. The amount of erosion inland of the escarpment is more difficult to estimate; extrapolation of the paleo-isotherms would suggest significant erosion inland of the escarpment but the fact that FT-ages do not seem to correlate with elevation inland of the escarpment argues against this.

The amount of sediment deposited in the Red Sea basin was determined from seismic reflection profiles (Izzeldin, 1987) and the amounts of eroded and deposited material were backstacked/stripped using different models for the strength of the lithosphere (Figure 2-7(b)). Results are shown for a local isostatic model and constant flexural rigidity models with T_e = 15 to 60 km (D = 3.0×10^{22} - 1.9×10^{24} Nm) encompassing the minimum and maximum strength values I expect at rifted margins. A local isostatic model suggests that tectonic subsidence decreases from the present-day elevation maximum towards the coastline, as a result of the large isostatic rebound component. In contrast, all models incorporating flexural strength of the lithosphere predict significant tectonic uplift of the external area, as a result of filtering of the isostatic response and interaction with downward compensation of the sediments in the basin. Maximum tectonic uplift of the margin is calculated to be 3.5 km for T_e = 60 km and 2.7 km for T_e = 15 km. The difference between the minimum and maximum reasonable strength estimates is mainly reflected in the flexural wavelength of the tectonic uplift pattern. Assuming that there has been erosion up to 200 km inland of the escarpment also affects the wavelength of the tectonic uplift pattern but only slightly suppresses the maximum tectonic uplift (to 2.6-3.3 km), which is located just inland of the coastline.

Transantarctic Mountains

Contrary to the Saudi Arabian Red Sea margin, the youngest fission track ages in the Transantarctic Mountains are not encountered at the coastline but somewhat inland (Figure 2-8(a)). Samples which have experienced paleo-temperatures >120°C (FTA <55 Ma; adopting onset of exhumation at 60 Ma) have only been encountered some 20 km inland, at elevations <900 m. Paleo-isotherms reach an elevation maximum here and dip both towards the coast (where they are displaced by normal faulting) and towards the hinterland. Maximum erosion is estimated to be around 4.5 km, adopting a geothermal gradient of 30°C/km and a surface temperature of 0°C. No fission track data are available for areas more than 50 km inland. I have assumed that no erosion has taken place landward of the present-day elevation maximum of around 3 km, some 80 km inland, since the basement is buried under the Antarctic ice cap there. The Tertiary Victoria Land Basin in the Ross Sea reaches a depth of 7 km and is underlain by another 8.5 km of presumably Mesozoic sediments (Cooper et al., 1991a). Since there is fission track control on the Cenozoic exhumation of the Transantarctic

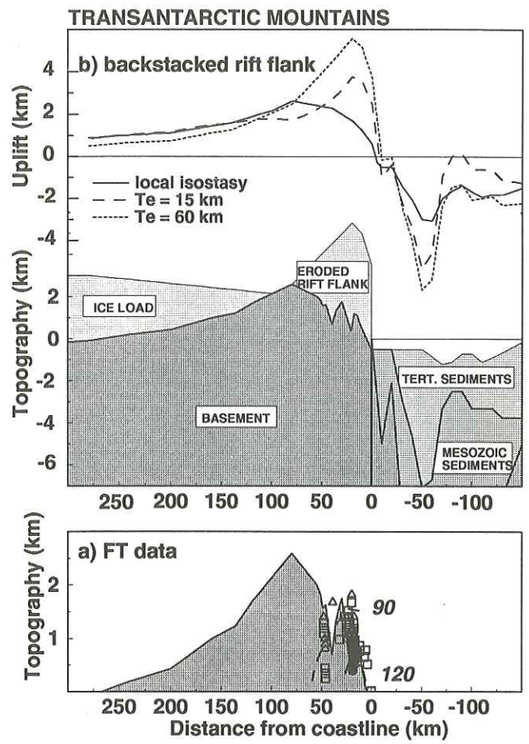

Figure 2-8. (a) Apatite fission track data from the Transantarctic Mountains (from Gleadow and Fitzgerald, 1987; Fitzgerald, 1992). Labelling of data points is the same as in Figure 2-7(a); here model is exhumation of 150 Ma old crust at a constant rate since 60 Ma. (b) Results of backstripping/backstacking; lower panel shows sediment fill of the Victoria Land basin (from Cooper et al., 1991a) and estimated amount of erosion of the Transantarctic Mountains. Mesozoic sediments in the Victoria Land basin were not backstripped, in contrast to the continental ice sheet. Upper panel shows reconstructed tectonic uplift/subsidence patterns for different flexural rigidities.

Mountains only, I will not consider older vertical motions. A load which should be also taken into account is the ice sheet which covers the Antarctic continental interior and reaches a thickness of up to 3 km. This load acts to suppress the inland topography to below sea level.

Backstripping reveals that maximum tectonic uplift in the Transantarctic Mountains reaches 5.8 km for T_e = 60 km or 3.7 km for T_e = 15 km, occurring at the same position as maximum erosion, i.e. 20 km inland (Figure 2-8(b)). The upward directed effect of backstripping the basin sediments is so large that, for large T_e values, the backstacked rift flank uplift overlaps the restored topography.

Southeastern Australian margin

The most seaward samples in southeastern Australia have syn-rift fission track ages of ~80-100 Ma (Figure 2-9(a)). These samples resided at temperatures of ≥100°C prior to rifting, suggesting that maximum exhumation reached approximately 2.5 km (adopting exhumation of 300 Ma crust at a constant rate since 100 Ma, a 30°C/km geotherm and a surface temperature of 20°C). Samples which record paleotemperatures >60°C are not encountered more than

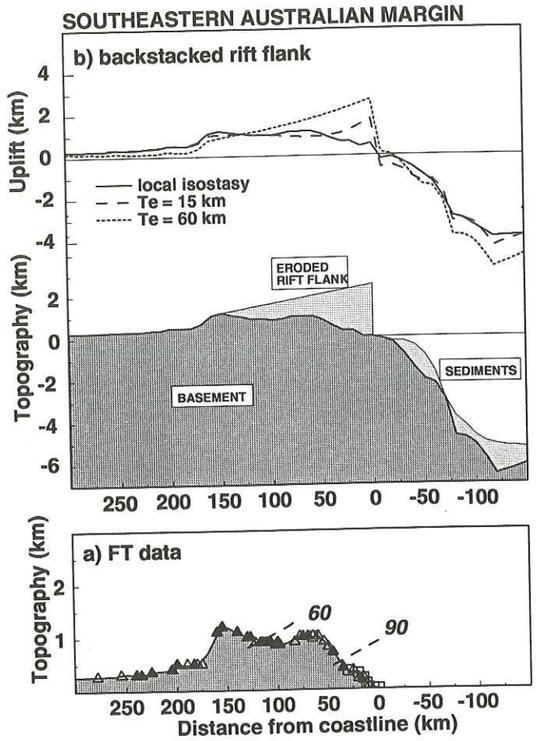

Figure 2-9. (a) Apatite fission track data from southeastern Australia (from Moore et al,. 1986; Dumitru et al., 1991). Labelling of data points is the same as in Figure 2-7(a); model is exhumation of 300 Ma old crust at a constant rate since 100 Ma. (b) Results of backstripping/backstacking; lower panel shows sediments of the offshore continental margin (from Etheridge et al., 1989) and estimated amount of erosion onshore. Upper panel shows reconstructed tectonic uplift/subsidence patterns for different flexural rigidities.

approximately 100 km inland, indicating that erosion amounted to ≤1 km there.

The offshore continental margin of southeastern Australia is sediment-starved, with maximum sediment thickness not more than 1 km (Etheridge et al., 1989). Backstripping/stacking results indicate that, for T_e between 15 and 60 km, maximum tectonic uplift reached 2-2.5 km at the coastline. Tectonic uplift affected areas up to 150 km inland.

Namibian Atlantic margin

In contrast to the other margins studied here, the apatite fission track ages from onshore Namibia present a remarkably invariable pattern. Most of the data suggest that the samples resided at temperatures between 90-120°C prior to rifting (Figure 2-10(a)). The 120°C paleo-isotherm should lie at a more or less constant elevation of >500 m. This pattern suggests that approximately 3 km of erosion affected the entire area since ~130 Ma, adopting a 30°C/km geotherm and a surface temperature of 30°C (Figure 2-10(b)). Geological indicators suggest that the exterior area is more deeply denuded than the interior (Gilchrist et al., 1994) but such estimates are difficult to quantify.

Figure 2-10. (a) Apatite fission track data from Namibia (Brown et al., 1990). Labelling of data points is the same as in Figure 2-7(a); model is exhumation of 350 Ma old crust at a constant rate since 130 Ma. (b) Reconstructed amount of erosion onshore and of depositon offshore (basin fill after Gerrard and Smith, 1982).

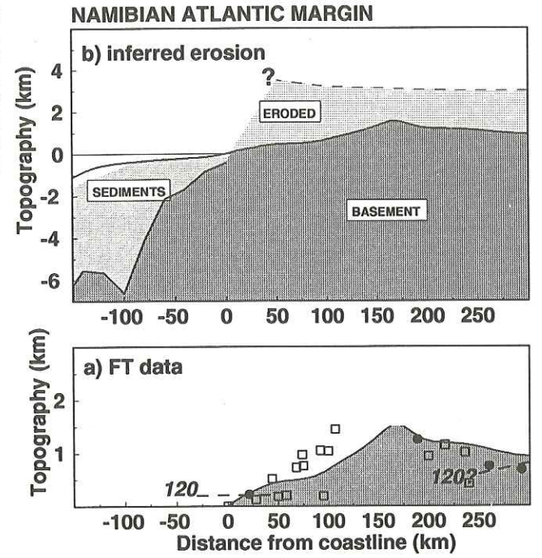

The inferred erosion pattern suggests that uplift took place on a much larger (sub-continental) scale or that the pre-rift elevation of southern Africa was significant. If the pre-rift elevation was >1500 m then the observed amounts of erosion can be explained without any rift-related tectonic uplift (cf. eq. 2-6; Brown et al., 1990; Brown, 1991). In any case, little additional rift flank uplift can be detected at the margin. Because the amount of uplift is not readily quantified from the data presented here, I will postpone a further discussion of the Namibian margin to Section 2.4.

2.3.5 Forward modelling of rift margin uplift

Now that we have some idea of the uplift and subsidence patterns for these basin / flank systems, we can compare them to forward modelling predictions. Note, however, that the inferred magnitudes of tectonic uplift from backstacking are subject to relatively large uncertainties. Whereas the fission track data themselves are internally consistent (cf. Figures 2-7 to 2-10), the largely unconstrained geothermal gradients and lithospheric strength values constitute sources of error. Both introduce errors of approximately 1.0±0.5 km into the inferred values of maximum tectonic uplift.

For forward thermo-mechanical modelling, I employ the model outlined in Section 2.3.1, parameters pertaining to the case studies are given in Table 2-2. The strength of the lithosphere (T_e) is determined by the depth to the 400°C isotherm (e.g., Beaumont et al., 1982). I adopt this T_e as representing a good estimate from both coherence analyses and dynamic

models of lithospheric extension. Stretching distributions and the kinematics of extension (i.e. depth of the kinematic reference level z_c) are taken as free parameters. β-values are chosen so as to provide a fit to the tectonic subsidence of the basin for the chosen kinematic model; the model predicts tectonic uplift of the rift flank and crustal structure, which are compared with observations.

Saudi Arabian Red Sea margin

For the Saudi Arabian Red Sea margin I adopt a rifting period from 30 to 25 Ma (Bohannon, 1986). From 25 Ma onwards, extension is concentrated at the axis of the Red Sea and proceeds towards ocean spreading (modelled by taking $\beta = 8$ and $\delta = 50$). The regional uplift of the Arabian peninsula is implemented in the forward model by a general uplift from 30 Ma onward. A model of thermal uplift of the rift flanks is capable of explaining the present-day topography of the Saudi Arabian margin when local isostasy is adopted (Figure 2-11).

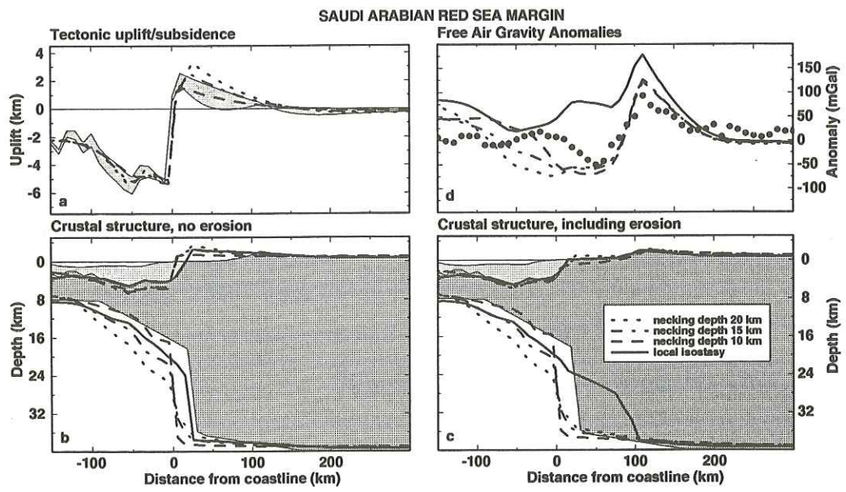

Figure 2-11. Results of forward modelling of vertical motions and crustal structure for the Saudi Arabian Red Sea margin, for a thermal uplift model assuming local isostasy and different mechanical (flexural) uplift models (see legend in (c)). (a) Vertical motions; shaded band denotes inferred range of tectonic uplift/subsidence from backstripping/stacking (cf. Figure 2-7). (b) Crustal structure without erosion and (c) including erosion of the exterior area. Shaded crustal structure is observed from seismic and gravity data (Gettings et al., 1986). (d) Calculated free-air gravity anomaly patterns for the different models, including erosion of the exterior area. Anomalies resulting from both crustal (basement and Moho depth) and thermal structure are calculated (cf. Janssen et al., 1993); the compensation depth lies at the lithosphere/asthenosphere boundary. Adopted densities (at 0°C) are: 2400 kgm^{-3} for sediments, 2800 kgm^{-3} for continental crust and 3300 kgm^{-3} for mantle material (cf Table 2-1). Sediment compaction is not corrected for, which may underestimate the gravity anomalies in the basins. Observed gravity anomalies are from the Bureau Gravimétrique International database.

However, in this case the large isostatic rebound component related to erosion of the area seaward of the escarpment, predicts a degree of crustal attenuation below the exterior area not observed in the data; the margin is characterised by a steep Moho step under the edge of the basin (Gettings et al. 1986). This is consistent with gravity modelling; the local isostatic model produces far too high Free Air anomalies over the exterior area.

The crust below the coastal plain could have been thickened by magmatic underplating (e.g., Bohannon, 1986; Bohannon and Eittreim, 1991) although there seems to be no evidence for this from the seismic refraction data (Gettings et al. 1986). In any case, the presence or absence of a crustal underplate does not affect the requirement of crustal attenuation from the present-day escarpment towards the coast in order to explain the topography and erosion patterns, if local isostasy is assumed.

The pattern of residual isostatic anomalies over the Red Sea margin, which is strongly negative (i.e. local isostatic anomalies are much higher than those observed) seaward, suggests that it is in an upward state of flexure (cf. Kooi, 1991) and that mechanical uplift of the rift flank plays a major role. A mechanical pure-shear (necking) model for rift flank uplift is able to reproduce both the tectonic uplift/subsidence patterns and the crustal structure for the Saudi Arabian Red Sea margin (Figure 2-11). Best fitting z_c levels lie in the middle crust (10-15 km).

Transantarctic Mountains

For the Transantarctic Mountains, I have employed continuous extension from 60 Ma onwards in the forward model. The Mesozoic extension that affected the west Antarctic rift system (cf. Section 2.2.2) is included in the model by first removing the Cenozoic sediments from the basins and modelling the Mesozoic basin formation. The resulting crustal and thermal structure at 60 Ma is then the starting point for modelling of the Cenozoic extension. When the load of the continental ice-sheet covering Antarctica is backstripped, the hinterland of the Transantarctic Mountains has an elevation of around 500 m., similar to what was previously inferred to be the pre-uplift elevation of the mountain range (Gleadow and Fitzgerald, 1987; Fitzgerald, 1992). I take this as the elevation of the area prior to rifting.

As was the case for the Saudi Arabian margin it is, in principle, possible to explain the uplift of the Transantarctic Mountains by local isostatic compensation to thermal processes (Figure 2-12). However, the excessive mantle thinning ($\delta > 7$) that has to be employed to model uplift of the mountains leads to strongly negative Free Air anomalies, which are not observed. The model is also incapable of explaining the existence of the very deep (7 km) Victoria Land Basin; extreme stretching values ($\beta > 10$) lead to crustal thinning strongly in excess of that observed, but still too little basin subsidence.

Again, strongly negative residual isostatic anomalies over the west Antarctic rift system suggest that the whole system is in an upward state of flexure and that mechanical uplift is important. Here, however, a pure-shear 'necking' model is not very successful. Very deep necking levels (>40 km) are required to explain the large uplift of the Transantarctic

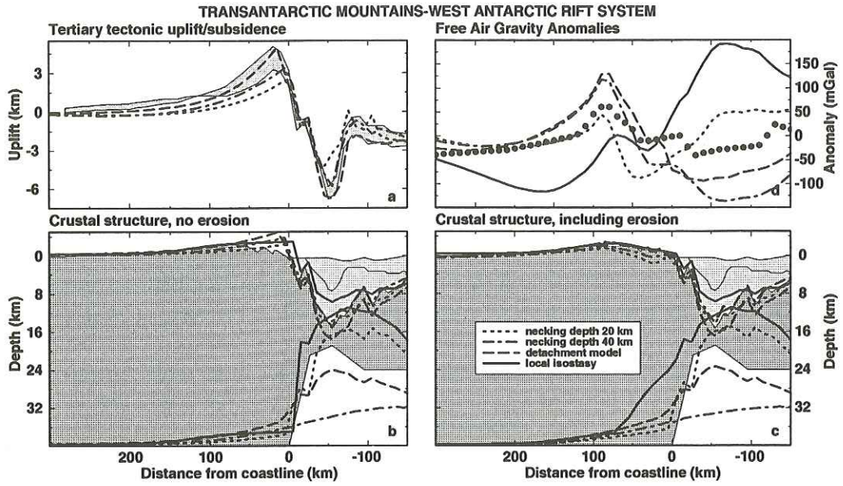

Figure 2-12. Same as Figure 2-11 for the Transantarctic Mountains-west Antarctic rift system. Detachment model denotes model with z_c at 30 km and asymmetric stretching distribution, with δ concentrated beneath the Transantarctic Mountains uplift and β beneath the west Antarctic rifts. Crustal structure is from Cooper et al. (1991a,b); gravity data are compiled from Stern and Ten Brink (1989) and Cooper et al. (1991b).

Mountains, but these are incompatible with the crustal structure and gravity pattern. Deep levels of necking predict a very smooth Moho topography and large negative gravity anomalies in the basin, which are not observed. A best-fit model (Figure 2-12) adopts a lower crustal z_c level (30 km) with asymmetric extension, where lithospheric stretching δ is concentrated under the Transantarctic Mountains and crustal stretching β in the west Antarctic rift system. Such a detachment model reproduces the observed tectonic uplift/subsidence patterns while maintaining a crustal structure that is compatible with observations. A simple shear scenario for uplift of the Transantarctic mountains has been proposed previously and is consistent with petrological data that suggest the existence of anomalously hot upper mantle under the Transantarctic Mountains (Fitzgerald et al., 1987; Fitzgerald, 1992). The quantitative modelling performed here indicates that the Transantarctic Mountain uplift is indeed partly thermally supported; the bulk of the uplift appears to be, however, a result of upward flexure.

Southeastern Australian margin

For modelling the uplift of the eastern highlands of Australia, I adopt a rifting period between 100-80 Ma, followed by concentration of lithospheric thinning in the Tasman Sea to reach oceanic spreading at 70 Ma. The present-day elevation of the Australian continental interior (~200 m) is taken as representing the pre-rift elevation of the area.

Figure 2-13 shows modelled tectonic uplift, crustal structure and gravity anomalies for different scenarios of rift flank support. Unfortunately, no good quality crustal structure data exist for this margin, so that model predictions cannot be tested against this. However, the inferred width of the region affected by tectonic uplift is difficult to explain by flexural support of the highlands alone. Also, the observed negative Bouguer gravity anomalies over the range suggest that non-flexural uplift plays a role. There have been several suggestions to explain this uplift.

Lambeck and Stephenson (1986) pointed out that the eastern highlands may contain significant remnant topography resulting from Paleozoic orogeny and crustal thickening. Etheridge et al. (1989) suggested a thermal support for the highlands uplift as a result of simple shear extension. Proposed heating of the margin, as suggested by fission track length distributions (Moore et al., 1986; Dumitru et al., 1991), is compatible with a simple shear model. However, a thermal support would lead to post-rift subsidence of the rift shoulders which is not observed (Wellman, 1987). In contrast, Veevers (1984) and Wellman (1987) suggested that accelerated uplift may have resulted from crustal underplating during the Cenozoic.

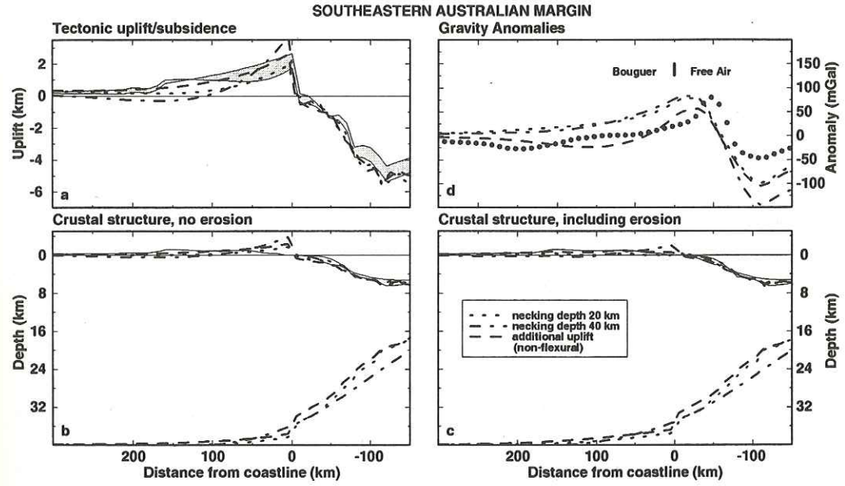

Figure 2-13. Same as Figure 2-11 for the southeastern Australian margin. Modelling results are shown for flexural uplift alone, as well as a model with additional uplift created by non-uniform thinning (β = 1; δ > 1) under the eastern highlands. Observed gravity anomalies (Free Air offshore, Bouguer onshore) were provided by P. Johnston (Research School of Earth Sciences, ANU); crustal structure data are not available.

Table 2-2. Modelling parameters employed in this study

Parameter	General	SARS	TAM	SEA	NAM
Tectonic model					
lithospheric thickness L (km)	150	200	200	150	200
crustal thickness c (km)	35	40	40	40	40
max. elastic thickness Te (km) (400°C isotherm)	45	60	60	45	60
necking depth z_c (km)	5-15-25	15	30*	20**	10
Surface processes model					
short-range diffusion coefficient κ (m^2y^{-1})	3	5	3	2	10
long-range fluvial transport coefficient × precipitation $K_f v_r$ (my^{-1})	0.01	0.01	0.004	0.004	0.005
length scale for fluvial erosion l_e (km)	20	20	1§	20	100
length scale for fluvial deposition l_s (km)	1	1	1	1	1

*notations: SARS = Saudi Arabian Red Sea margin; TAM = Transantarctic Mountains; SEA = southeastern Australia; NAM = Namibian Atlantic margin. *: detachment model, additional mantle thinning under TAM; **: with additional mantle thinning under the highlands; §: transport-limited fluvial model used.*

A best-fit model employs additional (non-flexural) uplift of the margin, accomplished by thinning the lithosphere but not the crust underneath the highlands ($\beta = 1$; $\delta > 1$). In order to maximise the effect of this additional (thermal) uplift, it is taken to occur from 20 Ma onward. A discussion of this inferred timing will be given in Section 2.4.3.

2.4 Morphotectonic evolution of rifted margins*

In the previous section, we have concentrated on the integrated vertical motions and amounts of denudation that have affected rifted margins. In the following, I will focus on the evolution of these margins through time. To this aim, I will combine tectonic uplift patterns, as predicted by the forward model of rifted margin evolution presented above, with a surface processes model developed by Beaumont et al. (1992) and Kooi and Beaumont (1994), in order to predict the morphological evolution and erosional history of rifted continental margins (Figure 2-14). The tectonic model predicts the evolution of the lithospheric tempera-

* This section is based on: van der Beek, P.A., Andriessen, P.A.M. and Cloetingh, S. 1995. Morphotectonic evolution of rifted continental margins: Inferences from a coupled tectonic-surface processes model and fission track thermochronology. *Tectonics*, in press.

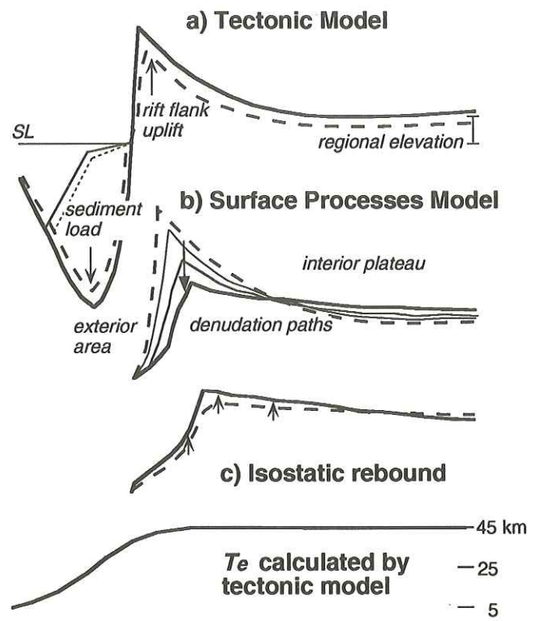

Figure 2-14. Cartoon of approach for modelling the temporal evolution of rifted margins, showing the coupling between tectonic and surface processes models as well as the modelling sequence through successive time steps. The lithospheric extension model (a) calculates tectonic uplift; the surface processes model (b) calculates the degradation of topography, the denudation history is tracked for points across the margin in order to predict fission track patterns; isostatic rebound (c) is calculated adopting a temporally and spatially varying T_e, as predicted by the tectonic model.

ture and strength (T_e) distribution, as well as the tectonic uplift, through time. This is input into the surface processes model which calculates the degradation of topography and associated isostatic rebound. Modelled denudation histories across the margin are used to predict apatite fission track age and length patterns; the model predictions are compared to present-day topography and fission track data.

2.4.1 Surface processes model

Dynamic erosion/sedimentation models rely on developing a relationship between topography $h(x)$ and erosion rate (dh/dt) (e.g., Leeder, 1991; Summerfield, 1991b). Previous models have either used an a-priori defined erosion rate (e.g., Gilchrist and Summerfield, 1990; Ten Brink and Stern, 1992) or adopted a rate of erosion that is linearly dependent on elevation (e.g., Stephenson and Lambeck, 1985).

Simple linear diffusion models have been used in studies of stratigraphic basin development (e.g., Kenyon and Turcotte, 1985; Flemings and Jordan, 1989; van Balen and Cloetingh, 1994) as well as for modelling the erosion of fault scarps (e.g., Hanks et al, 1984) and tilted fault blocks (Waltham, 1992). Whereas linear diffusion laws are adequate to simulate either sub-aerial or sub-marine slope processes, they fail to predict the characteristic

behaviour of an escarpment system: preservation of topographic roughness and parallel retreat (Newman and Turcotte, 1990; Weissel, 1990; Figure 2-15(a)). Instead, the initial relief is smoothed out and erosion is distributed over a wide area.

Fluvial transport needs to be incorporated when studying morphological evolution on this scale. Therefore, I will use a general model developed by Beaumont et al. (1992) and Kooi and Beaumont (1994) that combines short-range hillslope transport with long-range fluvial transport. The model proceeds from combining the (1D) continuity equation:

$$\frac{dh}{dt} = -\frac{\delta q}{\delta x} \tag{2.8}$$

with a sediment transport law q (Kirkby, 1971). Hillslope transport is modelled as a diffusive process (Culling, 1960; Carson and Kirkby, 1972) with a transport law q_s:

$$q_s = -\kappa\frac{\delta h}{\delta x} \tag{2.9}$$

where κ is a linear transportation coefficient with unit m^2y^{-1}. Long-range fluvial transport is based on the carrying capacity q_f^{eqb} of river systems transporting sediment away from the escarpment:

$$q_f^{eqb} = -K_f\, q_{r_{(x)}}\frac{\delta h}{\delta x} \tag{2.10}$$

This expression includes a discharge term q_r (m^2y^{-1}) which is a function of the distance from the drainage divide (the escarpment) and a (dimensionless) long-range fluvial transport coefficient K_f.

If we assume that the actual river transport is equal to the carrying capacity of the rivers ($q_f = q_f^{eqb}$) we have a situation of transport-limited erosion/sedimentation (Kirkby, 1971). However, this is not necessarily the case and the morphology of an eroding landscape may be strongly dependent on the ability of rivers to reach carrying capacity. Specifically, it is the interplay between rates of sediment supply by weathering, and transport by hill-slope and fluvial processes which determines the resulting morphology (Kooi and Beaumont, 1994; Tucker and Slingerland, 1994). This supply-limited behaviour can be modelled by introducing a 'reaction length scale' in the equation for fluvial transport (Beaumont et al. , 1992):

$$\frac{\delta q_f}{\delta x} = \frac{1}{l_f}\left(q_{f\,(x)}^{eqb} - q_{f_{(x-1)}}\right) \tag{2.11}$$

Note that the length scale l_f controls the rate at which the disequilibrium of the system tends to be reduced. l_f can take different values for erosion (l_e) or sedimentation (l_s). When $l_f \rightarrow 1$, equation (2.11) reduces to ($q_f = q_f^{eqb}$) and the model becomes transport-limited.

Figure 2-15 shows the evolution of a simple initial escarpment by these different surface process models. Whereas a transport-limited model amplifies erosion rates away from

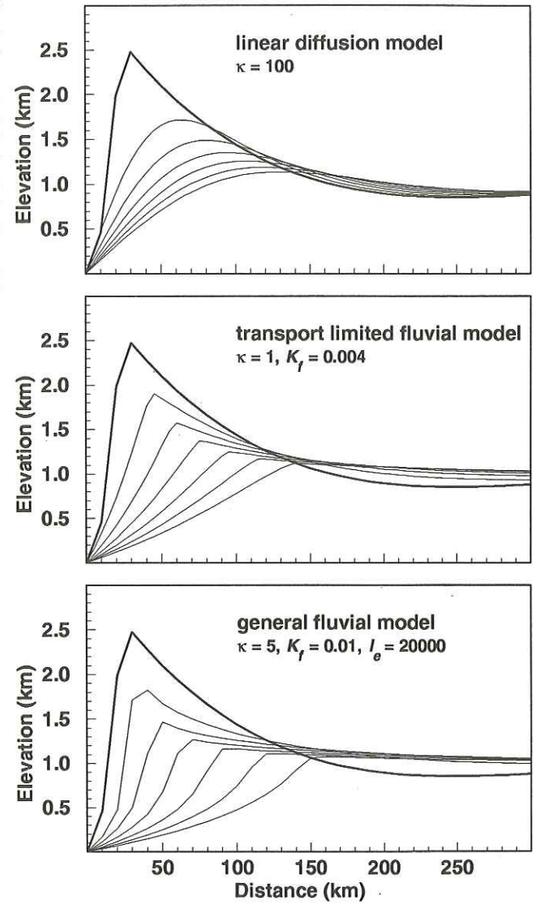

Figure 2-15. Topographic evolution of an escarpment system for different surface processes models. (a) Linear diffusion (e.g., Flemings and Jordan, 1989; Waltham, 1992); (b) transport-limited fluvial erosion (Kirkby, 1971); (c) general fluvial erosion model (Beaumont et al., 1992; Kooi and Beaumont, 1994). Thick line indicates initial topography; thin lines: erosional topography after successive 5 My steps (isostatic rebound is not included). Model parameters were chosen to have a similar amount of retreat in all models.

the elevation maximum, there still is a strong diffusive component which tends to smooth the topography, except near the drainage divide. Only the supply-limited fluvial model presented above produces the characteristic concave margin morphology and parallel retreat of the escarpment.

The evolution of a model escarpment system is strongly dependent on the adopted values for the surface process parameters κ, K_f and l_f (cf. Kooi and Beaumont, 1994). Their relative magnitudes determine the morphology of the escarpment system whereas their absolute magnitudes determine erosion rates. The control of these parameters on escarpment evolution and their interpretation in terms of climatic and lithological factors was elaborated

upon by Kooi and Beaumont (1994) and Gilchrist et al. (1994). I will use average values that lead to reasonable erosion/retreat rates (Table 2-2). Although these values were chosen from 10-20 model runs for each modelled margin to provide the best fit to the observed topography, one should be cautious when inferring a direct morphological significance to them. The use of single parameter values throughout a model run implies that the model is strictly valid only for constant climatic conditions and uniform bedrock.

Numerical implementation

The modelling procedure involves determining, for each time step, the position of the drainage divide x_d, $(dh/dx)_x$ and $(d^2h/dx^2)_x$ using backward differences for the slopes. q_s, q_f and $(dh/dt)_x$ are subsequently tracked from the escarpment downwards to the left and right sides of the model. The spatial step size is 10 km in all models; time steps are adapted to keep the explicit finite difference scheme stable and are in the order of 500 to 1000 y. The model is 2D; stream convergence and divergence effects are ignored and I interpret the resulting profile to be the along-strike average of topography. Discharge $q_{r(x)}$ is assumed to increase linearly away from the escarpment: $q_{r(x)} = v_r | x - x_d |$, where v_r is a constant precipitation rate (my^{-1}). As boundary conditions I take $(dh/dt)_0 = 0$ and $(dh/dt)_{xmax} = 0$ so that both sides of the model act as sediment sinks.

The surface processes model does not include deposition of sediments into the offshore basin. Instead, subsidence induced by sedimentation is calculated by the tectonic model, adopting a sediment fill up to a given water depth profile (Figure 2-14(a)). I have chosen for this procedure to have a better control on sediment loading; if only the material eroded from the seaward side of the escarpment was deposited into the basin, it would be strongly underfilled because sediment supply by river systems breaching the escarpment, along-axis transport and non-clastic sedimentation are ignored (cf. van Balen and Cloetingh, 1994). Topography is updated by incremental tectonic uplift and isostatic response to erosion every 1-5 My (Figure 2-14(c)). Note that 'tectonic' uplift of the flank in this case includes the effects of thermal subsidence and sediment loading within the adjacent basin, i.e. it is the topography the flank would attain in the absence of erosion. When updating the topography for uplift and isostatic rebound the shoreline ($x = 0$) is kept fixed, the right side of the model ($x = x_{max}$) is free to move. The grid on which flexure calculations are performed extends several 100 km beyond the surface processes model grid in both directions.

2.4.2 Controls on margin evolution; general modelling results

In this section the importance of the different components of tectonic uplift, erosion and isostatic rebound in creating topography at elevated rifted margins will be assessed. I investigate how the relative contributions of regional plateau uplift and flexural rift flank uplift affect the morphological evolution and fission track patterns of a model rifted margin. Subsequently, I discuss the effects of a different timing of regional uplift with respect to

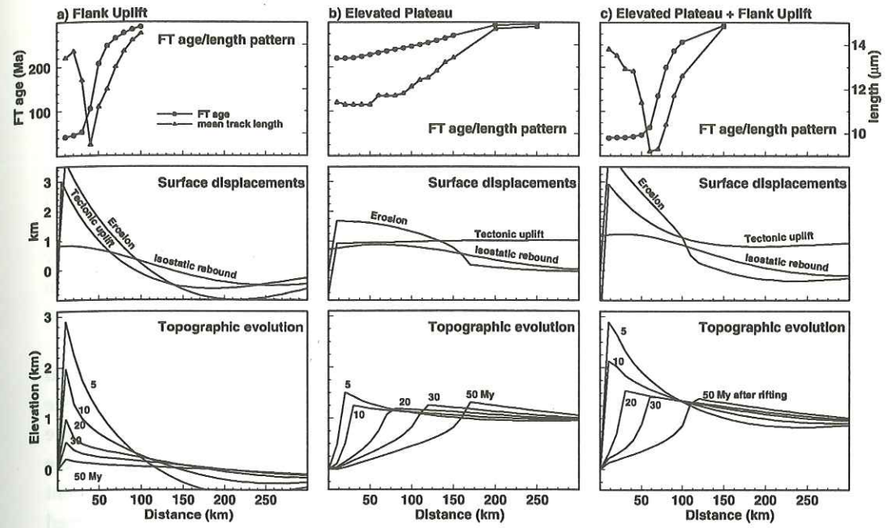

Figure 2-16. Model rift flank evolution (lower panels), contributions to surface displacements (middle panels) and fission track age/length patterns (upper panel), 50 My after rifting; for different amounts of rift flank uplift and regional plateau uplift. Modelling parameters are given in Table 2-2. (a) Interior area is at sea level, 3 km high rift flank is supported by lithospheric necking with z_c = 25 km; (b) interior plateau with a regional elevation of 1 km; no additional tectonic uplift of rift flank (z_c = 5 km); (c) interior plateau with elevation of 1 km; tectonic uplift (2 km) of rift flank is induced by z_c = 15 km.

rifting on the resulting topographic evolution and erosion patterns. These questions are of direct interest for understanding the dynamics of rifted margin uplift (cf. Section 2-1).

Figure 2-16 illustrates the effect of varying regional elevation (caused by pre-rift plateau uplift) and syn-rift flank uplift. Modelled rift flank uplift is flexural in nature; different amounts of uplift are created by varying the kinematic level of 'necking' (cf. Section 2.3.1). The figure shows the topographic evolution of the margin, the total amount of uplift, erosion and isostatic rebound, and predicted fission track patterns across the escarpment, 50 My after rifting.

Figure 2-16(a) illustrates the evolution of a high rift flank, supported by a deep level of necking (25 km), and a low-lying interior area. Because of high topographic gradients inland of the rift flank, erosion towards the hinterland is very effective. The more or less symmetrical gradients inhibit hinterland-ward retreat of the escarpment, which remains at the locus of maximum tectonic uplift. The rift flank degrades within 50 to 100 My, depending on the constants adopted in the erosion model. Maximum erosion, amounting to more than 3 km, takes place just behind the locus of maximum tectonic uplift, leading to young fission

track ages close to the basin. From ~100 km landwards, net sedimentation occurs in what can be called a 'hinterland basin' (Ten Brink and Stern, 1992).

In contrast, Figure 2-16(b) shows the evolution of an escarpment along an elevated plateau. The regional elevation of the interior plateau is 1000 m, and very little additional flank uplift takes place during rifting, as a result of shallow necking (5 km). In this case erosion takes place seaward of the escarpment and escarpment retreat is initiated virtually instantly after rifting. Retreat rates start out relatively fast and slow down during the post-rift evolution. Maximum erosion is less than 2 km. The elevation of the escarpment increases as it retreats, as a result of increasing isostatic response to erosion. Because of the relatively small amounts of erosion seaward of the escarpment, no rocks have been exhumed from temperature ranges >90°C. As a consequence, fission track ages across the margin are much older than the age of rifting.

Finally, Figure 2-16(c) displays a model that includes both an elevated plateau and rift flank uplift. This model leads to maximum erosion of the exterior area and the development of an escarpment system. Escarpment retreat can only commence when the initial rift flank has eroded away; after that, the tectonic uplift pattern is not reflected in the topography. Predicted fission track ages and track length distributions across the escarpment agree well with those often observed: rocks exposed in the exterior area have been exhumed from depths >3 km and have fission track ages younger than the initiation of uplift, with high mean track lengths; ages increase rapidly towards the escarpment; samples with intermediate ages have lowest mean lengths.

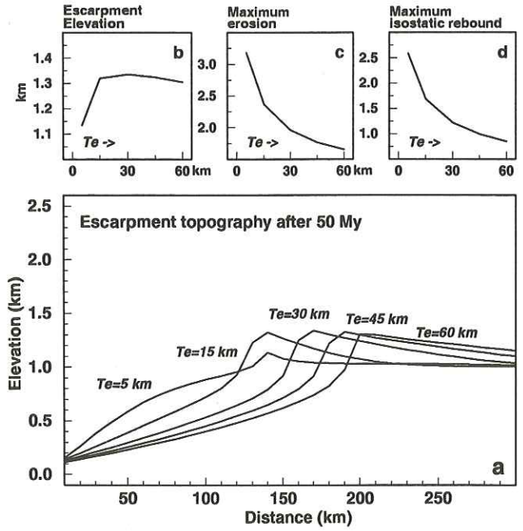

Figure 2-17. Topographic and erosional development for the model of Figure 2-16(b) (interior plateau with 1 km elevation; no additional rift flank uplift) for different constant flexural rigidities (elastic thickness T_e) of the lithosphere. (a) escarpment morphology 50 My after rifting; note that for very low strength (T_e < 15 km) creation of the characteristic concave morphology is inhibited by large local rebound. (b) Maximum escarpment height, (c) maximum erosion and (d) maximum isostatic rebound 50 My after rifting, as a function of T_e.

The behaviour observed in Figure 2-16 suggests that the existence of an escarpment along a rifted continental margin is in itself not an indication of rift flank uplift. Uplifted escarpments are maintained by a high-elevation interior plateau and erosion of the exterior area; flank uplift alone does not lead to development of an escarpment system. However, the several kilometers of erosion of the exterior area that are recorded by fission track data from a number of rifted margins (e.g., Moore et al., 1986; Bohannon et al., 1989; Gallagher et al., 1994a) require that additional rift flank uplift has taken place (see Sections 2.3.2 - 2.3.4). This is illustrated in Figure 2-17, which shows the dependence of model results on the adopted strength of the lithosphere (expressed in terms of the equivalent elastic thickness T_e). Models in Figure 2-16 have T_e varying between 15 and 45 km. For reasonable strength values ($Te \geq$ 15 km) and a model of rifting of an elevated plateau, the elevation of the escarpment (~1.3 × initial elevation) and maximum amount of erosion (~2 × initial elevation) are not very sensitive to T_e. These numbers slowly increase with increasing retreat of the escarpment and associated widening of the exterior area (Gilchrist et al., 1994). Large amounts (>3 km) of erosion, without additional rift flank uplift, thus require either extreme escarpment retreat (>300 km), very high initial elevation of the interior plateau (>1.5 km) or extremely low T_e values (<5 km). The latter inhibit the development of the characteristic margin morphology as a result of strong local rebound; moreover, they are not in keeping with strength estimates from coherence analyses nor with the crustal structure observed at rifted margins (cf. Section 2.3.5).

I will now turn to the issue of the timing of uplift with respect to rifting. Figure 2-18 shows predicted topographic evolution, erosion and fission track patterns for pre-rift, syn-rift and post-rift regional uplift. Regional (plateau) uplift is generated in this case by an excess mantle thinning with a factor 2 over a 400 km wide area, in order to simulate the effect of active mantle upwelling; mantle thinning simultaneously reduces the strength of the lithosphere. Because the regional uplift is thermal in nature, it will relax with time. Pre-rift uplift is assumed to be initiated 30 My before rifting (at 50 Ma), post-rift uplift 30 My after it. Additionally, there is ~1 km of flexural (rift flank) uplift during rifting. The results indicate that it is very difficult to detect pre-rift uplift phases from fission track data alone. Even for extreme pre-rift thermal uplift values (~2 km), pre-rift erosion is less than 1 km and takes place mainly inland of the present-day escarpment. Erosion patterns and topographic evolution are very similar for pre-rift and syn-rift regional uplift; the resulting patterns of fission track ages across the escarpment are, therefore, also nearly indistinguishable (Figure 2-18(d,e)). Both models predict fission track ages which are younger than the age of rifting seaward of the escarpment. Post-rift uplift shows a contrasting evolution with far less erosion taking place and the development of a high and steep escarpment, because erosion rates can not keep up with recent tectonic uplift. The timing of initiation of uplift can be inferred from plots of fission track age against mean track length (e.g., Omar et al., 1989). Here, there is a slight difference between the predictions of the pre-rift and syn-rift regional uplift models; mean track lengths increase at older fission track ages for the pre-rift model (figure 2-18(e)) as a result of (slow) pre-rift exhumation/cooling. The young-age peak in these plots,

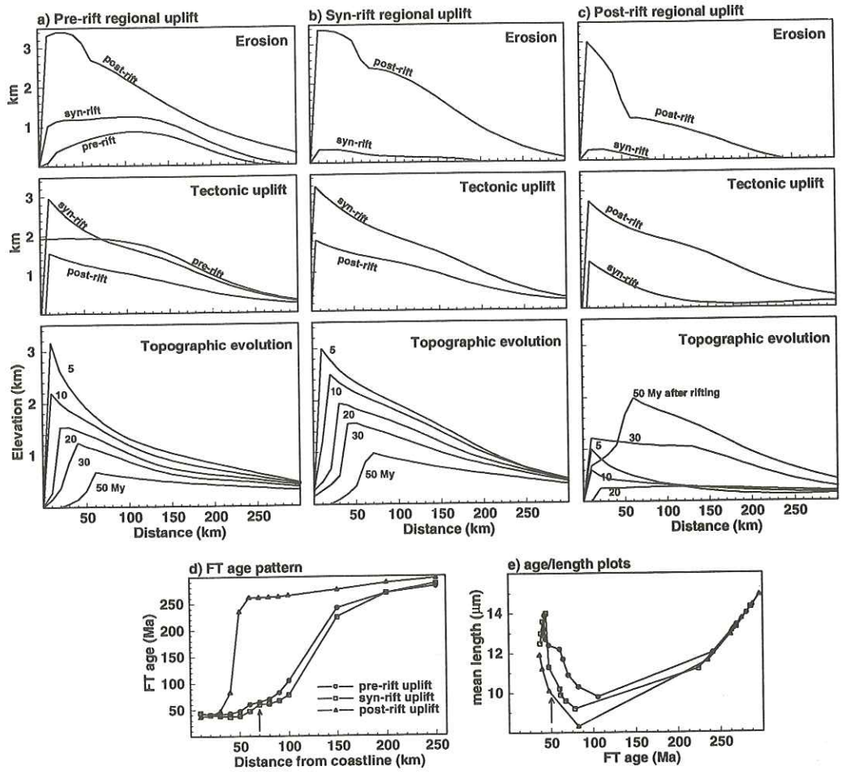

Figure 2-18. Model rift flank evolution for regional plateau uplift resulting from excess lithospheric thinning; (a) pre-dating rifting by 30 My, (b) occurring simultaneous with rifting at 50 Ma, and (c) post-dating rifting by 30 My. Lower panels show post-rift evolution of rift flank morphology, middle panels pre- syn- and post-rift contributions to tectonic uplift and upper panels pre- syn- and post-rift erosion of the margin. (d) Pattern of fission track ages across the escarpment 50 My after rifting; vertical arrow denotes position of escarpment. (e) Corresponding age/length plots; arrow denotes timing of initiation of rifting.

however, dates the onset of rapid rift-related erosion in all three cases.

2.4.3. Modelling regional examples

In the following, I show modelling results for the evolution of the four rifted margins presented in Section 2.2. For these case studies, I concentrate on two questions, regarding the problems posed in the previous section: (1) can the timing of margin uplift with respect to rifting be determined? and (2) can the relative magnitude of rift flank uplift compared to

regional plateau uplift be quantified? Of course, in modelling the complex morphotectonic evolution of an actual rifted margin, simplifying assumptions are inevitable. For instance, I do not consider possible changes in erosional parameters as a result of climate or lithology. Also, possible effects of pre-rift topography are not taken into account.

Saudi Arabian Red Sea margin

Figure 2-19 shows the evolution of topography, tectonic uplift, erosion and predicted fission-track ages when the preferred forward model from Section 2.3.5 (cf. Figure 2-11) is combined with the surface processes model, employing the parameters of Table 2-2. In this inititial model, all regional (plateau) uplift occurs syn-rifting, i.e. between 30 and 25 Ma. This leads

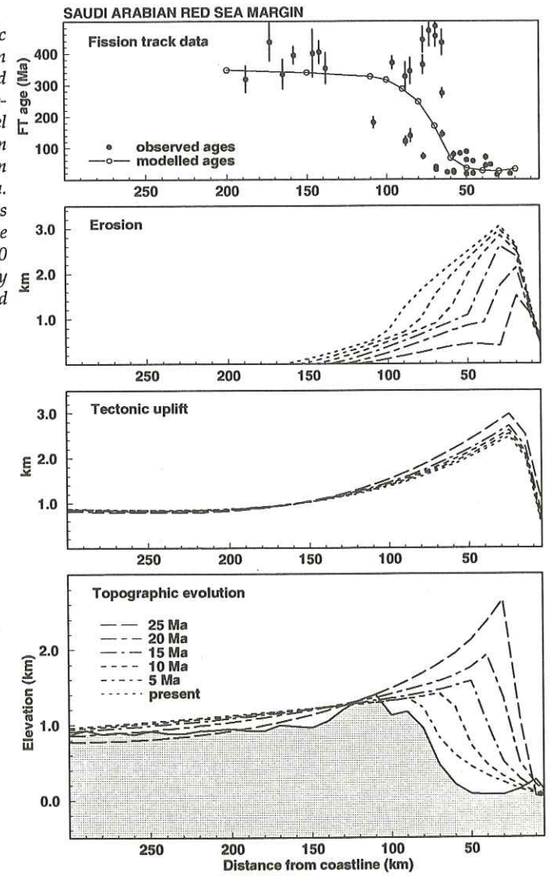

Figure 2-19. Modelled topographic evolution, tectonic uplift and erosion through time, as well as predicted fission track ages for the Saudi Arabian Red Sea margin, adopting a model with 200 km thick lithosphere, 2 km flexural uplift of rift flank and 1 km regional plateau uplift from 30-25 Ma. Shaded area in lower panel indicates observed present-day topography. The group of old fission track ages near 70 km are samples from significantly higher elevations than the modelled profile.

to a high (~2.5 km) flank at the end of rifting, which degrades in approximately 10 My and then starts retreating. Predicted present-day topography and fission track age patterns are in agreement with observed values. Fission track length distributions were reported for 5 samples only (Bohannon et al., 1989). Predicted mean track lengths seaward of the escarpment are about 1 µm lower than those observed, while on the interior plateau they are about 1 µm higher.

Alternative tectonic scenarios are depicted in Figure 2-20: Figure 2-20(a) shows the topographic evolution and calculated fission track ages for a model of continuous regional plateau uplift, from 30 Ma onwards to the present, and Figure 2-20(b) for a model in which regional uplift only commences after 15 Ma. Rift flank uplift is similar to the first model, both in timing (30-25 Ma) and amount (~2 km). These models predict much less pronounced topography during rifting. The flexurally supported rift flank reaches an elevation of approximately 1 km; while it degrades, the interior plateau is uplifted and an escarpment starts to develop. Because regional uplift occurs later in these models, a higher elevation of the area seaward of the escarpment and less erosion is predicted. It is difficult to discriminate between a model of syn-rift and continuous post-rift regional uplift; both models produce erosion patterns which fit the fission track data within error. Models in which most regional uplift occurs late, in contrast, predict too little erosion of the exterior area for constant erosion/retreat rates. Young (<20 Ma) fission track ages which were encountered in some samples from the Saudi Arabian and Yemenese margins have been cited as indicating relatively young uplift (Menzies et al., 1992). However, care should be taken in directly relating the exhumation recorded by fission track data into tectonic uplift. The modelling presented here suggests that, if anything, younger uplift leads to older fission track ages seaward of the escarpment. Of course, the assumption underlying this conclusion is that the parameters controlling erosion rates have been constant throughout the evolution of the margin, i.e. no climate change has taken place and a homogeneous bedrock has been eroded. The latter assumption is demonstrably not valid at the Red Sea margins, as erosion has stripped away both a Phanerozoic sedimentary cover and parts of the crystalline basement (Garfunkel, 1988; Steckler and Omar, 1994) which presumably have a lower erodibility.

The model has been rerun adopting a lithospheric thickness of 150 km and an associated maximum T_e = 45 km. This leads to significantly less flexural rift flank uplift (approximately 500 m) and more isostatic rebound as a response to erosion. As discussed in the previous section, a model without significant rift flank uplift leads to less erosion seaward of the escarpment (e.g., Figure 2-16). In the case of the Saudi Arabian Red Sea margin, such a model fails to explain the fission track data which record 3-4 km of erosion (Figure 2-20(c,d)).

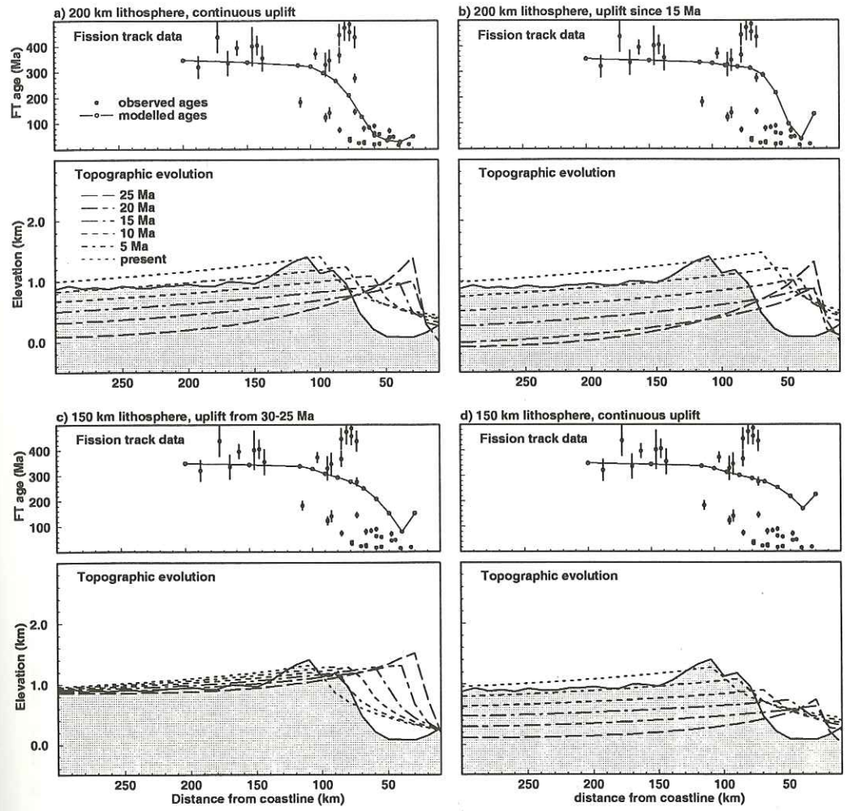

Figure 2-20. Modelled topographic evolution and predicted fission track ages for different uplift scenarios for the Saudi Arabian Red Sea margin: (a) 200 km lithosphere, 2 km flexural uplift of rift flank from 30-25 Ma, 1 km regional plateau uplift from 30 Ma onwards; (b) as (a) but with regional uplift starting at 15 Ma; (c) 150 km lithosphere, leads to much less (500 m) tectonic uplift of rift flank and more isostatic rebound, 1 km regional uplift from 30-25 Ma; (d) as (c) but with regional uplift from 30 Ma onwards.

Transantarctic Mountains

For the Transantarctic Mountains, I have combined the 'detachment' model of Figure 2-12 with a surface processes model employing the parameters in Table 2-2. In this case there is little difference between the predictions of a transport-limited and a supply-limited transport model; therefore, the results of the (simpler) transport-limited model are shown (Figure 2-21).

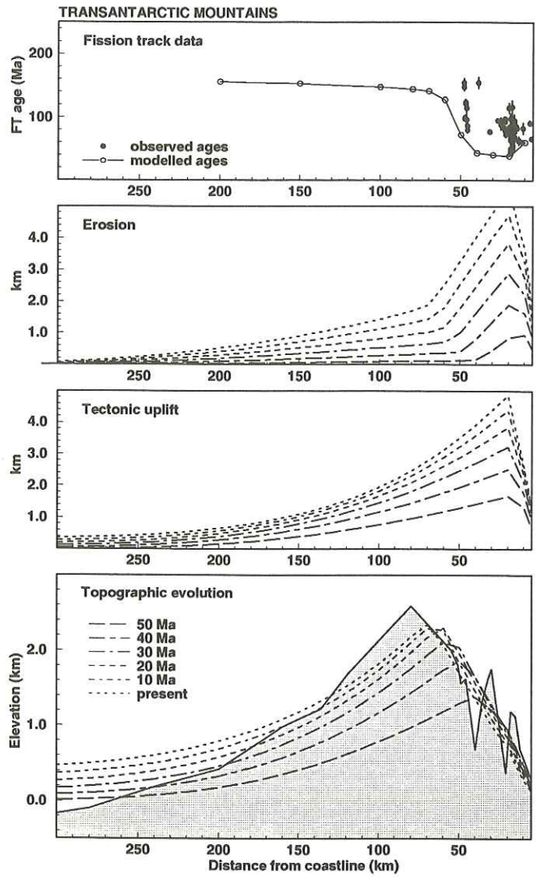

Figure 2-21. Topographic evolution, tectonic uplift and erosion through time, and predicted fission track ages for the Transantarctic Mountains, adopting a model of continuous uplift of the mountains by combined flexural and thermal mechanisms ('detachment' model of Figure 2-12). Note that most of the fission track data (Gleadow and Fitzgerald, 1987; Fitzgerald, 1992) were collected from vertical profiles.

Because of continuous tectonic uplift during the model run, with denudation lagging behind, the topography of the range grows continuously since the onset of rifting (at 60 Ma). During the last 20 My in the model, topographic gradients, and consequently denudation rates, become so large that the topography evolves towards a steady state. Continuous uplift of the area immediately adjacent to the basin inhibits rapid escarpment retreat (compare Figure 2-16(a)). During the entire model run, the locus of maximum denudation remains fixed at the locus of maximum uplift, while the topographic maximum slowly retreats towards the hinterland. Denudation rates are relatively constant and low behind the topographic maximum. Note that the effect of ice loading is not taken into account, so that the basement gradients behind the escarpment are lower than those observed.

The model shown in Figure 2-21 predicts present-day topographic maxima some 300 m lower than that observed, and also relatively low fission track ages compared with the data. This suggests that the amount of erosion predicted by the model is rather high. On the other hand, since most of the fission track data were collected from vertical profiles on sometimes isolated peaks (Gleadow and Fitzgerald, 1987; Fitzgerald, 1992) they may represent minimum amounts of erosion. A model with smaller erosional parameters predicts an overly steep mountain front and a topographic maximum closer to the locus of maximum tectonic uplift. A solution for this discrepancy might be that uplift has in fact not been continuous, but intermittent during the last 60 My. There is some evidence from inversion of fission track data (Fitzgerald, 1992; see also Section 2.5) for higher exhumation rates during the first and last 10 My of the Cenozoic history of the range, with lower rates in between. A recent acceleration in uplift rates, as suggested for instance by Behrendt and Cooper (1991) would indeed lead to somewhat less erosion and thus higher topography and older fission track ages. Also, the ice cover inland of the elevation maximum inhibits any denudation there, so that predicted erosion rates inland are inevitably too high.

Southeastern Australian margin

Figure 2-22 shows modelled topographic evolution, tectonic uplift, erosion and fission track patterns for two models of uplift of the southeastern Australian margin presented in Figure 2-13. The model with only Mesozoic (100-80 Ma) flexural rift flank uplift predicts that very little topography should be left at present. Because of the low elevation of the Australian interior, it is implausible that a high escarpment will develop. Note that denudation rates in this case must be much lower than for the Saudi Arabian margin and the Transantarctic Mountains (about a factor 2.5; see also Bishop, 1988). Maximum erosion is about 2 km; as a result, rocks exposed in the exterior area would have experienced peak temperatures not higher than 80°C during rifting. This is reflected in predicted fission track ages that are older than those observed seaward of the escarpment, and mean track lengths that increase monotonically inland from the coastline.

Therefore, the present-day high elevation of the eastern highlands of Australia, combined with the erosion rates inferred from the fission track data, suggests that they have been rejuvenated relatively recently. Tertiary uplift of the southeastern Australian margin could be a result of renewed lithospheric extension combined with crustal underplating. Modelling of the present-day stress field of the Indo-Australian region (Cloetingh and Wortel, 1986) suggests that, whereas western Australia is presently under compression, eastern Australia should experience tension. Recent lithospheric thinning is also suggested by Tertiary volcanics occurring within the range (e.g., Veevers, 1984). Cloetingh et al. (1992a) inferred from the stratigraphy of the northwestern Australian margin that the present state of stress may have prevailed since approximately 15 Ma. A model with renewed uplift from 20 Ma onwards (modelled by thinning the lithosphere but not the crust; Figures 2-13, 2-22(b)) reproduces the present-day topography as well as the amounts of erosion inferred from the

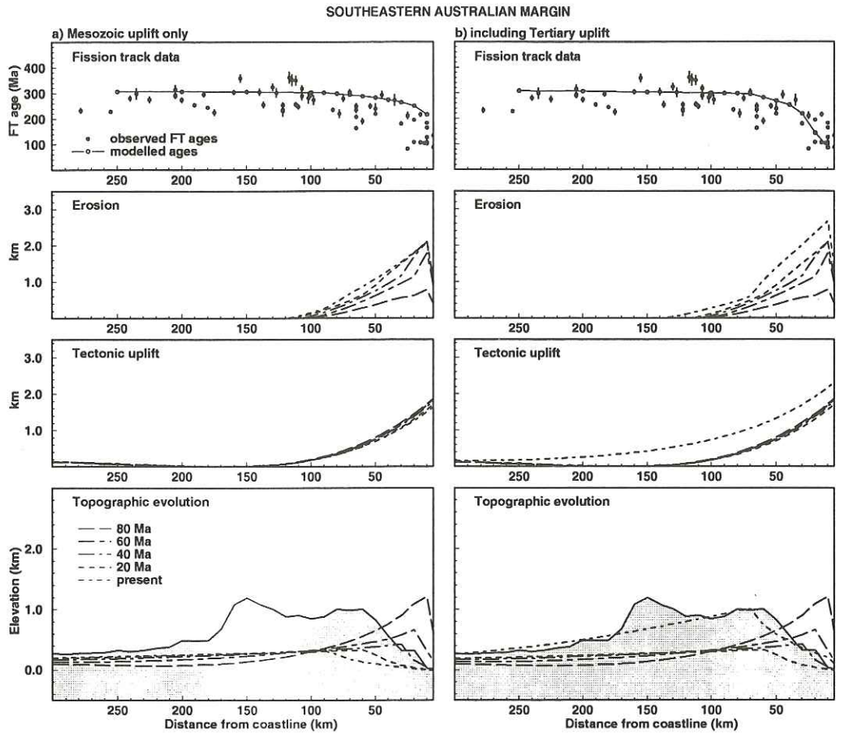

Figure 2-22. Topographic evolution, tectonic uplift, erosion, and modelled fission track ages for two models of uplift of the eastern highlands of Australia. (a) Rift flank uplift takes place from 100-80 Ma as a result of lithospheric necking (z_c = 20 km) during rifting; (b) model including rejuvenation of topography by lithospheric thinning and underplating from 20 Ma onward.

fission track data better. The topographic misfit that both models predict could indicate that, at the onset of rifting, there was residual topography from the Paleozoic orogenies that occurred in the highlands, and that the assumption of a low pre-rift elevation is incorrect. The erosion of antecedent topography during the Meso-Cenozoic would lead to an increased isostatic rebound component aiding in maintaining regional elevation (e.g., Stephenson and Lambeck, 1985). However, models which explain the topographic evolution of the eastern highlands solely as a result of Paleozoic orogeny (e.g., Lambeck and Stephenson, 1986) adopt erosion rates which are an order of magnitude lower than those inferred from fission track thermochronology (see also Brown et al., 1994), although a comparison between measured erosion rates and the long-term spatially averaged erosional time constants employed in

Lambeck and Stephenson's (1986) model is not straightforward. Thus it seems that Paleozoic orogeny, Mesozoic rifting and Cenozoic margin reactivation all played a role in creating the present-day physiography of southeastern Australia.

Namibian Atlantic margin

For modelling the evolution of the Great Escarpment of southwestern Africa, I have developed a model of rifting that predicts a small amount of tectonic uplift of the margin. I employ a pure-shear model (comparable to the one adopted for the Saudi Arabian Red Sea margin) with z_c = 10 km. The continental margin of Namibia is very wide, with the continent-

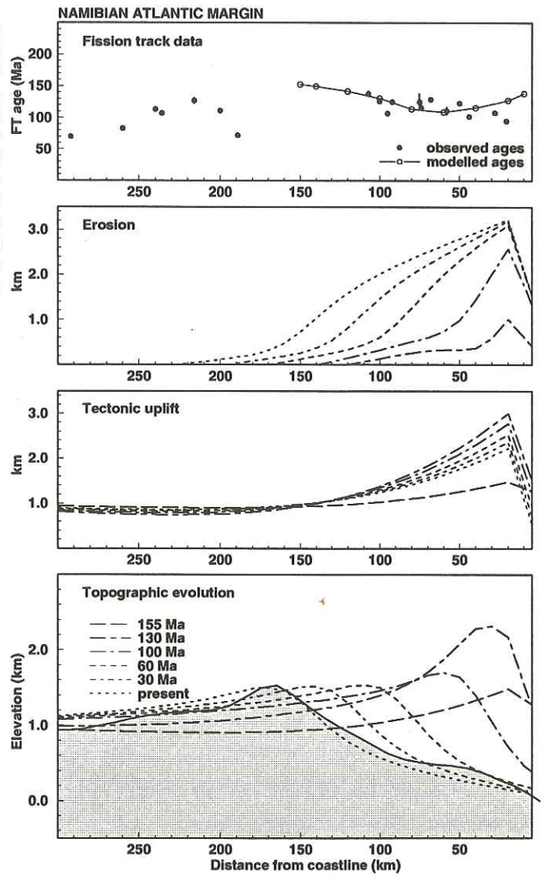

Figure 2-23. Topographic evolution, tectonic uplift and erosion through time, and predicted fission track ages for the Namibian Atlantic margin, adopting a model in which the initial elevation of the southern African interior is 1000 m and there is ~1 km of additional rift flank uplift due to a shallow z_c level. Note that erosion only takes place seaward of the escarpment; because the model is not compatible with the inferred evolution of the hinterland, fission track ages are only calculated for sites in the exterior area.

ocean boundary some 300 km offshore (Gerrard and Smith, 1982); this also tends to dampen the amount of flexural uplift (cf. Figure 2-5). The initial elevation of the continental interior is taken to be 1000 m, this is probably a conservative estimate (e.g., Section 2.2.4). Rifting is assumed to commence at 160 Ma and lead to continental breakup after 30 My. Maximum rift margin uplift as predicted by the forward model amounts to ~1 km and takes place close to the shoreline. Because of the large amount of sediment loading during the post-rift phase, the near-shore area tectonically subsides below its initial elevation after rifting.

The topographic evolution predicted by such a model is depicted in Figure 2-23. The model suggests that some flexurally supported topography existed at the end of rifting, at 130 Ma, but this decayed within 30 My and after that the escarpment retreated laterally, without significant changes in elevation. Retreat rates in this case are intermediate between those of the Saudi Arabian and the Australian margins. Note that the present-day topography has no correlation to tectonic uplift patterns.

The present-day topography predicted by the model compares favourably with that observed. As long as there is rift-related topography, maximum denudation rates are predicted at the locus of maximum tectonic uplift; when the escarpment starts retreating, maximum denudation rates migrate inland with it, so that the total amount of denudation seaward of the escarpment becomes more uniform. However, the model predicts extremely little erosion landward of the escarpment, as a result of the strong asymmetry in basin- and hinterland-ward gradients. This is clearly not compatible with the observed pattern of fission track ages, which do not show an age jump over the escarpment (Brown et al., 1990; see Sections 2.2.4, 2.3.4).

An alternative model was presented by Gilchrist et al (1994), who suggested that interior base level lowering, as a result of breaching of the escarpment by the Orange river, had a profound effect on the morphological evolution of southern Africa. In their model, once breaching has taken place, the escarpment is being eroded from both sides; because the exterior and interior catchments start competing in trying to expand their drainage, escarpment retreat slows down. The model of Gilchrist et al (1994) predicts ~1 km of erosion of the interior area, versus ~2 km in the exterior area. While their inferred erosion pattern is much more homogeneous than the one produced here, the amounts of erosion predicted are still lower that those inferred from the fission track data, suggesting that the initial elevation of southern Africa and subsequent base level lowering were (much) larger than assumed here.

2.5 Discussion

The models generated in this chapter indicate the necessity and potential of studying the tectonic and surface processes acting on a rifted margin and recorded by fission track thermochronology, in order to understand the dynamics of rift basin evolution and its

sedimentary infill. Erosion of rifted margin uplifts is an important process in modifying topography as well as the sedimentary evolution of rifted basins. In the following I will sum up the major inferences from this study.

Vertical motions and topography at rifted margins

One of the main results of the modelling performed here is the notion that the observed present-day topography may have very little connection to the pattern of tectonic uplift (Figure 2-16). Rifted margins which today have relatively subdued topography, as for instance the eastern margin of North America, can have experienced several kilometers of tectonic uplift, which has subsequently eroded away, even though the uplift itself was permanent in nature. Conversely, the development of an escarpment system is mainly controlled by the elevation of the interior plateau and any tectonic uplift is generally not reflected in the present-day escarpment topography. Therefore, an interpretation of long-lived escarpments along, for instance, the Mesozoic margins of Gondwanaland as tectonically supported rift flanks is too simple.

Tectonic uplift at rifted margins can be detected by backstacking the amount of denuded material as constrained, for instance, by fission track data (Section 2.3.4). For reasonable assumptions of lithospheric strength, the present-day topography combined with the amount of erosion indicate significant rift-related tectonic uplift of the exterior area for some margins, while it is not obvious at others. Maximum inferred tectonic uplift values vary from ~2 km for the southeastern Australian margin and 3 km for the Saudi Arabian Red Sea margin to >5 km for the Transantarctic Mountains. Gallagher et al. (1994a) showed, using a similar approach, that the southeastern Brazilian margin could have experienced 1.5-2.5 km of rift-related uplift, although they prefer a model in which flexural rigidity below the exterior area is so low that no differential uplift is required. The conjugate Namibian Atlantic margin, in contrast, presents a case where uplift was much more homogeneous, and not evidently related to rifting.

The strong variation in morphology between different elevated rifted margins (Figure 2-2) thus seems to be the result of varying amounts of rift flank uplift and regional elevation. At one end of the spectrum (regional elevation has strongest control on the margin morphology) could be, for instance, the southern African margin; at the other end (topography is mainly controlled by rift flank uplift) the Transantarctic Mountains. The Saudi Arabian Red Sea and southeastern Brazilian margins would then be intermediate cases where both regional elevation and rift flank uplift play a role. Ten Brink and Stern (1992) explained such differences in morphology by different boundary conditions at the margin: a continuous elastic plate would lead to a 'southern African' morphology while a broken plate would result in 'Transantarctic Mountain-like' rift flanks. The mechanism proposed here, however, seems to be much more logical and self-consistent.

Dynamics of rift margin uplift

The several kilometers of rift flank uplift that are inferred from fission track data at several rifted margins require a dynamic explanation. Thermal mechanisms for uplift of rift flanks have been questioned before, using arguments such as the long-standing nature of rift flank uplifts and the observed gravity anomaly pattern over rifted margins (cf. Weissel and Karner, 1989; Kooi et al., 1992). Thermal mechanisms are only effective when combined with zero flexural rigidity (local isostasy) models for lithospheric rheology (Section 2.3.1). Coherence studies of gravity and topography, in contrast, indicate that the lithosphere retains significant flexural strength adjacent to continental rifts or rifted margins (Section 2.3.3). Forward models employing thermal uplift and local isostasy result in crustal structures and gravity anomaly patterns that deviate strongly from those observed, when erosion of the margin is taken into account (Section 2.3.5). Moreover, the predicted morphological evolution of a rifted margin with low flexural rigidity is not consistent with the generally observed topography at rifted margins (Figure 2-17).

Therefore, a mechanical (flexural) support of rift flanks seems much more plausible. An upward state of flexure at rifted margins, which is required to support the flanks, is most logically explained as the consequence of stretching around an kinematic necking level (z_c) which would stay horizontal in the absence of isostatic compensation. Such kinematics are predicted by dynamic models of lithospheric stretching (e.g., Braun and Beaumont, 1989; Chéry et al., 1992; Bassi et al., 1993) but the exact physical significance of this level is not clear at the moment. The examples studied here suggest that mid-crustal z_c levels are required to produce the observed amount of tectonic uplift and arrive at a realistic crustal structure. Deep (sub-crustal) levels of necking that were proposed as the cause for large uplift of rift flanks, as for instance at the Transantarctic Mountains (Chéry et al., 1992), appear incompatible with gravity data and Moho topography. A more extensive discussion of the significance of z_c, as derived from kinematic modelling studies performed here and in the next chapter, will be presented in Section 6.1.

Flexural uplift does not, however, appear to be the only mechanism supporting rift flanks. For the west Antarctic rift system mantle thinning should be concentrated under the rift flank (the Transantarctic Mountains) in order to explain the uplift/subsidence patterns while maintaining a reasonable crustal structure (Section 2.3.5). In the case of the southeastern Australian margin, the observed gravity and topography patterns also suggest that additional mantle thinning took place underneath the highlands. In this case, however, this thinning may have taken place much later than initial rifting (Sections 2.3.5, 2.4.3).

The need to adopt a lateral offset between crustal extension β and mantle extension δ in a number of kinematic modelling studies could indicate that intracrustal detachments were operating during extension (e.g., Karner et al., 1992). Mid-crustal necking levels may thus be rheologically coupled to lower crustal detachments (Le Pichon and Chamot-Rooke, 1991), suggesting that lower crustal weak zones have a strong rheological control on the kinematics of extension. This point will be discussed further in Chapter 3.

Timing of uplift with respect to rifting

We have seen that escarpments at rifted continental margins are maintained by a high elevation of the continental interior (e.g., Arabia, southern Africa, Brazil). The high elevation of such interior plateaus, of course, also needs a dynamic explanation. It may result from regional uplift driven by active mantle upwelling, initiated sometime during rifting (Camp and Roobol, 1992; Bois, 1993; Ziegler, 1995), and/or crustal underplating associated with flood basalt-type magmatism (Cox, 1980; McKenzie, 1984; Gallagher et al., 1994a).

The timing of regional plateau uplift with respect to rifting is critical in evaluating the dynamic processes responsible for uplift, e.g. 'passive' versus 'active' asthenospheric upwelling (Section 1.1). Pre- syn- as well as post-rift regional uplift has been proposed, for instance, for the Arabian peninsula (e.g., White and McKenzie, 1989; Bohannon et al., 1989; Menzies et al., 1992). Attempts have been made to constrain the timing of regional uplift from fission track studies. However, as shown in Figures 2-18 and 2-24, the interpretation of fission track ages in terms of timing of uplift is not straightforward, because the erosional response acts as a filter between them (see also Steckler and Omar, 1994). Basically, fission track data record the onset of rapid erosion which coincides with generation of major relief. Pre-rift thermal domes may have a high elevation but, because of their long-wavelength nature, have low relief and, consequently, denudation will be slow (up to an order of magnitude slower than for high-relief rift flanks). This is exemplified by the East African dome, the Miocene-Recent uplift of which is not well recorded by fission track data (e.g., Wagner et al., 1992). Therefore, the best approach to determine the presence or absence of significant pre-rift uplift remains studying the stratigraphic relationships between pre-rift and syn-rift rocks on the margin and analyzing the basin fill (e.g., Garfunkel, 1988; Menzies et al., 1992).

Rates of uplift and erosion; morphological evolution

A critical assumption in the models presented above concerns the rates at which different processes take place. Whereas the rate of tectonic uplift is controlled by the duration of rifting, which can be estimated from field relationships of datable rift-related sediments and magmatic rocks, the rates of surface processes are much more difficult to assess. In the model, erosion rates are controlled by the parameter values κ and $K_f v_s$, which are essentially unconstrained. An independent check on (long-term and spatially averaged) erosion rates can be performed by comparing them to results of mass-balance studies (e.g. Garfunkel, 1988; Leeder, 1991) and fission track data.

Figure 2-24 shows modelled tectonic uplift and exhumation paths for the four margins studied, compared to cooling paths which were obtained by inversion of apatite fission track ages and length distributions (see Appendix 1 for the approach taken). Note that modelled exhumation histories may differ significantly from the tectonic uplift paths that were input into the model. Maximum exhumation rates lag behind maximum tectonic uplift by 5-20 My and occur in the exterior area in the early post-rift phase, when the rift flank starts degrading.

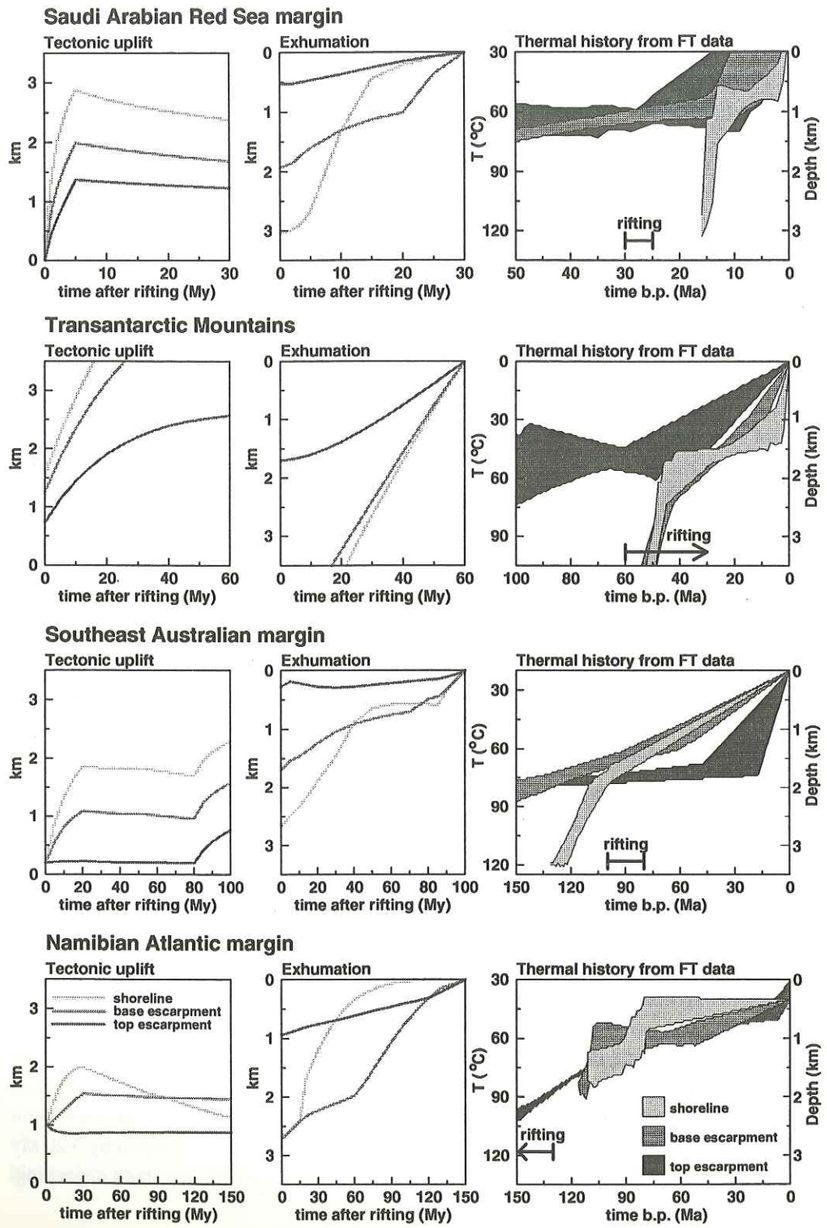

Figure 2-24 (facing page). Comparison of modelled tectonic uplift and erosion rates with cooling/exhumation paths from inversion of fission track data for the four margins studied. Modelled tectonic uplift and exhumation histories are calculated from the preferred models (cf. Figures 2-19; 2-21; 2-22(b); 2-23). Thermal histories were calculated for representative samples from Bohannon et al. (1989) for Saudi Arabia, Gleadow and Fitzgerald (1987) for the Transantarctic Mountains; Moore et al. (1986) for Southeastern Australia and Brown et al. (1990) for Namibia. Note different time scales between figures. Inversion of fission track age and length distribution was done using the Monte Carlo approach of Lutz and Omar (1991) and the annealing model of Laslett et al. (1987; cf. Appendix 1).

After the escarpment has retreated away, exhumation rates decrease by a factor of 5-10. For the Transantarctic Mountains, input tectonic uplift paths decrease exponentially, while the resulting exhumation paths are more or less linear. Inverted thermal histories suggest an exhumation path with discreet pulses. Note that, generally, exhumation paths from forward modelling and inversion of fission track data agree reasonably well. Only for the Namibian Atlantic margin, the fission track data record much more denudation than predicted inland of the escarpment (cf. Section 2.4.3).

Maximum 'syn-rift' exhumation rates from both forward and inverse modelling are 125-225 m/My for the Red Sea, ~200 m/My for the Transantarctic Mountains and 20-40 m/My for the SE Australian highlands. Syn-rift tectonic uplift rates from forward modelling are in the order of 600 and 100 m/My, respectively. Post-rift exhumation rates are an order of magnitude lower, at 10-30 m/My for the Saudi Arabian margin, <10 m/My for SE Australia and 5-30 m/My for the Namibian Atlantic margin. These values are consistent with rates of syn-rift uplift and erosion for rifted margins derived from geomorphological and mass balance studies, which show the same order of magnitude difference between syn- and post-uplift denudation rates. Leeder (1991) quotes rates of 50-350 m/My for actively uplifting rift flanks. These contrast strongly with values of 6-15 m/My given by Wellman (1987) for the eastern highlands of Australia and 5-20 m/My by Gilchrist et al. (1994) for Namibia. Of course, these values could vary in time as a result of climatic change or varying bedrock lithologies. However, temporal variations in erosion parameters seem exceedingly difficult to detect and can, at present, be dealt with in a speculative manner at best.

In a recent paper, Kooi and Beaumont (1995) emphasize the importance of phase shifts or delays in landform response to tectonic forcing. A similar behaviour is observed in the simple evolutionary models presented above (Figure 2-24). The inferred rates of tectonic uplift and erosion suggest that, generally, the topography of a rift flank should grow during rifting until a certain threshold value is reached, where denudation can keep up with tectonic uplift and dynamic equilibrium is attained. Continuous uplift of the area immediately adjacent to the basin, as predicted by most models of rift flank uplift, inhibits the evolution of an effective fluvial transport system towards the basin. It is during the early post-rift phase that the most rapid degradation of the rift flank takes place and a retreating escarpment system can start to develop. The Transantarctic Mountains pose an example of an actively uplifting rift flank system. Because of continuous tectonic uplift, with denudation lagging

behind, the elevation of the mountain range has grown continuously since the onset of rifting (Figure 2-21).

Rift flanks which are supported by permanent uplift mechanisms (e.g., flexure) should degrade within 50-100 My after active tectonic uplift wanes (Figure 2-16(a)). This may have happened at the eastern margin of North America, where Early Cretaceous sediments overstepped the paleo-rift flank 60-65 My after Early-Middle Jurassic rifting in the North Atlantic (Steckler et al., 1988). Late Jurassic-Early Cretaceous fission track ages (~140-150 Ma; Miller and Duddy, 1989; Steckler et al., 1993) along the margin support such a hypothesis. The Egyptian margin of the Red Sea appears to be in a such a state of degradation at present. It is conspicuously lower than the Arabian margin (Figure 2-2(a)) and the morphology of the margin suggests significant erosion and transport towards the Nile river system in the hinterland (J.K. Weissel, pers. commun., 1992). The marked differences between the eastern and western margins of the Red Sea seem, therefore, to be mainly the result of the elevation difference of the Egyptian and Arabian interior plateaus and the consequent effectiveness of material transport towards the hinterland.

CHAPTER 3

MECHANISMS OF SYN-RIFT FLANK UPLIFT: A STUDY OF THE BAIKAL RIFT (SE SIBERIA) AND A COMPARISON WITH THE MALAWI RIFT (EAST AFRICA)

3.1 INTRODUCTION

In the previous chapter, we have seen that a number of rifted continental margins record significant syn-rift flank uplift, on the order of 3-5 km. Forward modelling suggested a mechanical (flexural) origin for most of this uplift. However, as was also noted in Chapter 2, the present-day topography at rifted continental margins is probably not related in a straightforward manner to the tectonic uplift patterns associated with rifting. The pattern of gravity anomalies over rifted margins can be used to test the predictions of forward models on the state of isostasy (e.g., Kooi, 1991), but the gravity field is complicated by continent-ocean boundary effects. For intracontinental rifts, the situation appears to be clearer. Modern continental rifts which developed in cratonic lithosphere are characterised by large isostatic residual gravity anomalies, deep (>5 km) basins and high (>1 km) uplifted flanks but relatively low ($\beta < 2$) stretching values. Rift formation mechanisms involving a finite flexural strength of the lithosphere were proposed as early as the 1930's for these rifts, and have become generally accepted (Bullard, 1936; Vening-Meinesz, 1950; Artemjev and Artyushkov, 1971; Bott, 1976; Weissel and Karner, 1989; Kooi et al., 1992; van Wees and Cloetingh, 1994). Dynamic models also suggest that narrow deep rifts tend to develop in strong cold lithosphere (Bassi, 1991; Buck, 1991).

In this chapter, I will examine syn-rift uplift by studying two young intracontinental rifts which show pronounced rift shoulder topography: the Baikal rift in southeastern Siberia and the Malawi rift in Tanzania. Rifting started at approximately 35 Ma in Baikal and <10 Ma in the Malawi Rift; the major phase of activity took place within the last 5-8 My in both cases. The rifts exploited a pre-existing fault system; in the case of the Malawi rift, Mesozoic extension along these faults preceded the present phase.

I present apatite fission track data which record the denudation history of the flanks of these rifts. As demonstrated in Chapter 2, erosion can strongly modify the topography of rift flanks and, therefore, the amount of tectonic and erosional exhumation that has taken place needs to be known in order to infer vertical motions from the present-day topography. Previous fission track studies of modern rift flanks, in Kenya and Burundi, showed no evidence for major (more than a few hundred meters) recent rift-related erosion (e.g., Van

den haute, 1984; Wagner et al., 1992). There is sometimes evidence of tectonic exhumation across faults, as witnessed by jumps in fission track parameters (e.g., Foster and Gleadow, 1992; Fitzgerald, 1994).

The constraints on vertical motions obtained from the fission track analyses are used to test various models of rift flank uplift. I will show that the present-day topography of rift flanks, when combined with fission track estimates of the amount of exhumation, provides an effective test of these models. However, the 2-dimensional models employed only predict vertical motions along a profile across the rift. In order to determine whether simple flexural mechanisms can explain all of the observed topography, we need to look at 3-dimensional patterns of rift flank uplift. In the final section of this chapter, I will present a 3-dimensional model for the uplift of the Baikal rift flanks, which suggests that an additional mechanism must be taken into account to explain the basin and flank morphology of the northern Baikal basin.

3.2 Uplift of the Baikal rift flanks

3.2.1 Tectonic setting

The Baikal rift has developed on the border of the Siberian craton with the Sayan-Baikal mobile belt (Figures 3-1; 3-2). The structural heterogeneity across this boundary has strongly influenced the location and evolution of the rift system (Logatchev and Zorin, 1992; Sherman, 1992; Logatchev, 1993). Lake Baikal, the deepest lake and the largest fresh water body in the world, occupies the central one third of the rift zone, which stretches from northern Mongolia in the southwest to the Aldan shield, more than 1000 km to the northeast. At its southwestern termination, the zone breaks into the three NS trending rift basins of Busingol, Dharkat and Khubsugul and is terminated by the Bolnai fault. In its central part, the rift zone closely follows the NE-SW oriented southeastern margin of the Siberian craton, but it swings away from this in the northeast, where it evolves into an en-echelon suite of EW trending pull-apart basins (Logatchev and Zorin, 1992; Déverchère et al., 1993).

The Sayan-Baikal fold belt originated from Silurian-Devonian collision of several 'Transbaikalian' micro-continents with the Siberian craton to the northeast (Melnikov et al., 1994). A significant proportion of the belt is composed of Paleozoic granitic plutons. The Obruchevsky-Primorsky-Baikalsky fault zones, which constitute the major border faults of the Baikal rift, are also the site of the Paleozoic suture zone. However, this boundary zone records a much longer orogenic history, comprising also Proterozoic and Archean crustal fragments (Melnikov et al., 1994). During the Mesozoic, closure of the Central Asian Ocean and collision of the Siberian and Chinese-Korean cratons produced the Central Asian fold belt, which runs from the Tien Shan mountains in the west to the Sea of Okhotsk in the east (Khain, 1990; Ermikov, 1994). To the southeast of Lake Baikal, a number of sedimentary

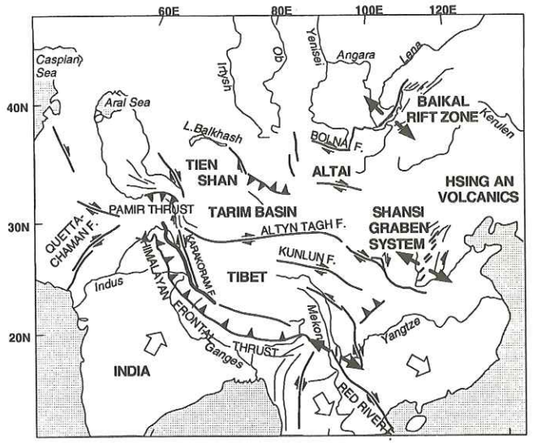

Figure 3-1. Cenozoic tectonics of Central Asia (after Molnar and Tapponier, 1975). Open wide arrows indicate movement of major crustal blocks.

basins developed in a convergent setting (Ermikov, 1994). The NW border of Mesozoic shortening in the area is the Angara thrust (Figure 3-2), which displaces an Archean crustal block over Jurassic foreland basin sediments covering the Siberian craton.

Extensional tectonics in the Baikal rift zone were under way by mid-Oligocene (35 Ma), as recorded by the basal beds of the sedimentary succession outcropping on the shores of Lake Baikal (Mats, 1992; Logatchev, 1993). Total extension, in an ESE-WSW direction, amounts to a maximum of 19 km in the central Baikal rift (Zonenshain and Savostin, 1981; Zorin and Cordell, 1991). A significant part of the extension has probably taken place from the mid-Pliocene (3.5 Ma) onward, as suggested by the morphology of the rift flanks and the sedimentary succession within the rift (Logatchev and Zorin, 1987, 1992; Hutchinson et al., 1992; Mats, 1992; see subsection on morphology and sedimentology).

Explanations for the evolution of the Baikal rift zone have evolved, since the late seventies, along two schools of thought: one considering mainly 'active' and the other 'passive' rifting mechanisms (cf. Section 1.1). Models of active rifting in Baikal (e.g., Zorin, 1981; Logatchev et al., 1983; Logatchev, 1993; Windley and Allen, 1993) suggest that rifting is the result of slow uprising of a mantle diapir, associated with broad doming of the area since the Oligocene. In this model, it is the interaction of upwelling mantle with crust since the middle Pliocene that caused the observed increase in rates of extension and vertical motions (Logatchev and Zorin, 1987; see also Westaway, 1993). On the other hand, passive rifting models (e.g., Molnar and Tapponier, 1975; Tapponier and Molnar, 1979; Zonenshain and Savostin, 1981; Khain, 1990) emphasize the significance of timing and location of events: the onset of extension in the Baikal rift zone is coincident with collision of the Eurasian and Indian continents from the late Eocene onwards. Indentation by India led to intraplate deformation throughout central and eastern Asia (Figure 3-1), inducing regional extensional stresses behind the southern tip of the strong Siberian craton. Recent kinematic modelling

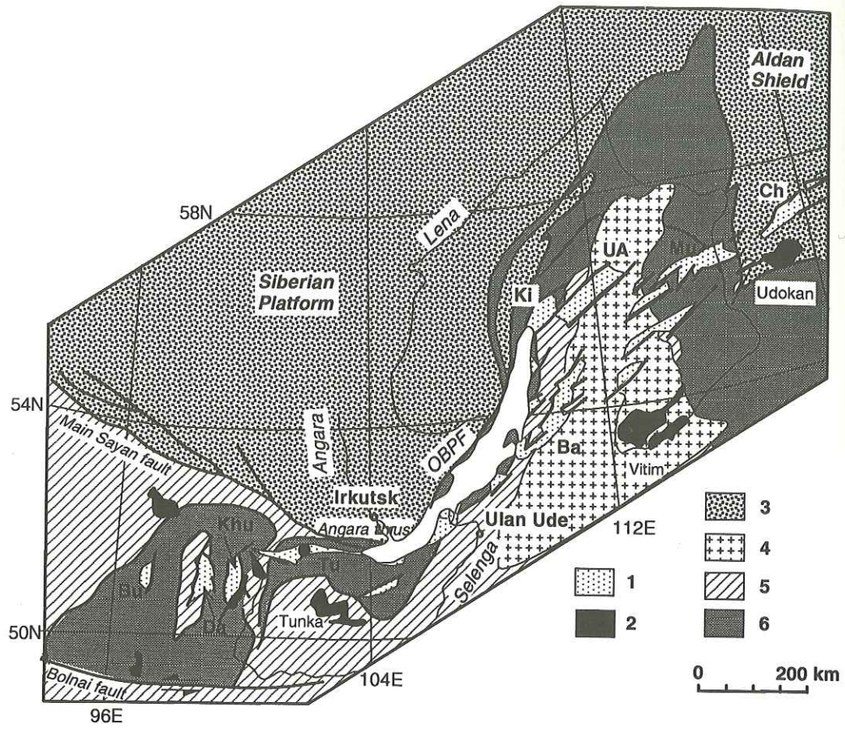

Figure 3-2. Simplified geological map of the Baikal region (modified from Logatchev, 1993). Notations: 1) Cenozoic rift basin sediments; 2) Cenozoic volcanics; 3) Sedimentary cover of the Siberian craton (Vendian-Cretaceous); 4-6: Sayan-Baikal mobile belt; 4) Paleozoic granites; 5) Paleozoic metamorphic terrains; 6) Precambrian 'Transbaikalian' basement. Cenozoic basins are indicated by letter codes: Ba: Barguzin; Bu: Busingol; Ch: Chara; Da: Dharkat; Khu: Khubsugul; Ki: Kitchera; Mu: Muya; Tu: Tunka; UA: Upper Angara. OBPF = Obruchevsky-Baikalsky-Primorsky fault zone.

(Balla et al., 1991) and paleo-stress analyses (Delvaux and Klerkx, 1994; Delvaux et al., 1995) indicate that the first phase of extension in the Baikal rift was associated with a regional strike-slip stress regime, favouring a 'passive' origin. However, some of the geophysical observations (see next section) do suggest the existence of an anomalous mantle structure below the rift zone and a combination of driving mechanisms may have operated together (e.g., Kiselev and Popov, 1992; Delvaux and Klerkx, 1994).

Figure 3-3. Lithospheric cross section across the central Baikal rift; after Krylov et al. (1981). Bold numbers indicate compressional P-wave velocities; italic numbers inferred density from gravity data (Logatchev et al., 1983).

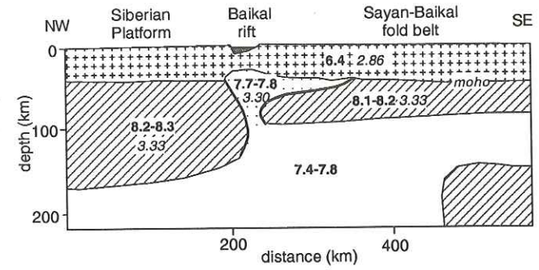

Geophysical data

The Baikal rift has been the focus of geophysical studies for over 30 years and an extensive geophysical database, including gravity, seismic, heat flow and seismological data, exists.

The gravity field over the Baikal region is dominated by strongly negative short wavelength anomalies over the lake basin, superimposed on a longer wavelength positive anomaly and a regional trend dipping to the southeast (Artemjev and Artyushkov, 1971; Diament and Kogan, 1990; Zorin and Cordell, 1991; Ruppel et al., 1993; Burov et al., 1994). Analysis of coherence between Bouguer gravity and topography (Diament and Kogan, 1990; Ruppel et al., 1993), and the pattern of isostatic residual anomalies (Artemjev and Artyushkov, 1971; Section 3.2.3) both indicate that the lithosphere has a relatively large flexural rigidity in the order of 3×10^{23} Nm (effective elastic thickness $T_e \approx 30$ km). From an analysis of the long wavelength gravity anomalies in the area, Zorin et al. (1989) inferred a wide zone of asthenospheric upwelling below the rift. However, Diament and Kogan (1990), who followed a similar approach, concluded that the gravity pattern could be explained by homogeneous pure-shear lithospheric thinning.

Deep seismic soundings (Krylov et al., 1981) indicate that the Moho depth decreases from 40 km under the Siberian craton and 45 km below the Sayan-Baikal fold belt to a minimum of 35 km below the central Baikal rift (Figure 3-3). P-wave velocities of the upper mantle below the rift zone are 7.6-7.8 km, as opposed to >8.1 km under the Siberian platform. A recent teleseismic study (Gao et al., 1994) suggests that the asthenosphere rises to a minimum depth of 50 km below the rift zone and that upwelling is asymmetric, with a steeper NW side. However, mantle xenoliths contained in the volcanics associated with the Baikal rift imply a source that is at least partly lithospheric (Kiselev and Popov, 1992), suggesting that the lithosphere cannot have been completely replaced by asthenosphere under the rift zone. These authors suggest that the anomalous mantle forms a layer below the crust down to a maximum depth of 60-100 km, thus representing an asthenospheric 'diapir', as originally proposed by Krylov et al. (1981; Figure 3-3).

Heat flow within the Baikal rift is highly variable, with a mean background value of ~75 mWm^{-2} (Lysak, 1992). For a comparison, the heat flow measured in the Siberian craton and Sayan-Baikal fold belt is 40-60 mWm^{-2}. Heat flow values in the range of 50-75 mWm^{-2}

within the rift zone can be explained by conductive heating of the crust (Lysak, 1992); local sharp thermal anomalies superimposed on this regional variation result from convective fluid flow within the basin (Crane et al., 1991; Golubev et al., 1993).

The Baikal rift zone is one of the most seismically active extensional regions in the world. Present-day seismicity is concentrated in a band running from the eastern shore of the southern and central basins, via the Academician ridge and the Barguzin basin (Figure 3-2), to the North Muya region; the northern Baikal basin shows very little seismic activity (Déverchère et al., 1991, 1993; Sherman, 1992). Earthquakes have been recorded up to unusual depths of 30 km (Déverchère et al., 1991), and define planes dipping 50-60° up to depths of at least 20 km (Déverchère et al., 1993). An integrated stress tensor calculated from instrumental seismicity reveals a present-day extension direction of N160E. This conforms well with paleostress data from Recent sediments, but contrasts with older paleostress directions, indicating a rotating stress field during the evolution of the rift (Delvaux and Klerkx, 1994; Delvaux et al., 1995).

Morphotectonic evolution, volcanism and sedimentary infill

The Baikal rift is composed of three asymmetric half graben basins: the northern, central and southern Baikal basins (Hutchinson et al., 1992; Mats, 1992; Scholz et al., 1993). The northwestern limits of the basins are formed by the Obruchevsky-Primorsky-Baikalsky border fault system; to the southeast the basement rises gradually. The rift zone is characterised by prominent rift flank topography on either side of lake Baikal (Figure 3-4). There is a clear morphological asymmetry between the western and eastern flanks of the rift. The western rift flank, which forms the Primorsky and Baikalsky ranges, is cut by the border fault system, forming major fault scarps up to 1 km high (Ufimtsev, 1991; Mats, 1992). Above the fault scarps, an inclined summit slope is usually present (Ufimtsev, 1991). The Primorsky and Obruchevsky faults enclose the Olkhon block, which can be regarded as a very large tilted fault block continuing into the sub-aqueous Academician ridge (Figure 3-5). Structural dips on the western flank are generally away from the basin centre. In contrast, the eastern flank, comprising the Khamar Dhaban range, is not cut by border faults but generally steps down to the lake in a number of terraces, the surfaces of which are tilted towards the basin centre. The Khamar Dhaban range is dissected by the Selenga river 'saddle'. Remains of a planation surface, believed to be Cretaceous-Paleogene in age on the basis of scattered continental deposits and paleosols ('weathering crust' in the Russian literature), are generally encountered at elevations of up to 2 km (Logatchev and Zorin, 1992; Mats, 1992; Kashik and Mazilov, 1994). According to Logatchev and Zorin (1992), this surface defines a large structural dome (the 'Sayan-Baikal domal uplift') but it is broken up into a large number of differentially uplifted blocks (Ufimtsev, 1991; Mats, 1992). Above the planation surface the mountain ranges have a rugged Alpine morphology. Topographic elevation reaches more than 2.5 km in the Baikalsky ridge to the northwest of the rift, the Barguzin ridge to the northeast and in the Khamar Dhaban mountains south of the basin. The highest elevations

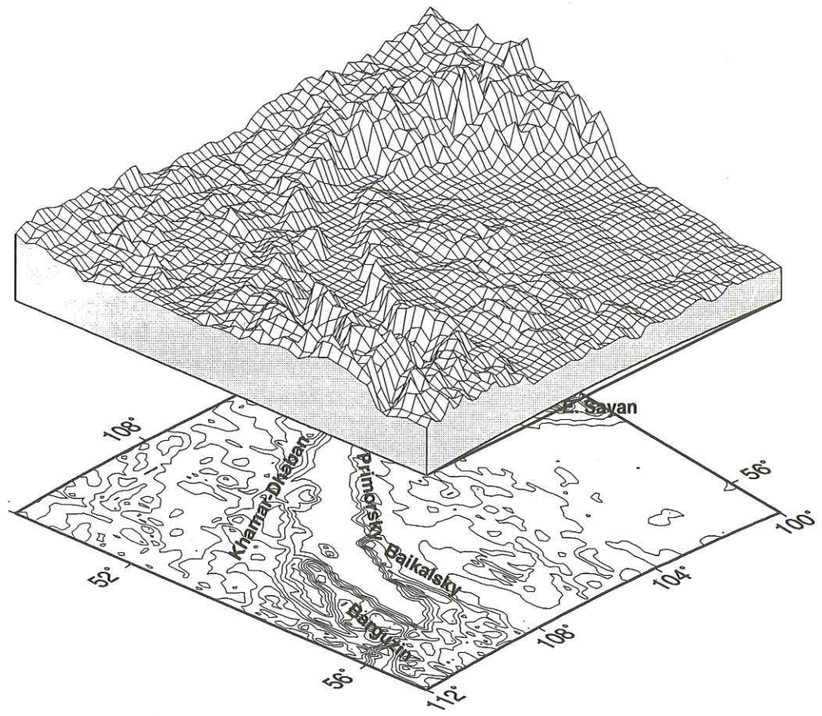

Figure 3-4. Topography of the Baikal rift region, constructed from the ETOPO-5 database. View is from the northeast.

(>3 km) occur in the eastern Sayan mountains, but seem related to transpressional tectonics along the main Sayan fault, rather than to rifting.

Two main stages are recognised in the sedimentary infill of the lake, as recorded by outcrops on its southeastern shore (Popova et al., 1989; Mats, 1992; Kashik and Mazilov, 1994). These apparently correlate with seismic facies recognised in the lake fill (Hutchinson et al., 1992; Scholz et al., 1993). The older (Oligocene -mid-Pliocene) sediments exhibit mainly fine grained alluvial-lacustrine facies, while coarse clastics dominate since the mid-Pliocene. The upper unit, which is locally disrupted by faults and slumps, generally constitutes more than half of the basin fill (Figure 3-5). The sedimentological difference between the two units is generally interpreted in terms of major relief generation on the flanks and deepening of the basin from the mid-Pliocene onwards (e.g., Mats, 1992). Climatic deterioration, from subtropical in the mid-Cenozoic to the present taiga type climate, also played a role (Popova et al., 1989; Mats, 1992).

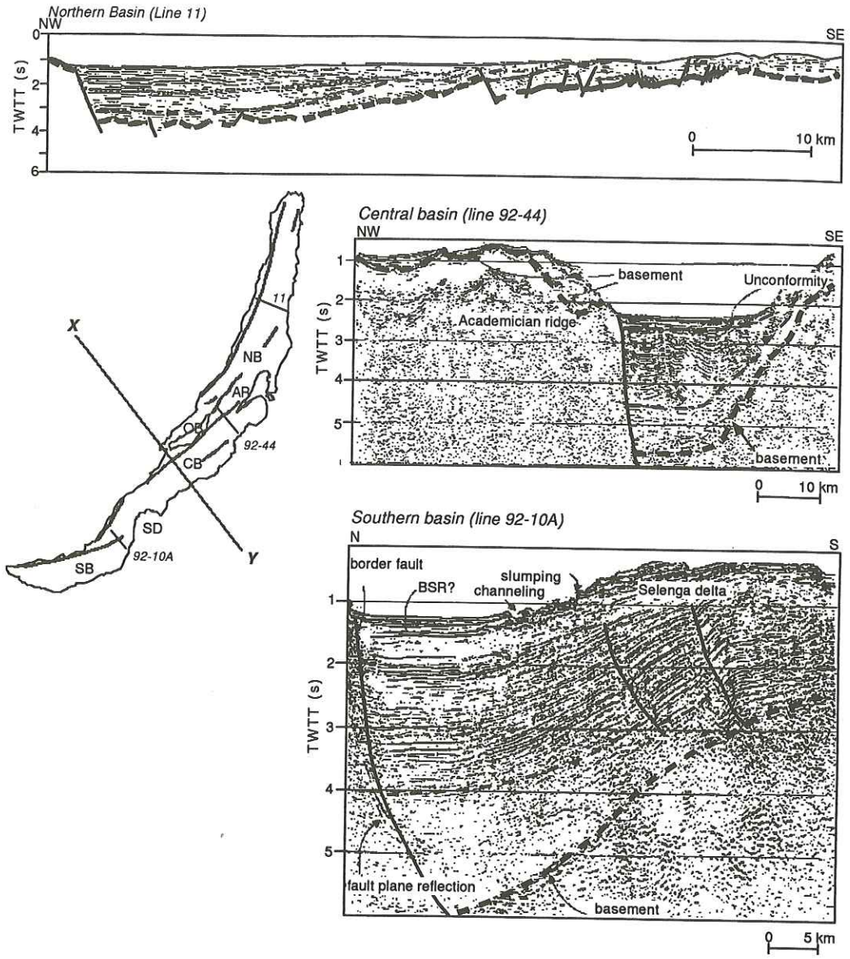

Figure 3-5. Multichannel seismic reflection profiles through the northern, central and southern Baikal basins, showing the half graben character of the basins and the two stage sedimentary infill. After Hutchinson et al. (1992; northern basin) and Scholz et al. (1993; central and southern basins). Thick dashed line indicates inferred basement; thinner dashed line separates lower (Oligocene-Lower Pliocene) from upper (Upper Pliocene-Recent) rift deposits. Inset shows location of lines within Baikal rift. Profile XY is modelled in Section 3.2.3. Notations: AR: Academician Ridge; CB: Central Basin; NB: Northern Basin; OB: Olkhon Block; SB: Southern Basin; SD: Selenga Delta.

Volcanism associated with the Baikal rift is of relatively minor importance (Logatchev, 1993; Rasskazov, 1994): the total amount of volcanics does not reach more than 5-10 × 10^3 km^3. The composition of the volcanics is remarkably uniform; most are alkali-olivine basalts (Rasskazov, 1994). Volcanism is not located within the rift zone itself, but is restricted to three areas to the south and east of it: the Tunka basin in the south and the Vitim plateau and Udokan ridge to the northeast (Figure 3-2). Although the oldest datings of volcanics in the Tunka basin go back to the late Cretaceous-Paleogene, the vast majority of the volcanics was erupted in the Miocene, between 16 and 20 Ma (Rasskazov, 1994). Field relations indicate that at the time of eruption only subdued relief existed. Minor younger volcanic flows have been influenced by greater relief.

3.2.2 Exhumation history of the Baikal region from fission track thermochronology

Samples for fission track analysis were collected from both sides of the rift (Figure 3-6; Table A2-1 in Appendix 2). On the western side of the rift, an age-elevation profile was collected in the Primorsky range, as well as a profile across it. A number of samples were taken from the Olkhon block in the Priolkhon region. On the eastern side of the rift, samples were collected in the Khamar Dhaban ranges north and south of the Selenga river valley.

Results

Apatite fission track (FT) ages and mean track lengths are summarised in Table 3-1 and depicted in Figures 3-6 and 3-7. All ages are reported as central ages* (Galbraith and Laslett, 1993) with ±1σ errors. Sample ages show a relatively large spread, varying between 57±10 and 227±19 Ma. Ages significantly younger than 100 Ma were, however, only encountered in samples from the Primorsky fault scarp, which yielded low quality apatites, affected by fluid leaching. Most samples have FT ages between 100-140 Ma, with relatively high mean track lengths (~13.5 μm) and narrow (σ ≤ 1.1 μm) symmetrical track length distributions (Figure 3-7).

There is no systematic geographical variation of FT ages (Figure 3-6). A clear variation of FT ages and track lengths with elevation neither exists (Figure 3-8). Samples from the Priolkhon area (Olkhon block) and the Khamar Dhaban mountains display nearly vertical age-elevation profiles, with track lengths around 13.0-13.5 μm. Samples from the Primorsky range (mainly the Primorsky fault scarp) show a very large scatter, the only observable trend being an unusual decrease of FT age with elevation. Here, nearly all track lengths are <13

* The central age is the age calculated from the logarithmic mean of the individual fission track counts. The age dispersion *D* is the relative standard error of the single grain ages. The central age and age dispersion are calculated following the algorithm of Galbraith and Laslett (1993).

Table 3-1. Apatite fission track results for the Baikal rift flanks

sample	elev. (m)	number of grains	age ±1σ (Ma)	D (%)	mean track length (μm)	st.dev. (μm)	number of tracks
Primorsky range/Priolkhon area (W flank)							
BA058	1040	18	87± 9	12			
BA060	1180	13	57±10	9			
BA061	1330				12.8±0.2	1.1	36
BAI 1	500	16	159±17	14	12.0±0.2	1.2	40
BAI 2	720	20	165±14	13	12.3±0.2	1.3	65
BAI 3	960	19	132±22	57			
BAI 4	1050	20	74±12	30			
BAI 5	820	20	221±32	10			
BAI 6	455	18	116± 9	11	13.7±0.1	1.0	100
BAI 7	990	15	132± 9	10	13.6±0.1	1.1	102
BAI 8	830	16	142±11	13	13.6±0.1	1.1	100
BAI 9	625	17	130±14	30	13.7±0.1	1.1	100
BAI 10	455	20	120± 9	11	13.3±0.1	0.9	100
BAI 11	455	19	133±14	24			
BAI 14	675	20	139±10	15	13.4±0.1	1.0	100
BAI 15	730	20	101±10	12			
BAI 16	730	20	195±16	15	12.6±0.1	1.3	102
Khamar Dhaban mountains (E flank)							
BAI 17	1020	20	107± 6	14	13.1±0.1	1.1	101
BAI 18	1200	20	116± 9	22	13.4±0.1	1.1	100
BAI 19	1300	20	111± 8	9	13.3±0.1	1.0	100
BAI 20	700	20	112± 7	9	12.6±0.1	0.9	70
BAI 21	500	18	133± 9	12			
BAI 22	700	20	227±19	15	13.8±0.1	1.0	100
BAI 27	1250	15	96± 9	12	12.7±0.2	1.3	30
BAI 30	1030				13.2±0.1	1.1	100
BAI 32	640	14	130±14	6	13.5±0.2	1.2	30

μm. On a plot of mean track lengths against FT age (Figure 3-9), however, the data define two clearly distinguished groups. Most samples fall in a trend of decreasing track lengths from 140 Ma (~13.7 μm) down to 100 Ma (~12.6 μm), with four samples defining a separate trend from 160 Ma (~12 μm) up to 230 Ma (13.8 μm).

Interpretation

The long and narrow track length distributions, vertical age/elevation profiles and clear grouping into two FT age/track length groups suggest that most samples record a rapid cooling event that occurred around 140-120 Ma. Samples which record ages >150 Ma would have been exhumed from temperatures within the apatite partial annealing zone (~60-120°C) during this event; samples with ages <140 Ma from temperatures >120°C. As most track length distributions are relatively long (only 1-1.5 μm shorter than those recorded in

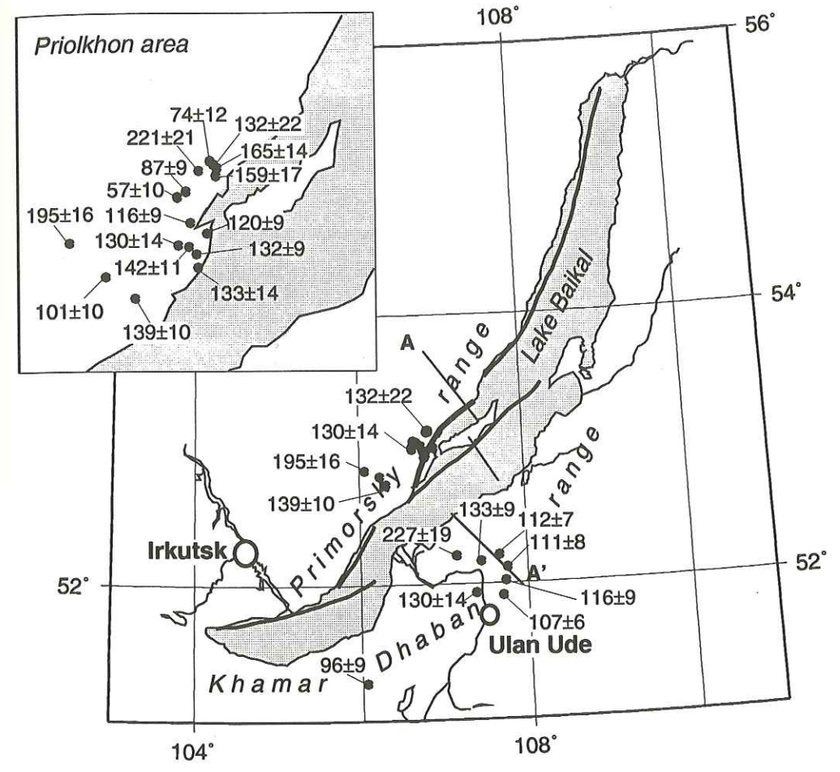

Figure 3-6. Map showing distribution of apatite fission track ages. Composite profile A-A' is shown in Figure 3-7. Inset is a blow up of the Priolkhon area to the west of the rift.

undisturbed volcanics; Gleadow et al., 1986) and narrow, it is suggested that most samples cooled rapidly, reaching surface temperatures (i.e. <50°C) at around 100-120 Ma. Samples from the Primorsky fault scarp, some of which record ages significantly younger than 100 Ma, are considered less reliable; they seem to have been influenced by (fault related?) fluid leaching. The samples with oldest FT ages (BAI16 and 22) record Triassic cooling (around 230-195 Ma). This first cooling phase could have brought these rocks to temperatures around 60°C, from which they cooled during the second event, at 140-120 Ma. The old age and high mean track length for sample BAI22, however, probably results in par6t from the high Cl-content of this sample, as indicated by very wide etch pits.

The inferred cooling event during the Early Cretaceous took place during a protracted history of Mesozoic orogenic activity in the area (e.g., Khain, 1990; Ermikov, 1994). The area

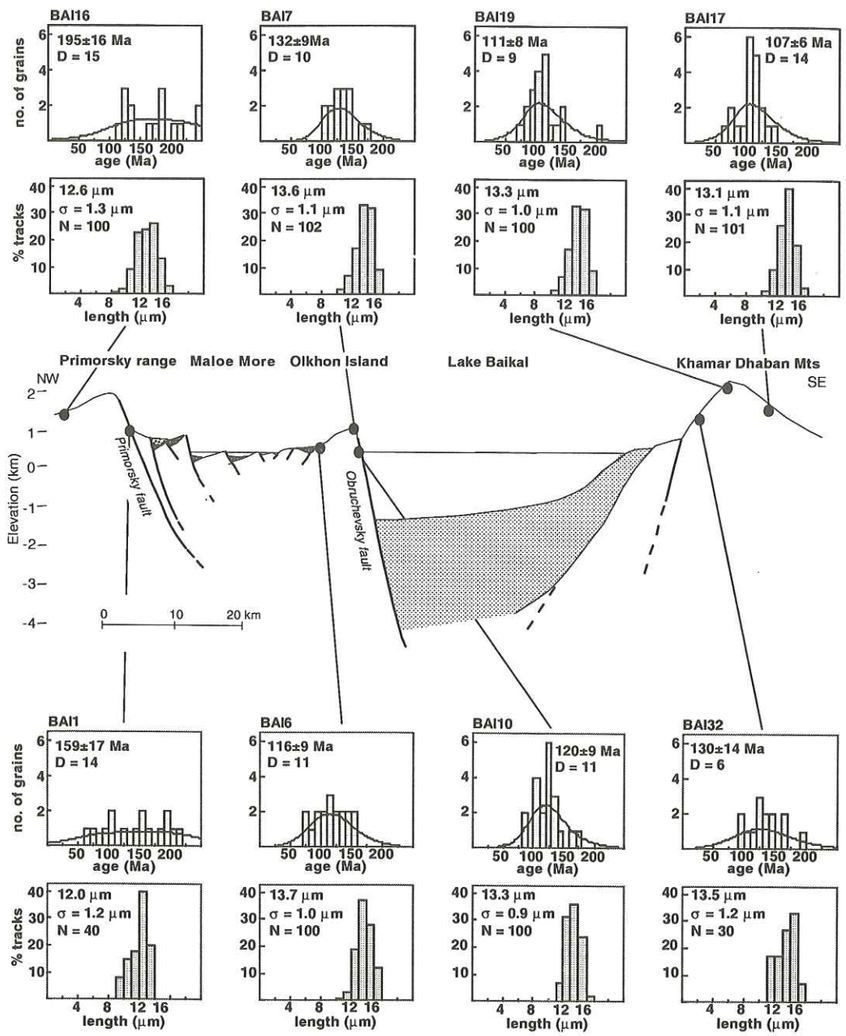

Figure 3-7. Profile through the Baikal rift (after Mats, 1992), with fission track results. Stippling indicates Neogene-Recent rift deposits. Sample sites are projected onto the profile. Upper panels of fission track data show histograms of the distribution of single grain ages with probability density curves; lower panels show histograms of track length distributions.

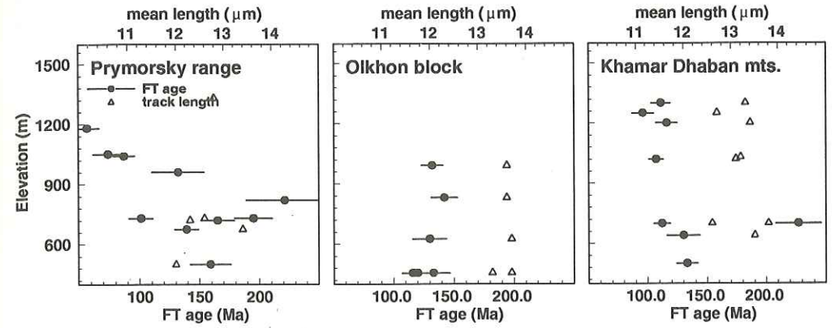

Figure 3-8. Age/elevation plots for samples from the Prymorsky range and the Olkhon block (western flank of the Baikal rift), and the Khamar-Dhaban mountains (eastern flank).

to the east of lake Baikal (Khangai-Yablonovy province in Russian literature) was affected by major vertical motions and magmatic activity during this time while, in the west Baikal province, thin skinned thrusting and molasse sedimentation prevailed. In the area to the southeast of lake Baikal, basalt flows and mafic dykes occur with radiometric ages of 100-127 Ma (Ermikov, 1994). Upper Jurassic-Lower Cretaceous coal-bearing continental deposits, occurring in intermontane basins, have been affected by contact metamorphism. Thus, the more or less random variation of FT ages throughout the study area could be, at least partly, a result of different geothermal structure and activity. However, differential denudation as a result of vertical block movements probably also played a role. The amount of denudation is difficult to estimate because geothermal gradients for the Mesozoic are unknown, and probably variable. However, the age-length plot (Figure 3-9) suggests that samples with ages around 100 Ma and track lengths <13 µm (e.g., BAI17, BAI27) were exhumed from temperatures significantly above 120°C.

Figure 3-9. Plot of mean track length against fission track age for the Baikal rift samples.

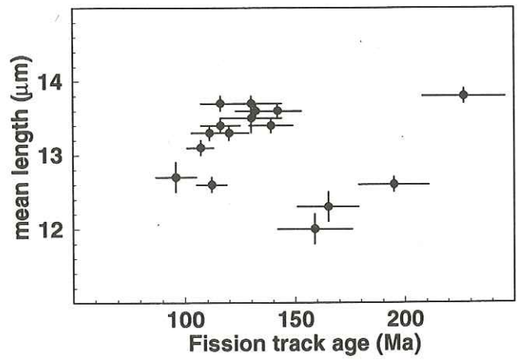

Mesozoic denudation of the Baikal region is also documented by the widespread occurrence of the planation surface mentioned earlier. The age of this surface is generally described as Late Cretaceous-Paleocene in the Russian literature (e.g., Mats, 1992; Kashik and Mazilov, 1994). The fission track data presented here suggest that onset of exhumation took place already during the Early Cretaceous. The elevation of this planation surface, which is mostly encountered near the summits of the mountain ranges, can be used as a pre-rift reference surface. The FT data indicate that very little erosional denudation has affected the flanks adjacent to the central Baikal rift since their formation, so that the present-day topography reflects rift-related tectonic uplift. This is a significant result which I will use in modelling the tectonic uplift of the Baikal rift flanks.

3.2.3 Modelling rift flank uplift adjacent to the central Baikal basin

Introduction and modelling approach

The gravity anomaly pattern and morphology of intracontinental rifts suggest that the lithosphere retains flexural strength during rifting. Figure 3-10 shows the crustal structure and associated gravity anomalies predicted by a model of local isostatic compensation of the basin and flanks. The strongly negative isostatic residual anomalies over the basin, associated with a much thinner crust than observed below the rift, indicate that the lithosphere retains finite strength and that the system is in a state of regional upward flexure (cf Section 2.3.5).

Kinematic rifting models based on the concept of a strong lithosphere, generally proceed from a prescribed deformation of basement and Moho topography, after which the

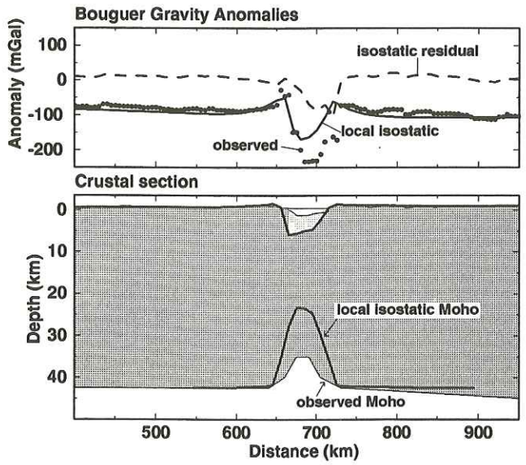

Figure 3-10. Crustal cross section and associated Bouguer gravity anomalies for the Baikal rift, calculated for a model of local isostatic compensation. Crustal thinning is calculated assuming Airy isostasy under the rift basin (e.g., McKenzie, 1978); rift flanks are supported thermally by depth-dependent stretching (e.g, Royden and Keen, 1980; Beaumont et al., 1982). Gravity anomalies are calculated as in Chapter 2 (cf Figure 2-11). Note the strongly negative isostatic residual (= observed - local isostatic) anomalies below the rift.

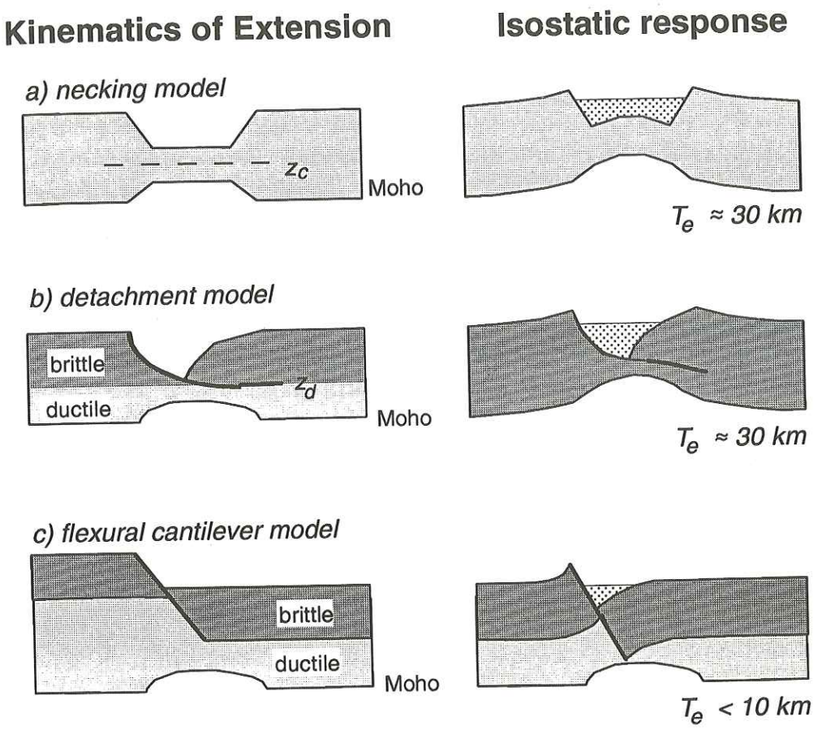

Figure 3-11. Kinematics of extension and regional isostatic response for three different models: (a) necking model (Braun and Beaumont, 1989a; Kooi et al., 1992); (b) detachment model (Kusznir et al., 1987; Weissel and Karner, 1989); (c) flexural cantilever model (Kusznir et al., 1991; Kusznir and Ziegler, 1992). See text for discussion.

buoyancy forces resulting from the deformation are integrated and regionally compensated (cf. Section 2.3.1). However, the kinematic description of deformation varies widely between different models, reflecting different views on the deformation processes involved (Figure 3-11). In chapter 2, I used a model of lithospheric 'necking' (Braun and Beaumont, 1989; Kooi et al., 1992) to predict crustal structure and topographic evolution at rifted continental margins. This can be regarded as an end member model, as motion along faults is not explicitly taken into account. The entire crust is assumed to deform in a pure-shear mode; deformation is described as lithospheric necking around a level z_c (Figure 3-11(a), see also Figure 1-4).

There is, however, mounting evidence that the geometry of continental rifts is strongly influenced by border faults (e.g., Rosendahl, 1987; Kusznir and Ziegler, 1992; cf. Section 1.1) along which most of the extension takes place. Models that explicitly include motion along faults in the upper crust are generally termed 'simple shear-pure shear' models and can be classified in two categories. In the 'detachment' model of Kusznir et al. (1987) and Weissel and Karner (1989), extension is accommodated along a (generally) listric border fault which soles out into a detachment level; a depression is caused by collapse of the hanging wall. Below the detachment depth z_d, stretching occurs by pure-shear. The second class of models builds on the 'flexural cantilever' concept originally proposed by Vening-Meinesz (1950). In such a model (Kusznir et al., 1991; Kusznir and Ziegler, 1992), the border faults are planar and the surface deformation is produced by upper crustal flexure. This model implicitly assumes large amounts of lower crustal deformation. The basin width and basement curvature are directly controlled by the flexural rigidity or equivalent elastic thickness T_e, which results in very low predicted T_e when this model is applied to actual examples. The low rigidities predicted by the flexural cantilever model are often interpreted in terms of decoupling of lithospheric layers, whereas in the necking and detachment models the resulting rigidity is interpreted as a 'bulk lithospheric' rheology (e.g., van Wees, 1994).

The formulations of the different models have mainly been based on deep seismic reflection data (e.g., Pinet et al., 1987; Klemperer, 1988; Brun et al., 1991, Le Pichon and Chamot-Rooke, 1991), rheological considerations (cf. van Wees, 1994) and dynamic modelling results (e.g., Braun and Beaumont, 1989a; Dunbar and Sawyer, 1989; cf. discussion section). Although the different models have been widely used during the last few years, and often even applied to the same data sets (e.g. Ebinger et al., 1989; Marsden et al., 1990; Karner et al., 1992; Kusznir and Ziegler, 1992; Magnavita et al., 1994; Hendries et al., 1994; Odinsen et al., manuscript in prep.), there have been hardly any attempts, as yet, to discriminate between the different models on the basis of their ability to predict observed basement and topographic deflections in a given setting. Kusznir et al. (1991) compared a detachment model and a flexural cantilever model for predictions of basement topography in the Jeanne d'Arc basin offshore western Canada, but there the flanks of the basin are submerged and buried.

The Baikal rift provides a good test case for the various kinematic models of rift formation. The central segment of the rift evolved mainly under pure WNW-ESE extension and the major phase of basement subsidence and topography generation has taken place during the last 3.5 My. The available fission track data indicate that erosion has been minor in this rapid episode of rifting and geomorphological data suggest that there was little relief in the area before this phase. Thus, present-day topography surrounding the basin reflects recent rift-related tectonic uplift. In the following, I will present modelling results for a profile across the central Baikal basin (cf. Figure 3-5) adopting the different models presented above. For all three models, parameters are adjusted to provide a fit to the observed basement depth, adopting a sediment fill up to the observed water depth. The models predict topography and Moho depth, from which gravity anomalies can be calculated. These are

compared to observations. I adopt crustal and lithospheric thicknesses of 42.5 and 200 km, respectively, and a rifting duration of 5 My. Other modelling parameters are the same as in Table 2-1. Gravity and topography data were provided by E. Burov; the Russian Bouguer gravity data were corrected for a more conventional density reduction (2600 kgm^{-3} instead of the original 2300 kgm^{-3}; cf. Burov et al., 1994). Moho depth was digitised from the map of Zorin et al. (1989), while basement depths below the basin are from the map by Hutchinson et al. (1992). In the data, a regional trend in both topography and gravity is obvious, from 300 m and -60 mGal in the northwest to >1200 m and -100 mGal in the southeast. These trends result from the thinner crust and thicker lithosphere under the Siberian craton (30 km and 200 km, respectively) compared with the Sayan-Baikal fold belt (45 km and 150 km; Zorin et al., 1989). I approximate these asymmetries by adding the observed trends to the model results, which were calculated for mean values of crustal and lithospheric thickness, in order to compare these with observations.

Modelling results

Figure 3-12 shows the modelled crustal structure, topography and gravity anomaly patterns for the pure-shear lithospheric necking model. Free parameters in this model include the

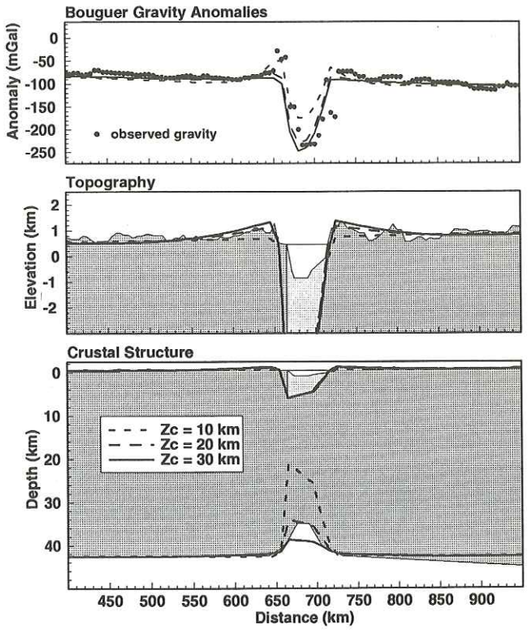

Figure 3-12. Predicted crustal structure, topography and Bouguer gravity anomalies for Profile X-Y across the central Baikal basin, adopting a lithospheric necking model (Kooi, 1991) and different levels of z_c.

stretching (β and δ) distribution, the depth of the 'necking level' (z_c) and the elastic thickness (T_e). A good fit is obtained for T_e = 30 km and z_c = 20 km. Shallower z_c levels do not predict sufficient rift flank uplift, while requiring unreasonable crustal thinning in order to create a sufficiently deep basin; this is reflected in Bouguer anomalies that are higher than observed over the basin. Deeper z_c levels, on the other hand, predict too little crustal thinning. Maximum β factors below the rift are in the order of 1.6; β averaged over the rift zone is approximately 1.3, for z_c = 20 km. A homogeneous pure-shear model (β = δ) is able to fit the observed topography and gravity patterns, indicating that no anomalous mantle upwelling is required underneath the central Baikal basin to explain these features. The constraint on flexural rigidity is not very tight for this model; I have adopted constant flexural rigidities here, in contrast to isotherm defined rigidities in Chapter 2, because the thermal perturbation associated with rifting (and thus T_e reduction) is relatively small.

Results from a detachment model of extension are shown in Figure 3-13. Here, I have used a model developed recently by ter Voorde and Cloetingh (1995). This model extends earlier detachment models (Kusznir et al., 1987; Weissel and Karner, 1989) in that it incorporates a fully time-dependent finite difference solution to the kinematic displacement field (cf. ter Voorde and Bertotti, 1994). Free parameters in this model are: the depth of the detachment z_d, the amount of extension h, the shape of the fault and the width of the region of pure-shear extension. The latter was taken to be 75 km, corresponding to the width of the Moho upwarp from Zorin et al. (1989). Seismic hypocentres in the north Baikal region define fault planes that remain straight into the middle to lower crust (Déverchère et al., 1993). However, models including straight faults to these depths invariably predict a basin which is much deeper and narrower than observed. Therefore, I have adopted a slightly listric fault

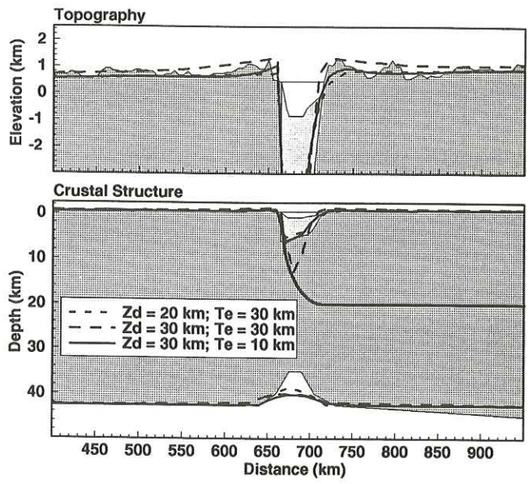

Figure 3-13. Predicted crustal structure and topography for profile X-Y, adopting a detachment model (ter Voorde and Cloetingh, 1995) for different detachment depths z_d and elastic thicknesses T_e. Fault geometry is indicated for z_d = 20 km.

shape, which begins to deviate from a straight plane with an dip of 70° below ~10 km depth and flattens out 50 km east of its surface trace, below the eastern border of the rift. Best fitting models adopt a detachment depth (z_d) between 20 and 30 km, i.e. slightly deeper than z_c in the lithospheric necking model. The inferred extension on the fault is 15 km, which agrees well with the gravity inversion results of Zorin and Cordell (1991) and implies a mean β ≈ 1.3. All models, however, predict a Moho position under the rift a few km deeper than observed. Again, the best fitting T_e is in the order of 30 km; lower T_e values predict too narrow regions of flank uplift. Note that, although extension of the upper crust is inherently asymmetric in this model, maximum elevations are similar for both rift flanks, for sufficiently large T_e. An asymmetry is predicted in tilt direction, with the entire western (footwall) flank of the rift tilted towards the hinterland, while the basin-ward area of the eastern (hanging wall) flank is tilted towards the basin axis. Thus, the model correctly predicts the observed comparable elevations of the eastern and western flanks of the Baikal rift, and the tilting of terraces towards the lake on its eastern shores.

Finally, Figure 3-14 illustrates the results of a flexural cantilever model, using the original formulation of Kusznir et al. (1991). As this model assumes instantaneous rifting, I show the results at 5 My after extension. Free parameters are the amount of extension on the border fault, the width of the pure shear zone and the flexural rigidity of the upper crust. The width of the pure-shear zone is taken to be the same as in the previous model. Only 8 km of extension on a planar fault dipping 60° is required to produce a sufficiently deep basin. A very low rigidity (T_e ≈ 7.5 km) has to be assumed in order to obtain a 50 km wide basin. Such a low T_e value, however, leads to topographic patterns which are completely different than those observed. On the footwall side of the rift, an extremely high (> 4 km)

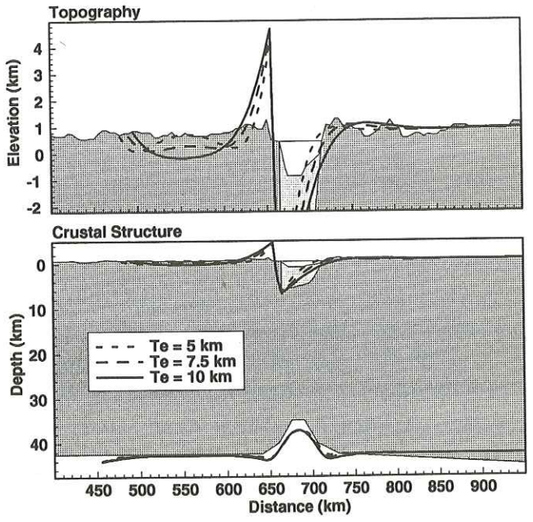

Figure 3-14. Predicted crustal structure and topography for profile X-Y, adopting a flexural cantilever model (Kusznir et al., 1991; Kusznir and Ziegler, 1992) with a single border fault and different flexural rigidities.

and narrow rift flank is predicted, while on the hanging wall side hardly any flank uplift occurs. In order to make this model compatible with the observed topography, erosion of the footwall flank is often assumed (e.g., Marsden et al., 1990; Kusznir and Ziegler, 1992; Magnavita et al., 1994). For the Baikal rift, at least 4 km of erosion would be required; this is a conservative estimate because it does not take isostatic rebound into account, which is substantial for such low rigidity values (cf. Section 2.3.4). As discussed above, this is not compatible with fission track data from the Primorsky range. A flexural cantilever model with a single border fault, therefore, does not seem appropriate to model flank uplift for the Baikal rift.

In contrast, the necking and detachment models yield good results, and suggest a T_e ≈ 30 km. One could argue that the kinematics implicit in the detachment model are more realistic that those of the necking model. However, predictions of crustal structure from these models do not allow to discriminate between them. The only significant difference between the two models is that the detachment model better predicts the opposing tilt directions of the eastern and western rift flanks. The dynamic significance of these results, as well as rheological considerations, will be discussed in Section 3.5.

3.3 A COMPARISON WITH THE MALAWI RIFT, E. AFRICA*

3.3.1 Introduction and tectonic setting

In order to place the inferred kinematics and evolution of the Baikal rift with in a broader perspective, I have made a comparison with the Malawi rift in East Africa. I present fission track data which indicate that, in contrast to the Baikal rift, the flank topography in Malawi has been influenced by erosion. These erosion estimates are incorporated in a kinematic model of rifting; the inferred flexural rigidity and detachment depth are compared to those found for the Baikal rift.

The Malawi rift (Figure 3-15) forms the southernmost part of the western branch of the East African rift system, which bifurcates around the Tanzanian craton. The western branch is characterised by a series of deep and narrow half grabens with alternating polarity (Rosendahl, 1987; Rosendahl et al., 1992), partly occupied by lakes (Tanganyika, Rukwa, Malawi), and much less intense volcanism than the eastern branch. Volcanism in the western branch is confined to rather small areas, often in between different rift zones (eg. the Rungwe volcanic province between the Rukwa and Malawi rifts).

Three distinct episodes of rifting activity are recognised in the western rift system: Permo-Triassic, Cretaceous and Cenozoic. During these periods, rifting was concentrated in

* This section contains material from: Delvaux, D., Mbede, E.I., van der Beek, P.A. and Andriessen, P.A.M., manuscript in prep.

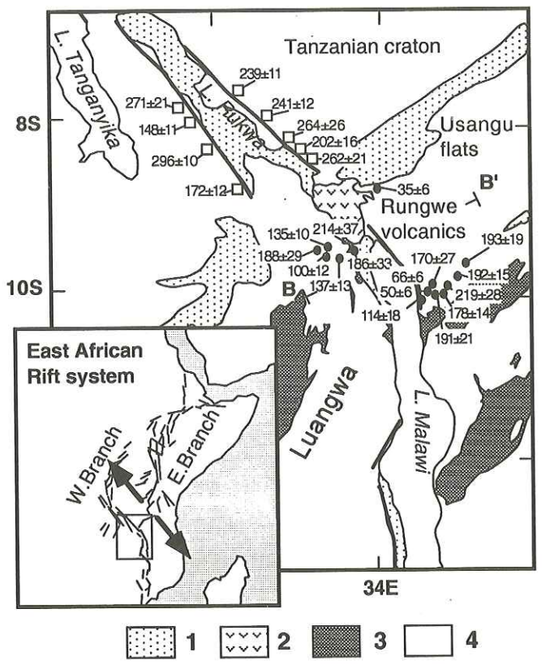

Figure 3-15. Tectonic map of the Malawi rift region (modified from Delvaux et al., 1992) showing distribution of apatite fission track ages. Filled dots are samples presented in Table 3-2; open squares around Rukwa rift are from Mbede et al. (1993). Notations: 1) Cenozoic (Miocene-Recent) rift sediments; 2) Cenozoic volcanics; 3) Permo-Triassic (Karroo) sediments; 4) Precambrian basement. B-B' denotes profile shown in Figure 3-16 and modelled in Section 3.3.3. Inset shows location within East African rift system; bold arrows indicate present-day extension direction.

coinciding zones, which were strongly controlled by the pre-existing basement structure (Daly et al., 1989; Versfelt and Rosendahl, 1989; Theunissen et al., 1995). The border faults of the Rukwa and Malawi rifts are superimposed on major Pan-African shear zones which separate the Tanzanian craton from blocks to the west. The Karroo formation (Late Carboniferous-Triassic) and red sandstones ('Dinosaur Beds') of unknown (Cretaceous-Miocene?) age were deposited in half-grabens bounded by the same faults that were active during late Cenozoic rifting (Dypvik et al., 1990; Mbede, 1993). Karroo rifting also took place along NE-SW oriented zones (Figure 3-15). Some of these were reactivated during the Pleistocene but only very shallow (<2 km) basins evolved (cf. Delvaux et al., 1992).

The latest stage of rifting in Malawi commenced at around 8 Ma, as indicated by $^{40}Ar/^{39}Ar$ dating of rift-related volcanics and field relationships (Ebinger et al., 1993). The oldest rift-related deposits contain late Miocene mammalian fossils. Some 4½-6 km of upper Miocene-Recent sediments have infilled the Malawi rift (Specht and Rosendahl, 1989), whereas lake Malawi has a maximum present depth of ~750 m. Thickest, and probably coarsest sediment deposits are encountered close to the border faults (cf. Figure 3-16) which are straight up to a depth of at least 10 km (Specht and Rosendahl, 1989; Rosendahl et al.,

1992). Paleostress analyses (Delvaux et al., 1992; Ring et al., 1992) show that the rifts initially developed in a near-radial extensional stress field, which changed during the mid-Pleistocene (~2 Ma) to a strike-slip regime with a NW-SE extensional stress direction. This is consistent with the present-day stress regime deduced from earthquake focal mechanisms (Shudofsky et al., 1987; Delvaux et al., 1992; Camelbeeck and Iranga, 1993; Jackson and Blenkinsop, 1993). Earthquakes occur up to depths of 30 km below the Malawi rift. The deepest earthquakes occur on planes dipping 20-30° and define a plane dipping 30-35° when connected to the surface trace of the Livingstone fault, the surface dip of which is ~70° (Jackson and Blenkinsop, 1993). In the Mbeya area, north of lake Malawi, earthquakes define a plane down to ~20 km depth, while between 20 and 30 km they delineate a horizontal zone underlying the rift (Camelbeeck and Iranga, 1993).

Lake Malawi is bordered on the east by the Livingstone Mountains, which reach an elevation of 2500 m. The Livingstone fault, the border fault of the rift, runs along the northeast shore of the lake. The fault forms an escarpment up to an elevation of ~1000 m, above which the flank shows an erosional escarpment (Delvaux and Wopfner, 1992; Figure 3-16). The summit of the Livingstone mountains forms a flat erosion surface which represents the 'Gondwana peneplain' (King, 1963); an surface of inferred Jurassic age that has been correlated across southern Africa. The western flank of the rift, in contrast, shows planation surfaces that have been tilted towards the rift axis (Coussement et al., 1993)

3.3.2 Fission track data

Samples for apatite fission track analysis were collected from both sides of the rift by D. Delvaux and E. Mbede in 1992 (Figures 3-15, 3-16; Table A2-2). In the Livingstone Mountains, a profile spanning an elevation from lake level (400 m) to 2200 m was collected, as well as a transect from the lake shore up to 70 km east of it. In the Kyela region, to the west of the rift, samples were collected from areas within the rift up to 50 km west of it, spanning an elevation range from 600 to 2020 m. Two samples were collected from the basement underlying the Karroo sediments in the Songwe coal mine, in the northwestern sector of the Malawi rift. Sample preparation and processing techniques were similar to those for samples from the Baikal rift (cf. Appendix 2).

Results

Apatite fission track (FT) results are given in Table 3-2 and depicted in Figures 3-15 to 3-17. Analytical data are given in Table A3-2 (Appendix 3). The Livingstone Mountains profile shows a clear increase in FT age with elevation (Figure 3-17). Samples from below 1000 m have ages of 50±6 - 66±6 Ma, with low mean track lengths (MTL = 11.0-11.8 µm) and wide standard deviations (σ = 1.8-2.0 µm). The lowest sample (DD485a) has an anomalously high FT age and MTL (128±20 Ma, 12.1 µm); etch pit widths suggest that this sample has a high Cl content. A sample from the foot of the Livingstone fault scarp more to the north (DD503)

Table 3-2. Apatite fission track results for the Malawi rift flanks

sample	elev. (m)	number of grains	age ±1σ (Ma)	D (%)	mean track length (µm)	st.dev. (µm)	number of tracks
Livingstone Mountains profile							
DD013	1890	16	217±20	15	12.6±0.1	1.3	100
DD298	1840	16	192±15	13	11.7±0.2	1.6	100
DD486	1990	20	246±31	10	12.3±0.2	1.6	80
DD115a	2200	20	216±15	15	12.5±0.2	1.5	100
DD478	2060	15	214±22	10			
DD122	1530	15	178±14	9	12.2±0.2	1.5	64
DD483	1340	13	30±15	145			
DD482	1110	20	170±27	5	12.1±0.4	2.0	28
DD484	905	15	66± 6	25	11.8±0.3	2.0	62
DD480	675	16	50± 6	11	11.0±0.4	1.8	24
DD485a	460	15	128±20	7	12.1±0.3	1.7	40
DD503	890	15	35± 6	36			
T22B	1280	15	64±16	70			
T22A	1970	12	33± 8	3			
Kyela profile							
DD512	2020	20	135±10	14	12.4±0.2	1.5	100
DD510	1250	12	188±29	9	12.0±0.3	1.8	33
DD509	1120	9	100±12	12			
DD508	1000	20	137±13	13	11.4±0.2	1.6	60
DD514a	650	20	214±37	4			
DD329a	600	18	186±33	4			

also has a low FT age of 35±6 Ma. Samples from the summit of the Livingstone Mountains and more inland were all taken close to the 'Gondwana surface' (King, 1963), at elevations between 1900 and 2200 m. All these samples have concordant FT ages of 192±15 - 246±31 Ma and similar track length distributions, with MTL between 12.1 and 12.7 µm and standard deviations of 1.3-1.6 µm. There are three outliers with anomalously low FT ages; samples DD483, T22A and T22B. All these samples have very low uranium content and widely differing single grain ages. There is no apparent explanation for this deviation in the FT data and, therefore, these samples have been excluded from my interpretation.

The Kyela profile shows a very different pattern of FT ages. Samples from the sub-Karroo unconformity in the Songwe coal mine (DD514a, DD329a) have ages similar to those from the 'Gondwana surface', i.e. 186±33 - 214±37 Ma. Unfortunately, uranium contents of these samples were too low to perform reliable track length measurements. Samples taken 10-15 km west of the rift (DD508, 509, 512) have ages between 100±12 and 137±13 Ma, with MTL = 11.4 - 12.4 µm and σ = 1.5 - 1.6 µm, at elevations between 1000 and 2020 m. The most westerly sample (DD510) has an age of 188±29 Ma, with a corresponding MTL of 12.0 µm (σ = 1.8 µm), very similar to the samples from the 'Gondwana surface' east of the rift.

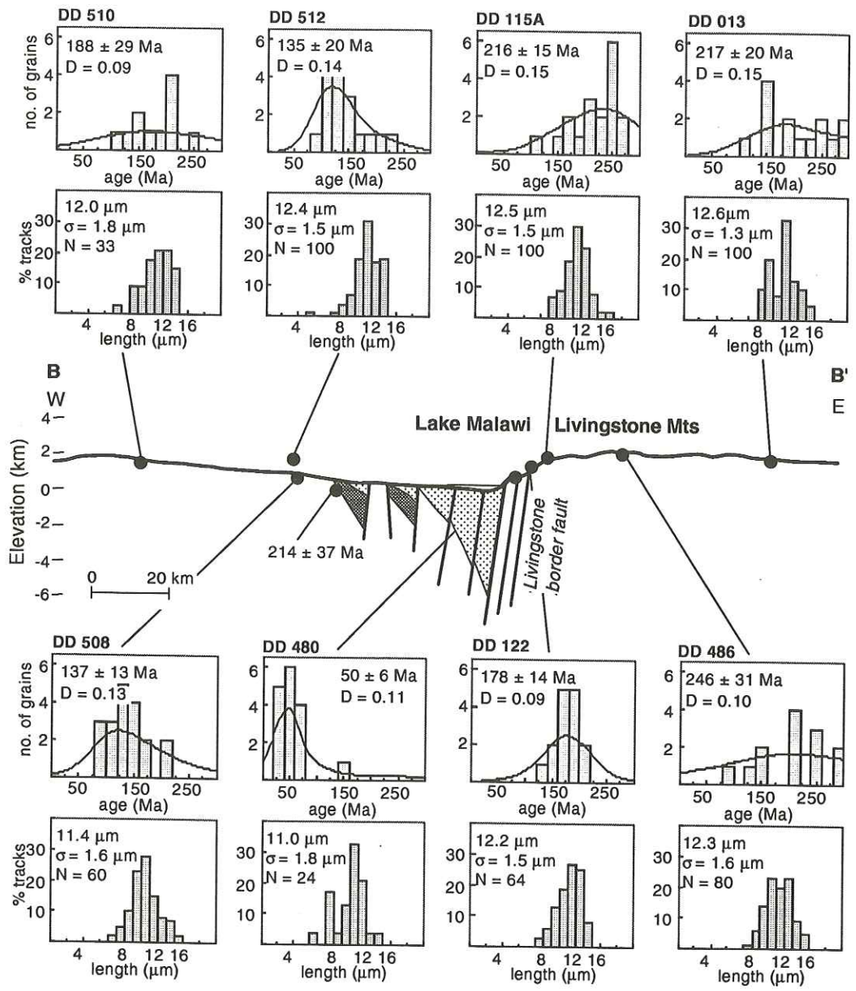

Figure 3-16. Cross section of the Malawi rift (after Ebinger et al., 1993), showing distribution of fission track ages and length distributions (notations as in Figure 3-7). Light stippling in profile indicates Neogene rift sediments; darker stippling: Karroo sediments.

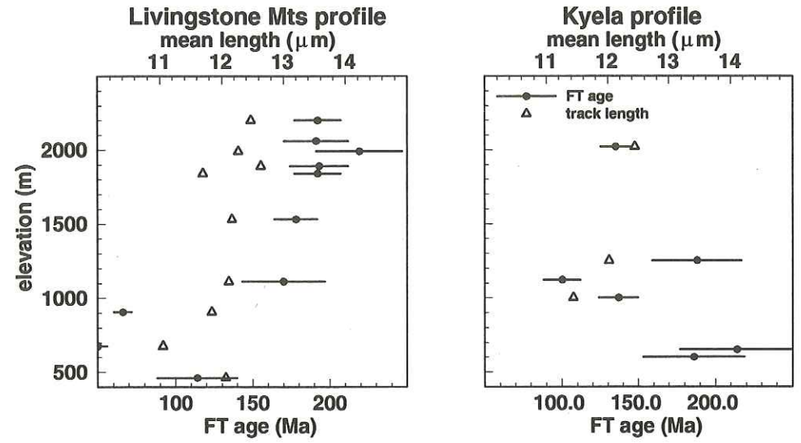

Figure 3-17. Age/elevation and mean track length/elevation profiles for fission track samples from the Livingstone Mountains (left) and the Kyela region (right).

Interpretation

In order to interpret the fission track data in terms of a cooling/exhumation history, I have modelled thermal histories using the inversion scheme presented in Appendix 1 (Figure 3-18). No chemical composition data for the apatites analysed are available; I have adopted the annealing model of Laslett et al. (1987) for Durango apatite in the inversion. The track length distributions of samples from the Livingstone mountains summit and 'Gondwana surface' (Figure 3-16) indicate a relatively protracted exhumation history. Thermal history modelling suggests that these samples cooled below 60°C at around 200 Ma, i.e. during the Early Jurassic. These sample ages are concordant with those reported by Mbede et al. (1993) from similar elevations around the Rukwa rift, supporting the interpretation of the 'Gondwana surface' as a continuous planation level. However, the inferred Jurassic age of the surface (e.g., King, 1963) is not unequivocally supported by the data; the thermal history inversions suggest that cooling to surface temperatures could have taken place as late as the Tertiary. Note, however, that because of uncertainties in the kinetics of annealing at low temperatures (<~60°C) thermal histories are essentially unconstrained in this range (cf. Corrigan, 1993; Ravenhurst et al., 1994). Samples from near the lake-shore show a very different thermal history; they were at temperatures >120°C until ~70 Ma (i.e. Early Tertiary) and only cooled from ~80°C in the last 10 My or so. These samples thus indicate that a significant amount of exhumation has taken place since the early Tertiary, more than half of which took place

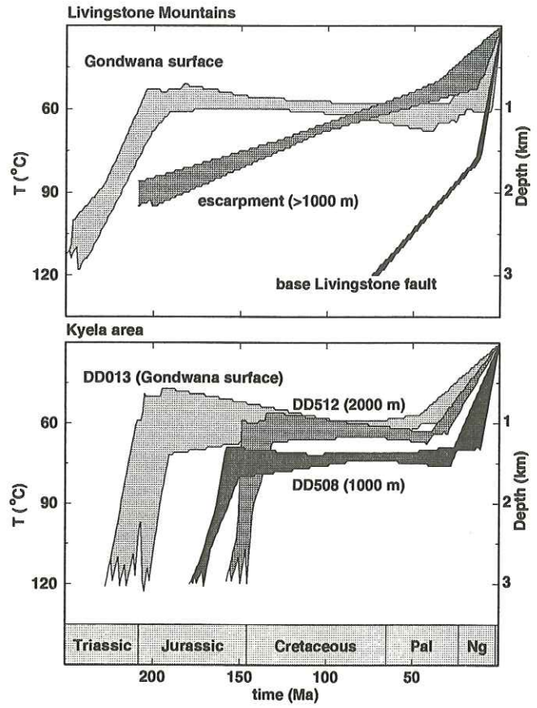

Figure 3-18. Modelled thermal histories for representative samples from the Malawi rift flanks; for the Livingstone Mountains (top) samples with similar ages and track length distributions were combined for the inversion in the following manner: Gondwana surface: DD013, 298, 486, 115A; escarpment > 1000 m: DD122, 482; base Livingstone fault: DD484, 480. For the Kyela area (bottom) single samples were modelled.

recently and is probably related to rifting.

To the west of the rift, basement samples from the Songwe coal mine have similar FT ages as those from the Gondwana surface. Although not enough track lengths could be measured to perform a thermal history inversion, the track length distribution of sample DD510 suggests that these samples have experienced a similar cooling history as those from the Gondwana surface. Vitrinite reflectance and Rock Evaluation (T_{max}) data for Karroo sediments from the Songwe coal mine (Dypvik et al., 1990) indicate that these rocks have experienced maximum temperatures of 100-120°C. The FT data presented here indicate that maximum temperatures should have been reached shortly after the deposition of these sediments during Permian-Triassic times, and that an overburden equivalent to a 50-60°C temperature difference was removed during Early Jurassic denudation. Samples immediately to the west of the rift record a Late Jurassic-Early Cretaceous cooling event around 150 Ma. Mbede et al. (1993) also report Cretaceous FT ages from the western flank of the Rukwa rift. Late Jurassic-Early Cretaceous cooling/exhumation could be related to renewed rifting and the deposition of the red sandstones of possible Cretaceous age. Samples from elevations of ~1000 m (DD508, 509) have younger ages and shorter mean track lengths than sample

DD512, which was collected at an elevation of 2020 m. Modelling suggests that the lower samples have remained at temperatures 20-30°C higher than DD512 since the Late Jurassic (Figure 3-18). Although the inversion does not constrain the final exhumation of these samples tighter than the last 150 My, this difference can be explained by recent rift-related erosion of the western (hanging wall) flank.

The inferred regional exhumation events during the Early Jurassic, Early Cretaceous and Early Tertiary, on which more local rift-related erosion is superimposed, are roughly coeval with those reported by Foster and Gleadow (1993) for samples from central Kenya. These events correspond to periods of plate reorganisation and intracontinental deformation of the African lithosphere (Foster and Gleadow, 1993; see also Janssen et al., 1995).

In order to asses the amount of exhumation that has taken place, some bounds need to be placed on geothermal gradients. Mbede (1993) presents well log data from the Rukwa rift which indicate a high geothermal gradient of ~40°C/km within the rift. A regional study by Nyblade et al. (1990) indicates that heat flow within the Karroo and Recent rifts is similar to that of the Pan-African mobile belts (~60-80 mWm^{-2}), whereas the Tanzanian craton has a much lower heat flow of about 35 mWm^{-2}. If I adopt a mean geothermal gradient of 30°C/km, the apatite fission track results presented above indicate that approximately 2.0±0.5 km of rift-related denudation affected the scarp of the Livingstone Mountains. The Gondwana surface, which seems a good pre-rift horizontal marker, lies at elevations 1500-2000 m above the lake level at the summit of the Livingstone mountains. This elevation difference agrees well with the inferred exhumation of samples from close to the lake shore. Areas behind the scarp, at some 10-20 km away from the rift, have not experienced any significant erosion during the late Cenozoic. On the western (hanging wall) flank, maximum erosion reached 1.0±0.5 km but affected a much wider area, possibly up to 100 km away from the rift. In the next section, I use these erosion estimates, together with the observed topography, to constrain kinematic models for the Malawi rift.

3.3.3 Modelling uplift and erosion of the Malawi rift flanks

I have used the detachment model of ter Voorde and Cloetingh (1995; cf. Section 3.2.3) to model a profile which runs across the northern termination of Lake Malawi (cf. Figures 3-15, 3-16). The same profile was modelled by Ebinger et al. (1991, 1993), using the instantaneous extension model of Weissel and Karner (1989). Their analysis did not take erosion of the rift flanks into account. Mbede (1993) performed a study of the Rukwa rift, using the same model as Ebinger et al. (1991, 1993), and came to conclusions which agree with those that I present here.

The modelling procedure is similar to that described in section 3.2.3. As there are no deep seismic reflection/refraction data available for the Malawi rift, the predicted crustal structure cannot be used as a constraint. I adopt a 40 km thick crust and a 150 km lithosphere here, and an initiation of rifting at 8 Ma. A pre-rift elevation of 1500 m was adopted,

equivalent to the elevation of the Tanzanian craton away from the rift zone. The geometry of the rift basin is taken from Specht and Rosendahl (1989; line 804; see also Rosendahl et al., 1992). The fault geometry can be loosely constrained from seismological data (Jackson and Blenkinsop, 1993; Camelbeeck et al., 1993) which do not contradict a slightly listric fault shape; I have used a fault shape similar to that used for modelling the Baikal rift.

Figure 3-19 shows model results for a detachment depth of 30 km; 7.2 km of extension on the Livingstone fault was needed to fit the observed basement depth, leading to $\beta = 1.24$. A model that does not take erosion of the flanks into account does not predict sufficient topography of the footwall flank but overestimates the elevation at the hanging wall side of the rift. If erosion of the flanks is incorporated, the additional isostatic rebound provides a much better fit to the observed topography, for T_e values of 20-30 km. The amounts of erosion to be adopted are derived from the fission track data: in the Livingstone mountains maximum erosion was taken to be 2 km, reducing to 0 at 20 km east of the rift; in the west, maximum erosion is 1 km, affecting a 50 km wide area.

A similar model with a detachment depth at 40 km (i.e. at the base of the crust) is shown in Figure 3-20. In this case, only 5.6 km of extension on the Livingstone fault ($\beta = 1.19$) is required to produce the observed basement depth. Such a model tends to overestimate the topography close to the rift flank, both with and without erosion, except for very high T_e values of 50 km. In the absence of erosion, this model, like the previous one, fails to explain the high elevation of the Livingstone mountains inland from the rift zone.

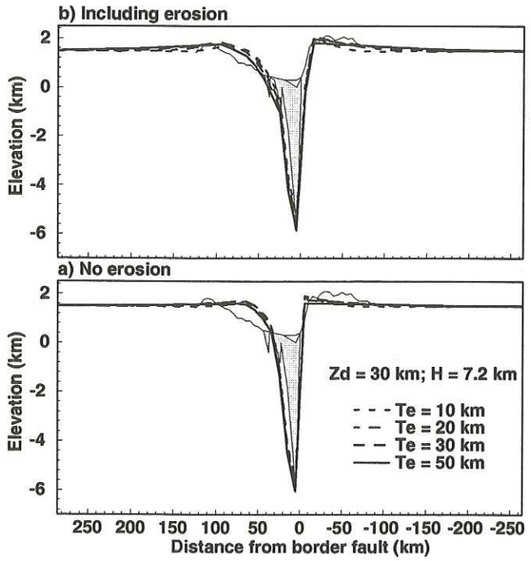

Figure 3-19. Predicted basin geometry and topographic patterns for profile B-B'across the northern Malawi rift, adopting a detachment model with z_d = 30 km and 7.2 km extension on the Livingstone fault; (a) without erosion and (b) including 2 km erosion of footwall flank, 1 km erosion of hanging wall flank, and associated isostatic rebound. Thin line indicates observed topography; stippled pattern: observed basin geometry (Profile 804 of Specht and Rosendahl, 1989).

Figure 3-20. Same as Figure 3-19 for z_d = 40 km (base of the crust) and 5.6 km extension across the Livingstone fault.

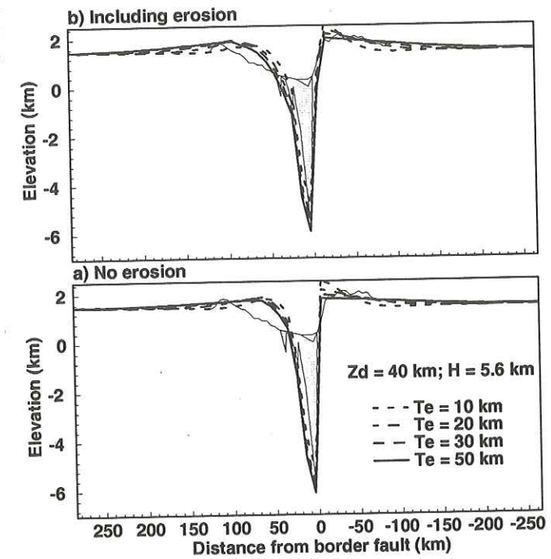

These results indicate that for the Malawi rift, in contrast to the situation at Baikal, rift-related erosion of the flanks has modified the observed topography. Specifically, the high elevation of the Livingstone Mountains away from the rift zone seems to be related to regional isostatic rebound, whereas the elevation of the hanging wall flank has probably been lowered significantly by erosion. A similar conclusion was reached by Mbede (1993) for the Rukwa rift. Ebinger et al. (1993) also suggest that several hundred meters of erosion affected the hanging wall side of the Malawi rift. Erosion was probably more important for modifying topography on the hanging wall side of the rift than on the footwall flank, although the latter displays much larger topographic relief. Erosion of the footwall flank takes place mainly by slope processes and escarpment retreat, whereas on the hanging wall flank, initial structural

Figure 3-21. Predicted amount of erosion (i.e. tectonic uplift + isostatic rebound - present day topography) for the models depicted in Figures 3-18 and 3-19, compared to the amount of erosion inferred from apatite fission track data.

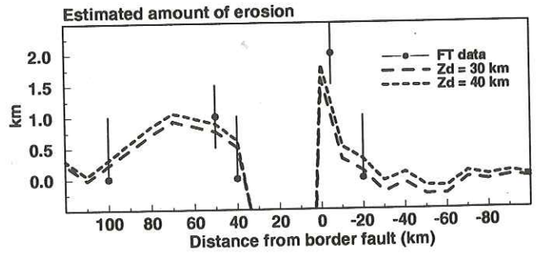

tilts towards the rift basin would have facilitated fluvial pathways (compare Section 2.4). Erosion of the rift flanks also influences the inferred kinematics of extension (Figure 3-21). Ebinger et al. (1991, 1993) adopted a model in which the detachment level was assumed to be located at the base of the crust, but did not discuss the constraints on that level. I have shown here that, if erosion and isostatic rebound are taken into account, a best fit detachment level would be located closer to 30 km, for $T_e \approx 30$ km.

3.4 3D MODELLING OF UPLIFT PATTERNS AROUND THE BAIKAL RIFT

In order to evaluate whether the flexural models employed in the previous sections are capable to explain all of the observed topography along the Baikal rift, I have employed a three dimensional model of lithospheric thinning and flexure developed by van Wees (1994). I adopt a 3D expansion of the lithospheric necking model here, since this provided a good fit to the observed topography and crustal structure, while assuming relatively simple kinematics. This differs from the approach of van Wees and Cloetingh (1994), who modelled basement deflections in the Tanganyika rift adopting a 3D flexural cantilever model. However, as was shown in Section 3.2.3, such a model fails to predict the observed topography of the rift flanks. The approach I take is similar to that outlined in Section 3.2.3: for a given level of lithospheric necking z_c and elastic thickness T_e, I adapt the stretching (β-factor) distribution until a reasonable fit to the observed basement depth is obtained. The model then predicts topography and Moho depth distribution, which are compared to observations. A major additional constraint imposed by 3D models is that, due to the size of the input, it is not possible to adjust the β factor at a single point; the choice of a β distribution is thus not completely free, as in a 2D model. Calculations are performed on a 1000 × 1000 km grid, with a grid spacing of 20 km. Constant parameters are the same as those listed in Table 2-1.

Figure 3-22 shows map views of model predictions for different parameter combinations and a comparison with the observed patterns. The model that provided the best fit to the profile across the central Baikal basin (i.e. $z_c = 20$ km; $T_e = 30$ km) also performs best in 3D. The 2D and 3D models, in fact, lead to very similar predictions for the central basin (Figure 3-23). As in 2D, a low T_e (10 km) leads to very narrow and high rift flanks, predicts narrow and deep 'hinterland basins' which are not observed, and overestimates crustal

Figure 3-22 (next two pages). Results of three dimensional modelling of lithospheric thinning for the Baikal rift: (a) Maps of observed basement depth within the basin (Hutchinson et al., 1992), topography (ETOPO-5) and Moho depth (Zorin et al., 1989); (b) predicted basement depth, topography and Moho depth for a model with a kinematic necking depth z_c = 20 km and elastic thickness T_e = 10 km; (c) same for a model with z_c = 20 km and T_e = 30 km; (d) same for a model with z_c = 30 km and T_e = 30 km.

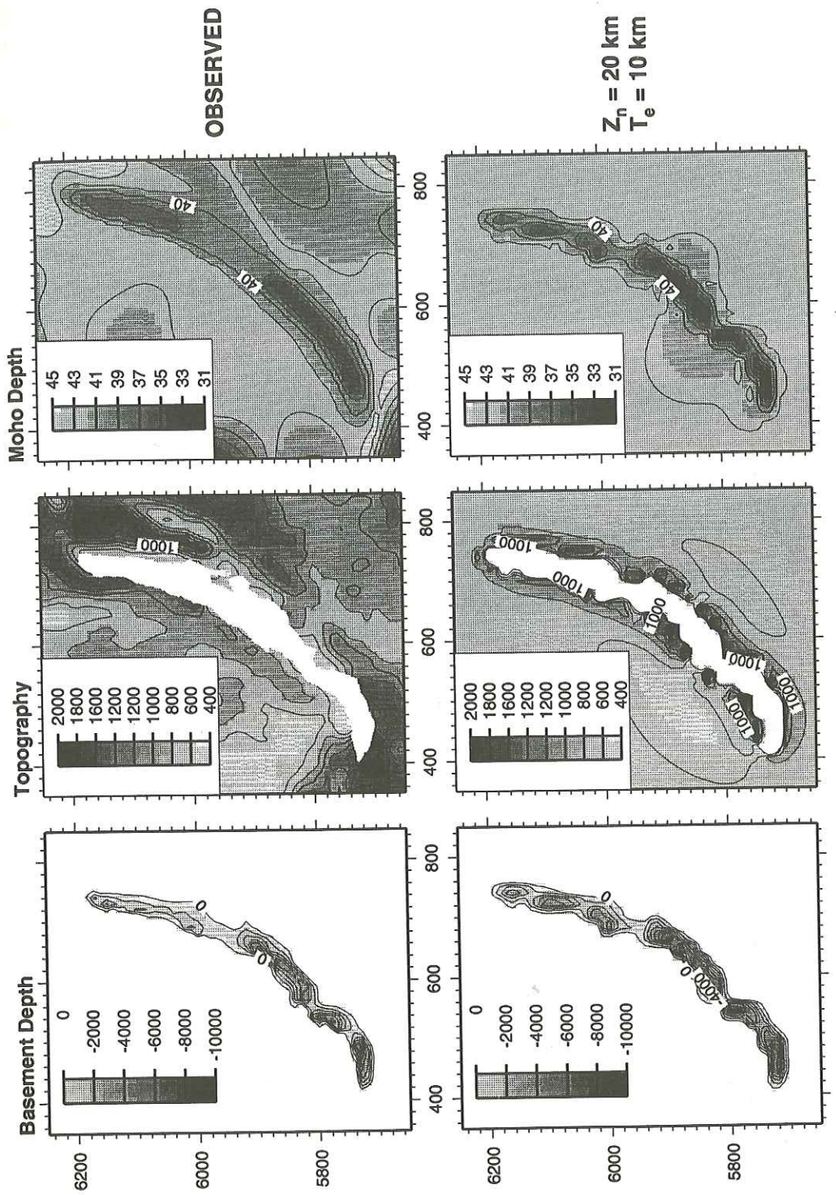

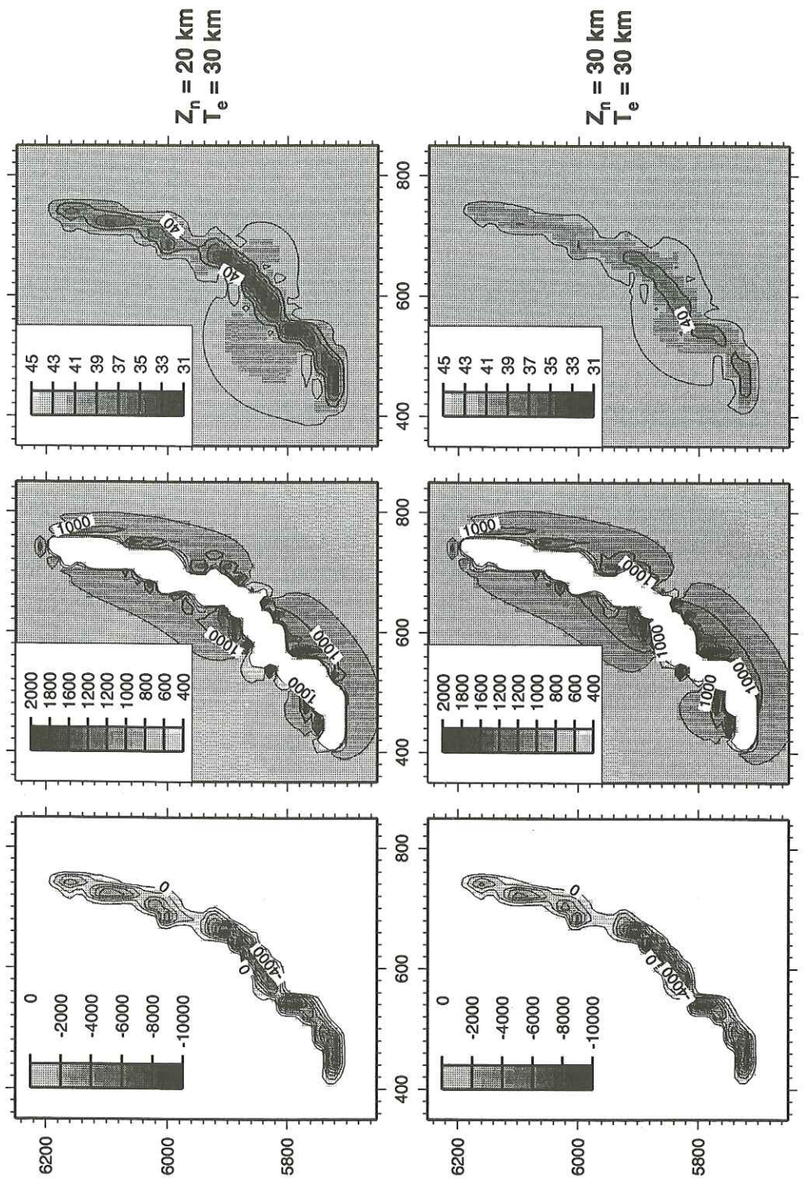

thinning. In contrast, for a deep level of necking (z_c = 30 km) too little crustal thinning is predicted. Even the best-fit model, however, fails to reproduce the observed 3D patterns of basin depth and rift flank topography. Whereas the predictions are satisfactory for the central basin, the predicted northern basin is deeper than observed and the high elevation of the Barguzin range is not reproduced (Figure 3-24). In contrast, for the southern basin the elevation of the model rift flanks is about right, but the model basin is shallower than observed. The model predicts a high northern (footwall) flank for the southern basin, which is not observed. The southern Baikal basin is, however, not opening under pure extension but in a transtensional mode. Also, there is no fission track control of the amount of rift related erosion in this area.

The fact that the model predicts an overly deep basin and inadequate flank topography for the northern Baikal region points to an additional source of buoyancy there (e.g., Ebinger et al., 1991). The model does not take crustal thinning below the Barguzin basin into account. However, the loads associated with this relatively shallow basin (<2 km; Logatchev and Zorin, 1992) do not seem to be sufficiently large to explain all of the topography of the Barguzin range. I have recalculated the uplift patterns for a model with independent crustal and sub-crustal extension. Crustal stretching factors (β) are reduced in the northern and increased in the southern basin, compared to the model with z_c = 20 km and T_e = 30 km. For the sub-crustal stretching factors (δ) I adopt a 3D sinusoidal function, with a wavelength of 400 km in the EW direction and 600 km in the NS direction, and a maximum of δ = 2 (Figure 3-25). I do not claim that this represents the actual shape of lithospheric thinning; the above δ distribution is chosen for simplicity and demonstrative purposes. The non-uniform extension model does predict a wide area of uplift adjacent to

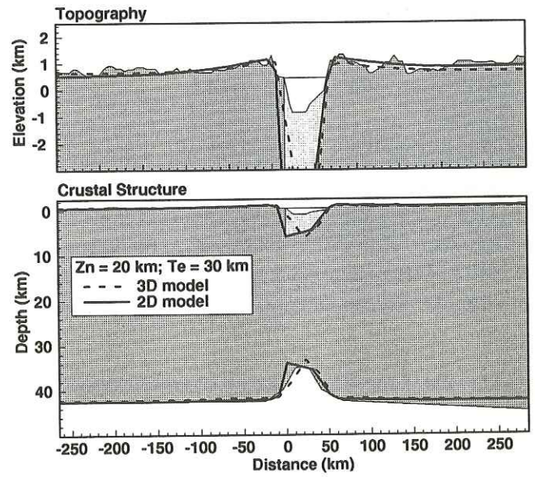

Figure 3-23. Comparison of predictions for crustal structure and topography along profile X-Y, by the 2D necking model employed in section 3.2.3 and the 3D model. The slight offset between the two models at the eastern side of the profile results from the fact that a surface trend was added to the 2D model (cf. Section 3.2.3), whereas the results of the 3D model simply have the average elevation of 700 m added to them.

050 036366 2

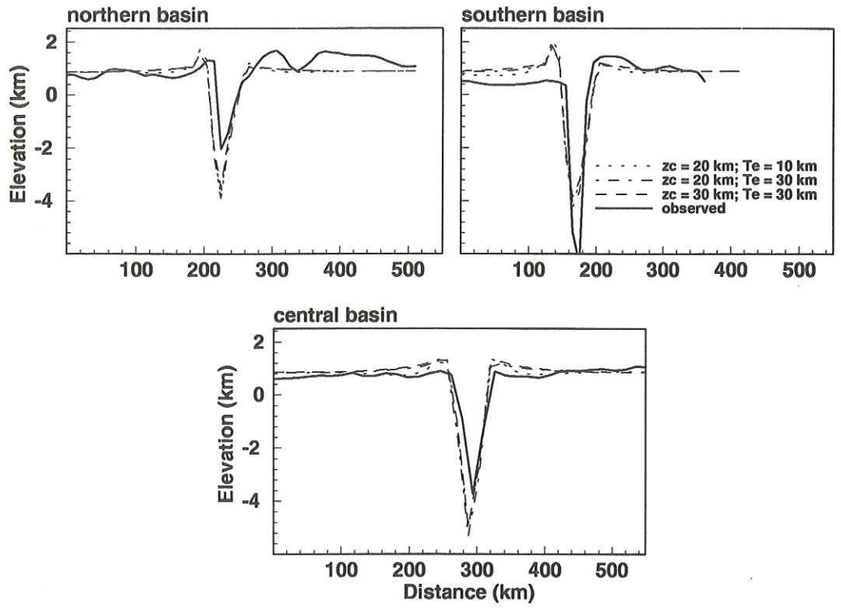

Figure 3-24. Topographic profiles across the northern, central and southern Baikal basins for the models depicted in Figure 3-22.

the northern Baikal basin (Figure 3-25). Compared to the uniform extension model, approximately 1 km of additional uplift is predicted for the Barguzin range (Figure 3-26). Although this model still does not provide more than an admissible fit to the observed basin depths, it does perform significantly better than the uniform extension model. Sub-crustal thinning appears to be concentrated below the northeastern side of the rift. This is in accord with the deep seismic refraction and teleseismic data which suggest an asymmetric asthenosphere 'diapir' below the eastern side of the rift (cf. Section 3.2.1), as well as with the observed concentration of magmatism east of the rift and the inferred migration of rifting from the northern Baikal basin to the Barguzin basin (Sherman, 1992; Déverchère et al., 1993). This asymmetry may result from the large differences in lithospheric structure between the Siberian craton west of the rift zone and the Sayan-Baikal fold belt east of it.

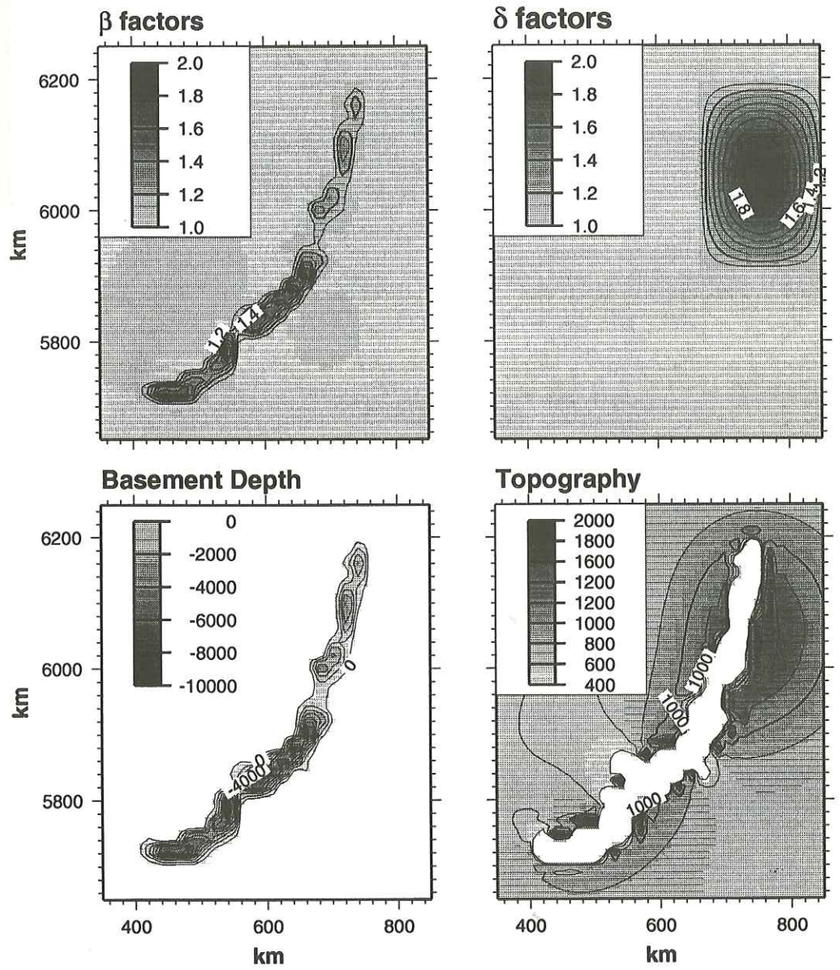

Figure 3-25. Predictions of a three dimensional model of non-uniform extension, with a concentration of sub-crustal thinning below the northern Baikal basin: (a) adopted crustal stretching (β) factors; (b) adopted sub-crustal stretching (δ) factors; (c) predicted basement depth; (d) predicted topography.

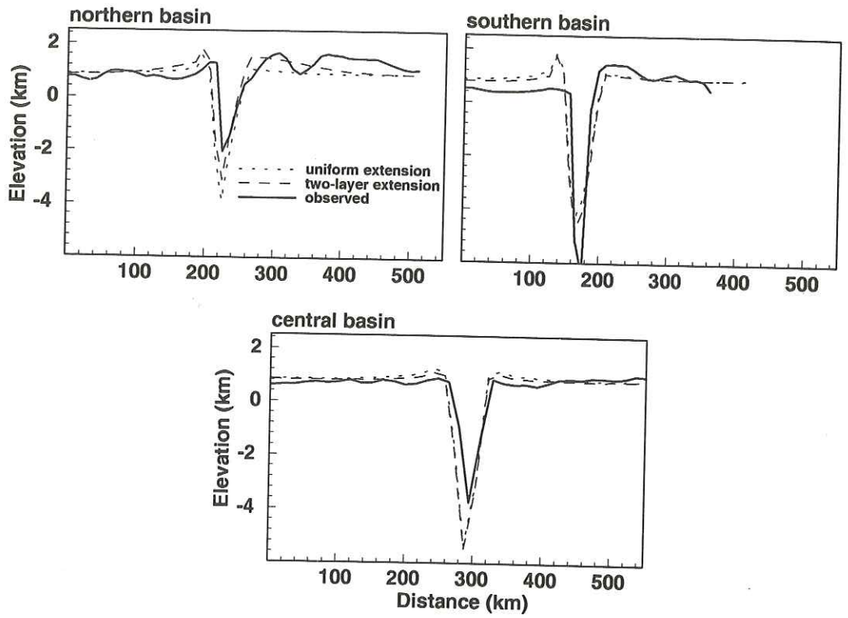

Figure 3-26. Comparison of results from a uniform extension model with z_c = 20 km and T_e = 30 km (cf Figure 3-23) with results from the non-uniform model.

3.5 Discussion and conclusions

Above, I have shown that the observed topography, in combination with erosion estimates from fission track data, can constrain the kinematics of extension in continental rifts. For both the Baikal and Malawi rifts extension appears to be controlled by a level of lithospheric necking within the middle to lower crust, a detachment level within the lower crust, and significant flexural rigidity ($T_e \approx 30$ km). However, in the case of Baikal, not all of the topography seems to be flexurally supported and an additional source of buoyancy is needed. Here, I will discuss briefly the rheological and dynamic implications of these findings.

Rheological implications

The inferred strength of the lithosphere below both rift systems agrees with findings from coherence studies and with previous forward modelling results (Ebinger et al., 1989, 1991; Diament and Kogan, 1990; Ruppel et al., 1993). An independent estimate of lithospheric

strength can be made by constructing rheological profiles, from an extrapolation of rock mechanics data (cf. Cloetingh and Banda, 1992). A comparison of the predictions of rheological models with observations is, however, often limited because of uncertainties concerning the thermal and mechanical structure of the lithosphere, as inferred from geophysical data.

The Baikal and Malawi rifts have the advantage that at least the thermal structure of the lithosphere is known with some confidence. For the Baikal rift, surface heat flow varies from 40-45 mWm^{-2} on the Siberian craton to 50-60 mWm^{-2} in the Sayan-baikal fold belt (Lysak, 1992), with a concordant decrease in lithospheric thickness from 200 to 150 km. For the Malawi rift, heat flow varies from as low as 20-47 mWm^{-2} in the Tanzanian craton to 44-77 mWm^{-2} in the Mesozoic basins and surrounding Panafrican mobile belts of the Luangwe-Zambezi valleys (Nyblade et al., 1990). This large difference can be partly explained by differences in upper crustal heat production; for another part it probably reflects different

Table 3-3(a) Material constants for strength profile calculations

layer	density (kgm^{-3})	conductivity ($Wm^{-1}K^{-1}$)	heat capacity ($J\ kg\ K^{-1}$)	heat production ($\mu W\ m^{-3}$)	skindepth (km)	rheology
upper crust	2650	2.5	1136	3	10	granite
lower crust	2900	2.0	1029	0	0	diorite
mantle	3300	3.5	1212	0	0	dunite

Material constants are as in Beekman (1994), heat production follows an exponential decay rule $H_z = H_0 e^{-cz}$ with c = skindepth; rheological parameters are from Carter and Tsenn (1987) for experiments on 'wet' rocks

Table 3-3(b) Crustal structure for strength calculations

	Baikal rift		Malawi rift	
	Siberian craton	Sayan-Baikal fold belt	Tanzanian craton	Luangwe-Zambezi belt
surface heatflow (mWm^{-2})	45	51	40	62
mantle heatflow (mWm^{-2})	19	25	16	24
upper crustal thickness (km)	20	20	20	20
lower crustal thickness (km)	20	25	20	20

Surface heat flow data are from Lysak (1992) for the Baikal rift and from Nyblade et al. (1990) for Malawi (for Malawi, skindepths have been adjusted to obtain realistic surface and mantle heat flow combinations). Crustal structure for the Baikal rift is from the refraction results of Krylov et al. (1981).

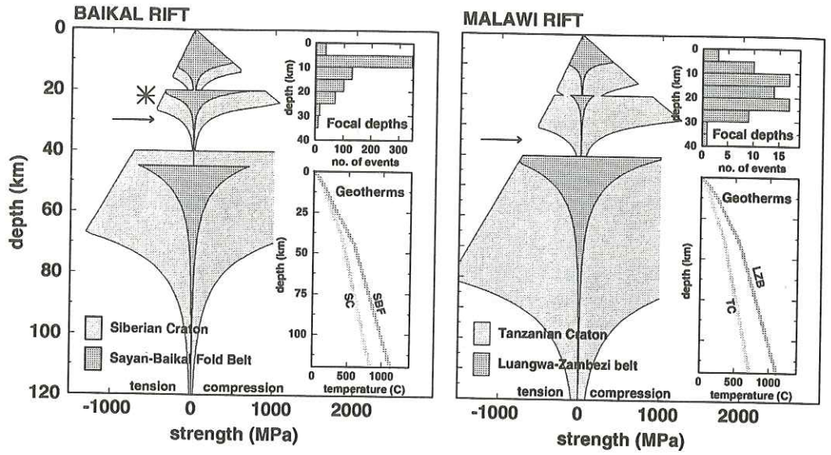

Figure 3-27. Calculated rheological profiles for the Baikal (left) and Malawi (right) rifts, adopting the parameters listed in Table 3-3. Insets in upper right corner show depth distribution of earthquakes (from Déverchère et al. (1991, 1993) for the Baikal rift; from Jackson and Blenkinsop (1993) and Camelbeeck and Iranga (1993) for Malawi); insets in lower right corner show calculated geotherms for the different sides of the rifts. Horizontal arrows denote best-fit depths of detachment for both rift systems; star in Baikal rift plot denotes best fitting necking depth.

mantle heat input (Nyblade et al., 1990). For the Baikal rift, seismic refraction data (Krylov et al., 1981; Zorin et al., 1989) also constrain the mechanical structure of the lithosphere.

Figure 3-27 presents strength profiles, calculated for the Baikal and Malawi rifts. Thermal and mechanical parameters for the calculations are given in Table 3-3, rheological parameters are from Carter and Tsenn (1987). The difference in thermal structure between the flanks of both rifts is reflected in rheological differences (Figure 3-27). Overall, however, the rifts have developed in strong and cold lithosphere. Burov and Diament (1995) provide a formula to estimate T_e from rheological profiles: $T_e = (\Sigma h^3)^{1/3}$, where h is the thickness of the individual layers (decoupled if the strength drops to <50 MPa between them). Adopting this approach, I find T_e = 28 km for the Sayan-Baikal fold belt and T_e = 70 km for the Siberian craton. This compares well with the best fitting T_e from my forward modelling and the coherence analyses of Diament and Kogan (1990) and Ruppel et al. (1993). For the Malawi rift, estimated T_e varies from 31 km for the Luangwa-Zambezi belt to >91 km for the Tanzanian craton, also within the range of coherence estimates (Ebinger et al., 1989).

The inferred rheological profiles also compare well with the seismicity of the rift zones. In the Baikal rift, earthquakes occur up to depths of 35 km but most are restricted to <20 km, with a peak around 10 km (Déverchère et al., 1991, 1993), whereas in the Malawi rift, earthquakes have been reported as deep as 40 km and have a bimodal distribution with

peaks around 15 and 25 km (Shudofsky et al., 1987; Jackson and Blenkinsop, 1993; Camelbeeck and Iranga, 1993). The peaks of the earthquake distributions appear to correlate with the strength maxima close to the brittle ductile transition within the crust. The slightly deeper occurrence of earthquakes below eastern Africa compared to Baikal suggests that the lithosphere is somewhat stronger in the previous case.

A comparison of the predicted depths of lithospheric necking and detachment levels with the calculated lithospheric strength profiles suggests that the depth of lithospheric necking correlates with the brittle-ductile transition, while the inferred detachment depth lies somewhat lower, within the ductile lower crust. The slightly stronger lithosphere below the Malawi rift, as compared to the Baikal rift, is translated into a somewhat deeper predicted detachment level (30-35 km vs. 20-30 km). Thus, it seems that the kinematics of extension, as predicted by kinematic models, bear significant information on the rheological structure of the lithosphere below the rifts.

Plastic or elastic behaviour of the upper crust during extension?

The results of Section 3.2.3 indicate that rift flank uplift is supported by a strong lithosphere with T_e in the order of several tens of km. A flexural cantilever model, which by its nature employs a low rigidity model lithosphere, fails to predict uplift patterns that are compatible with observations at the Baikal rift. Previous applications of such models (e.g., Marsden et al., 1990; Kusznir et al., 1991; Kusznir and Ziegler, 1992; Magnavita et al., 1994; Hendries et al., 1994) only presented modelled patterns of basement subsidence and did not show the coupled rift flank uplift.

The inferred low T_e values in flexural cantilever models are justified by the associated large bending stresses which would lower T_e in the upper crust from initial values of 10-20 km to <5 km (e.g., Hendrie et al., 1994). The assumption here is that the lower crust and mantle possess negligible strength. However, dynamic rifting models indicate that the strength of the lithosphere during extension is controlled by the sub-crustal lithosphere and is not strongly reduced as a result of rifting (e.g., Braun and Beaumont, 1989; Chéry et al., 1992; Bassi et al., 1993; Boutilier and Keen, 1994).

The original rationale for designing a flexural cantilever model was that "both footwall block and hanging wall blocks [should possess] similar mechanical properties" (Kusznir et al., 1991). This paradigm, however, does not seem to hold. If the elevation of the rift flanks is maintained by flexure of a strong ($T_e \geq 30$ km) elastic plate, then additional deformation is required to explain the basement deflection below the rifted basin. In detachment models, this deformation is assumed to take place by vertical simple shear. Such a formulation relies on the existence of listric border faults, as planar faults give highly unrealistic results. This apparently deviates from most geological and geophysical data, which suggest that rift bounding faults are planar up to at least the depth of the brittle upper crust (Jackson, 1987; Rosendahl et al., 1992). However, the geometry of the border faults at middle to lower crustal levels is not so well resolved; earthquake epicentres mostly define gently dipping to

subhorizontal planes at these depths. Moreover, the assumption of vertical shear in the hanging wall is clearly a simplification; different modes of shear will lead to very different basin geometries (e.g., ter Voorde and Cloetingh, 1995).

Rheological models support the notion of additional deformation in the hanging wall block upon rifting; they indicate that, in the presence of pre-existing faults, extensional stresses will be concentrated in the hanging wall (Boutilier and Keen, 1994; van Wees, 1994), leading to amounts of strain which quickly rise above the elastic limit. Even when a very low strength border fault is incorporated, at least 1/3 of the extension is distributed in the upper crust above the fault (Boutilier and Keen, 1994). These results suggest that plastic behaviour of the upper crust may be more important than assumed by the flexural cantilever model, and that the resulting basement geometry is more controlled by the spacing of pre-existing faults, the deformation field in the upper crust and lower crustal flow (e.g., Le Pichon and Chamot-Rooke, 1991; ter Voorde and Cloetingh, 1995) than by an 'upper crustal flexural rigidity'.

Additional sources of buoyancy

Three dimensional modelling of rift flank uplift at Baikal suggests that an additional source of buoyancy is supporting the northern part of the rift basin (Section 3.4). A similar conclusion was reached by Ebinger et al. (1989, 1991) for parts of the East African rift system. A logical candidate for this additional source is thermal support from non-uniform mantle thinning, as modelled in the above section, or dynamic support from upwelling asthenosphere (e.g., Houseman and England, 1986). In any case, the additional source of buoyancy suggests that the lithosphere-asthenosphere boundary is actively destabilised during rifting, instead of reacting merely passively to extension and thinning.

Delvaux and Klerkx (1994) present paleostress data for the Baikal rift that indicate a change from transtension to pure extension during the Pliocene, which they relate to the inferred acceleration in basement subsidence and rift flank uplift (e.g. Mats, 1992; Logatchev, 1993). This suggests that destabilisation of the lithosphere-asthenosphere boundary is a result rather than a cause of rifting. Bois (1993) presents evidence from a number of western European rift zones that also indicate a transition from 'passive' to 'active' rifting (see also Ziegler, 1995). Such a transition could result from a growing plastic instability in the lithosphere, as suggested by dynamic rifting models (Dunbar and Sawyer, 1989; Bassi et al., 1993; Boutilier and Keen, 1994; cf. Section 6.3). In fact, these models predict strong, cold lithosphere that contains pre-existing weak zones to be particularly vulnerable to extension-induced destabilisation.

CHAPTER 4

MECHANISMS OF POST-RIFT MARGIN UPLIFT: THE CASE OF SOUTHERN NORWAY

4.1 INTRODUCTION

In the previous two chapters I have concentrated on syn-rift uplift adjacent to continental rifts and rifted margins. It has become apparent in recent years that rifted margins may also record significant post-rift (late stage) uplift events (e.g., Cloetingh and Kooi, 1992; Sales, 1992). For instance, I have shown in Sections 2.3.4 and 2.4.3 that Tertiary thermal rejuvenation possibly affected the southeastern Australian margin. Cloetingh et al. (1990; 1992b) have stressed the importance of accelerated post-rift subsidence, in conjunction with margin uplift, for various basins on both sides of the North Atlantic during the Neogene (Figure 4-1). In this chapter, I will look at one of those areas, the Norwegian margin of the northern North Sea, in more detail.

The geomorphology of Norway and the almost complete absence of post-Paleozoic sediments have led geoscientists for decades to suggest large scale, late stage uplift of western Fennoscandia (e.g., Holtedahl, 1953; Torske, 1972). The rugged morphology of the Paleozoic Caledonide orogen, the preservation of planation surfaces at high altitudes (Gjessing, 1967; Peulvast, 1985) and the absence of a crustal root under the orogen (Theilen and Meissner, 1979; Andersen et al., 1991), suggest that the morphotectonic evolution of Norway was strongly affected by Meso-Cenozoic tectonic and climatic events in the North Sea and North Atlantic regions, rather than being solely the result of Caledonian orogeny. However, the exact timing and mechanism of uplift and erosion, as well as the influence of Quaternary glaciations, remain a matter of controversy.

Over the last 20 years, knowledge of the tectonic and paleogeographic evolution of the Norwegian offshore sedimentary basins has increased dramatically as a result of intense hydrocarbon exploration (cf. Ziegler, 1990; Doré, 1991). The basins record substantial late Cenozoic uplift and erosion of the Norwegian mainland, evidenced by a structural basinward dip of the pre-Neogene strata and the build-up of large clastic wedges (Stuevold et al., 1992; Jensen and Schmidt, 1993). In contrast to the basins, the onshore Meso-Cenozoic evolution, by its erosional nature, remains largely unresolved.

In this chapter, apatite fission track (AFT) thermochronology is applied to the basement rocks of onshore southern Norway, in order to elucidate its denudation history, and to study the relation between basin and margin evolution. New data are presented and integrated with the results of earlier studies (Van den haute, 1977; Andriessen and Bos, 1986;

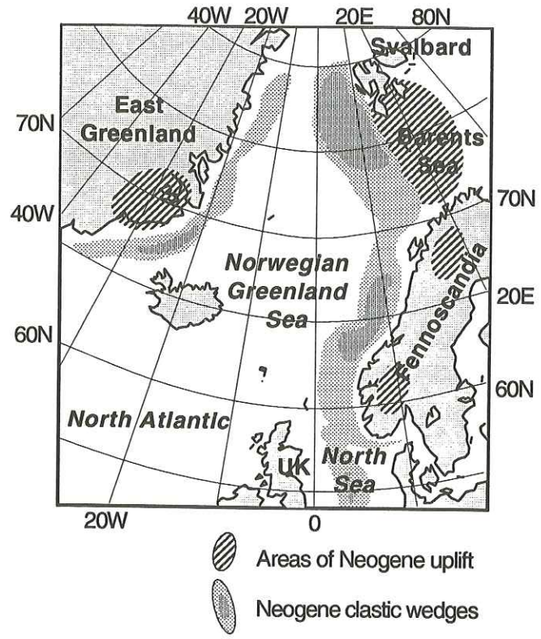

Figure 4-1. Regional map of the North Atlantic, showing areas of Neogene uplift and Neogene clastic wedges. Dense stippling indicates thick (>~1 s TWT) Neogene deposits; finer stippling: thinner deposits. Distribution of wedges is after Riis and Fjeldskaar (1992) for Norway and the Barents Sea, Kooi et al. (1991) for the North Sea and Larsen (1990) for East Greenland.

Andriessen, 1990; Stiberg, 1993; Grønlie et al., 1994) which focused on more local areas. Using this approach, AFT data were mapped over a large region, extending over nearly 500 km from the Skagerrak in the southeast to the Møre-Trøndelag area in the northwest (Figure 4-2). Mapping regional variations in AFT ages and confined track length distributions has proven to be a powerful approach in unravelling the history and style of uplift and exhumation of areas devoid of sediments (e.g., Kamp and Tippett, 1993; Brown et al., 1994).

The results are compared with geomorphological studies and offshore seismic-stratigraphic data, which I will first briefly review, to arrive at an exhumation history of southern Norway from Triassic to Recent times. The data indicate that substantial Neogene domal uplift has taken place. I will attempt to quantify the amount of tectonic uplift using the backstacking approach outlined in Chapter 2, and an estimate of lithospheric flexural rigidity obtained from a coherence analysis of Bouguer gravity and topography. Finally, I will evaluate several mechanisms of late stage uplift that have been proposed.

4.2 Tectonic and Paleogeographic Evolution of Southern Norway

Onshore record: Precambrian - Paleozoic orogenies

The onshore geology of southern Norway is dominated by Precambrian basement rocks of the Baltic Shield, which are overthrust from the northwest by the crystalline and sedimentary nappes of the Caledonides. In the southeast, the basement is intersected by the NS trending Permo-Carboniferous Oslo Rift (Figure 4-2). The southwestern segment of the Baltic Shield, exposed in southern Norway, was accreted and partially reworked during the Gothian (1.75-1.5 Ga) and Sveconorwegian/Grenvillian (1.25-0.9 Ga) orogenies (Verschure, 1985; Starmer, 1993). The Sveconorwegian orogeny terminated with the intrusion of post-orogenic granites at ~900 Ma and final uplift and denudation, followed by the opening of the Iapetus Ocean during the latest Vendian - earliest Cambrian (~650 Ma).

Subduction of oceanic crust led to closing of the Iapetus ocean at ~400 Ma and suturing of the Baltic and Laurentian plates during the Caledonian orogeny. The Caledonides represent a major continental collision belt, exposing obducted oceanic fragments, exhumed eclogitic rocks and reworked Baltic basement (e.g., Roberts and Gee, 1985). Post-orogenic collapse resulted in removal of the crustal root, asymmetric extension and the development of fault-bounded Devonian molasse basins (Andersen et al., 1991). The Caledonian structural elements strongly influenced the position and development of later Mesozoic extensional basins in the North Sea - North Atlantic (Doré, 1991).

In the Late Carboniferous, regional E-W extension, possibly related to Variscan orogenic activity towards the south (Ziegler, 1990) caused the formation of the highly magmatic Oslo Rift in southeastern Norway (Neumann et al., 1992; cf. Chapter 5) and precursors of the Central and Viking grabens in the North Sea area. The onshore geological record ceases at the end of the Permian, leaving little trace of the post-Permian evolution.

Offshore record: Meso-Cenozoic basin development

The offshore sedimentary record in the northern North Sea and Norwegian-Greenland Sea, as currently sampled by seismic and well data, dates back to the Permian. A phase of Permian-Early Triassic rifting is evidenced by thick Permo-Triassic clastic sequences, deposited in half grabens underlying the Viking Graben and Horda Platform (e.g., Gabrielsen et al., 1990; Figure 4-3). Major faulting activity, especially along the Øygarden Fault Zone, dates back to this time. Permo-Triassic sedimentation was almost entirely continental, except for a Late Permian transgression leading to the deposition of a thick evaporite sequence (Zechstein salts) in the south and carbonates in the north (Ziegler, 1990; Doré, 1991). A second transgression took place in the Early Jurassic, possibly as a result of ongoing or renewed extension. During the Middle Jurassic (Toarcian-Bathonian), regional uplift, accompanied by extensive alkaline volcanism, affected the central North Sea area (Ziegler,

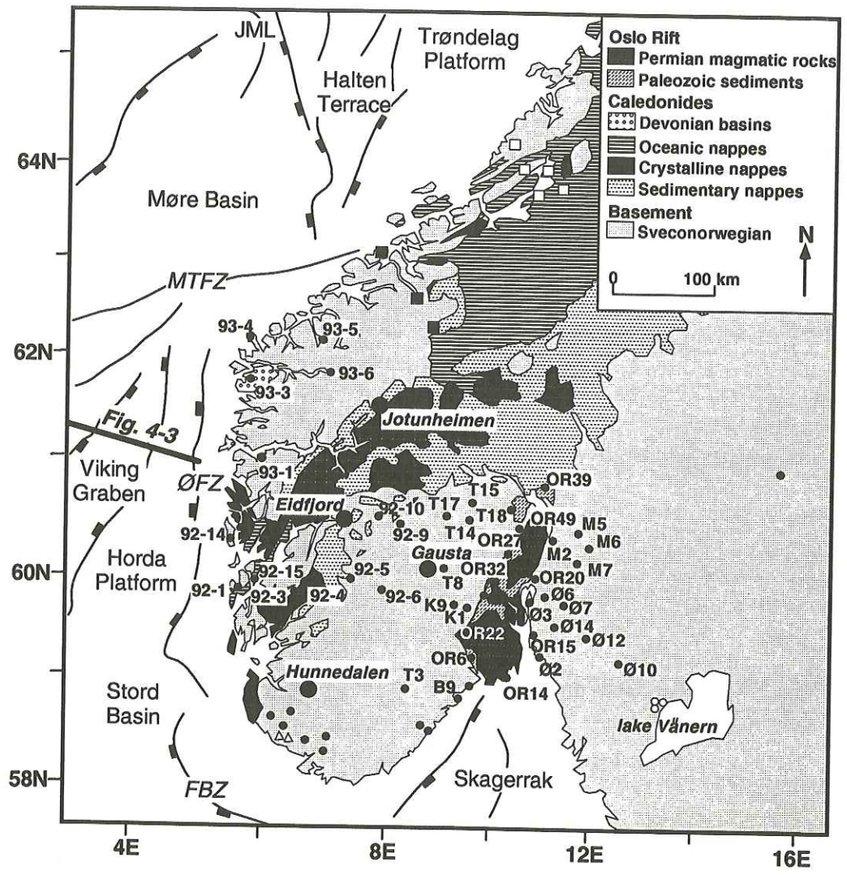

Figure 4-2. Simplified tectonic map of southern Norway showing onshore geology (after Roberts and Gee, 1985), offshore structural elements (Vollset and Doré, 1984) and AFT database. Labelled dots are samples collected for this study (Tables 4-1 and 5-1), large dots with names in italics give locations of elevation profiles. Unlabelled dots are previously unpublished data presented by Rohrman et al. (1995a); open circles are samples from Zeck et al. (1988); filled squares: Stiberg (1993); open squares: Grønlie et al. (1994); open triangles: Van den haute (1977). Other notations: FBZ: Fennoscandian Border Zone; JML: Jan Mayen Lineament; MTFZ: Møre-Trøndelag Fault Zone; ØFZ: Øygarden Fault Zone. Thick line accross Viking Graben indicates position of profile shown in Figure 4-3.

1990). This event led to the development of large deltaic systems throughout the northern North Sea which are now the main target of hydrocarbon exploration. The North Sea 'dome'

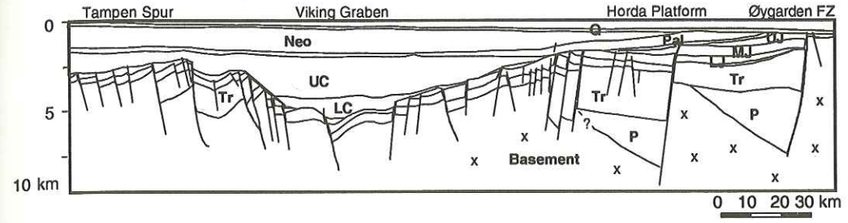

Figure 4-3. Interpreted deep seismic reflection profile SG8043-403 through the northern North Sea (Viking Graben and Horda Platform), after Gabrielsen et al. (1990). Letter codes indicate stratigraphic ages of sediments.

collapsed in the Late Jurassic (Oxfordian-Volgian) giving way to the final and major phase of rifting in the Viking Graben. Mesozoic extensional episodes are also recorded by Permian to Middle Jurassic alkaline dikes cropping out on the islands of western Norway (Færseth et al., 1976). The build-up of coarse clastic sequences throughout the Triassic and Jurassic in the Viking Graben and Horda Platform (Gabrielsen et al., 1990; Steel, 1993) indicates a continuous supply of clastics from the Norwegian mainland and, thus, significant erosion there. During the Cretaceous the influx decreased which, together with rapid post-rift subsidence, led to deep starved basins and extensive organic shale sedimentation. A major transgression during the Late Cretaceous caused widespread chalk deposition in the North Sea area. Early Jurassic and Late Cretaceous sedimentary inliers which have been discovered onshore, along the Møre-Trøndelag Fault Zone in mid Norway (Bøe and Bjerkli, 1989), indicate that the edges of the basin substantially overstepped the present-day coastline of Norway during Mesozoic highstands (Ziegler, 1990; Doré, 1991).

While the North Sea developed into a failed rift basin after Late Jurassic times, Cretaceous-Paleocene extension in the Norwegian-Greenland Sea created deep basins along the Vøring and Møre margins (Brekke and Riis, 1987), culminating in major volcanic activity and continental break-up between Norway and Greenland at 55 Ma (Skogseid et al., 1992). During the Paleogene, clastic influx from the Norwegian mainland was minor; the North Sea was dominated by deep water sedimentation, with most sediment supply coming from the Shetlands and Scottish highlands (Galloway et al., 1993). Sediment supply from Norway increased during the Oligocene (Stuevold et al., 1992; Jordt et al., 1995), suggesting that Cenozoic erosion of Fennoscandia was initiated during this time. Pre-Neogene sedimentary strata show a structural dip away from the coastline and toplap against the overlying sediments (Figure 4-3), suggesting uplift of the mainland (Doré, 1992; Stuevold et al., 1992; Jensen and Schmidt, 1993). Although the Øygarden and Møre-Trøndelag Fault Zones continue to display some earthquake activity (Gabrielsen, 1989), seismic reflection data do not record important post-Cretaceous vertical motions across these faults (Figure 4-3). Neogene uplift and Plio-Pleistocene glaciations resulted in extensive erosion and redeposition on- and offshore, leading to a thick Neogene sedimentary wedge. The base of the Neogene

wedge is dated at 33 Ma (Rundberg and Smalley, 1989); it contains several unconformities and becomes sandier and more dominated by a Fennoscandian source upwards (Galloway et al., 1993). Late Miocene and younger deposits comprise approximately half the volume of the wedge (Rundberg and Smalley, 1989; Jordt et al., 1995), suggesting an increase in erosion rates since then. A major unconformity occurs at ~2 Ma; this is interpreted as recording the onset of glacial erosion and redeposition (Rundberg and Smalley, 1989). Jansen and Sjøholm (1991) infer an age of 2.57 Ma for the onset of major ice sheet expansion, based on dating of ice rafted detritus; smaller scale glaciations may have occurred from 5.45 Ma onward. The Neogene wedge can be traced all around the coast of southern and western Norway. A similar pattern of Neogene erosion and redeposition is encountered in the southwestern Barents Sea (Doré, 1991; Riis and Fjeldskaar, 1992).

Geomorphology

The morphology of southern Norway is characterised by mountain peaks rising above an elevated upland plateau which, itself, is deeply incised by narrow valleys and fjords. The slightly undulating upland plateau is generally termed the 'paleic surface', after Gjessing (1967). It is thought to have been formed by deep weathering in relatively warm climates (Gjessing, 1967; Nesje and Whillans, 1994; Riis, 1995) and can be mapped throughout Norway (cf. Riis and Fjeldskaar, 1992). The elevation of the paleic surface follows the mean and summit elevation patterns, forming two distinct asymmetric domes, one in southwestern Norway and another in northern Sweden and Finnmark, with a low saddle in between in mid Norway (Figure 4-4). In southwestern Norway the paleic surface reaches maximum elevations of >1500 m (cf. Figure 4-14). Peaks rising above this level (e.g. Jotunheimen and Gaustatoppen in Telemark) are generally interpreted as residual or 'old' mountains with a strong lithological control (Peulvast, 1985). The mountain peaks define an enveloping surface which can be (speculatively) correlated to Jurassic deposits offshore (Peulvast, 1985; Riis, 1995).

Although there is consensus on the events leading to the present geomorphology of Norway (i.e. peneplanation of the Caledonian mountain range followed by renewed uplift and incision) the timing of events and the age of the paleic surface remain controversial. Gjessing (1967) merely refers to the surface as 'pre-glacial'. Tentative dating of the paleic surface and the onset of uplift has been based mainly on a correlation with offshore unconformities. Riis and Fjeldskaar (1992) propose a Pliocene onset of uplift as an isostatic reaction to glacial erosion. On the other hand, Torske (1972) suggests a pre-Eocene age for the surface and 'Tertiary' uplift, while Doré (1992) proposes a late Cretaceous age, based on a correlation of the paleic surface with the base Tertiary surface offshore. Riis (1995) suggests that uplift may have commenced in the Paleogene in northern Norway and in the Pliocene in southern Norway. Late Paleocene and early Eocene marine diatoms are encountered on planation surfaces in Sweden and Finland (Fenner, 1988), indicating that these were at or near sea level then (see also Jordt et al., 1995). The correlation of these surfaces to erosion

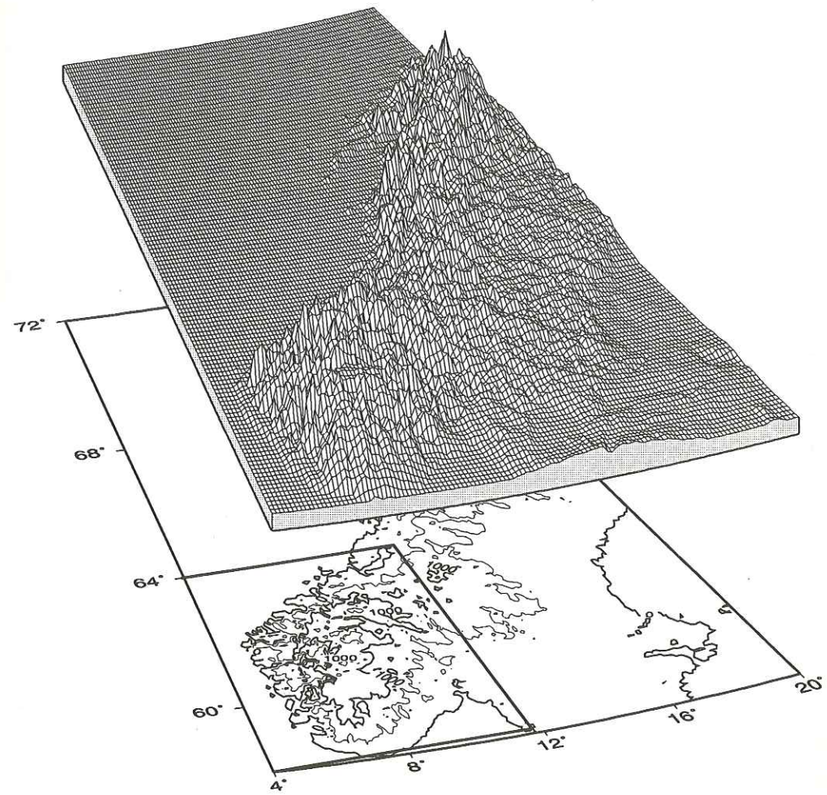

Figure 4-4. Elevation model of western Fennoscandia, constructed from the ETOPO-5 data base. View is from the southwest; inset shows extent of study area (Figure 4-2).

surfaces in southern Norway is, however, not straightforward (Riis, 1995). The morphology of the fjords in western Norway suggests that they were incised by glacial erosion into pre-existing valleys cut into the paleic surface (Nesje and Whillans, 1994). Therefore, uplift of the paleic surface seems to significantly predate glaciation and most probably started in the Oligocene (e.g., Stuevold et al., 1992).

4.3 MESO-CENOZOIC MORPHOTECTONIC EVOLUTION OF SOUTHERN NORWAY FROM APATITE FISSION TRACK THERMOCHRONOLOGY*

4.3.1 Fission track data

Samples for apatite fission track thermochronology were collected throughout southern Norway (Figure 4-2; Table A2-3 in Appendix 2). Three elevation profiles were sampled. A profile at Eidfjord, at the edge of the Hardangervidda plateau where the paleic surface lies around 1000 m, samples an elevation interval from 0 to 1620 m. The second profile was collected at Jotunheimen, where the highest peaks of Norway occur, and ranges from 0 to 2465 m. At Gaustatoppen, a single peak rising ~800 m above the paleic surface in Telemark, a profile spanning an elevation from 480 to 1883 m was collected. In addition, I reproduce a profile collected by Andriessen (1990) over a limited elevation range at Hunnedalen, in the southwest of the study area. Samples comprise Precambrian as well as Caledonian metamorphic rocks, a Devonian sandstone and a Triassic dike (cf. Table A2-3). Employed sample preparation and processing techniques are outlined in Appendix 2, constants and procedures will be described in detail by Rohrman (manuscript in prep.).

Results

Apatite fission track (AFT) data are summarised in Table 4-1; ages are quoted as central ages (Galbraith and Laslett, 1993) with an error of ±1σ throughout. Analytical data are given in Table A3-3 (Appendix 3). Results from the Oslo rift area are presented in Table 5-1.

The four age-elevation profiles are depicted in Figure 4-5. The Eidfjord profile was already the focus of a reconnaissance study by Andriessen and Bos (1986). Additional data collected for this study show a strong correlation of AFT ages with elevation; ages vary from 99±9 Ma near sea level to 166±31 Ma at 1620 m. Mean track lengths increase from <12 to >13 µm with increasing elevation, while track length distributions become narrower. The highest sample (EID3 in Rohrman et al., 1995a) has an anomalously low mean track length of 12.4 µm, however, only 28 tracks could be measured.

The Jotunheimen suite of samples encompasses the largest relief. AFT ages range from 106±13 Ma at sea level to 164±13 Ma at 2465 m. Although the age/elevation gradient is steeper than that at Eidfjord, the overall trend is the same. Track lengths increase from a mean of 11.6 µm and a standard deviation of 2.0 µm at sea level to 13.5 µm, with a symmetrical narrow distribution (σ = 1.2 µm), at 2465 m.

* This section is based on: Rohrman, M., van der Beek, P.A., Andriessen, P.A.M. and Cloetingh, S., 1995. Meso-Cenozoic morphotectonic evolution of southern Norway: Neogene domal uplift inferred from apatite fission track thermochronology. *Tectonics*, in press.

Table 4-1. Apatite fission track results for southern Norway

sample	elev. (m)	number of grains	age ±1σ (Ma)	D (%)	mean track length (µm)	st.dev. (µm)	number of tracks
92-1	35	13	181±22	15	12.9±0.1	1.3	100
92-3	35	20	152±17	37	12.9±0.2	1.5	102
92-4	525	13	155±23	38	11.3±0.2	1.5	100
92-5	990	20	163±20	13	13.0±0.2	1.3	60
92-6	640	20	134±11	14	12.4±0.1	1.4	100
92-9	1020	20	154±14	12	12.2±0.1	1.4	100
92-10	1020	20	133±10	12	12.8±0.1	1.2	100
92-14	30	20	200±20	22	13.4±0.1	1.3	100
92-15	0	17	189±19	18			
93-1	0	20	121±11	21			
93-3	0	20	122±12	12	12.5±0.2	1.5	71
93-4	100	4	153±29	3			
93-5	0	20	138±15	14	12.1±0.3	0.9	7
93-6	0	6	111±20	13			
Eidfjord							
EID11	1230	20	152±12	13	13.1±0.1	1.3	100
EID13	965	18	181±17	14	12.4±0.2	1.6	100
EID15	345	23	143±13	14	12.0±0.2	1.6	100
EID16	180	20	99± 9	15	11.5±0.2	1.6	100
EID17	0	20	111±11	31	12.0±0.2	1.9	100
Jotunheimen							
JOT1	2465	23	164±13	14	13.5±0.1	1.2	100
JOT3	2150	20	170±16	13	13.3±0.1	1.3	100
JOT5	1855	20	156±13	9	13.4±0.1	1.3	100
JOT9	1240	12	138+13	11			
JOT11	1430	20	168±12	9	12.6±0.1	1.2	100
JOT12	1010	19	135±12	19	12.5±0.1	1.4	100
JOT14	560	20	146±13	14			
JOT17	0	19	106±13	11	11.6±0.2	2.0	100
Gausta							
GAU1	1845	14	195±18	9	13.6±0.4	1.4	12
GAU3	1670	10	243±28	13			
GAU5	1590	19	171±26	10	13.7±0.1	1.4	100
GAU7	1385	19	159±17	17	12.9±0.2	1.5	100
GAU9	1250	20	199±40	7	13.5±0.2	1.7	100
GAU11	980	7	183±41	15	13.3±0.2	1.5	100
GAU12a	870	20	180±26	24	13.4±0.2	1.4	60
GAU15	480	18	174±18	15			

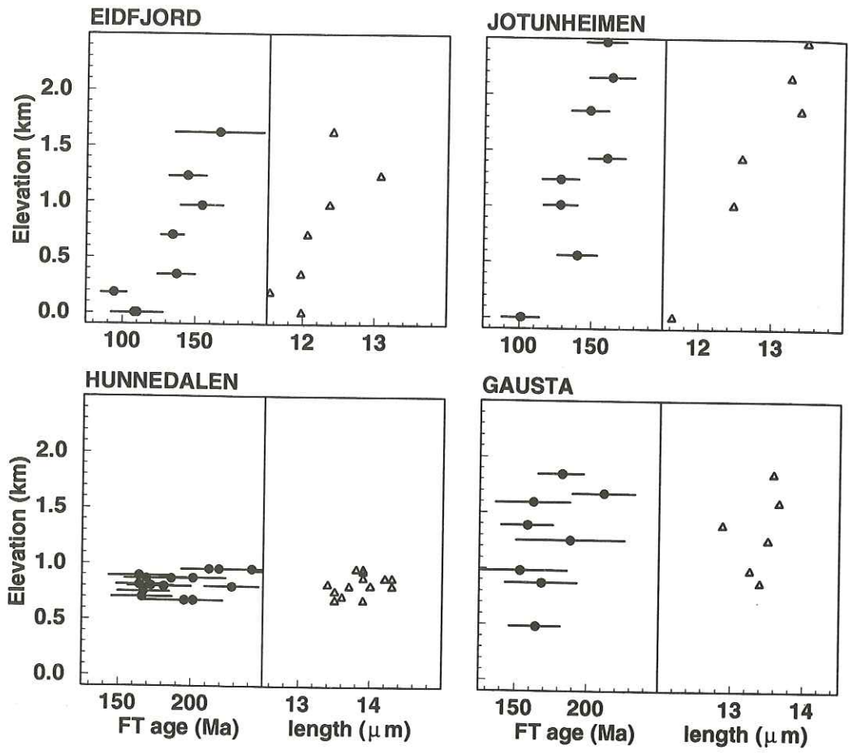

Figure 4-5. AFT age/elevation and mean length/elevation trends for four localities in southern Norway (see Figure 4-2 for locations). Hunnedalen profile is from Andriessen (1990); Eidfjord profile partly from Andriessen and Bos (1986). Note change in horizontal scale between upper and lower panels.

In contrast, the profile at Hunnedalen shows a very poor correlation of AFT age with elevation. Ages vary from 160 to 260 Ma, with mean track lengths varying between 13.4 and 14.3 μm and standard deviations between 1.0 and 1.8 μm (Andriessen, 1990).

The Gausta profile shows a weak age/elevation correlation with some scatter, ages vary from 174±18 Ma at 480 m to 195±18 Ma at the top. Mean track lengths range from 12.9 to 13.7 μm, with a mean around 13.4 μm.

A plot of AFT age versus mean length, including data from Rohrman et al. (1995a) and Andriessen (1990), is shown in Figure 4-6. There is a clear decrease in mean track length with age for the younger samples (<160 Ma), with a concurrent broadening of the standard deviation to ~2 μm. Highest mean track lengths are recorded by samples in the 170 to 220

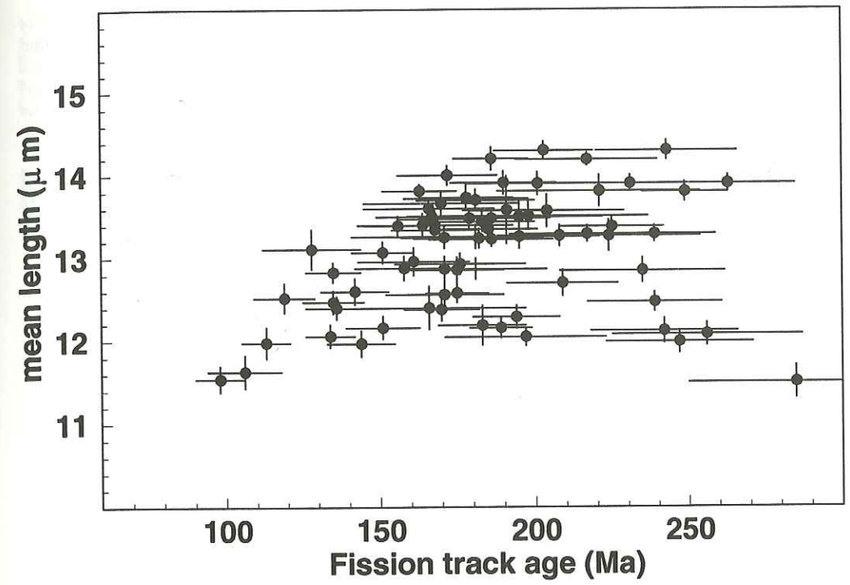

Figure 4-6. AFT age/mean length trend for southern Norway, including data from Rohrman et al. (1995a) and Andriessen (1990).

Ma age range; mean track length decreases again for ages exceeding 220 Ma. These old ages are mostly recorded by samples from the Oslo rift area (Table 5-1). Age dispersions (Table 4-1) follow this trend; samples with young AFT ages and low mean track lengths have significantly higher dispersions than other samples.

The AFT age distributions do not show a relationship with the Caledonian orogenic structure. Two samples of post-Caledonian rocks were collected: an alkaline dike with a K-Ar age of ~220 Ma (Færseth et al., 1976; sample 92-15) and a Devonian sandstone (sample 93-3). AFT ages from these samples are indistinguishable from those of surrounding Precambrian rocks at 189±19 Ma and 121±11 Ma, respectively. This confirms the pattern observed in the age/elevation and age-length plots, indicative of a temperature history dominated by cooling since the Triassic-Jurassic.

While there is no relationship between AFT ages and onshore geology, there is a strong correlation between AFT ages and mean elevation. Figure 4-7 shows the distribution of AFT isochrons from samples at an elevation of less than 500 m. The areas of highest mean elevation in southwestern Norway are correlated with the lowest AFT ages at sea level, around 100 Ma in the inner fjords. Ages increase towards the mountains peaks, towards the west coast (~160 Ma), as well as to the south and east (>200 Ma). The pattern thus defines

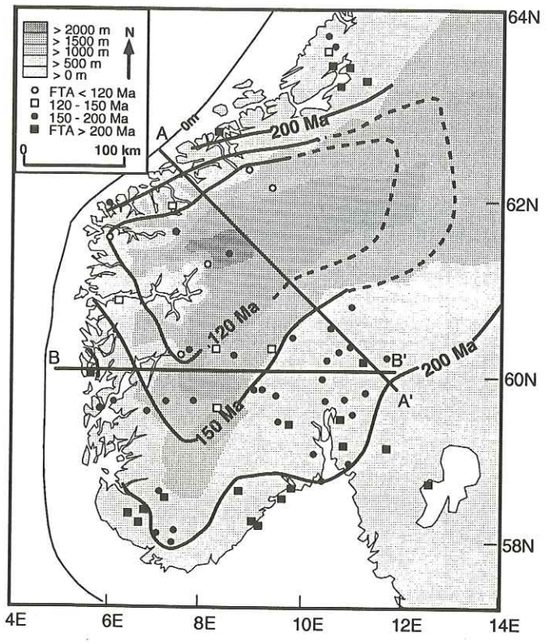

Figure 4-7. Regional variation of AFT ages plotted onto a map of mean topographic elevation. Fission track samples are labelled according to age; isochrons of AFT ages are drawn for samples with an elevation < 500 m. Profiles A and B are depicted in Figure 4-8. Thick line labelled '0 m' offshore delineates the hinge line of uplift as determined by Doré (1992) and Riis and Fjeldskaar (1992).

a large scale structural dome with a half wavelength of approximately 200 km and a slight asymmetry, with a steeper age gradient on the northwestern than on the southeastern side.

The domal pattern is also exhibited when AFT results are plotted in cross-section (Figure 4-8). Profile A-A′ has a NW-SE orientation; ages near sea level decrease from 153±29 Ma at Vestkappen (93-4) to 106±13 Ma at Jotunheimen (JOT 17), increasing again in the Oslo region and towards the Swedish border. Additional data from Grønlie et al. (1994) and Stiberg (1993), from the Trondheim and Kristiansund areas respectively, show ages exceeding 200 Ma at sea level in the north. An E-W transect (B-B′) shows a similar anticlinal pattern. AFT ages are >180 Ma at the west coast (92-1, 92-14) and decrease in age in the direction of Eidfjord to around 100 Ma (EID16, EID17). Moving further to the east the ages increase again in the Oslofjord area to >170 Ma and reach values of 220 Ma in southern Sweden, at elevations of around 300 m (Zeck et al., 1988). A sample from the Siljan area in central Sweden has an age of 285±35 Ma and a mean track length of 11.5 μm; it fails χ^2 (Rohrman et al., 1995a). This agrees with the results in Figure 4-6, which suggest a decrease in mean track length for ages >220 Ma. The profiles show that the half amplitude of the AFT age dome is about 2 km.

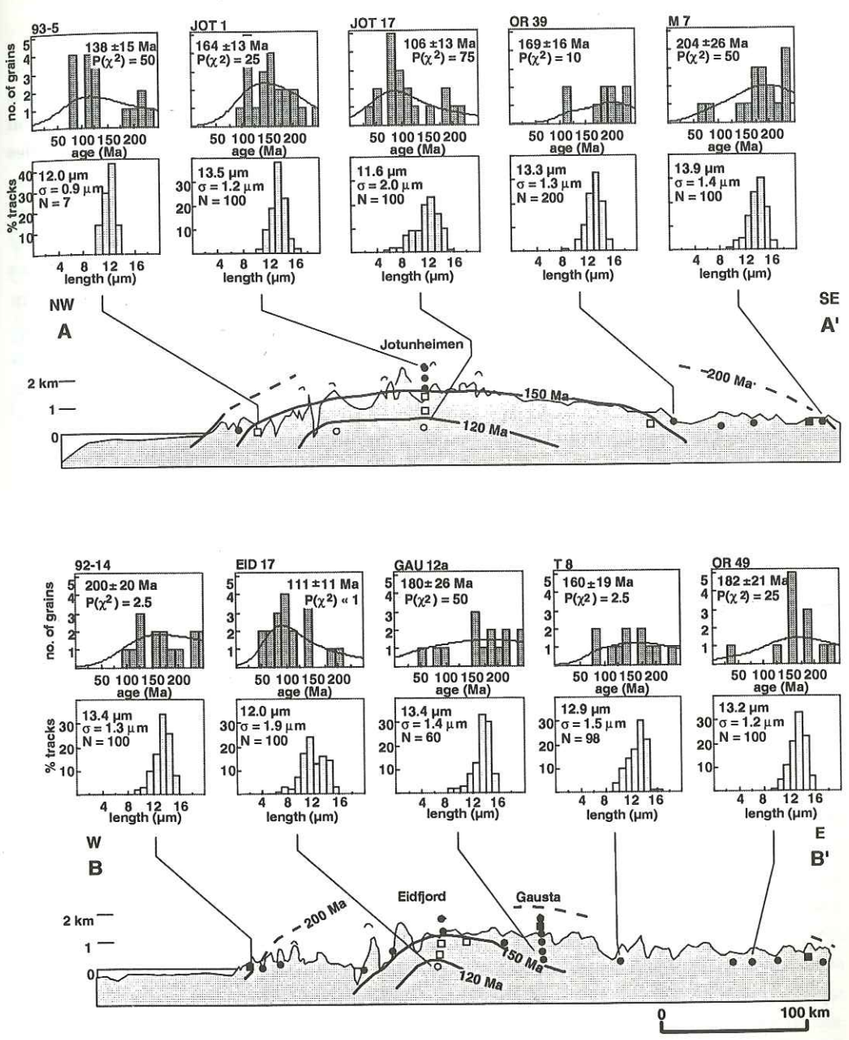

Figure 4-8. Selected AFT samples projected onto two profiles (location in Figure 4-7), showing domal deformation of AFT isochrons. Labelling of samples is the same as in Figure 4-7. Upper panels show AFT age histograms and probability curves; lower panels give length distribution histograms for selected samples. Topographic profiles are from Torske (1972). Results for samples OR39, M7, T8 and OR49 are summarised in Table 5-1.

Interpretation

To interpret the AFT age/elevation patterns I employ the concepts outlined in Section 1.3.3. In rapidly exhumed terrains, a break in slope in the age/elevation plot locates the base of the fossil (pre-exhumation) partial annealing zone (PAZ) and dates the onset of exhumation (Gleadow and Fitzgerald, 1987; Brown et al., 1994; cf. Figure 1-9). AFT age/elevation profiles in southern Norway (Figure 4-5) do not show such breaks in slope. The Jotunheimen, Eidfjord and Gausta profiles show a slow but consistent linear increase in age with elevation, with the Gausta profile having somewhat older ages and longer mean track lengths. The Hunnedalen profile shows a more rapid increase with considerably more scatter. All profiles were collected in spatially restricted areas (highest and lowest samples are <20 km apart) in structurally homogeneous Precambrian basement. Thus, it is highly unlikely that age scattering results from the profiles crossing large faults, and the different elevation profiles are interpreted to record different parts of a regional age/elevation trend. In this interpretation, the Eidfjord and Jotunheimen suite of samples originate from below a Jurassic PAZ, the Gausta samples from its base and the Hunnedalen samples from within this PAZ (Figure 4-9), indicating an increase in cooling rates at around 160 Ma. Such an interpretation also explains the scatter in the Gausta and Hunnedalen profiles, as long residence times in the PAZ causes differential annealing of grains, resulting in scattered ages (e.g., Green et al., 1989a). Differing age/elevation patterns across an area have been used to suggest that the different profiles were separated by major faults (e.g., Foster and Gleadow, 1992; Fitzgerald, 1994). However, no important post-Permian fault movements are known for onshore southern Norway; the entire area behaved as a single block from the Permian onwards.

The observed age/length trend also indicates an onset of rapid cooling in the Jurassic; the age/length peak in Figure 4-6 agrees with the constructed break in slope at ~160 Ma in Figure 4-9. A cooling event at ~160 Ma is coeval with the progradation of large deltas from the Norwegian mainland (Doré, 1991; Steel, 1993). Mean track lengths in Figure 4-6 decrease for ages >220 Ma. This is more typical for the southern and eastern samples located around the Skagerrak, dating onset of exhumation for that area (Zeck et al., 1988; Chapter 5). Evidence for erosion of this part of Fennoscandia is found in thick Triassic deposits associated with normal faulting in the southern Skagerrak (e.g., Jensen and Schmidt, 1993). Even though AFT thermochronology strictly records cooling only, the rapid cooling intervals are interpreted as erosional events because they coincide with periods of coarse clastic deposition, with a Fennoscandian source, offshore. This implies that the Triassic-Jurassic represents a major period of erosion in western Fennoscandia.

The youngest samples (~100 Ma) also have shortest mean lengths, broad track length distributions and wide age dispersions (Figures 4-5, 4-6, Table 4-1), suggesting a long residence time in the PAZ before recent cooling. The pattern of isochrons (Figures 4-7, 4-8) shows bending of isochrons as young as 100 Ma, indicating that final cooling was at least post-Cretaceous in age.

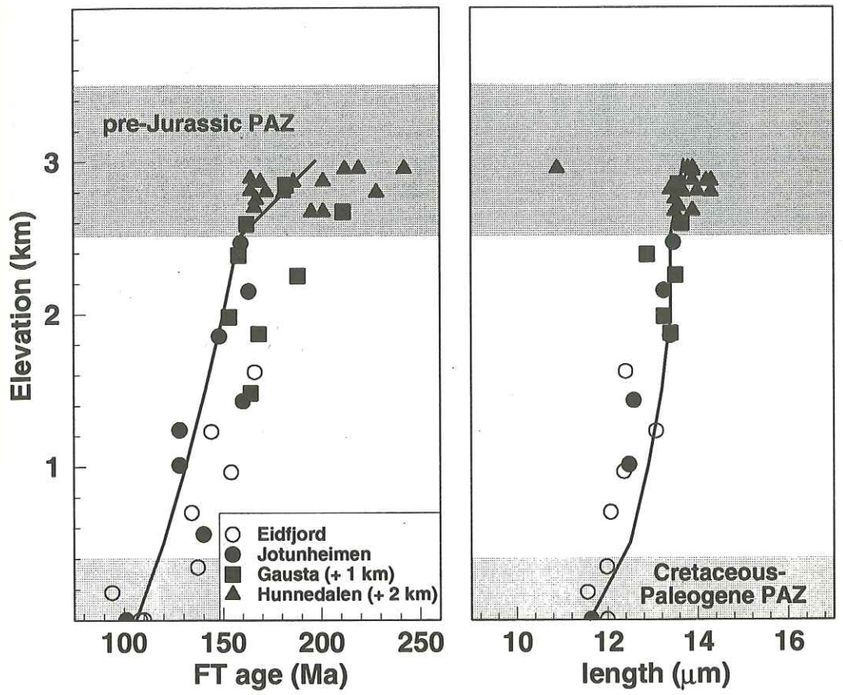

Figure 4-9. 'Stacked' profile of AFT ages and mean track lengths against elevation, constructed by relative vertical displacement of Gausta and Hunnedalen samples by 1 and 2 km, respectively. Thick line shows modelled age-elevation trend for preferred cooling/exhumation history (Figure 4-11). Also shown are the positions of inferred pre-Jurassic and Cretaceous-Paleogene partial annealing zones. See text for discussion.

Thus, cooling appears to have taken place during two distinct time periods, one pre- and the other post-Cretaceous. I have performed forward and inverse modelling of AFT ages and length distributions in order to further constrain the thermal history of the area, using the kinetic annealing model for F-apatites of Crowley et al. (1991). Chemical composition data from some of the apatites in this study suggest mainly F-rich varieties (Cl/(F+Cl)~0.0; Andriessen, 1990), although there is probably considerable scatter in Cl content in the samples, since so many different lithologies were collected. The Cl/(F+Cl) ratio is important for a quantitative interpretation of AFT data, since F-rich apatites anneal somewhat faster than Cl-rich grains (Green et al., 1989a). I choose to employ the Crowley et al. (1993) annealing model here because the (more popular) model of Laslett et al. (1987) seems to underestimate low temperature and overestimate high temperature annealing (e.g., Corrigan, 1993; Wagner et al., 1994), thus possibly overemphasizing the importance of recent cooling.

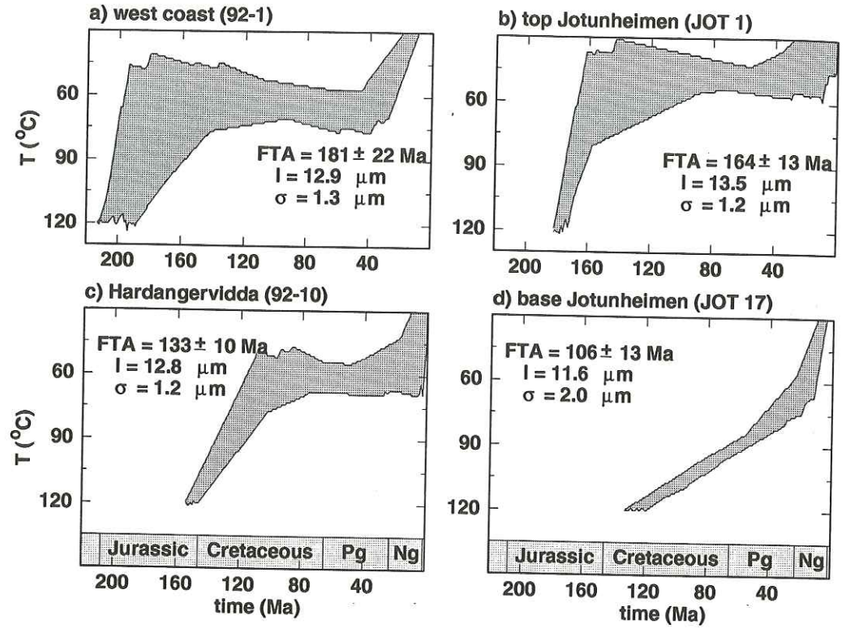

Figure 4-10. Thermal histories for selected samples, calculated from inversion of AFT data (cf. Appendix 1) using the annealing model of Crowley et al. (1991) for F-apatites.

The Crowley et al. (1991) model exhibits an opposite behaviour (Corrigan, 1993); therefore, application of this model provides a firmer basis for inferring recent cooling events. Note, however, that the low-temperature (<~60°C) history in any AFT inversion is not well constrained because of uncertainties in the annealing behaviour for this temperature range (e.g., Corrigan, 1993; Ravenhurst et al., 1994).

Samples from the coastline and from the mountain peaks are characterised by rapid Triassic-Jurassic cooling, with a rate of ~2-2.5°C/My (Figure 4-10(a,b)). These samples cooled through 60°C as early as Late Jurassic-Early Cretaceous. In contrast, samples from sea level in the inner fjords indicate Neogene (<30 Ma) final cooling from temperatures of 60-80°C, at a rate of 1-1.5°C/My (Figure 4-10(d)). In between these periods of rapid cooling, lower rates (in the order of 0.5°C/My) are inferred for the Cretaceous and Paleogene. A possible Plio-Pleistocene acceleration of cooling rates, resulting from an increase in uplift rate since the late Miocene and locally large glacial erosion in the fjords, is beyond the resolution of the data.

Most reconstructions of the paleic surface place it at an elevation of a few hundred meters near the shoreline (e.g., Riis and Fjeldskaar, 1992). However, modelled thermal histories from coastline samples (e.g., Figure 4-10(a)) resemble those of samples from the

mountain peaks (Figure 4-10(b)) more than those from the paleic surface at Hardangervidda (Figure 4-10(c)). The coastline samples show rapid cooling to temperatures <60°C in the Early Jurassic, while the Hardangervidda samples were still at temperatures ≥120°C around that time. Cooling of the Hardangervidda samples commenced in the late Jurassic, followed by slow cooling to <60°C during the Cretaceous and Paleogene. This suggests a Cretaceous or Paleogene age for the paleic surface at Hardangervidda, in agreement with geomorphological interpretations (Nesje and Whillans, 1994; Riis, 1995). The samples that are now at sea level near the coastline seem to have come from the same structural level as those on the mountain peaks, i.e. 1-1.5 km above the paleic surface.

Figure 4-11 shows the preferred exhumation history, based on forward modelling of the 'stacked' age/elevation plot (thick line in Figure 4-9) and inversion of length distributions for selected samples (Figure 4-10). The model results suggest that late stage exhumation and related doming of AFT isochrons is a post-Paleogene event. The AFT isochrons represent pre-Neogene isotherms which were probably near-horizontal planes. Neogene doming of isotherms could be either the result of a thermal event which caused partial resetting of AFT ages, or of uplift and exhumation. There is little independent geological evidence for the first scenario; thus, the domal pattern most probably reflects differential uplift and erosion, as also indicated by offshore seismic data (Doré, 1992; Stuevold et al., 1992; Jensen and Schmidt, 1993; cf. Section 4.2).

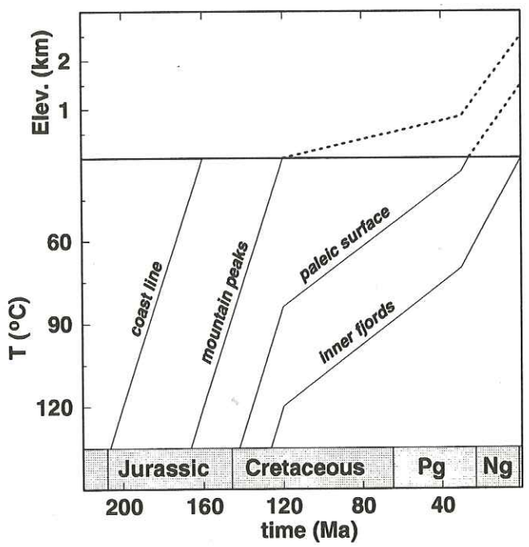

Figure 4-11. Preferred cooling and uplift trajectories for different groups of samples in the study area, based on forward modelling of the 'stacked' age-elevation profile (thick line in Figure 4-9) and inverse modelling of selected samples (Figure 4-10). See text for discussion.

Estimated amounts of erosion

The coincidence of rapid cooling intervals, during the Triassic-Jurassic and the Neogene, with periods of coarse clastic deposition offshore, leads me to conclude that cooling was caused by erosional denudation. In order to estimate the amount of exhumation, the geothermal gradient has to be known or estimated (cf. Figure 1-10). The present-day geothermal gradient for southern Norway is approximately 20°C/km (Balling, 1990). AFT samples from the Siljan deep drill hole in central Sweden (Andriessen and Verschure, 1988) show total annealing at 105°C (~5 km depth), indicative of heating times ≥100 My (cf. Section 1.3.2). The present-day geothermal gradient thus seems to have been more or less stable since ~100 Ma, at least for the inland areas.

However, thermal history modelling suggests that, for example, samples from the top and base of the Jotunheimen profile, with a difference in elevation of 2.5 km, experienced a temperature difference of at least 70±20°C during the Late Jurassic-Early Cretaceous (Figures 4-10, 4-11). Therefore, Mesozoic geothermal gradients could have been significantly higher than at present, in the order of 28±8°C/km. It is impossible to deduce geothermal gradients for the Triassic-Jurassic; if I take values to be similar to those for the Late Jurassic, an estimate for Triassic-Jurassic erosion is 2.4±1.1 km (i.e. 50-70°C cooling along a 20-36°C/km geotherm). Neogene exhumation of samples from the inner fjords amounts to 2.0±0.5 km (30-50°C cooling; 20°C/km geothermal gradient), decreasing radially outward to <0.5 km near the coastline. Cretaceous-Paleogene cooling can be related to relaxation of the geothermal gradient, combined with minor denudation resulting from ongoing deep weathering and slow removal of regolith.

4.3.2 Paleogeographic implications

The apatite fission track data presented above and in Chapter 5, indicate that Mesozoic denudation of southern Norway was initiated during the Triassic in the southeastern Skagerrak/Oslo rift area. During this time, thick continental clastic deposits accumulated in the Viking and southern Skagerrak grabens (Ziegler, 1990; Gabrielsen et al., 1990; Jensen and Schmidt, 1993). Rohrman et al. (1995b) present apatite and zircon fission track data from wells on the Horda Platform and Stord Basin, offshore southern Norway. Triassic samples from these wells have zircon fission track (ZFT) ages of 257±34 - 275±36 Ma, representing source ages unaffected by annealing (Rohrman et al., 1995b). In contrast, ZFT ages from the Caledonides and the Precambrian basement of southern Norway are consistently >300 Ma old (Andriessen and Bos, 1986; Grønlie et al., 1994; Chapter 5). This discrepancy suggests that the source of Triassic deposits within the offshore basins consisted for a large part of the Permian volcanics associated with the Oslo Rift (Figure 4-12(a)); these probably covered a large area of southeastern Norway at that time (Ramberg and Larsen, 1978; cf. Chapter 5).

Samples from the western part of the study area indicate a major Jurassic phase of exhumation. During this time, rifting within the northern North Sea reached its climax

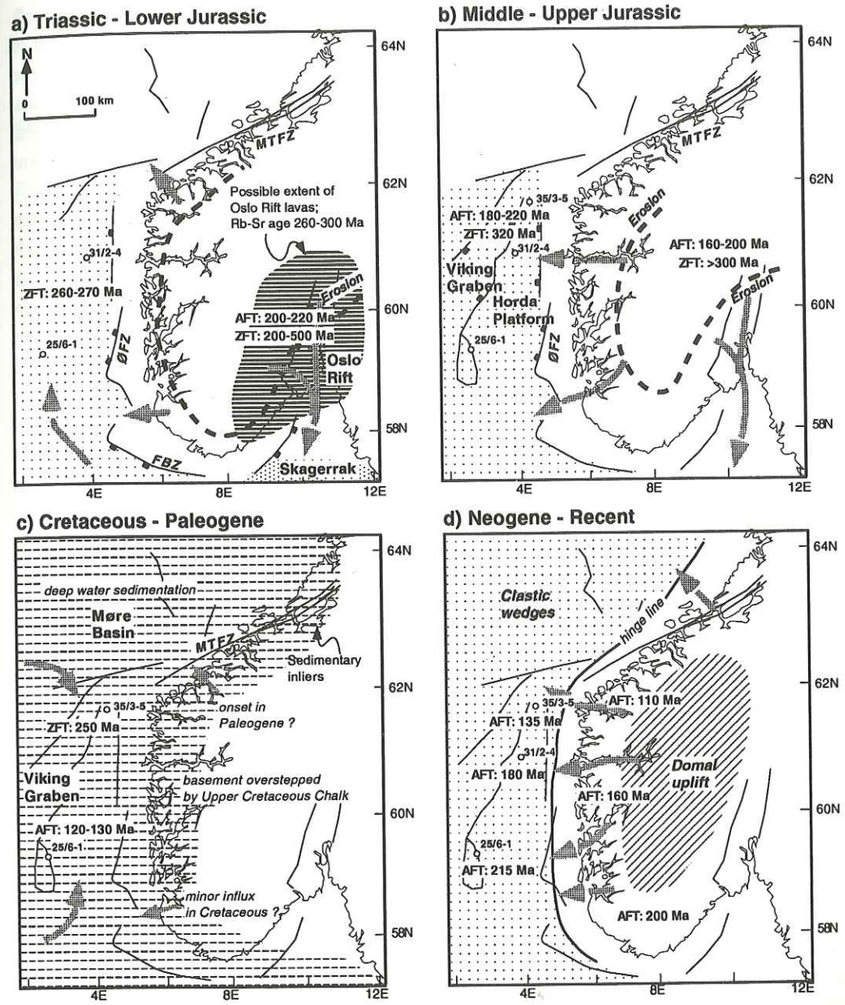

Figure 4-12. Paleogeographic evolution of southern Norway, inferred from the AFT results and offshore data. (a) Triassic-Lower Jurassic paleogeography, extent of Oslo Rift lavas is based on Ramberg and Larsen (1978) and Olaussen et al. (1994); (b) Middle-Upper Jurassic paleogeography; (c) Cretaceous-Paleogene paleogeography, extent of marine sediments onshore is after Ziegler (1990); (d) Neogene paleogeography. Labelled circles offshore indicate the positions of wells studied by Rohrman et al. (1995b), abbreviations are as in Figure 4-2. Dot pattern indicates continental - shallow marine clastic sedimentation; line pattern: deep marine / non-clastic sedimentation (after Ziegler, 1990; Doré, 1991). Large grey arrows indicate probable sediment pathways.

(Ziegler, 1990) and large deltaic systems filled the rift basins from the south and east (Doré, 1991; Steel, 1993). Samples from Jurassic formations in the offshore wells have AFT ages of 175±22 - 224±20 Ma (Rohrman et al., 1995b), similar to or slightly older than those from the peaks of southern Norway (Figure 4-5). ZFT ages are also concordant with those onshore. These results suggest that Jurassic sediments were eroded from levels structurally above the highest mountain peaks (i.e. the pre-Jurassic PAZ), and confirm the inferred significant denudation of the mainland during this time (Figure 4-12(b)). The inferred exhumation was probably the result of erosional base level lowering during rifting, combined with an unknown amount of tectonic rift flank uplift (compare Section 2.4). The deposition of thick sequences of continental deposits within the Triassic-Jurassic rifts over long periods of time (Gabrielsen et al., 1990; Steel, 1993), as well as a major Triassic unconformity in the northern Skagerrak Graben and the absence of post-rift sediments in the Oslo Graben (Neumann et al., 1992; Olaussen et al., 1995; Chapter 5) suggest that the Norwegian mainland remained at a high elevation throughout the Triassic and Jurassic.

During the Cretaceous and Paleogene, inferred exhumation rates dropped by an order of magnitude (Figure 4-11) and Upper Jurassic and Cretaceous sediments probably covered parts of southern Norway (Bøe and Bjerklund, 1989; Ziegler, 1990; Doré, 1991). The offshore sedimentary record also indicates little transport of material from the Norwegian mainland, which was a peneplain with an elevation close to sea level at that time (Figure 4-12(c)). This is confirmed by AFT and ZFT data from Cretaceous deposits within the offshore wells, which indicate derivation from different sources than Fennoscandia (Rohrman et al., 1995b).

Late Paleocene-Early Eocene diatoms found in Sweden and Finland (Fenner, 1988) indicate that most of Fennoscandia was at or near sea level prior to the Neogene. The present topographic elevation of southern Norway, the Neogene erosion recorded by AFT data and the deposition of Neogene wedges thus result from uplift of the mainland which commenced around 30 Ma. Uplift was not accommodated by movement along major fault zones (Doré, 1992). Detailed sedimentological studies of the Neogene wedge indicate that Neogene erosion was not an instantaneous event. Build-up of the wedge started in the Early Oligocene in the Norwegian-Danish basin and the Viking Graben (Jensen and Schmidt, 1993; Jordt et al., 1995); it accelerated in the late Miocene-Pliocene after a late Oligocene-early Miocene period of low sedimentation rates. Angular unconformities indicate that most of the erosion probably occurred from the late Miocene-Pliocene onwards (e.g., Rundberg and Smalley, 1989), coeval with increased basin subsidence (Cloetingh et al., 1990; Jordt et al., 1995). AFT ages within Oligo-Miocene wedge deposits decrease from 213±17 Ma in the south (Stord basin) to 133±32 Ma in the northern Horda Platform (Rohrman et al., 1995b), mirroring the onshore pattern (Figures 4-5, 4-12(d)) and suggesting that the present-day drainage through the large fjords was already exploited for the deposition of the Neogene wedges. The fact that relatively few single grain ages <160 Ma are encountered in these samples suggests that a large part of the onshore erosion may indeed have taken place relatively late, from the late Miocene-Pliocene onwards.

UNIVERSITE JOSEPH FOURIER GRENOBLE 1
INSTITUT DE GEOLOGIE
DOCUMENTATION
15, RUE MAURICE GIGNOUX
F 38031 GRENOBLE CEDEX
TEL. (33) 76 63 59 00
FAX. (33) 76 87 82 43

4.4 Mechanisms of Neogene tectonic uplift in southern Norway

4.4.1 Quantification of uplift and erosion patterns

The pattern of uplifted paleo-isotherms, as recorded by the apatite fission track data presented in the previous section (Figures 4-7, 4-8), correlates well with the dome pattern defined by the elevation of the paleic surface in southern Norway. Also, the inferred maximum denudation at sealevel in the inner fjords (2.0±0.5 km) is consistent with the elevation of the paleic surface (1500-2000 m) in these areas. These observations, together with the inferred position of inland correlatives of the surface close to sealevel in the Paeogene (Fenner, 1988; Riis, 1995), make the paleic surface a useful reference in quantifying Neogene uplift and erosion.

In Sections 2.3.2-2.3.4 it was explained how estimates of erosion can be 'backstacked' onto the present-day topography to arrive at estimates of tectonic uplift. Here, I will apply this concept to reconstruct 3-dimensional patterns of Neogene tectonic uplift for southern Norway. The approach I take is outlined in Figure 4-13. By combining equations (2.5) and (2.6) the tectonic uplift u_T is given by:

$$u_T = (H_0 + \Delta E - H_i) - I; \tag{4.1}$$

$$I = \left(\frac{\Delta E \rho_c}{\rho_a}\right)\left(1 + \frac{D k_E^4}{(\rho_a - \rho_c) g}\right)^{-1}$$

where H_0 = present-day elevation, ΔE = amount of erosion, H_i = initial elevation, I = isostatic rebound, ρ_c = density of (eroded) crust, ρ_a= density of sublithospheric mantle, k_E = wavenumber of erosional unloading, g = acceleration of gravity and D = flexural rigidity.

The amount of Neogene denudation can be calculated by simply subtracting the present-day elevation H_0 from the elevation of the paleic surface. The result (Figure 4-14) shows a mean amount of Neogene erosion of ~400 m, with maxima of 800-1000 m at the

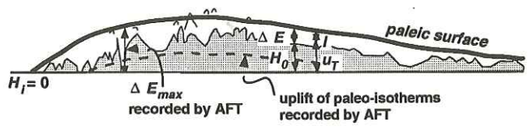

Figure 4-13. Schematic profile across southern Norway showing application of backstacking concept (compare Figure 1-11). Also shown are (schematic) deformed paleo-isotherms and maximum erosion (at sea level) inferred from fission track thermochronology (compare Figure 4-8). Notations refer to Equation 4.1.

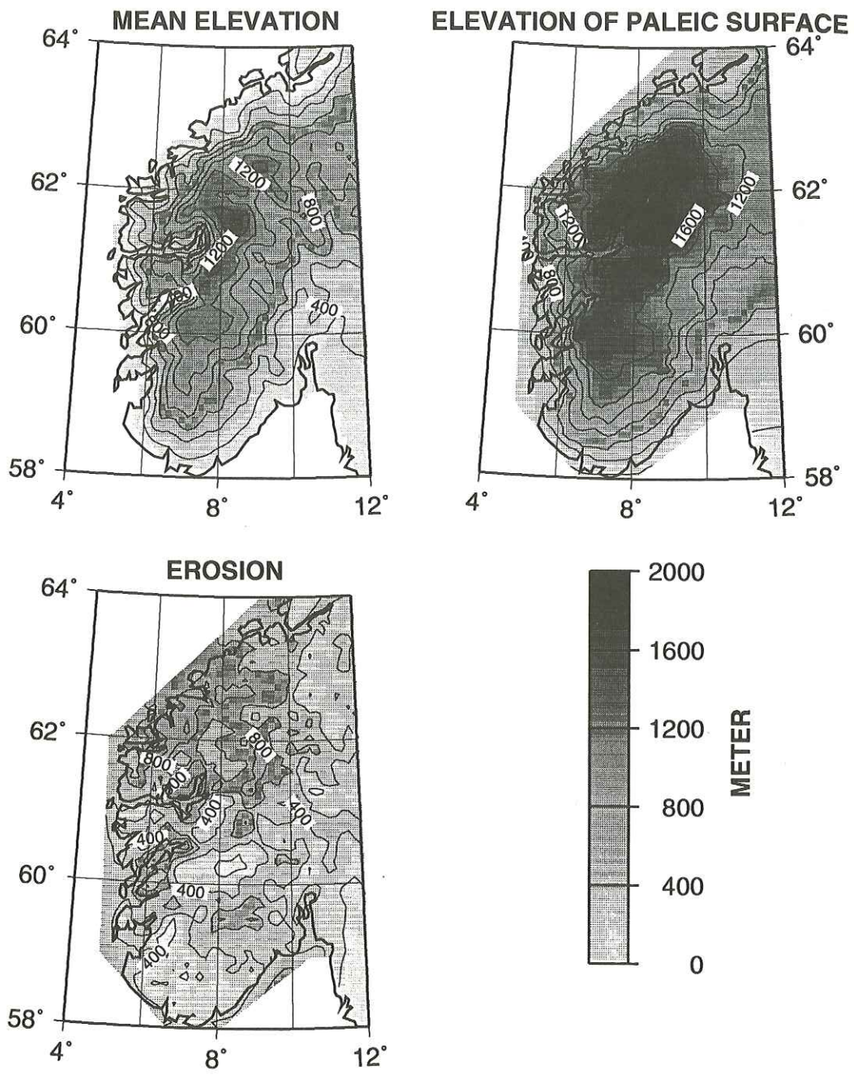

Figure 4-14. Maps of mean elevation of southern Norway (derived from the ETOPO-5 database), elevation of the Paleic surface (after Riis and Fjeldskaar, 1992) and amount of erosion, calculated by subtracting mean elevation from the elevation of the Paleic surface. Calculations were performed on 10×10 km UTM grids.

inner fjords and along the northwestern coast. Note that this is the amount of denudation removed from the mean present-day topography. Apatite fission track samples from elevations close to sealevel, i.e. below the mean present-day elevation, record much higher amounts of exhumation. The pattern of erosion that is calculated in this manner is, however, largely consistent with the pattern deduced from fission track thermochronology (e.g., Figure 4-7).

There are indications that the paleic surface was located close to sea level prior to Neogene uplift (cf. Section 4.2). Therefore, I assume that $H_i = 0$ and that the present-day elevation of the paleic surface represents $H_0+\Delta E = u_T+I$ (Figure 4-13). In the case of local isostasy, the amount of isostatic rebound reduces to $I = \Delta E\rho_c / \rho_a$ ($\approx 0.8\Delta E$ for $\rho_c = 2600$ kgm^{-3} and $\rho_a = 3250$ kgm^{-3}). Figure 4-15 shows calculated amounts of tectonic uplift and isostatic rebound for the local isostatic case. Tectonic uplift has the same domal pattern as the mean elevation and the elevation of the paleic surface, reaching maximum values of ~1500 m for the high mountain areas. However, the assumption of local isostasy is not a very realistic one and, therefore, the pattern and amount of tectonic uplift will also be a function of the flexural rigidity D of the southern Norwegian lithosphere.

Estimating flexural rigidity

In order to make a realistic assessment of the amount of tectonic uplift, the flexural rigidity, or corresponding equivalent elastic thickness T_e must be estimated. Flexural rigidity estimates for the entire Fennoscandian shield have been published from glacial rebound studies (e.g., Fjeldskaar and Cathles, 1991), suggesting $D \leq 10^{24}$ Nm ($T_e \leq 50$ km). On the other hand, an analysis of residual anomalies by Balling (1980) suggests that most of the topography of Fennoscandia is close to local isostatic compensation. An alternative way of estimating flexural rigidity is from a coherence analysis of topography and Bouguer gravity anomalies. Gravity and topography will be coherent at long wavelengths but not at shorter ones, the wavelength at which coherence breaks down being dependent on D. The observed coherence γ_0^2 is defined as (cf. Stephenson, 1981; Forsyth, 1985):

$$\gamma_0^2 = \frac{C^2_{(\bar{k})}}{E_{0(\bar{k})}E_{1(\bar{k})}} \tag{4.2}$$

where $E_{0(k)}$ = average power of topography for a discrete wavenumber band, $E_{1(k)}$ = wavenumber average power of gravity, $C_{(k)}$ = cross-spectral power of gravity and topography and $\bar{k}$ = average k for a particular wavenumber band. The theoretical coherence for a plate loaded both at its surface and base is given by (Forsyth, 1985):

$$\gamma^2 = \frac{\langle H_T W_T\rangle \langle H_B W_B\rangle}{\langle H_T^2 + H_B^2\rangle \langle W_T^2 + W_B^2\rangle} \tag{4.3}$$

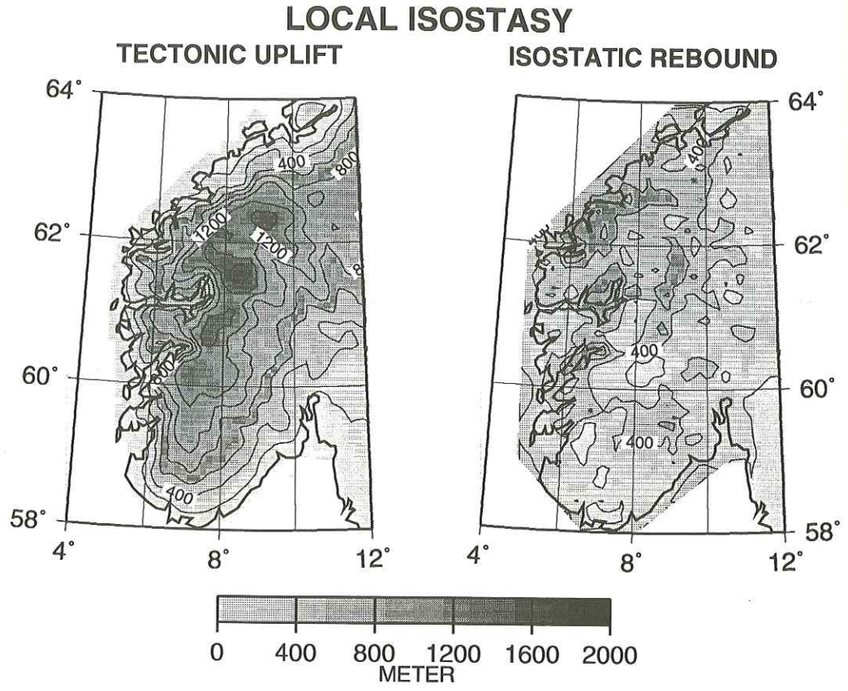

Figure 4-15. Calculated tectonic uplift and isostatic rebound for a model of local isostatic response to erosion. In this case isostatic rebound equals 0.8 × amount of erosion; tectonic uplift was calculated by subtracting this amount from the elevation of the Paleic surface.

where H_T = amplitude of surface deflection as a result of surface loading; W_T = amplitude of deflection of the base of the plate (i.e. Moho) as a result of surface loading; H_B = amplitude of surface deflection resulting from loading at the base of the plate and W_B = amplitude of Moho deflection resulting from base loading. H_T, H_B, W_T and W_B depend on the wavenumber k and flexural rigidity D via:

$$\begin{aligned} H_{B(k)} &= f\ \rho_c\ H_{T(k)}\ /\ \psi\ \Delta\rho; \\ W_{T(k)} &= -\ \rho_c\ H_{T(k)}\ /\ \psi\ \Delta\rho; \\ W_{B(k)} &= -\ \rho_c\ H_{B(k)}\ \phi\ /\ \Delta\rho \end{aligned} \qquad (4.4)$$

with f = ratio of surface to base loading; $\Delta\rho = (\rho_a - \rho_c)$; $\phi = 1 + (D\ k^4\ /\ \rho_c\ g)$ and $\psi = 1 + (D\ k^4\ /\ \Delta\rho\ g)$.

The gravity data that were used for this analysis are from the SGU (1985) map (cf. Figure 4-19). Gravity and topography data (from the ETOPO-5 database, cf. Figure 4-14) were projected onto a 500×720 km UTM grid; the gridsize is 10×10 km. Data were clipped in the deep offshore areas (white in Figure 4-19) and tapered towards the mean value at the sides of the grid, before being transformed into the wavenumber domain using a fast fourier transform algorithm (cf. Stephenson, 1981 for a detailed description of the method).

Results of the coherence analysis are shown in Figure 4-16. Although a best-fit f and T_e can be estimated independently (e.g., Forsyth, 1985; Ebinger et al., 1989), this may put too much emphasis on a best fitting number for the present data quality. Visual inspection of Figure 4-16 indicates a best fit T_e between 10 and 20 km (D = 8.9×10^{21} - 7.1×10^{22} Nm), assuming f = 1. This value is surprisingly low, considering the tectonic history of onshore southern Norway, characterised by quiescence since the Permian (cf. Section 4.2). It is also on the low end of estimates of flexural rigidity for the whole of Fennscandia from glacial rebound studies (Fjeldskaar and Cathles, 1991). It is, however, in accord with T_e estimates from forward stratigraphic modelling studies of the central and northern North Sea rifts (Kooi and Cloetingh, 1989; Thorne and Watts, 1989; Kooi et al., 1991; van Wees, 1994). There are other geophysical data that suggest a destabilisation of the lithosphere underneath southern Norway; these will be addressed in the next section.

I have calculated the isostatic response to erosion adopting constant T_e values of 10 and 20 km, using a 3 dimensional finite difference scheme (van Wees and Cloetingh, 1994). The predicted isostatic rebound has a much smoother pattern than the local isostatic case, reaching a maximum of ~700 m near the northwestern coastline (Figure 4-17). The magnitude of isostatic rebound is, however, not much smaller than for the local isostatic case, since the inferred flexural rigididity is not very large. Resulting tectonic uplift patterns are also shown in Figure 4-17; a model incorporating flexural rigidity shows an even better defined domal uplift pattern as the local isostatic case. Uplift is centred of the peaks of southern Norway and reaches a maximum of ~1500 m.

Figure 4-16. Results of coherence analysis for southern Norway. Dots indicate observed coherence for average wavenumber bands, bars denote 1σ errors. Continuous lines are the theoretical coherence functions for a ratio of surface to base loading of 1, labelled according to corresponding T_e (km).

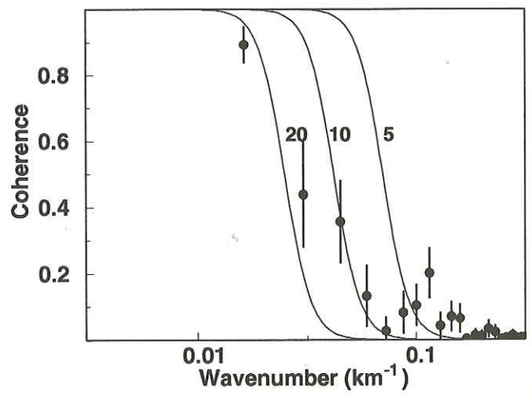

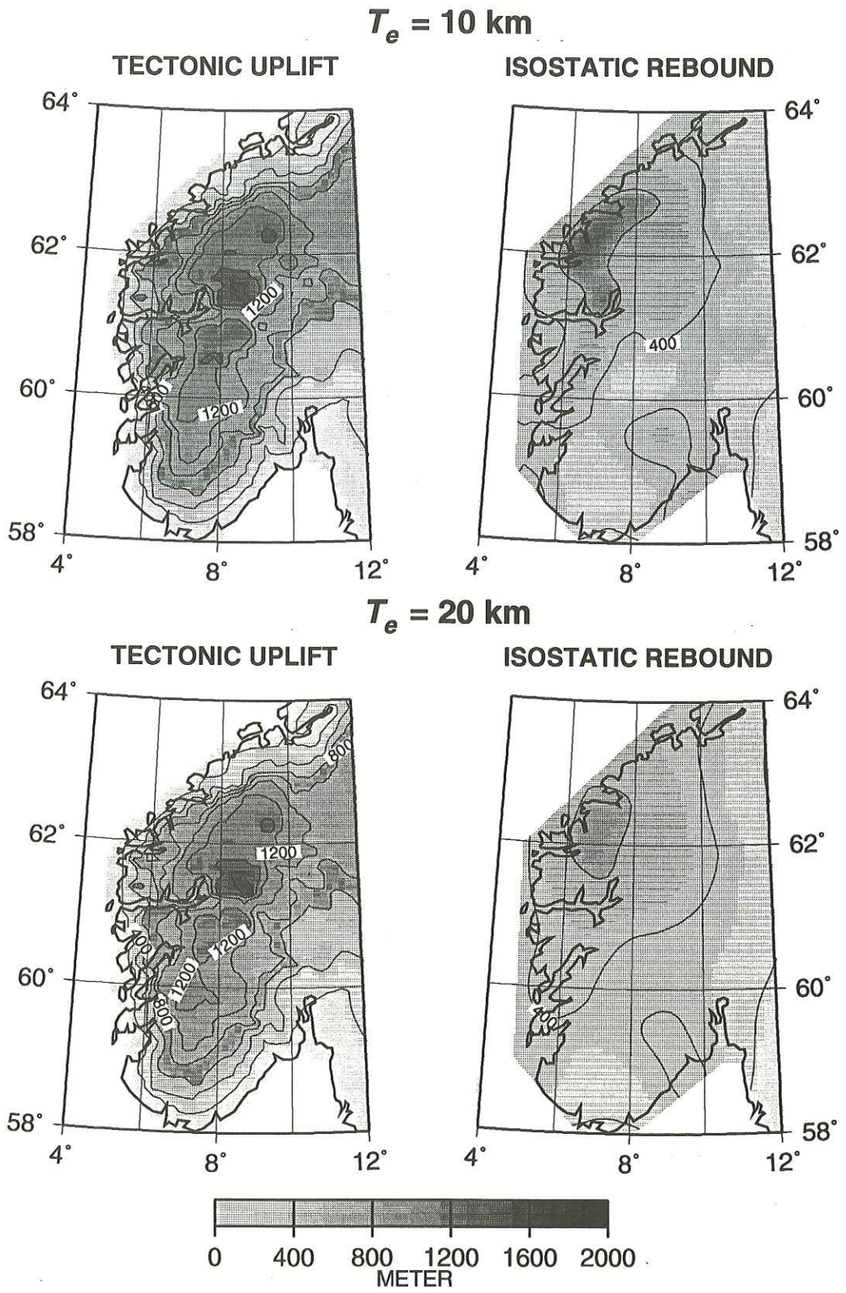

Figure 4-17 (facing page). Calculated tectonic uplift and isostatic rebound for a model of regional isostatic response to erosion and two constant flexural rigidities, corresponding to T_e = 10 km ($D = 8.9 \times 10^{21}$ Nm; top) and T_e = 20 km ($D = 7.1 \times 10^{22}$ Nm; bottom).

4.4.2 A comparison with other North Atlantic margins

In Section 4.2 it was noted that Neogene tectonic uplift in western Fennoscandia forms three distinct structural and topographic domes, one in southwestern Norway, one in northern Sweden and Finnmark, and one in the Barents Sea/Svalbard area. Tertiary uplift has been documented in other North Atlantic margins as well, and often appears to be associated with rapid subsidence in the bordering basins (Cloetingh et al., 1990; 1992b). Here, I will present a short review of 'uplift' studies around the North Atlantic. Since methods and terminology vary between different authors, a comparison between these results is not straightforward. In this discussion I will stick to the terminology outlined in Section 1.3.3.

Fission track data collected on- and off-shore Ireland (McCulloch, 1993) suggest two distinct exhumation events. During the middle Jurassic (160-180 Ma) 1-3 km of overburden was removed, followed by ≤2 km of erosion during the Early Tertiary (50-80 Ma). Surface and well samples from northern England record 2-3 km of erosion since 60-65 Ma (Lewis et al., 1992; Green et al., 1993). Early Tertiary tectonic uplift and erosion of the British Isles are generally associated with contemporaneous, widespread igneous activity throughout the North Atlantic (White and McKenzie, 1989) and possibly result from magmatic underplating (Brodie and White, 1994). However, Green et al. (1993) showed, from modelling of AFT length distributions in well samples, that exhumation is intermittent during the Tertiary, and that possibly >50% of it took place after 30 Ma.

In East Greenland, which constitutes the conjugate margin of mid Norway, deeply eroded Paleo-Mesozoic basins and uplifted Paleocene flood basalts, emplaced near sea level, indicate 1.5-2.5 km of post-eruptive uplift and erosion of this margin (Larsen, 1990; Christiansen et al., 1992). The fanning coastal dike complex of East Greenland, as well as the regional morphology, indicates a domal style of uplift (Brooks, 1985). AFT data suggest periods of rapid exhumation around 200 Ma and 35 Ma (Gleadow and Brooks, 1979; Hansen, 1992). The build-up of a large Late Oligocene-Recent offshore clastic wedge probably dates the initiation of uplift and erosion (Larsen, 1990). Uplift of East Greenland is thus roughly synchronous with (or slightly precedes) Norwegian uplift, but post-dates volcanism and continental break-up by at least 15 to 25 My

Uplift and erosion patterns in the Svalbard/Barents Sea area define a large asymmetric dome. Approximately 3 km of erosion is recorded on Svalbard, decreasing to 1-1.5 km in the SE Barents Sea (Wood et al., 1989). Maximum tectonic uplift on Svalbard is on the order of 1 km (Vågnes and Amundsen, 1993). The morphology of Svalbard again suggests a domal style of uplift, without reactivation of major fault zones. The timing of uplift is not well constrained: post-Eocene to pre-Pliocene. Wood et al. (1989) suggest that a major phase

of tectonic uplift took place during the Oligocene (30-35 Ma). On the other hand, tectono-stratigraphic modelling by Reemst et al. (1994) suggests that the stratigraphy of the Barents Sea basins can be explained by a Miocene (15 Ma) sea level drop combined with flexural uplift from the Pliocene (5 Ma) onward and Pleistocene (<2 Ma) glacial erosion.

Finally, the topography and inferred uplift patterns in northern Norway (Finnmark) and Sweden also define a structural dome (Riis and Fjeldskaar, 1992; Riis, 1995). Superimposed on this is the uplift of the Lofoten ridge, which probably originated as a Cretaceous rift flank (Brekke and Riis, 1987; Mokhtari and Pegrum, 1992). Uplift of northern Norway may have commenced as early as Paleocene (Riis, 1995). However, a thick Oligocene-Recent wedge has been encountered in the deeper offshore areas, whereas the Lofoten shelf was eroded during this time (Mokhtari and Pegrum, 1992), suggesting that also in this area a large part of the uplift and erosion is Neogene in age.

4.4.3 Models for uplift

Several mechanisms have been proposed to explain the Neogene uplift of western Fennoscandia and other North Atlantic margins (Figure 4-18). There are a number of critical geological and geophysical observations which should be incorporated into any model for it to be acceptable.

Geological constraints have been presented above: geomorphological, structural and seismic data indicate that tectonic uplift of western Fennoscandia, the Barents Sea and East Greenland was not associated with large fault displacements. The typical half wavelength of the domal uplifts is ~200 km, with a half amplitude of ~2 km. Uplift in areas around the

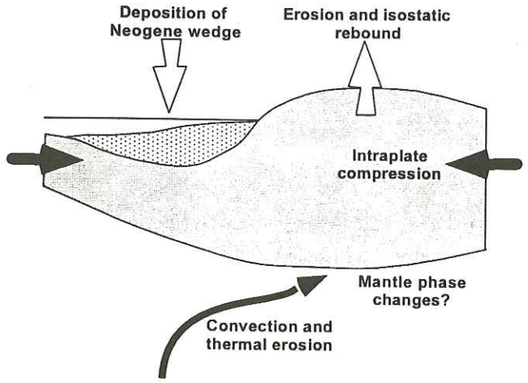

Figure 4-18. Cartoon showing the different factors that could contribute to domal uplift in southern Norway and other North Atlantic margins.

Figure 4-19. Bouguer gravity anomaly map for southern Norway, data from SGU (1985).

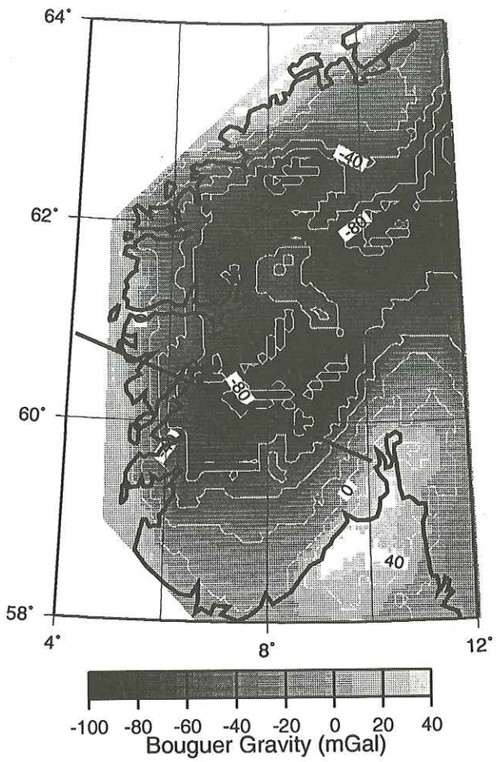

North Atlantic appears to be contemporaneous, being initiated at ~30±5 Ma. This timing coincides with a major phase of plate reorganization in the North Atlantic (Srivastava and Tapscott, 1986; Ziegler, 1988) but postdates initial break-up by 20-30 My and predates the onset of glaciations by the same amount of time. Tectonic uplift and erosion of the British Isles was initiated earlier and probably corresponds to Early Tertiary igneous activity.

Important geophysical constraints are provided by gravity and seismic tomography studies in western Fennoscandia. Both areas of domal uplift show strongly negative Bouguer gravity anomalies, down to -80 mGal in southern Norway and -100 mGal in the north (SGU, 1985; Figure 4-19). Although the anomaly pattern can be partly explained by variations in crustal thickness, residual isostatic anomalies of approximately -20 mGal in southwestern Norway and -40 mGal in Finnmark indicate a deeper compensation (Balling, 1980). Moreover, southern Norway shows a very different correlation between Moho depth and topography than the rest of Fennoscandia (Balling, 1980). An anomalous mantle structure and temperature underneath the domes is also indicated by locally reduced lithospheric P- and

S-wave velocities, down to -3%, which correlate with topography and gravity (Bannister et al., 1991).

During the past few years, there has been a debate as to what extent elevated areas record actual tectonic uplift or just isostatic response to increased erosion rates (e.g., England and Molnar, 1990; Molnar and England, 1990). In the case of western Fennoscandia, I have shown that even local isostatic rebound amounts to at most 1/3 of the observed Neogene uplift. This result supports earlier findings by Riis and Fjeldskaar (1992). Neither can uplift be a result of regional isostatic response to mass transfer by erosion onshore and redeposition offshore, as suggested by Doré (1992). Such a mechanism was shown to be responsible for ~130 m of Miocene-Recent uplift at the eastern US Atlantic margin (Pazzaglia and Gardner, 1994). Figure 4-20 shows the predicted flexural bulge before and after deposition of the Neogene wedge offshore southwestern Norway. The resulting differential uplift is of the order of tens, rather than hundreds, of meters. Thus, there must be an external, 'active' cause which generates the uplift.

Early models suggested that uplift of western Fennoscandia and other margins around the North Atlantic is associated with Paleocene break-up and plume activity (e.g., Torske, 1972). Such models, however, obviously predict a timing for uplift of the margins around the Norwegian-Greenland Sea that is not consistent with available geomorphological, sedimentological and thermochronological data. Moreover, dynamic plume generated uplift is transient and should reverse into subsidence 10-30 My after break-up. Permanent uplift can be generated by magmatic underplating (cf. Chapter 2) but there is no evidence for this below the Norwegian mainland; magmatic activity associated with break-up took place 300-400 km offshore (e.g., Skogseid et al., 1992).

Riis and Fjeldskaar (1992) suggest that the tectonic component of Fennoscandian uplift is driven by mantle phase changes resulting from erosional unloading. However, although the major phase of erosion and redeposition possibly occurred during the Pliocene and Quaternary, as indicated by sedimentological data (Section 4.2), this model cannot explain the initiation of uplift at ~30 Ma, well before the onset of glaciation. Moreover, the dynamics of mantle phase changes are poorly understood, so that it is presently impossible to validate or falsify such a model.

Two uplift models will be adressed in more detail here, because they seem to be consistent with at least part of the geological and geophysical observations. These mechanisms are intraplate compression and sub-lithospheric thermal erosion. The synchronous timing of margin uplift and anomalous basin subsidence around the North Atlantic could indicate that coupled uplift and subsidence is flexural in nature and is induced by intraplate stress fluctuations (Cloetingh et al., 1990, 1992b; Sales, 1992). Such a model explains the domal pattern of tectonic uplift and its synchroneity over a wide region. The onset of domal uplift in southern Norway is coincident with a Late Oligocene plate reorganization; another reorganization at ~5 Ma could have resulted in accelerated uplift rates (Cloetingh et al., 1990). The present-day stress field onland and offshore Fennoscandia is compressional and NW-SE oriented (Müller et al., 1992) which is generally attributed to a

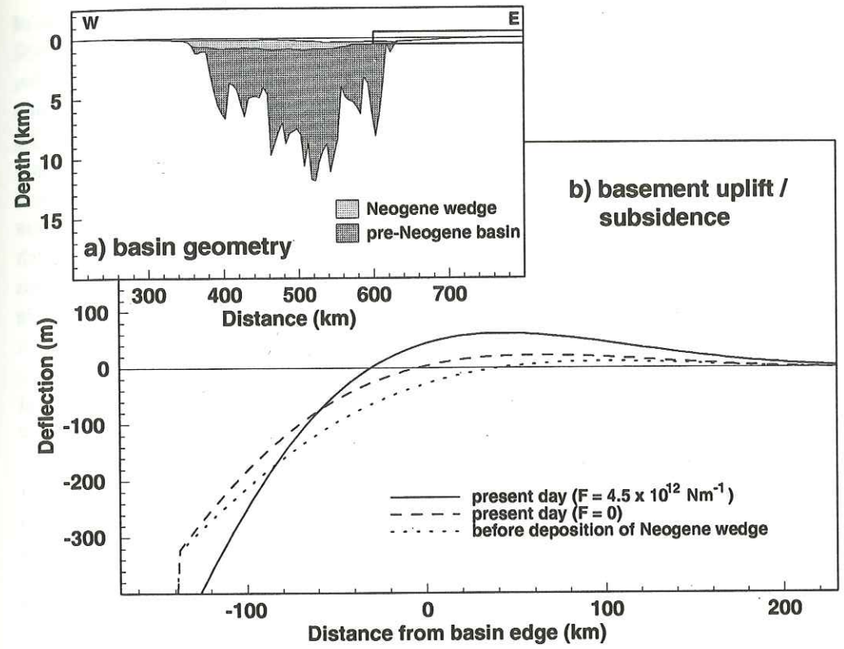

Figure 4-20. Predicted flexural bulge uplift resulting from deposition of the Neogene wedge and in-plane compression. The inset (a) shows the adopted basin geometry (after Odinsen et al., manuscript in prep.). The modelled profile (b) is a blow-up of the box in (a); its location is shown in Figure 4-19. Basement deflection has been calculated for a T_e controlled by the 400°C isotherm and an intraplate stress level of 1 GPa (compressional force $F = 4.5 \times 10^{12}$ Nm).

combination of mid-Atlantic ridge push forces and Alpine compression (e.g., Ziegler, 1988; 1990). However, flexurally induced uplift is not consistent with the observed correlation of uplifted regions with strongly negative Bouguer anomalies, as regional isostatic support of the uplift would be associated with positive anomalies (see also Chapter 2). The wavelength and amplitude of the compressional upwarp depends on the flexural rigidity of the lithosphere and the distribution of pre-existing vertical loads (Kooi, 1991; Kooi et al., 1991).

I have quantified the effect of intraplate compression, using the forward tectono-stratigraphic model of Odinsen et al.* for the section depicted in Figure 4-3 as a starting point. Figure 4-20 shows the predicted flexural bulge prior to deposition of the Neogene

* (Odinsen, T., Berge, A., Reemst, P.H.M. and van der Beek, P.A., Crustal structure across the northern North Sea: implications from tectono-stratigraphic modelling - in prep.)

wedge and at present, both with and without additional compression. In the model of Odinsen et al. the elastic thickness of the lithosphere is controlled by the depth to the 400°C isotherm, which implies $T_e \approx 45$ km onland. I employ an in-plane force of 4.5×10^{12} Nm, which corresponds to an intraplate stress level of 1 GPa for the flexural model adopted. Such a value is considered very high for continental lithosphere (cf. Cloetingh et al., 1989). The results indicate that, while the modelled wavelength of the deflection is close to that observed, the maximum amplitude of uplift in this case is <100 m, i.e. an order of magnitude smaller than observed. A late stage compression model does predict several hundred meters of additional subsidence offshore. This initial model employs a strong elastic plate, which tends to suppress the amount of flexural uplift. Larger amounts of uplift are predicted when adopting a lower T_e, more in keeping with the coherence analysis results (Figure 4-21). In this case, however, the predicted wavelengths of uplift are much too small, leading to maximum uplift at the offshore Horda Platform, instead of ~100 km inland.

Thus, it seems that late stage intraplate compression, which can have a profound effect on basin stratigraphy (e.g. Kooi and Cloetingh, 1989), is in itself incapable of explaining the large amplitude and long wavelength tectonic uplift patterns in western Fennoscandia. This is consistent with modelling predictions for uplift and erosion in the Barents Sea (Reemst et al., 1994), which suggest that Pliocene compression leads to <200 m of tectonic uplift. A 3D model of stress-induced flexure in the North Sea area (van Wees, 1994) also predicts <400 m of tectonic uplift for SW Norway. Larger amounts of uplift can only be generated by significantly larger in-plane forces (>10^{13} Nm), which are close to the buckling stresses of continental lithosphere (Cloetingh et al., 1989; Beekman, 1994).

A number of authors have proposed that Neogene uplift of western Fennoscandia is a result of thermal instability caused by large horizontal temperature gradients between the

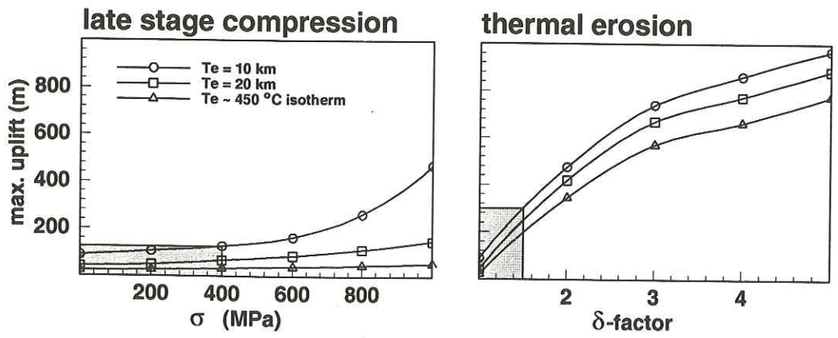

Figure 4-21. (a) Predicted maximum tectonic uplift for different flexural rigidities and different levels of intraplate compression σ; (b) different amounts of lithosperic thinning δ. The boxes in the lower left corners of both plots show approximate extent of reasonable parameter space.

Fennoscandian mainland and the Norwegian-Greenland Sea (e.g., Theilen and Meissner, 1979; Peulvast, 1985; Vågnes and Amundsen, 1993). This would set up secondary convection in the sub-lithospheric mantle (Keen, 1985; Buck, 1986; Fleitout et al., 1986), resulting in thermal erosion of the lithosphere underlying western Fennoscandia. A model of thermal uplift is consistent with the observed gravity and seismic velocity lows under the uplifted regions in Norway, as well as with the inferred anomalously low flexural rigidity. Xenolith thermobarometry and the occurrence of hot springs on Svalbard suggest an anomalously hot lithosphere there (Vågnes and Amundsen, 1993). In southern Norway, however, (sparse) heat flow data do not indicate an increased geothermal gradient (Balling, 1990). The model is also consistent with the inferred simultaneous uplift on both margins of the Norwegian-Greenland Sea, but why the uplift should be distributed into regional domes is not readily understood. Also, the timing of uplift with respect to break-up is not easily explained. Most models of small scale convection predict syn-rift flank uplift (e.g., Steckler, 1985; Buck, 1986), although models which include a basal heat flow boundary show delayed uplift (e.g., Keen, 1985; Stephenson et al., 1989). It is also possible that the convection pattern was not initiated by rifting and break-up itself, but by the arrival of the Iceland plume in the region, approximately 30-40 Ma ago (Brooks, 1985; Lawver and Müller, 1994). Indeed, geoid and bathymetry data suggest that the mantle underlying the Norwegian-Greenland Sea is anomalously hot (Cochran and Talwani, 1978). I have calculated the amount of uplift that is generated by a thermal dome with a half wavelength of 200 km (Figure 4-21). The results indicate that, for a finite-strength lithosphere, excessive lithospheric thinning ($\delta > 5$) is required to explain the observed amounts of uplift (compare Figure 2-5). Such amounts of lithospheric thermal erosion should have obvious surface expressions, such as extensive volcanism, which are not observed.

Thus, none of the mechanisms proposed above provide a satisfactory explanation for the observed uplift patterns. It is possible that I have overestimated the 'observed' Neogene

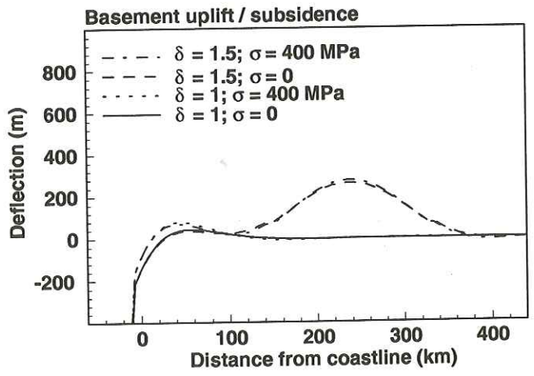

Figure 4-22. Predicted tectonic uplift pattern for a model with uplift caused both by thermal erosion (modelled by adopting a sinusoidal δ distribution with a half wavelength of 200 km and $\delta_{max} = 1.5$) and intraplate compression ($\sigma = 400$ MPa). $T_e = 15$ km.

uplift, by not taking into account possible pre-existing topography. If pre-Neogene topography existed in southern Norway, the correlation between the paleic surface and planation surfaces in Sweden, which were demonstrably at sea level, is incorrect. There is evidence from the fission track data that the correlation of surfaces may not be so straightforward (Section 4.3.1; see also Riis, 1995). However, a different correlation of planation surfaces would only affect the inferred timing of uplift, not the total amount.

Alternatively, one could speculate that both thermal erosion and intraplate compression played a role, the initiation of uplift at around 30 Ma being thermally induced, whereas amplification of uplift rates since 5 Ma was generated by intraplate stresses. Figure 4-22 shows an attempt to model such a scenario, adopting reasonable parameter values. As the wavelength of uplift is now controlled by the wavelength of anomalous mantle thinning, a low rigidity lithosphere can be adopted, maximising the amount of flexural uplift. However, such a model still fails to predict the observed amplitude of uplift. Note that the amount of flexural uplift is nearly negligible compared to thermal uplift. Therefore, the conclusion must be that the origin of (at least part of) the Neogene uplift of western Fennoscandia remains enigmatic.

CHAPTER 5

THERMAL AND MAGMATIC EVOLUTION OF A FAILED CONTINENTAL RIFT: THE OSLO GRABEN, SE NORWAY

5.1 INTRODUCTION

Thus far, the focus in this thesis has been mainly on vertical motions associated with rifting. These were studied by backstacking the amounts of erosion of rift flanks, using fission track thermochronology as a constraint. The implicit assumption in this approach is that the thermal structure of the crust during rifting is known. In Section 2.3.2 it was shown that pure-shear models of rifting predict very little thermal disturbance in the upper crust underlying rift flanks. In this chapter, I test these assumptions and model predictions, by looking at the thermal evolution of a specific continental rift in more detail.

The Permo-Carboniferous Oslo Graben in southeast Norway is particularly well suited for such a study. It is a failed continental rift which has not developed into a deep sedimentary basin. Post-rift sediments were either not deposited or have been removed by erosion; the syn-rift succession comprises mainly volcanics. Whereas conventional basin analysis techniques, based on investigation of the sedimentary record, can thus not be applied here, this situation does provide the possibility to directly sample the syn-rift structural, magmatic and sedimentary record of a failed rift system.

A remarkable feature of the Oslo Graben is its highly magmatic character. The rift preserves a ~3 km thick successsion of rift-related volcanics, and a significantly larger amount of magmatic intrusions (e.g., Neumann et al., 1986). The Oslo Graben has been compared to the present-day Kenya Rift in East Africa, in terms of the amounts and composition of magmatism involved (e.g., Ramberg and Larsen, 1978; Olaussen et al., 1995). The amount and composition of magma generated in extension depends on the amount of mantle upwelling, as well as the temperature and composition of the mantle (McKenzie and Bickle, 1988; Arndt and Christensen, 1992; Gallagher and Hawkesworth, 1992). Studying rift-related magmatism may thus provide an insight into deep seated rifting processes and mantle conditions (e.g, Wilson, 1993).

The Oslo Graben has been a classical area for studying intracontinental magmatism for more than a century, and a detailed picture has emerged on its syn-rift tectonic and magmatic evolution (e.g., Ramberg and Larsen, 1978; Ro et al., 1990a; Neumann et al., 1992). However, a major problem is presented by the amount of magmatism associated with the rift, which seems to be at least an order of magnitude larger than predicted by decompression melting models (e.g., McKenzie and Bickle, 1988). Also, very little is known about the post-

rift history of the area and, for instance, the question of why post-rift sediments are absent remains unresolved.

In the first part of this chapter, I present decompression melt modelling results obtained by Pedersen and van der Beek (1994), with the aim to better understand the processes which accompany melt generation in continental rifts. Subsequently, fission track data on apatites, zircons and sphenes from the Oslo Graben and surrounding areas are presented, in order to obtain a more complete picture of its syn- and post-rift thermal evolution. The high-temperature (200-300°C) zircon and sphene fission track systems provide details about maximum paleo-temperatures and the distribution of heat during and after rifting. Apatite fission track thermochronology, quantified by modelling of ages and track length distributions, records the post-rift cooling and erosional history of the area. In particular, I will address the dynamics (active versus passive asthenosphere involvement) and kinematics (simple versus pure shear; homogeneous versus depth-dependent stretching) of rifting, the roles of advective and conductive heat transport in establishing peak temperature conditions, the nature of the mantle underlying the rift, and the timing and amount of post-rift vertical motions.

5.2 Tectonic setting

The Oslo Rift consists of an onland part known as the Oslo Graben and its offshore continuation, the Skagerrak Graben (Figures 5-1, 5-2). The Oslo Graben is, itself, subdivided into two segments: the Akershus Graben segment (AGS) in the north and the southern Vestfold Graben segment (VGS). The rift system spans a total length of some 400 km, from the Fennoscandian border zone in the south to lake Mjøsa and the Caledonian deformation front in the north. Its present-day width is around 50 km; crustal thinning, reactivated basement faults and evidence of magmatic activity, however, occur over an area about 3 times as wide (Ramberg and Larsen, 1978; Ro et al., 1990a; Pallesen, 1993).

The rift developed within a high-grade Precambrian basement, which was metamorphosed during the Gothian (1750-1500 Ma) and Sveconorwegian (Grenvillian; 1200-950 Ma) orogenies (Verschure, 1985; Starmer, 1993). The basement consists of a number of terrains or tectonic blocks, which were accreted mainly during the Gothian orogeny (Starmer, 1993). The boundaries between these blocks constitute major shear zones, which later influenced the evolution of the rift (e.g., Ramberg and Larsen, 1978). Post-Sveconorwegian magmatic activity includes intrusion of massive I-type 'anorogenic' granites (e.g. Flå, Bohuslän) at ~850 Ma and development of the carbonatitic Fen complex at 540 Ma (Andersen and Taylor, 1988).

Within the Oslo Graben, Precambrian basement gneisses, Cambro-Silurian sediments and Permo-Carboniferous magmatic rocks (with minor sedimentary intercalations) are exposed (Figure 5-2). The lower half of the 2.5 km thick Cambro-Silurian succession consists of shallow marine platform sediments, whereas the upper part is dominated by Upper

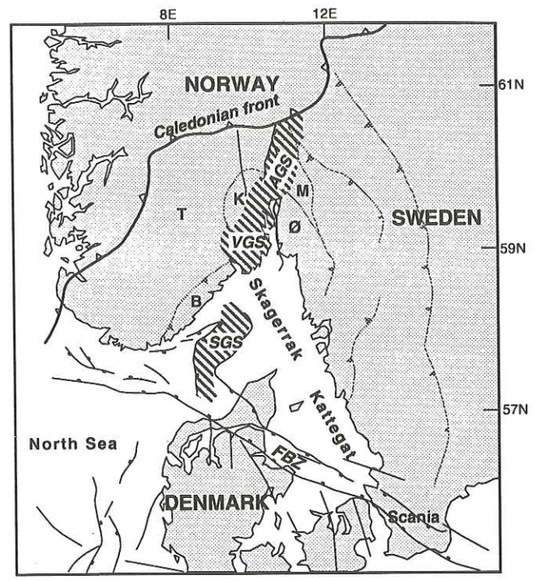

Figure 5-1. Simplified tectonic map of southern Norway, the Skagerrak area and the Fennoscandian Border Zone (modified from Ro et al., 1990b). Diagonal line pattern indicates extent of Oslo Rift; AGS, VGS and SGS denote Akershus, Vestfold and Skagerrak Graben Segments, respectively; FBZ = Fennoscandian Border Zone. Dark grey hachured lines are Proterozoic shear zones, delineating different tectonic blocks: T = Telemark, B = Bamble, K = Kongsberg, Ø = Østfold and M = Median Segment (Hedmark).

Silurian continental sandstones, deposited in a foreland basin setting (Bjørlykke, 1983). These sediments were deformed by folding and thin-skinned thrusting during the Caledonian Orogeny; the area was peneplained in the Devonian-Early Carboniferous. Unconformably above the Cambro-Silurian succession lie the alluvial and shallow marine sediments of the Upper Carboniferous Asker Group (Henningsmoen, 1978; Olaussen, 1981), which is conformably overlain by the Oslo Graben plateau lavas. The preservation of Lower Paleozoic sediments in fault blocks within the Oslo and Skagerrak grabens excludes the possibility of regional pre-rift uplift, while the Asker Group sediments indicate that the area was at sea level immediately prior to rifting.

Evolution of the rift

The Oslo Rift was active during the Late Carboniferous and Permian. Its evolution, within the late Variscan framework, of Europe is probably associated with late orogenic transtensional movements along the Fennoscandian Border Zone (Figure 5-1; e.g., Ziegler, 1990).

Rift-related magmatic activity started with the intrusion of syenitic sills and extrusion of plateau basalts ('B1'-lavas) at 305-295 Ma (Sundvoll et al., 1990, 1992). This incipient phase was followed by the extrusion of latitic ('rhomb porphyry'; RP) plateau lavas between 295 and 275 Ma. The maximum thickness of the volcanic succession is 3 km in the VGS and 1 km in the AGS. The presence of RP boulders in conglomerate fans associated with the border

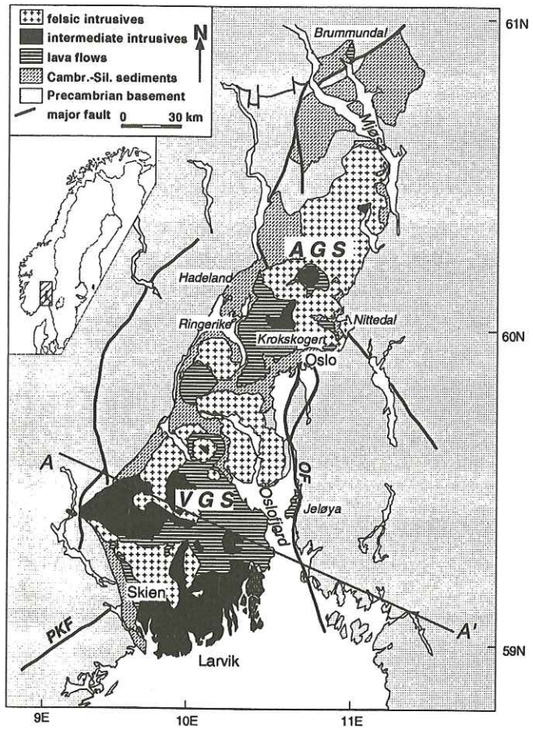

Figure 5-2. Simplified geological map of the Oslo Graben. VGS = Vestfold Graben Segment; AGS = Akershus Graben Segment; PKF = Porsgrunn-Kristianssand fault; OF = Oslofjorden fault. A-A' is the location of the transect of Figure 5-3. Based on Neumann et al. (1992); inset shows location within Scandinavia.

faults, as well as the occurrence of feeder dykes up to 50 km away from the rift, indicates that the initial area covered by RP lavas was much more extensive than at present (Ramberg and Larsen, 1978; Neumann et al., 1986; Olaussen et al., 1995). After 275 Ma, the magmatic style changed from extrusion of plateau lavas to caldera formation along (N)NW-(S)SE trends, followed by the intrusion of intermediate to granitic composite batholiths.

Extension is estimated to be initiated at ~290 Ma, coinciding with the main phase of RP volcanic activity (Sundvoll et al., 1990; Sundvoll and Larsen, 1994). ENE-WSW to EW extension, associated with the reactivation of Precambrian fault systems, created the three half graben segments, which have an alternating polarity (Sundvoll and Larsen, 1994; Olaussen et al., 1995). Vertical displacements along the eastern border fault of the VGS, the Oslofjorden fault zone, amount to 3 km in the south and decrease towards the north to 1-2 km (Ramberg and Larsen, 1978). The amount of upper crustal extension, as measured by faults and dykes, is 3-8 km (Ramberg and Larsen, 1978; Pallesen, 1993). Due to the large area (60-75%) of the Oslo Graben covered by magmatic rocks, these estimates are uncertain. However, the upper crustal extension (β) factor is definitely <1.1 for a 100 km wide rift zone. Seismic and gravity data (Ro et al., 1990a; Neumann et al, 1992) indicate that crustal thinning, corrected for

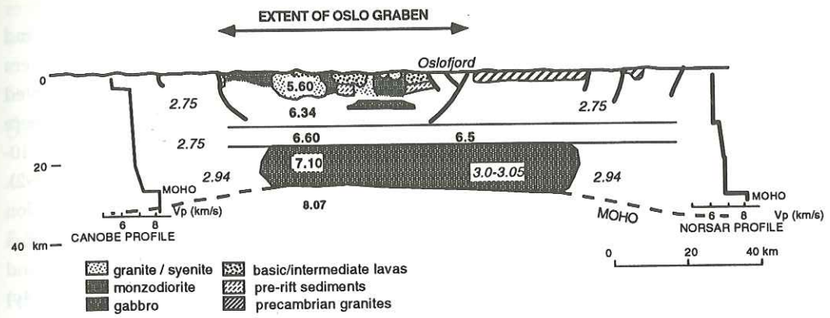

Figure 5-3. NW-SE crust/upper mantle transect across the Oslo Graben (A-A' in Figure 5-2). Modified from Neumann et al. (1992) and Ro and Faleide (1992). Italic numbers denote densities in gcm^{-3} (after Ramberg, 1976); bold numbers: P-wave velocities in kms^{-1} (Tryti and Sellevoll, 1977). Also shown are projected velocity/depth plots from the NE-SW CANOBE and NORSAR profiles, roughly perpendicular to the transect (mainly from Cassell et al., 1983; Kinck et al., 1991).

magmatic accretion, is substantially larger than this (Figure 5-3). In the SW part of the Oslo Graben, total crustal thinning amounts to some 30% (β = 1.3; Pallesen, 1993). Stretching factors for the offshore Skagerrak Graben are estimated at 1.4-1.6 (Pedersen et al., 1991; Ro and Faleide, 1992).

Syn-rift sediments in the Oslo Graben are restricted to intercalations between the lava flows and local fan-delta deposits associated with faulting (Henningsmoen, 1978; Olaussen et al., 1995). In the southeastern part of the graben, conglomerate fans exposed on small islands along the Oslofjorden fault attest of relative uplift and erosion of the eastern flank of the rift. The youngest sediments of the Oslo Graben stratigraphy are found in the Brummundal area, north of lake Mjøsa. Here, fluvial-aeolian sandstones of the Brummundal formation overlie the youngest RP lavas encountered in the Oslo Graben, which have a Rb-Sr age of 279±9 Ma (Sundvoll et al., 1990). At 240 Ma, after about 60 My of rifting activity, the geological record in the Oslo Graben ends; there are no indications of any post-rift sediments. Estimates of post-Permian erosion, based on inferred intrusion depths of currently exposed batholiths from petrological (e.g., Neumann et al., 1986) and fluid inclusion (Olsen and Griffin, 1984) studies, lie between 2-4 km.

The sedimentary record is more complete offshore; seismic reflection data (Ro et al., 1990b) have revealed 4 to 6 km of Cambro-Silurian sediments preserved in down-faulted blocks, and up to 1 km of probable syn-rift sediments along the border faults of the Skagerrak Graben. The fault blocks are tilted away from the centre of the graben and are truncated by a Lower Triassic unconformity. The overlying (post-rift) Triassic sequence thickens towards the south and is covered by a thin (<1 km) layer of Jurassic and Cretaceous sediments. There is no geophysical evidence for a significant degree of magmatic activity in the Skagerrak Graben, in marked contrast to the Oslo Graben (Neumann et al., 1992).

Magmatism

Oslo Graben magmatism took place during a number of well defined phases (Ramberg and Larsen, 1978; Neumann et al., 1992): sill intrusion; extrusion of plateau lavas; caldera formation; emplacement of granitoid batholiths. Magmatic activity started later and lasted longer in the AGS (295-240 Ma) than in the VGS (305-265 Ma; Sundvoll et al., 1990). There is a general tendency towards more felsic magmatism as rifting proceeds; during the final 10-20 My, mantle-derived melts did not reach the surface within the rift (Neumann et al., 1992). This suggests that the style of emplacement of mantle melts changed from surfaceal extrusion to underplating. As the lower crust is heated and partially melts, it gets difficult for magma to cross this 'molten barrier' (e.g., Fyfe, 1992). The short time scale of crustal melting and crystallization caused by cooling mafic bodies in the lower crust (not more than a few My) means that anatectic melting is unlikely to persist long after the supply of hot mafic melts has ceased. Thus, mantle melting probably continued during the entire 60 My life span of the rift. In the Precambrian areas adjacent to the Oslo Rift, mafic dykes with ages as young as 250 Ma have been reported (J.-P. Stiberg and G. Åberg, pers. commun., 1994).

Gravity modelling (Ramberg, 1976; Wessel and Husebye, 1987; Neumann et al., 1992) and seismic refraction experiments (Tryti and Sellevoll, 1977; Cassell et al., 1983; Kinck et al., 1991) reveal the presence of a ≥10 km thick, high-density (3000-3100 kgm^{-3}), high P-wave velocity (>7.1 kms^{-1}) body in the middle to lower crust (Figure 5-3). This is interpreted as a fossil rift 'pillow' consisting of gabbros, cumulates and anatectic residues (Neumann et al., 1986, 1992; Neumann, 1994). It extends outside the Oslo Graben proper and correlates with the total area affected by extension. Based on the petrogenetic modelling results of Neumann et al. (1986) and Neumann (1994), Pedersen and van der Beek (1994) estimate that 8-12 km of mantle-derived melts were produced during rifting, more than two thirds of which reside within the lower crust. This gives a total volume of $3\pm1\times10^5$ km^3 and an average production rate of 0.005 ± 0.002 km^3y^{-1}. Although these are only rough estimates, the total volume is ~10 times less, and the production rate 10^2-10^4 times smaller, than estimated values for magmatic regions believed to be associated with mantle plumes (e.g., Hawkesworth and Gallagher, 1993; Latin et al., 1993).

Isotope ratios of the most primitive alkali basalts indicate a mildly depleted mantle source region that was relatively rich in radiogenic Pb ($\varepsilon_{Nd} \approx +4$, $\varepsilon_{Sr} \approx -5$, $^{206}Pb/^{204}Pb \geq 19.2$; Neumann et al., 1988, 1990). REE patterns show a strong enrichment in incompatible elements (Neumann et al., 1990). Younger lavas become more tholeiitic in composition and show less extreme enrichment in LREE. Intermediate to silicic magmas indicate increasing contamination by lower and upper crustal reservoirs (Neumann et al., 1986, 1988, 1990). The primitive Oslo Graben rocks define a mildly depleted ε_{Nd} time trend with Proterozoic rocks in Southern Norway. Their source had apparently been stable beneath SE Norway for several hundred My, suggesting that it was located in the lower lithosphere (Neumann et al., 1990). Carbonate segregations and CO_2 inclusions in the basaltic rocks suggest that the mantle source region was volatile-bearing (Neumann et al., 1992; Neumann, 1994). Estimated extrusion temperatures for the primitive magmas are 1270-1340°C (Neumann, 1994), indicating normal to slightly increased mantle potential temperatures.

5.3 A MODEL FOR EXTENSION AND MAGMATISM IN THE OSLO GRABEN*

5.3.1 Introduction and modelling approach

From the above, a number of particular features of rift-related magmatism in the Oslo Graben arise: (1) an estimated thickness of 8-12 km of mantle-derived melts was formed during a period of 40-60 My; (2) at least the early melts were produced from a 'lithospheric' source, as shown by their isotopic and trace element compositions; (3) the mantle source region was probably volatile-bearing; (4) there is no evidence for regional pre-rift uplift; (5) extrusion temperatures indicate normal or only slightly elevated mantle potential temperatures and (6) upper crustal extension is typically ≤10%, whereas the total crust may have been thinned by ≥30%.

Rift-related magmatism is generally attributed to extension and upwelling of the mantle, resulting in adiabatic decompression and partial melting (e.g., Foucher et al., 1982; McKenzie and Bickle, 1988). An adiabatic decompression melting model for anhydrous mantle (McKenzie and Bickle, 1988) is in general agreement with observed oceanic crustal thicknesses and compositions (White et al., 1992). However, such a model makes a number of critical assumptions which make it less useful when applied to continental rifts. Firstly, the model assumes that extension is instantaneous and that decompression melting is an adiabatic process. This is a reasonable assumption for mid ocean ridges, where the mantle wells up rapidly to the surface. However, continental rifts may be active during significant periods of time, with magmatism taking place during different stages of their evolution (e.g., Ziegler, 1995). This implies that conductive cooling of the upwelling mantle should be taken into account. Pedersen and Ro (1992) showed that conductive cooling leads to a considerable decrease in the amount of magma produced, even for rift periods shorter than 10 My. Furthermore, since extension is infinite at mid ocean ridges, the distribution of thinning is uniform. This is not necessarily the case in continental rifts, where a complex interplay between initial conditions, crustal and mantle rheologies, strain rate and temperature may give rise to a variety of deformation patterns (e.g., Dunbar and Sawyer, 1989; Buck, 1991; Bassi et al., 1993). Finally, mid ocean ridge basalts are apparently produced from a nearly uniform, depleted mantle reservoir of anhydrous peridotite (McKenzie and O'Nions, 1991;

* This section is based on: Pedersen, T. and P.A. van der Beek, 1994. Extension and magmatism in the Oslo rift, southeast Norway: No sign of a mantle plume. *Earth Planet. Sci. Lett.* **123**, 317-329.

White et al., 1992). This is also in contrast with continental rifts, where the mantle source composition is more heterogeneous (e.g., Wilson, 1993). In particular, mafic rocks in many continental rifts are interpreted to have a lithospheric source (e.g., McKenzie and O'Nions, 1991; Gallagher and Hawkesworth, 1992; Hawkesworth and Gallagher, 1993) whereas, for a mantle with an anhydrous solidus, >95% of the melt is generated within the asthenosphere (McKenzie and Bickle, 1988; Arndt and Christensen, 1992). It is, therefore, not surprising that predictions of the essentially mid ocean ridge model have been difficult to reconcile with observations in continental rifts (e.g., Latin et al., 1990; Hendrie et al., 1993), with modellers often having to resort to excessively high mantle temperatures (e.g., White and McKenzie, 1989) and/or recycling of mantle material through the melting zone (Mutter et al., 1988; Latin et al., 1993) in order to predict sufficient amounts of melt.

For these reasons, Pedersen and Ro (1992) and Pedersen and van der Beek (1994) developed a more general model for continental rift magmatism, incorporating syn-rift conductive cooling in addition to adiabatic cooling, as well as depth-variable extension and mantle composition (Figure 5-4). The model is described in detail by Pedersen and van der Beek (1994); only a qualitative description will be given here. Initial temperatures in the mantle are calculated, following McKenzie and Bickle (1988), for a 100 km thick mechanical boundary layer (MBL) separated by a thermal boundary layer (TBL) from the convecting

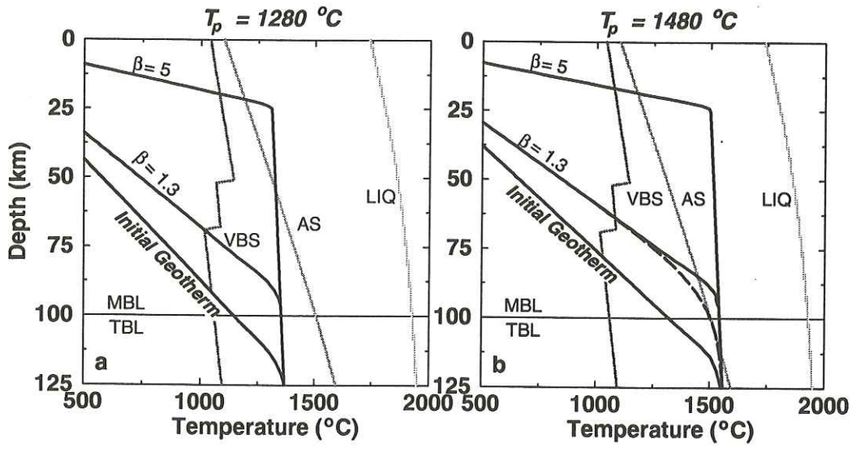

Figure 5-4. Decompression melting model. Steady state geotherms are calculated for a 100 km thick mechanical boundary layer (MBL) separated by a thermal boundary layer (TBL) from the convecting asthenosphere (viscosity: 4×10^{15} m^2s^{-1}), and potential temperatures (T_p) of (a) 1280 and (b) 1480°C. Also shown are the anhydrous (AS) and volatile-bearing (VBS) solidi and the liquidus (LIQ). Instantaneously stretched lithosphere crosses the solidus for high β factors, high T_p, and/or lower solidi (VBS instead of AS). The stippled line in (b) shows the effect of incorporating conductive cooling, for β = 1.3 and a 14 My extension duration.

asthenosphere. Lithospheric extension is assumed to occur by constant horizontal strain rate (pure shear), the upwelling velocity is calculated from the principle of incompressibility (e.g., England, 1983; Buck et al., 1988). The thermal evolution of the upwelling mantle column is tracked by numerical integration of the (1D) heat equation, incorporating advection and conduction. The local melt fraction $F_{(T)}$ is derived from analytical parameterisations of laboratory experiments for anhydrous peridotite (McKenzie and Bickle, 1988) and fluid-absent, volatile-bearing peridotite containing 0.4% H_2O and 0.7% CO_2 in amphibole (Gallagher and Hawkesworth, 1992; cf. Figure 5-4). Finally, integration of F over the thickness of the melting region (Foucher et al., 1982) yields the time-dependent melt thickness, which will be plotted in the consecutive figures.

The effect of syn-tectonic conductive cooling is exemplified in Figure 5-4(b), which shows the temperature after instantaneous stretching (β=1.3) of a lithosphere with potential temperatures (T_p*) of 1280 and 1480°C. For T_p = 1480°C, the anhydrous solidus is overstepped if extension is instantaneous (the temperature reduction due to latent heat is not illustrated). If, however, cooling during a 14 My rift period is incorporated, the anhydrous solidus is not crossed. Conductive cooling is largest in the TBL and substantially reduces the amount of melt that can be produced in this region. The temperature, and hence amount of partial melting, within the MBL is much less reduced.

5.3.2 Modelling results

Figure 5-5 illustrates the amount of magma produced by uniform extension of the lithosphere for a continental rift with β = 1.3. For an anhydrous lithosphere (Figure 5-5(a)), melt can only be produced for short rifting times (<15 My) and high T_p (1480°C). Clearly, if lithospheric extension in the Oslo Graben was uniform (β ≤ 1.3) no melt would be generated for an anhydrous lithosphere. Figure 5-5(b) shows the produced melt thickness assuming uniform extension (β = 1.3) and various T_p, for a model with volatile-bearing MBL. Again, insufficient melt is produced, regardless of T_p. Note that for high T_p, a significant portion of the melt is produced from the sub-lithospheric mantle (peak in T_p = 1480°C curve). A high potential temperature is implausible in the Oslo Graben, because of the lack of evidence for pre-rift uplift and the relatively low inferred extrusion temperatures. Moreover, a high T_p and a large contribution from the sub-lithospheric mantle to the melts produced would lead to strongly depleted tholeiitic magmatism, whereas the observed initial magmatism is only very slightly depleted and alkaline in nature. Consequently, uniform extension cannot explain the observed volumes of mantle-derived magma in the Oslo Graben, even for a volatile reduced solidus.

* The potential temperature is defined as the (extrapolated) surface intersection of the adiabatic temperature gradient in the asthenosphere (McKenzie and Bickle, 1988)

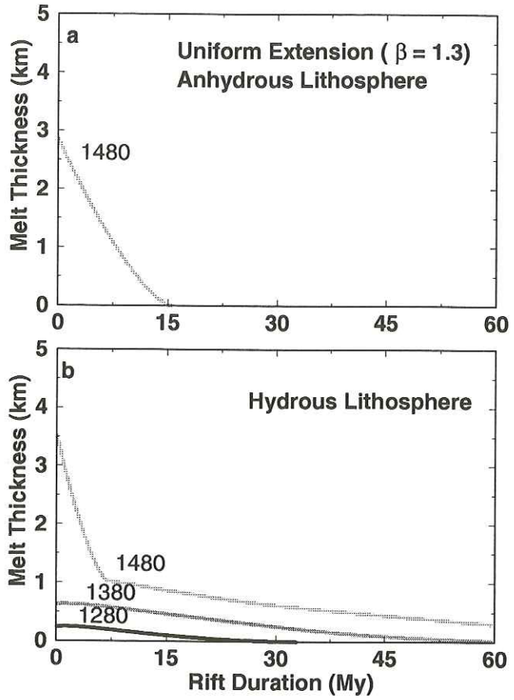

Figure 5-5. Melt thickness as a function of rift duration for uniform extension (β = 1.3), different T_p and an anhydrous (a) or volatile bearing (b) MBL. For anhydrous lithosphere, melt is only generated if T_p = 1480°C, for volatile-bearing MBL also for lower T_p (labelled on curves).

Depth-variable extension of a volatile-bearing lithospheric source was subsequently tested (Figure 5-6). Sub-crustal stretching factors (δ) exert a strong control on the amount of magma produced, especially for short rifting periods. However, it is still not possible to produce the required amount of melt for a rift duration longer than ~20 My, however large the thinning factor. Even for infinite δ the amount of melt produced is limited by the ~20 km post-rift crustal thickness in the Oslo Graben (β ≤ 1.3).

Therefore, the 'volatile-bearing' model with an anhydrous TBL neither seems capable of predicting the inferred amount of melt. There are three possible explanations for this discrepancy. Firstly, not only the MBL but also (at least the upper part of) the TBL may have been volatile-bearing, with a correspondingly reduced solidus. This assumption has the consequence that, even in the absence of major extension, several kilometres of melt can be generated by slightly raising the mantle temperature. Such a model (Figure 5-7) predicts the inferred amounts of melt within the time span estimated for the Oslo Graben, if depth-variable thinning and slightly increased potential temperatures are adopted. However, geotherms which cross the pre-rift solidus cannot represent steady state conditions (Gallagher and

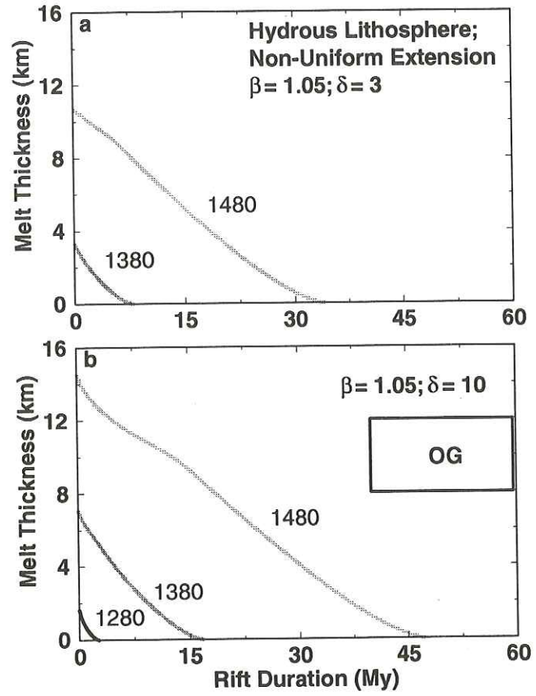

Figure 5-6. Melt thickness as a function of rift duration for volatile bearing MBL; non-uniform thinning with β = 1.05 and (a) δ = 3; (b) δ = 10. Curves are labelled according to potential temperature. Box labelled OG indicates estimated duration of rifting and melt thickness for the Oslo Graben.

Hawkesworth, 1992; Anderson, 1994). In this respect, it is interesting to note that early mantle-derived magmatism in the Oslo Graben slightly predates surfacial extension (cf.

Figure 5-7. Melt thickness as a function of rift duration for a hydrous lithosphere (both MBL and TBL characterised by volatile-bearing solidus). Results are shown for uniform thinning (β = 1.05) and T_p = 1480°C as well as non-uniform thinning (β = 1.05; δ = 3) and T_p = 1380°C. Note the generation of several km of melt without any significant stretching for increased mantle temperatures.

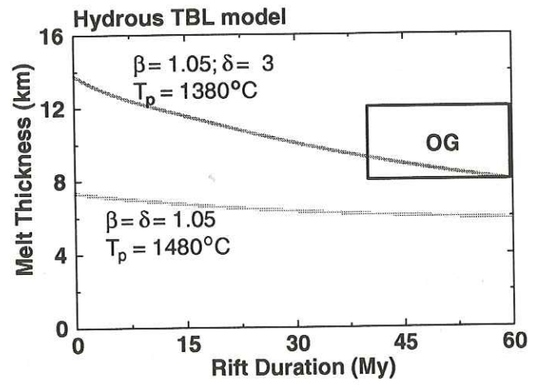

Section 5.2). Thus, it is possible that magmatism was triggered by a small thermal disturbance in the lower lithosphere (TBL).

Secondly, the pre-rift thickness of the lithosphere (MBL) may be different than was assumed in the calculations. An MBL thickness of 100 km leads to a minimum estimate for the amount of lithosphere derived melts for adiabatic upwelling (Gallagher and Hawkesworth, 1992). This is because there is a competing effect of lowering the geotherm but expanding the magma source region with increasing MBL. However, Pedersen and van der Beek (1994) showed that this effect is much reduced for finite duration extension. A model with thin MBL (70 km) can generate several km of melt (mostly from an asthenospheric source) for short rifting times. For a rift duration >15-20 My, however, no melt is generated. Moreover, such a model is not consistent with the isotope data which suggest a lithospheric source for the primitive melts. A thicker lithosphere (130 km) makes it possible to generate melts for longer time periods, but here low temperatures hamper the production of >5 km of melt for any time span of rifting.

Finally, the 'volatile-bearing' model may still underestimate the amount of lithosphere derived melts; the lithosphere may be locally more fertile than assumed in the parameterisation because of either higher Fe/Mg ratios (e.g., Wilson, 1993) or higher fluid contents, resulting from strong metasomation (Latin et al., 1990). The present experimental data, however, do not allow a quantitative assessment of these concepts.

The modelling presented here demonstrates some of the complexities in the study of continental rift magmatism. Syn-rift conductive cooling dramatically reduces the amount of melt that can be produced by mantle decompression. Allowing for depth variable mantle composition and thinning has the consequence that observed melt thicknesses alone cannot be used to uniquely infer the thermal state of the lithosphere prior to or during rifting. Combining melt volume modelling with independent information, in particular geochemical data, seems required to arrive at a better understanding of rift dynamics. However, the advantage of geochemical modelling (e.g., McKenzie and O'Nions, 1991; Latin et al., 1993) may be limited in continental rifts where the vast majority of magmatic rocks are either modified by crustal contamination and fractionation processes, or reside within the lower crust.

Nevertheless, incorporating the petrological, geophysical and field data discussed in Section 5.2, the models do provide some constraints on the processes accompanying magmatism in the Oslo Graben. The essentially mid ocean ridge model of decompression melting (Foucher et al., 1982; McKenzie and Bickle, 1988) does not apply to the Oslo Graben. Lithospheric extension was neither instantaneous nor uniform, as it effectively is at mid ocean ridges. Moreover, the mantle source composition adopted by this model seems different from that which produced the Oslo Graben magmas. The stretching observed at the surface (≤10%) is by far too low to yield the degree of mantle thinning necessary to produce the observed amount of decompression melts, regardless of mantle composition. Consequently, lithospheric thinning in the Oslo Graben must have been non-uniform. Although magmatism could have been triggered by a slight temperature disturbance in the lower lithosphere, mantle temperatures during rifting cannot have been excessively high; magmatism in the Oslo Graben is more the consequence of a 'wet' than a 'hot' mantle (see also Neumann, 1994).

5.4 Thermal evolution of the Oslo Graben from fission track thermochronology*

Samples for fission track analysis were collected along three roughly EW profiles perpendicular to the rift axis, from the rift itself as well as the different Precambrian tectonic blocks surrounding it (Figure 5-8). Samples comprise Precambrian basement rocks, Permian extrusives and intrusives as well as Ordovician and Silurian sediments (cf. Table A2-4). Sample processing details are given in Appendix 2. All FT ages will be reported as central ages (Galbraith and Laslett, 1993) with ±1σ standard errors.

5.3.1 Fission track results

Apatite

Apatite fission track (AFT) results are summarised in Table 5-1; analytical data are given in Table A3-4 (Appendix 3). Ages range from 112±16 to 283±40 Ma, are continuous between the Graben and surrounding areas and generally become younger towards the northwest (Figure 5-8). AFT ages show no clear correlation with elevation. The variation in ages for samples from similar elevations suggests long residence times in the patial annealing zone. Practically all samples have mean lengths between 12 and 14 μm (Table 5-1; Figure 5-8). The track length distributions are relatively narrow, with standard deviations <1.5 μm for most samples; none have standard deviations >2 μm. These narrow distributions result from a conspicuous lack of very short (<11 μm) and long (>14 μm) tracks.

A pilot study in the southwestern, low-elevation (<300 m), Bamble sector by van Haren and Rohrman (1988) revealed AFT ages between 195±17 and 256±31 Ma, with mean lengths between 12.0-12.9 μm and standard deviations between 1.1 and 1.5 μm. Additional samples collected for this study confirm these results. Samples with relatively high Cl contents, such as TN250 and DL129 (Cl/(F+Cl) ≈ 0.6-0.8; T.G. Nijland, pers. commun., 1993) show ages similar to samples with more normal Cl/(F+Cl) ratios of <0.2; their mean track lengths are slightly longer, due to the higher resistance of Cl-rich apatites to annealing. The boundary between Bamble and the adjacent Telemark sector is formed by the Porsgrunn-Kristiansand fault zone, a Precambrian shear zone which was repeatedly reactivated. As AFT

* This section is based on: Rohrman, M., van der Beek, P.A. and Andriessen, P.A.M., 1994. Syn-rift thermal structure and post-rift evolution of the Oslo Rift (southeast Norway): New constraints from fission track thermochronology. *Earth Planet. Sci. Lett.* **127**, 39-54.

Table 5-1. Apatite fission track results for the Oslo Graben

sample	elev. (m)	number of grains	age ±1σ (Ma)	D (%)	mean track length (µm)	st.dev. (µm)	number of tracks
Bamble							
B9	100	10	218±27	11	13.3±0.1	1.0	100
DL129		15	237±28	13	12.9±0.2	1.5	100
TN250		20	240±21	10	13.3±0.1	1.0	100
Telemark							
T3	180	13	238±23	13	12.5±0.1	1.2	100
T8	680	14	160±19	27	12.9±0.2	1.5	98
T14	400	11	163±15	18	12.6±0.2	1.4	128
T15[A]	1000	15	132±20	32	13.1±0.2	1.5	40
T17	200	18	141±11	14	12.6±0.2	1.6	100
Kongsberg							
K1	100	14	208±19	12	12.7±0.2	1.6	100
K5	340	13	112±16	27			
K9	900	15	194±27	31			
K11					13.4±0.1	1.1	100
Østfold							
Ø2	0	23	165±20	40	12.2±0.1	1.3	100
Ø3	0	21	219±33	12	13.8±0.2	1.2	60
Ø6	140	14	177±22	13	12.9±0.1	1.3	100
Ø7	100	20	204±26	14	13.6±0.2	2.0	100
Ø10	120	19	215±24	14	14.2±0.1	0.8	100
Ø12	70	12	194±16	11			
Ø14	10				12.7±0.1	1.0	101
Median segment (Hedmark)							
M1	200				12.8±0.2	1.2	40
M2	330	19	283±40	11			
M5	200	20	222±30	10	13.3±0.2	1.7	80
M6	320	20	179±15	11	13.8±0.2	1.5	100
M7	280	20	204±26	14	13.9±0.1	1.4	100
Vestfold Graben Segment							
OR9	100	23	162±12	12	13.8±0.1	0.9	110
OR14	0	13	192±15	14	12.3±0.1	1.4	100
OR15	0	18	225±23	11			
OR22	0	16	186±15	14	12.2±0.2	1.3	31
OR45	0	18	185±20	15	13.2±0.1	1.6	160
OR46	0	16	179±16	14	13.5±0.1	1.2	100
OR52	0	20	184±16	8	13.4±0.1	1.2	100
OR53	70	20	194±22	12	13.3±0.2	1.4	90
OR54	40	14	186±20	10			

Table 5-1 (continued)

sample	elev. (m)	number of grains	age ±1σ (Ma)	D (%)	mean track length (µm)	st.dev. (µm)	number of tracks
Akershus Graben Segment							
OR11	140	11	215±24	10	13.3±0.1	1.1	100
OR20	340	13	179±21	14	13.7±0.2	1.1	110
OR26	500	23	189±24	19			
OR27	590	12	131±32	13			
OR28	400	12	170±20	13	12.4±0.1	1.4	100
OR32	250	18	181±18	13	13.4±0.1	1.2	100
OR33	280	20	201±24	24			
OR38	320	23	136±14	32			
OR39	300	10	169±16	15	13.3±0.1	1.3	200
OR47	680				13.5±0.1	1.3	100
OR49	700	16	182±21	12	13.2±0.1	1.3	100

ages do not vary across this fault zone, it has not been active (to an amount detectable by AFT thermochronology) since the Permian.

AFT samples from the Kongsberg and Telemark sectors, with elevations between 300 and 1000 m, have overall younger ages (112±16 - 238±23 Ma) than those from Bamble. There is, again, no age difference across the fault separating the Kongsberg and Telemark sectors. Track lengths vary between 12.5 and 13.4 µm and standard deviations between 1.1 and 1.6 µm, track length distribution are symmetrical or slightly negatively skewed.

AFT ages on the eastern flank of the Oslo Rift, in the Østfold and Median sectors, are the oldest encountered in the study area, with ages of 177±22 to 283±40 Ma. Elevations here are lower than 150 m. Mean track lengths are slightly longer than in the west, varying between 12.2 and 14.2 µm, with standard deviations of 0.8-1.7 µm. Track length distributions are negatively skewed. The Triassic AFT ages of these samples agree with results from further east in Sweden, where ages around 220 Ma, with mean lengths of 12.9-14.0 µm, were reported (Zeck et al., 1988). Samples from within or near the eastern border fault of the Oslo Graben (Ø3, M2), have relatively old ages (219±33 - 283±40 Ma) and long mean lengths (13.8 µm; σ = 1.2 µm), suggesting that relatively low temperatures prevailed within the fault system during and after rifting.

The analysed pre-rift sediments in the Oslo Graben (OR11, 15, 22) all belong to the Upper Silurian Ringerike group. AFT ages lie between 186±15 and 225±23 Ma; track length distributions are similar to those from the Precambrian regions (mean length 12.2-13.3 µm; standard deviation 1.1-1.3 µm). The age of OR15 (225±23 Ma) is the oldest encountered in the Oslo Graben, again suggesting cooler conditions near the Oslofjorden fault.

Most of the rocks sampled in the Oslo Graben are Permian extrusives, from different stratigraphic levels. As a result of block faulting during rifting, all samples are now at

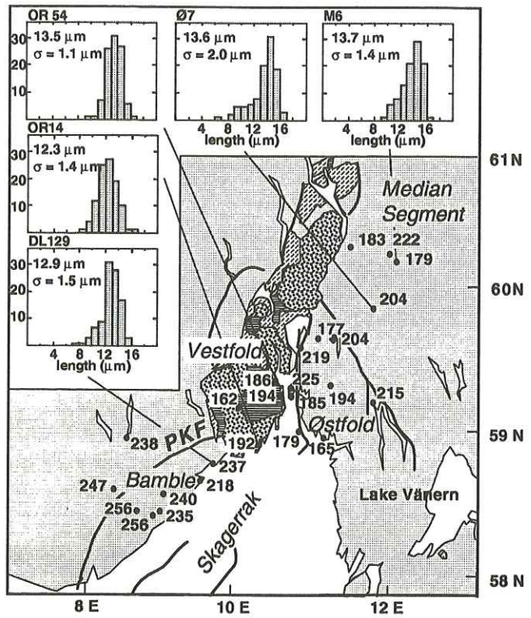

Figure 5-8(a). Apatite fission track results from Bamble, Østfold, the Median Segment (Hedmark) and the Vestfold Graben Segment, plotted onto a simplified geological map of the region (for legend see Figure 5-8(b)). Numbers indicate apatite fission track ages, track length distributions are given for selected samples. Samples from the southern Bamble block are from van Haren and Rohrman (1988).

approximately the same elevation (0 - 100 m). Rb-Sr ages for the lavas lie between 295 and 275 Ma (Sundvoll et al., 1990). Samples from the southwestern Vestfold lava plateau (OR9, 53, 54), the central Krokskogen plateau (OR32, 47) and from the lavas on Jeløya and surrounding islands in the southeast (OR45, 52) show similar results: all sampled extrusives from the rift have AFT ages in the range 162±12 - 194±22 Ma, with mean lengths around 13.4 µm. Track length distributions are typically narrow (σ = 0.9-1.3 µm) and slightly negatively skewed. The AFT ages are clearly discordant with Rb-Sr ages, while track lengths are significantly shorter than those in rapidly cooled volcanics (~14.5 µm, Gleadow et al., 1986). This implies complete annealing of the RP lavas following initial burial, which is also indicated by the growth of laumontites in vesicles of the lower lava flows (B.T. Larsen, pers. commun., 1991).

An AFT sample (OR38) from the Brummunddal sandstone, the stratigraphically highest level in the volcanic-sedimentary succession, yields an AFT age of 136±14 Ma, with $P(\chi^2) \ll 1$. The AFT age of intercalated lavas (OR39) is similar to that of the other RP lavas in the rift (169±16 Ma). These ages also support complete annealing since deposition of the syn-rift sediments in the Oslo Graben.

Permian intrusives in the Oslo Graben (OR14, 26, 28, 33) vary in AFT age between 170±20 and 192±15 Ma, mean track lengths are 12.3-12.4 µm (σ = 1.4 µm). These samples

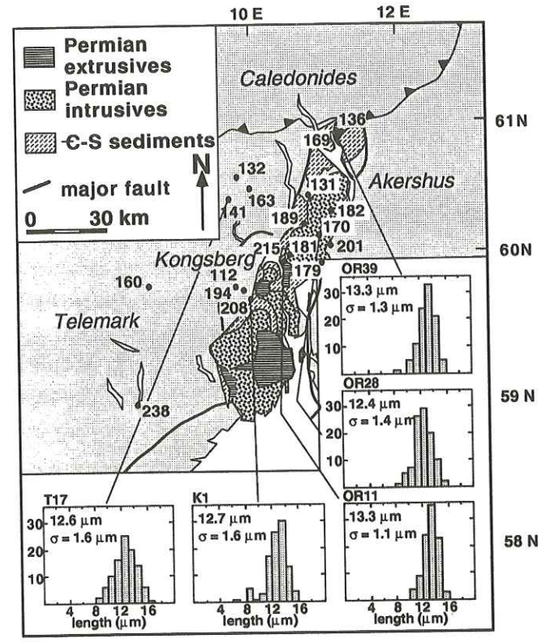

Figure 5-8(b). As Figure 5-8(a) for samples from Telemark, Kongsberg and the Akershus Graben Segment.

have similar AFT ages and track length distributions as the basement rocks immediately adjacent to the graben.

Zircon

Zircon fission track (ZFT) ages were determined for eight samples; results are summarised in Table 5-2 and depicted in Figures 5-9 and 5-10. Analytical data are given in Table A3-5 (Appendix 3). Only two samples from Precambrian basement outside the rift could be dated, other samples appeared metamict after etching. These two samples (T18 and M2) give very old ages of 600±65 Ma and 634±72 Ma, respectively (Figure 5-9(b,c)), with little age dispersion. Although both these samples were taken at distances of less than 1 km from the border faults of the rift, their ages indicate that they have not been affected by a Permian thermal overprint.

Within the Oslo Graben, four samples were taken from pre-rift sediments. Two of them (OR6 and 16) belong to the Langøyene formation, which has an Ashgillian (440-435 Ma) stratigraphic age (Owen et al., 1990). OR16 has a ZFT age of 520±59 Ma; most of the single grain ages are older than the stratigraphic age, suggesting that the sample has experienced minor partial annealing since deposition. The location of the zircon partial annealing zone (PAZ) is much less constrained than that of apatite. If I adopt a zircon PAZ between 170-

240°C (cf. Zaun and Wagner, 1985; Hurford, 1991, Jacobs et al., 1993) the ZFT data indicate that paleo-temperatures for OR16 have probably always been below 200°C. As the early Paleozoic sediments have also been buried during Silurian foreland basin development, it is difficult to estimate the temperature disturbance as a result of Permian rifting. OR6, however, has a post-rift Triassic age of 226±24 Ma, suggesting complete annealing and temperatures in excess of 240°C around that time. Two samples (OR11, 22) of the Ringerike sandstones (stratigraphic age Wenlockian-Ludlowian, i.e. 425-410 Ma; Worsley et al., 1983) also show discordant ZFT ages. OR11 fails the χ^2 test, single grain ages show a large dispersion (52%; Figure 5-9(d)). The fact that single grain ages both older and younger than the stratigraphic age are observed suggests partial annealing. The maximum temperature of this sample probably never significantly exceeded 200°C. OR22 has an age of 272±32 Ma, displaying much less age dispersion. No single grain ages older than depositional ages were encountered (Figure 5-9(e)), implying total annealing and maximum temperatures near the base of a zircon PAZ. This ZFT age is indicative of cooling since a Permian (syn-rift) heating event.

Two Permian samples were analysed, a rhyolite tuff from the Nittedal caldera (OR20) and a gabbro plug from Hadeland (OR26). Rb-Sr ages for these rocks are ~265±10 Ma (Sundvoll et al., 1990). Both show post-rift ZFT ages of 181±20 Ma and 205±23 Ma, respectively (Figure 5-9(f)). These ages indicate almost total annealing and temperatures near the base of the zircon ZFT prevailing into the Triassic, i.e. long after rifting activity in the Oslo Graben had ceased.

Table 5-2. Zircon and sphene fission track results for the Oslo Graben

sample	elev. (m)	number of grains	age ±1σ (Ma)	D (%)
Zircon				
T18	400	10	600±65	10
M2	330	10	634±72	9
OR6	0	14	226±24	11
OR11	140	15	378±62	52
OR16	0	12	520±59	8
OR20	340	10	181±20	13
OR22	0	10	272±34	10
OR26	500	11	205±23	7
Sphene				
T3	180	5	543±78	9
OR28	400	10	241±26	11

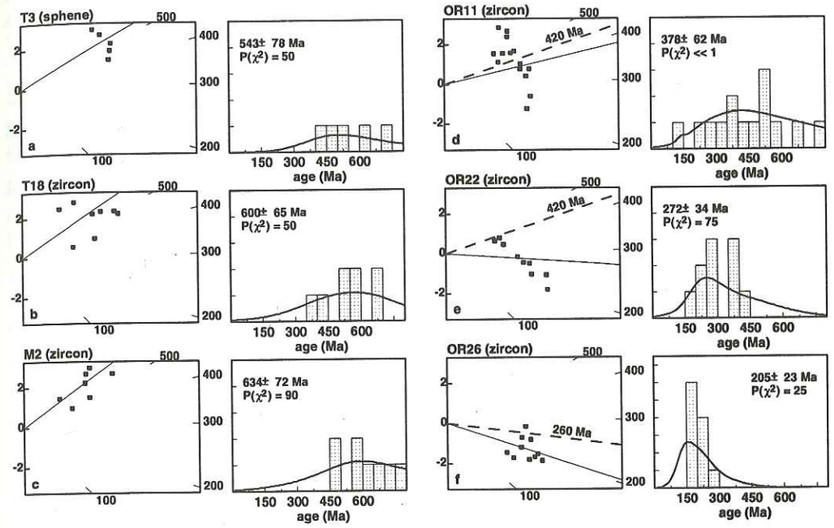

Figure 5-9. ZFT and SFT results for representative samples. Single grain age distributions are plotted in a radial plot (Galbraith, 1990) and as age histograms and probability curves; radial plots are aligned at 300 Ma (onset of rifting). Thin continuous lines denote sample ages; dashed lines in (d), (e) and (f) are depositional/intrusion ages.

Sphene

Sphene fission track (SFT) ages for a Precambrian and a Permian sample are listed in Table 5-2. Five additional SFT ages from the Bamble sector were reported by Rohrman et al. (1994). Samples from the Bamble sector and the adjacent part of Telemark have SFT ages of 484±44 - 693±69 Ma, similar to those reported at lake Vänern, Sweden (Zeck et al., 1988). At present, only the effective retention (i.e. total annealing) temperature for sphene is known with some confidence. Here, I adopt a total annealing temperature of 300°C (Gleadow and Brooks, 1979; Jacobs et al., 1993). The old (~600 Ma) SFT ages indicate, in accordance with ZFT results, that the flanks of the Oslo Rift have not experienced thermal resetting associated with Permo-Carboniferous rifting.

Sample OR28 is taken from a late Permian syenite in the AGS (Figure 5-10). Its Rb-Sr age is 248±4 Ma (Sundvoll et al., 1990), making it one of the youngest intrusions within the rift zone. The SFT age is concordant, at 241±26 Ma, indicating that the pluton cooled to temperatures <300°C immediately after intrusion.

5.3.2 Interpretation of fission track data

Syn-rift thermal evolution

The ZFT and SFT data indicate that rocks within the Oslo Graben have experienced temperatures up to the zircon PAZ (~ 170-240°C). The maximum temperature and the timing of heating, however, vary strongly between different localities. The presence of laumontite within vesicles of the lower lava flows of the VGS, and the absence of regional greenschist facies metamorphism (Bryhni and Brastad, 1980), limits the absolute temperature maximum for the currently exposed rift to <300°C. Peak temperatures prevailed during the syn-rift and early post-rift phases (~ 270-180 Ma). A possible older (~ 400 Ma) event, caused by Silurian burial in a foreland basin setting (Bjørlykke, 1983), remains obscured as a result of the Permian overprint. However, the inferred Silurian foreland basin had a much wider extent than the present-day rift; the fact that the flanks of the Oslo Graben record Late Proterozoic-Cambrian ZFT and SFT ages (~ 650-500 Ma) suggests that any Silurian burial heating would have been moderate. These ages probably reflect exhumation related to the formation of a regional sub-Cambrian peneplain (e.g., Zeck et al., 1988).

The fact that ZFT resetting was restricted to the graben makes a simple burial scenario implausible. Moreover, ZFT annealing by burial and conductive heating alone would imply either a post-Permian cover exceeding 5 km, or extremely high (>60°C/km) regional geothermal gradients. Both of these conditions seem highly unlikely. Therefore, advective heat transport must have played an important role in establishing Permo-Triassic peak temperatures. Thermal resetting around 240-270 Ma is probably associated with emplacement of the late syn-rift plutons. The Triassic to Early Jurassic ZFT ages (225-180 Ma) recorded in some samples are, however, more difficult to explain. Considering the large variation in ZFT age over relatively small distances and the fact that ZFT age patterns appear to be controlled by structural trends (Figure 5-10), this late resetting could well be controlled by hydrothermal fluid circulation. Several lines of evidence support this interpretation:

Conodont coloration studies (Aldridge, 1984) have demonstrated alteration indices (CAI) ranging from 3 to 5 in Silurian sediments of the Oslo and Ringerike areas, indicating local peak temperatures which vary between 110 and as much as ~400°C. Reflectance (R_0) of vitrinite-like macerals from the Cambrian-Ordovician alum shale varies between 2 and 6 (Buchardt and Lewan, 1990) and confirms the pattern indicated by the CAI values. However, temperatures are difficult to estimate from vitrinite reflectance at R_0 values above ~2. K-Ar dating of illites associated with hydrothermal ore deposits in the northern AGS, yields ages of 191±2 to 244±4 Ma (Ihlen et al., 1978); similar ages are found near Skien (Ineson et al., 1978). These ages are concordant with the reset ZFT ages and there appears to be a geographical correlation between the localities of reset ZFT ages and the occurrence of hydrothermal ore deposits (Figure 5-10). Although the hydrothermal veins have a Permian age, they were probably reactivated by later fluid circulation, as evidenced by the record of fluid inclusions in various parts of the rift (Olsen and Griffin, 1984; Ihlen, 1986). Estimated

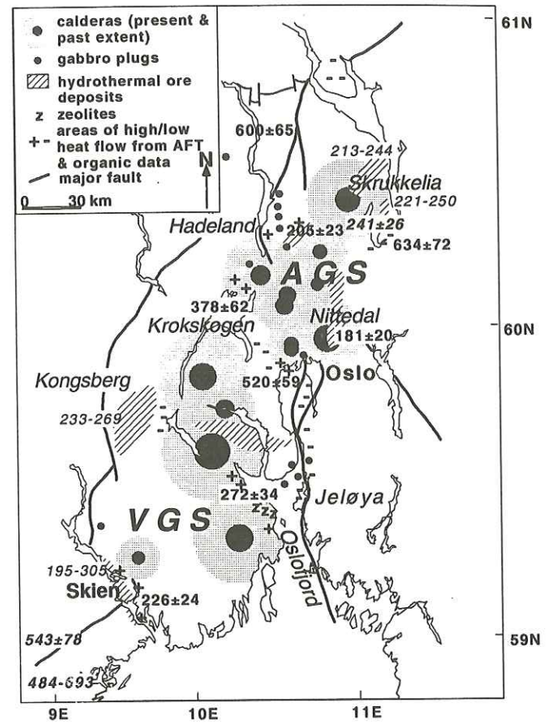

Figure 5-10. Map showing geographical correlation between volcanic structure, hydrothermal ore deposits, K-Ar ages of hydrothermally grown clay minerals (small italic numbers) and ZFT and SFT ages (big bold numbers with errors; those in italics denote sphene ages), within the Oslo rift. Modified from Olaussen et al. (1995) and Ihlen (1986); K-Ar ages are from Ihlen et al. (1978) and Ineson et al. (1978). Paleo-heat flow highs (+) and lows (-), from organic geochemical indicators (Aldridge, 1984; Buchardt and Lewan, 1990) and the AFT data presented in this chapter, are also indicated.

temperatures are in the order of 230-300°C (Ihlen, 1986), enough to reset ZFT and SFT thermochronometers. The only SFT sample within the rift, however, is not reset, which is again evidence for an irregular hydrothermal circulation pattern. A recent fluid inclusion study on cements of the Upper Silurian Ringerike sandstones (E.W. Zwart, pers. commun., 1995) provides further support for the inferred temperature structure. Homogenisation temperatures indicate maximum burial temperatures of ~100-125°C for samples in which ZFT ages are not reset (e.g., OR11), but up to 265°C in reset samples (OR22).

The complex circulation pattern seems to be controlled by the volcanic structure within the rift; both ZFT age lows and hydrothermal ore deposits are concentrated within collapsed calderas or their feeder plugs (Figure 5-10). This is in contrast with fission track results from the Late Triassic-Early Jurassic Newark basin in the eastern USA (Steckler et al., 1993) which show a more regular and large scale pattern of hydrothermal circulation. This discrepancy is probably the result of the great structural complexity attained by the Oslo Graben at the end of rifting. Old AFT ages near the eastern border fault of the Oslo Graben

suggest that this was a cooler area of fluid infiltration, similar to the border fault of the Newark basin.

Post-rift thermal evolution

AFT ages generally decrease from Triassic (~ 200-240 Ma) in the southeast (Bamble and Østfold/Median segment samples) to Jurassic (~ 150-200 Ma) in the northwest (Telemark and AGS samples). The pattern of AFT ages (continuous within and outside the rift, no jumps across faults, no correlation with elevation) suggests that post-Permian cooling took place on a much larger scale than the present study area, that the area behaved as a coherent block after ~240 Ma, and that Meso-Cenozoic exhumation took place in several pulses.

Figure 5-11 shows inferred thermal histories for a number of representative samples. Maximum temperatures are estimated from the ZFT and SFT data. The temperature history below 120°C is modelled from the AFT ages and length distributions (cf. Appendix 1), adopting both the Laslett et al. (1987) and Crowley et al. (1991) annealing models, for the reasons outlined in Section 4.3. The lack of short tracks (<10 µm) in most samples indicates that cooling from 120 to ~70°C took place relatively rapidly, whereas the general scarcity of long tracks (>14 µm) suggests that final cooling to surface conditions took place fairly recently (after ~30 Ma).

The youngest ZFT ages are Triassic-Early Jurassic (180-200 Ma), suggesting that hydrothermal activity continued to operate long after the main rifting period ended. This late fluid flow regime was probably destroyed by erosion at around 200 Ma, leading to a temperature drop from ~200°C (closure of ZFT system) to <120°C (AFT annealing zone). The cooling events inferred from the AFT thermal history modelling coincide with periods of sediment deposition offshore (cf. Section 4.3) and they are interpreted to record denudation. The Meso-Cenozoic evolution of southern Norway was described in detail in Section 4.3 and will not be reiterated here. Only some aspects which are relevant for the understanding of the evolution of the Oslo Rift will be outlined below.

Seismic reflection studies reveal a major base-Triassic unconformity in the northern Skagerrak Graben, while thick Triassic sequences are encountered towards the south (Ro et al., 1990b; Olaussen et al., 1995). Triassic denudation of the Oslo Rift region is thus probably the result of a shift in rifting activity, from north to south of the Fennoscandian Border Zone, at the Permo-Triassic boundary (Vejbæk, 1990; Pedersen et al., 1991). During the Triassic and Early Jurassic, the erosional front retreated hinterland-wards (cf. Figure 4-12), with the Oslo Rift possibly acting as a major sediment channel, analogous to the present-day Rio Grande rift (Olaussen et al., 1995).

The total amount of post-Permian erosion for the Oslo Rift region is estimated to be on the order of 3-4 km, assuming a normal post-rift geothermal gradient (~30°C/km). The present-day geothermal gradient for southwestern Scandinavia is ~20°C/km (Balling, 1990); AFT results from the Siljan borehole suggest that this geotherm has been more or less stable since ~100 Ma (Andriessen and Verschure, 1988; cf. Section 4.3.1). However, it was shown

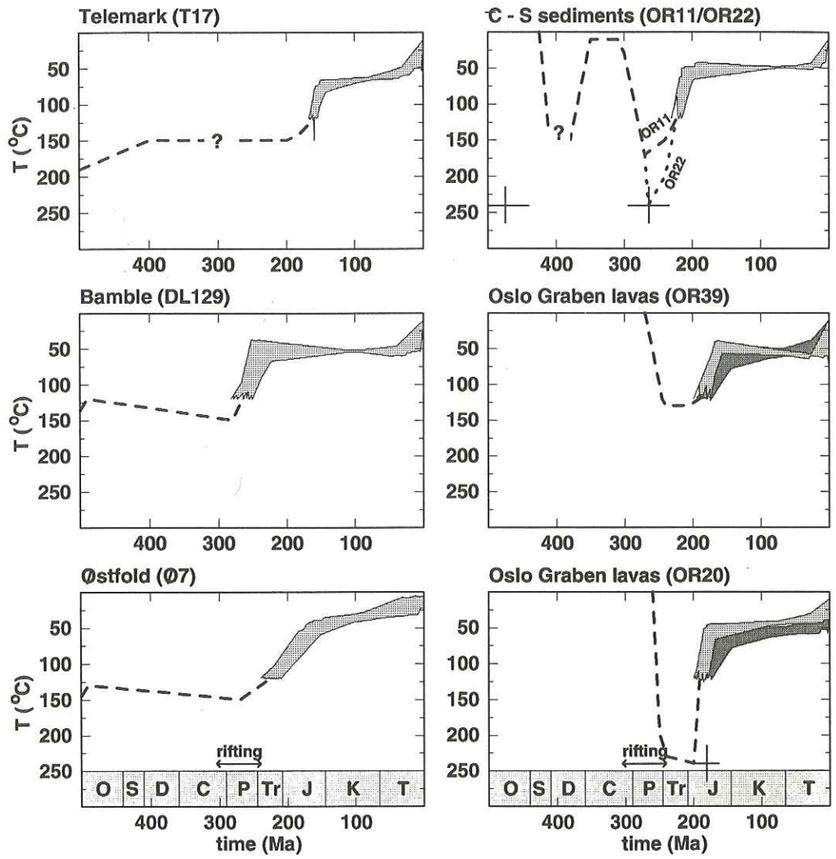

Figure 5-11. Thermal histories of representative samples from the Oslo Graben and surrounding areas. Shaded areas represent modelled thermal history below 120°C, from inversion of AFT data (cf. Appendix 1). Light shading denotes inversion using Durango apatite annealing model (Laslett et al., 1987); darker shading: F-apatite model (Crowley et al., 1991). Dashed lines indicate interpreted thermal histories using regional stratigraphic data as well as ZFT and SFT ages (shown as crossing error bars where appropriate).

in Section 4.3 that Mesozoic geothermal gradients for southern Norway could have been as high as 35°C/km. In the Oslo Rift region, the blanketing effect of eroded Cambro-Silurian and Permian sediments, as well as locally high (advective) heat fluxes during rifting, probably resulted in higher geotherms during the Permian and Triassic, compared to the present-day. Adopting a 20°C/km thermal gradient would increase the erosion estimate by

a factor 1.5 (cf. Figure 1-10), which seems rather high. An estimate of 3-4 km of erosion agrees well with the estimated intrusion depth of currently exposed Permian granitoids (Neumann et al., 1986; Pallesen, 1993). The flanks of the rift also experienced syn-rift uplift and erosion, as evidenced by the conglomerate fans along the eastern border fault of the rift. A detailed reconstruction of rift flank uplift and erosion using AFT data, as was performed in Chapter 3 for the Baikal and Malawi rifts, is not possible here, because of the large amounts of post-rift erosion. However, the absence of basement pebbles in the conglomerate fans indicates that syn-rift erosion did not expose crystalline basement. Thus, the amount of syn-rift erosion of the flanks cannot have surpassed the thickness of the Cambro-Silurian succession, i.e. 2-3 km. This limits total erosion of the areas bordering the rift is to 5-6 km, which is not enough to exhume rocks from the zircon PAZ; in accordance with the old ZFT ages encountered. The total amount of erosion within the rift zone corresponds well to the estimated maximum thickness of the Permian lava succession (e.g., Ramberg and Larsen, 1978; Olaussen et al., 1995) suggesting that no significant amounts (more than a few hundred meters) of post-rift sediments were ever deposited.

5.5 Discussion - implications for rift models

The melt modelling and fission track thermochronology results, presented above, have a number of consequences for tectonic models for the evolution of the Oslo Rift and may provide some insights into the processes operating at magmatic rifts in general. Here, I will specifically address the dynamics and kinematics of rifting, the nature of the mantle below the rift, the mechanisms of heat transport during rifting, and the post-rift evolution of the area.

Dynamics of rifting

The timing of extension, vertical motions and magmatism within a specific rift, and how these relate to the regional tectonic setting, are phenomena which can be used to discriminate between 'active' and 'passive' rifts, i.e. to infer the relative importance of mantle plume activity versus in-plane lithospheric forces in generating extension (cf. Chapter 1). The timing of regional uplift with respect to the onset of rifting constitutes an especially strong constraint in this respect (e.g., Garfunkel, 1988). The AFT data from the Oslo rift suggest that regional uplift and erosion post-dated rifting by some 40-80 My. Pre-rift uplift cannot be excluded from the AFT data alone because there has been such a large amount of post-rift erosion (cf. Section 2.4.2). The preservation of Cambro-Silurian sediments exclusively within the down faulted rift blocks, however, excludes major pre-rift erosion, while the sedimentology of the Asker Group indicates that the area was at sea level immediately prior to rifting. Collectively these observations strongly support a passive origin for the Oslo Rift, as also suggested by the timing of rifting activity, coeval with late Variscan transtensional movements along the

Fennoscandian border zone (Ziegler, 1990; Olaussen et al., 1995). This conclusion is in agreement with petrological, geochemical and isotope data, which suggest that Oslo Rift magmatism was more strongly controlled by the presence of fluids than by a major temperature anomaly within the lithosphere underlying the rift.

The melt modelling results suggest that the (volatile-bearing) lower lithosphere should have been heated in order to produce sufficient melt volumes. This is in accordance with the observed onset of magmatism 5-10 My before surface extension. However, the relatively small thermal perturbation that is required to initiate melting ($T_p \approx 1380°C$) is more compatible with the existence of an asthenospheric warm 'cell' (e.g., Anderson et al., 1992) in the area, possibly as a result of the heat lens effect associated with Variscan amalgamation of Pangea, than with a major mantle plume. Resulting weakening of the lower lithosphere could then have focused regional extension in the Oslo Rift, aided by pre-existing crustal scale discontinuities. Figure 5-12 displays, in cartoon form, a dynamic scenario for Oslo Rift formation and evolution, which incorporates the constraints provided by this study.

Kinematics of extension

In order to produce any substantial amount of melt, lithospheric thinning in the Oslo Rift area must have been considerably larger than expected from upper crust extension estimates.

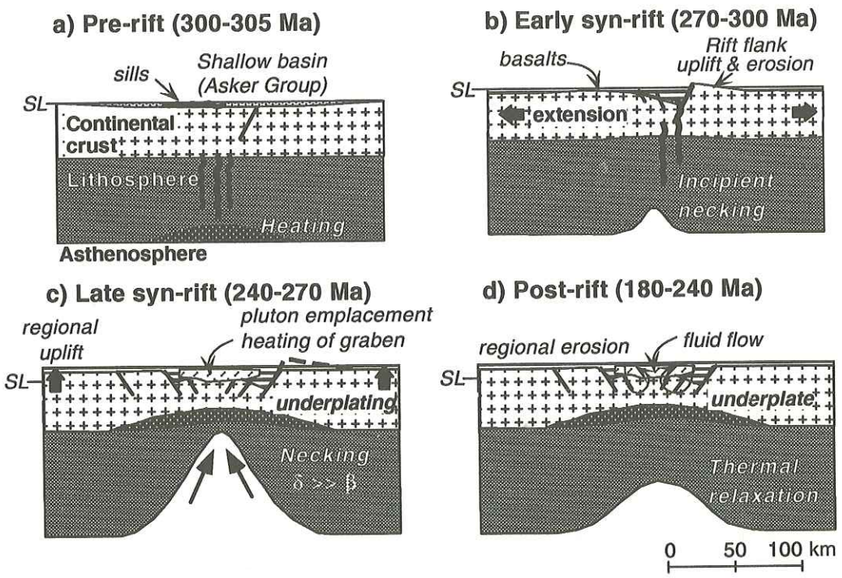

Figure 5-12. Cartoon of inferred dynamic evolution of Oslo Rift. See text for discussion.

One-dimensional depth dependent extension models, such as employed in Section 5.3, are incompatible with the requirement of volume conservation (e.g., Rowley and Sahagian, 1986). However, the distribution of mantle thinning can vary strongly over an extended area in two- or three dimensions (e.g., Keen and Dehler, 1993).

Dynamic models of lithosphere extension, incorporating a rheology with either pre-existing crustal and mantle weak zones (Dunbar and Sawyer, 1989; Boutilier and Keen, 1994) or inherent plastic instability (Bassi et al., 1993) show that 'necking' is a preferred rift mode for relatively cold lithosphere (Bassi, 1991; Buck, 1991) and results in $\delta > \beta$ below the rift zone. These models may, therefore, provide a physical basis for the inference of non-uniform extension, especially since the setting of the Oslo Graben (a relatively narrow rift which developed in Precambrian basement along pre-existing discontinuities) is predicted by these models to promote the development of necking instabilities (cf. Figure 5-12).

Three dimensional effects should also be taken into account. A large number of observations (e.g., Kinck et al., 1991; Larsson and Husebye, 1991; Ro and Faleide, 1992) suggest that the offshore extension of the Oslo Rift, the Skagerrak Graben, has developed as a relatively a-magmatic rift, although inferred stretching factors are higher than for the Oslo Graben (cf. Section 5.2). The development of a post-rift sedimentary basin in the Skagerrak Graben, as opposed to the Oslo Graben, suggests that these two rift segments are fundamentally different. Possibly, along strike melt transport or even along strike lithospheric volume conservation during rifting played a role. Testing such a hypothesis would require a three dimensional dynamic model of extension and decompression melting.

Recently, it has been argued that extension of, at least, the southern part of the Oslo Rift was controlled by lithospheric simple shear (Ro and Faleide, 1992; Lie and Husebye, 1994), with the Porsgrunn-Kristiansand Fault (PKF) acting as the main detachment fault of the system. Such a detachment, associated with large scale vertical movements (of the order of a few km), should show a strong contrast in thermal history between its footwall and hanging wall blocks, with the footwall block experiencing rapid cooling of several hundred °C (e.g., Dokka et al., 1986). The AFT and SFT data from the Bamble and Telemark regions do not show such a contrast, indicating that a simple shear model for the Oslo rift with the PKF as a breakaway fault is not very likely. Again, dynamic models of extension suggest that a pure shear mode of extension is favoured for rifts developed in old, cold lithosphere (e.g., Buck, 1991). Vertical motions along reactivated Precambrian faults outside the currently exposed rift (Ramberg and Larsen, 1978) were probably minor (<1 km), acting only to accommodate the regional tensile stress pattern.

Source of mafic melts

While both the observed amounts of decompression melts generated during rifting and their isotopic characteristics favour a volatile-bearing 'lithospheric' source, the origin of these volatiles is admittedly uncertain. A number of tectonic events could have introduced volatiles into the mantle underlying southwestern Scandinavia: prolonged Sveconorwegian sub-

duction, post-Sveconorwegian granite genesis, Fen carbonatite magmatism, Cambro-Silurian basin formation and Caledonian orogeny.

A lithosphere containing volatiles not only in the MBL but also in (parts of) the TBL seems necessary to generate enough melt in the Oslo Graben. The TBL is gravitationally unstable and will eventually be convectively overturned into the mantle; hence it cannot preserve mantle heterogeneities for time scales on the order of Gy (e.g., Wilson, 1993). Recently, Anderson (1994) suggested that a volatile-bearing TBL or 'mesosphere' could be chemically stable, because of immiscibility with the dry asthenosphere, and thus could preserve heterogeneity for a few hundred My. A model with a volatile-bearing TBL predicts the production of several km of melt, even without stretching, for slightly increased mantle temperatures. These cannot represent steady state conditions, implying that the lower lithosphere should have been heated just prior to rifting (Figure 5-12a).

In the case of an anhydrous TBL, the MBL must have been more fertile than predicted by the adopted wet melting parameterisations, to produce the observed amount of melt. Clearly, a better understanding of the initial lithospheric structure and composition below the Oslo Rift is essential to improve the schemes used in this study.

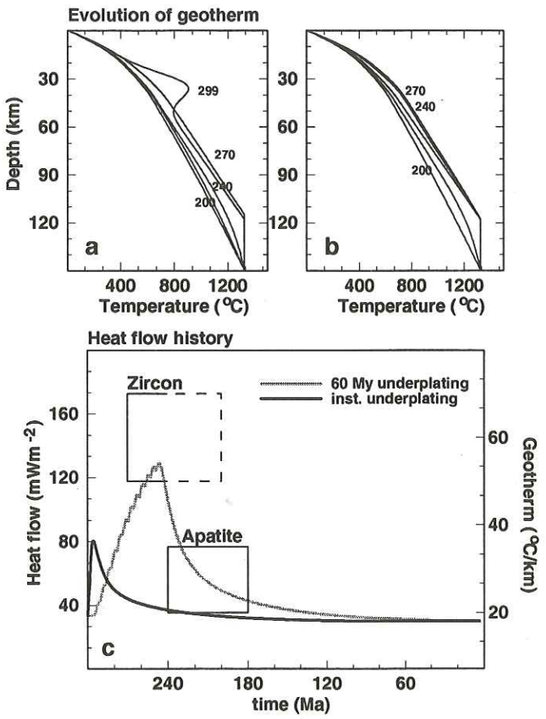

Figure 5-13. Modelled thermal evolution of the Oslo Graben, assuming only conductive heat flow. Upper panels show evolution of geotherms for a thinned lithosphere ($\beta = \delta = 1.3$) and intrusion of a 10 km thick gabbroic underplate (after Stel et al., 1993; Pedersen et al., manuscript in prep.). Lithospheric thinning and underplating take place either instantaneously at 300 Ma (a) or in a time span from 300 to 240 Ma (b). (c) Evolution of surface heat flow for a model of lithospheric thinning and underplating (Pedersen et al., manuscript in prep.). Boxes indicate maximum paleo-heat flow from ZFT data (dashed part of box corresponds to local high heat flows associated with fluid flow) and return to stable conditions, as indicated by AFT data.

Heat distribution during rifting

The ZFT and SFT ages in the Precambrian areas bordering the rift show that syn-rift heating was focused within the Oslo Graben, although crustal thinning and reactivation of faults took place over a much wider area. Present-day heat flow in southern Norway is relatively low (50-60 mWm^{-2}; Balling, 1990), as would be expected such a long time after rifting. Modern rifts (e.g. Rio Grande, East Africa, Rhinegraben) show relatively high and highly variable heat flow values, with means of 70-125 mWm^{-2}. High heat flow values appear to be restricted to the grabens and to be controlled by volcanic structures (Morgan, 1983; Lysak, 1992). ZFT ages within the Oslo Graben show a similar pattern, suggesting highly variable heat flow during rifting, with thermal activity located essentially within the graben. Assuming 3-4 km of post-rift erosion leads to an inferred syn-rift geothermal gradient varying locally from <50 to ~70°C/km. The syn-rift thermal structure thus appears compatible to that of modern magmatic rifts. A simple one dimensional model for the thermal evolution of the Oslo Graben (Figure 5-13), indicates a syn-rift increase of conductive gradients to ~50°C/km, when underplating during a 60 My time span is adopted (Pedersen et al., manuscript in prep.).

Post-rift evolution of the Oslo Graben

The estimates of erosion from the AFT data correspond well to the inferred thickness of the syn-rift lava succession, suggesting that very little post-rift sediments were ever deposited in the Oslo Graben. A number of mechanisms have been proposed to explain the absence of post-rift basin subsidence (e.g., Karner et al., 1992). First, sub-crustal stretching could have been absent below the rift zone, as a result of lithospheric simple shear. This is, however, not very likely in the Oslo Graben since it is associated with major volcanic activity. Conversely, the melt modelling performed here suggest that δ was much greater than β. Moreover, there is no basin which records only post-rift subsidence and can, as such, be 'linked' to Oslo Graben development. Secondly, the long duration of the syn-rift phase (60 My in Oslo) would allow most of the heat to dissipate during rifting, so that the lithosphere only retains a very minor temperature anomaly at the end of the rifting phase. In the case where sub-crustal thinning is substantially larger than crustal thinning, regional syn-rift uplift takes place and rapid subsidence is delayed to the post-rift phase. However, it is possible that Triassic subsidence was not recorded by sedimentation because, by this time, the major depocentres lay further towards the south, in the North Sea rifts, and sediments would thus have bypassed the Oslo Graben (see also Section 4.3.2 and Olaussen et al., 1995). The accumulation of thick continental clastic deposits, during Triassic and Jurassic times, in the North Sea rifts suggests that the Fennoscandian continent could have had a significant elevation above sea level during these times, possibly as a result of the continental 'heat lens' effect which might also have triggered magmatism itself (e.g., Anderson et al., 1992). Moreover, the existence of a ~10 km thick underplate below the Oslo Rift would also counteract post-rift subsidence (McKenzie, 1984; Stel et al., 1993).

CHAPTER 6

SYNTHESIS

In this thesis, I have presented fission track data and kinematic modelling studies, aimed at constraining the thermo-tectonic evolution and vertical motions of continental rifts and rifted margins. These studies illustrate the close coupling between deeper lithospheric and near-surface processes. In order to understand the mechanisms which lead to vertical motions, erosion and sedimentation, both the underlying geodynamic processes and those operating at the surface need to be adressed. I have shown in this thesis that the low- temperature thermal evolution of rocks exposed in and around continental rifts, carry an important geodynamic signal.

In Chapter 2, I showed that thermal mechanisms fail to explain the tectonic uplift patterns inferred from fission track thermochronology at a number of rifted continental margins. A mechanical support of rift flanks, resulting from an upward state of flexure, appears much more plausible. In Chapter 3, flank uplift at two young intracontinental rifts was studied, and it was shown that the observed topography implies a strong elastic lithosphere. Flexural cantilever models, which assume rift flank support by the low-rigidity upper crust, are incompatible with the topography and erosion patterns observed at the two rift systems that I studied. The upward state of flexure, which is required to support the flanks, can be understood as the consequence of stretching around an intra-crustal 'necking level' (z_c). However, an additional source of buoyancy is required to explain the anomalously high flanks and shallow basin of the northern Baikal rift.

In Chapter 4, an example of post-rift margin uplift was discussed. Geomorphological and seismic-stratigraphic data indicate that southern Norway has experienced Neogene uplift and erosion. Fission track thermochronology suggests that Neogene exhumation was initiated at around 30 Ma and amounted to a maximum of 2.0±0.5 km, for rocks that are nowadays at sea level. Backstacking the inferred Neogene denudation reveals a domal pattern of tectonic uplift, with a wavelength of ~400 km and a maximum amplitude of ~1.5 km. Seismic tomography and gravity data suggest that the lithosphere is anomalously warm under southern Norway. This is also suggested by relatively low T_e values (~15 km), obtained from a coherence analysis of gravity and topography. Thermal erosion of the lithosphere possibly explains part of the observed uplift pattern, which could have been amplified by compressional intraplate stresses.

Finally, Chapter 5 discussed the evolution of a highly magmatic paleorift. Magmatism in the Permo-Carboniferous Oslo Graben was probably not caused by a mantle plume, as there is evidence against pre-rift regional erosion, the area was demonstrably at sea level at the onset of rifting, and mantle temperatures were only slightly higher than normal. In order to explain the observed amounts of magmatism, the mantle thinning factor (δ) must have been substantially larger than the crustal stretching factor (β), and the lithospheric solidus

must have been reduced compared to that of anhydrous peridotite. The prefe
mode for the Oslo Graben is pure shear lithospheric necking. Zircon and sphene
data indicate that, whereas the rift zone itself experienced elevated geotherm
during the syn-rift and early post-rift phase, the flanks were not affected by h
pattern indicates that rift-related heating was focussed into the rift zone b
processes.

In this concluding chapter, I wish compare these results with dynamic models of
lithospheric extension and discuss the implications they might have for our un
of continental rifting. Some of the suggestions presented in this chapter are somewhat
speculative; they should be regarded as departure points for discussion and fur

6.1 What is the physical meaning of the 'level of necking'?

In Chapters 2 and 3, it was shown that the kinematics of intracontinental riftin
be controlled by lithospheric necking around a reference level (z_r), that would sta
in the absence of isostatic restoring forces. Such kinematics are compatible wi
models of lithospheric stretching, but the exact physical significance of this lev
to discussion. Pure shear models of lithospheric extension (e.g. Braun and Beaum
Chéry et al., 1992; Bassi et al., 1993) predict that necking will occur around the str
within the lithosphere which, depending upon the adopted crustal and lithospher
will be either the upper crust or upper mantle. This behaviour is still observ
crustal faults are included in the models (Boutilier and Keen, 1994). A model th
offset pre-existing weakness zones in the upper crust and upper mantle (Dunbar a
1989) predicts the development of a sub-horizontal detachment in the weak low
this case the level of necking varies over the model.

I have shown that mid- to lower-crustal z_r levels are required to rep
observed amounts of tectonic uplift, and a realistic crustal structure, for the examp
Best fitting z_r levels are 10-15 km for the Saudi Arabian Red Sea margin, 30
Transantarctic Mountains (Section 2.3.5), 20 km for the Baikal rift (Section 3.2.3) a
for the Malawi rift (Section 3.3.3). It is noteworthy that in all cases studied, i
necking is predicted; deeper (sub-crustal) levels of necking are incompatible with g
and inferred Moho topography. For the Baikal and Malawi rifts, the inferr
correspond to maxima in the depth distribution of earthquakes, and there seems to be a cor-
relation between necking depth and lithospheric strength, as inferred from the t
petrological structure of the lithosphere (Section 3.5, Figure 3-27).

To adress possible rheological controls on the style of rifting, we can make a
comparison with results obtained, using the same thermomechanical model, for
basins, which have a different initial lithospheric structure. Figure 6-1 shows a compilation

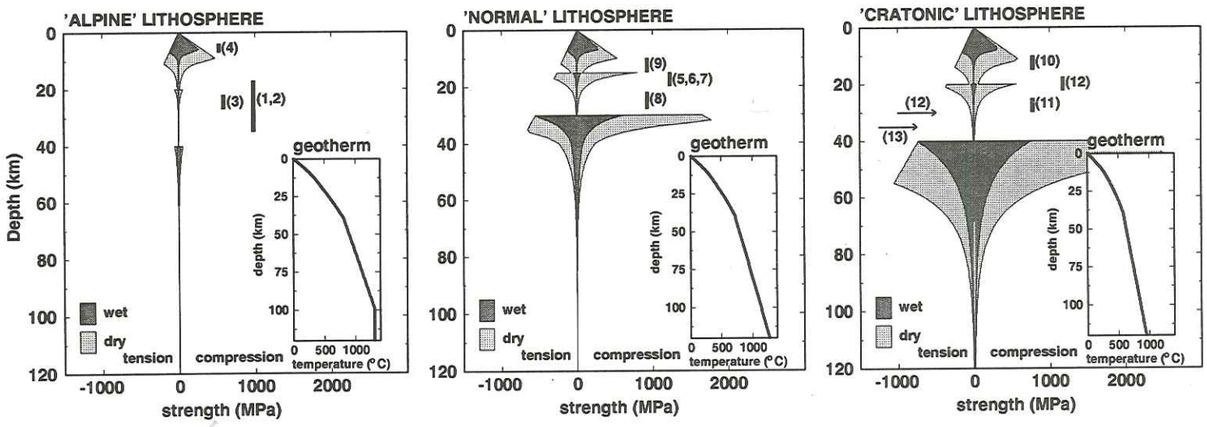

Figure 6-1. Comparison of depth ranges of the level of necking inferred from kinematic rifting models, with rheological models of the lithosphere. Strength profiles are calculated for a granitic upper crust, dioritic lower crust and an olivine mantle rheology; thermal and rheological parameters are as listed in Table 3-3(a). (a) 'Alpine' lithosphere (upper crustal thickness 20 km, lower crustal thickness 20 km, 100 km lithosphere, surface heat flow = 79 mWm^{-2}); (b) 'normal' lithosphere (upper crustal thickness 15 km, lower crustal thickness 15 km, 125 km lithosphere, surface heat flow = 74 mWm^{-2}); (c) 'cratonic' lithosphere (upper crustal thickness 20 km, lower crustal thickness 20 km, 200 km lithosphere, surface heat flow = 66 mWm^{-2}). Vertical bars denote inferred levels of necking for (1) Gulf of Lions (Kooi et al., 1992), (2) Valencia Trough (Janssen et al., 1993), (3) Tyrrhenian Sea (Spadini et al., 1995a), (4) Pannonian basin (van Balen et al., 1995); (5) Central Graben, North Sea (Kooi, 1991; van Wees, 1994), (6) Viking Graben, northern North Sea (Odinsen et al., manuscript in prep.), (7) Barents sea (Reemst et al., 1994), (8) Western Black Sea (Spadini et al., 1995c), (9) Eastern Black Sea (Spadini et al., 1995c); (10) Saudi Arabian Red Sea margin, (11) Transantarctic Mountains, (12) Baikal Rift (all this study). Arrows denote best fitting detachment level for (12) Baikal and (13) Malawi rifts.

of inferred necking depths, overlain on 'typical' strength profiles, for extensional basins developed on continental lithosphere with different thermomechanical 'age'. Whereas continental rifts developed in Caledonian/Variscan age (~400 Ma) 'normal' lithosphere and in cratonic (>1 Ga) lithosphere appear to be consistently controlled by mid-crustal (15-30 km) z_c levels (e.g., Kooi, 1991; Reemst et al., 1994; Spadini et al., 1995c; Odinsen et al., manuscript in prep.; this study), 'Alpine-Mediterranean' rifts show a wider variation in z_c levels, between 5 and 35 km (e.g., Kooi et al., 1992; Janssen et al., 1993; Spadini et al., 1995a; van Balen et al., 1995).

Kooi et al. (1992) suggested that young orogenic ('Alpine') lithosphere should be characterised by a weak mantle and, as a consequence, a shallow level of necking around the strong upper crustal layer. Cratonic lithosphere, in contrast, would be characterised by sub-crustal necking, around the strong mantle layer. However, an intra-crustal necking level seems to be controlling the kinematics of extension in every case discussed above. Figure 6-1 shows that the level of necking is not simply correlated with the strongest lithospheric layer. Instead, z_c may correspond to the depth at which concentrated (brittle) deformation in the upper crust gives way to more distributed ductile deformation in the lower crust. This is also the depth to which most of the major normal faults bounding rifts can be traced on deep seismic reflection records (e.g., Pinet et al., 1987; see also Allemand and Brun, 1991). Apparently, the continental lithosphere preferentially necks around the strongest crustal level near the brittle-ductile transition, suggesting a detachment between the upper crust and mantle strong layers (Figure 6-2).

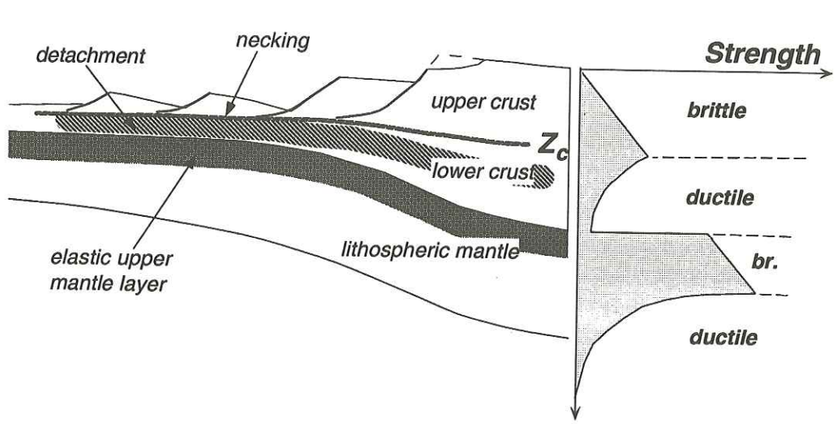

Figure 6-2. Cartoon showing possible relationship between rheological layering of the lithosphere, mid-crustal necking, lower crustal detachment and mantle flexure during evolution of a rifted continental margin.

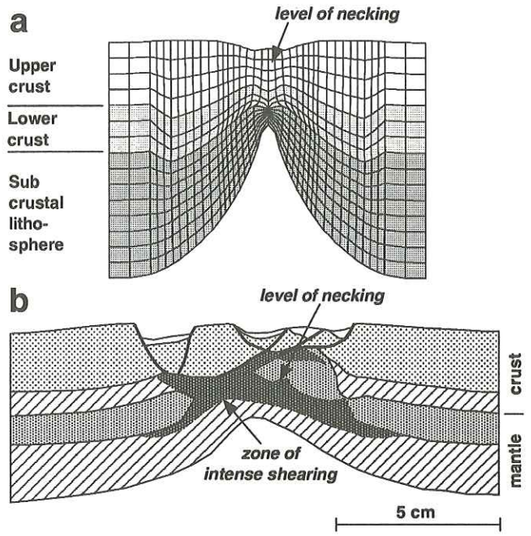

Figure 6-3 (a) Mid crustal necking level and strongly depth-dependent thinning in a dynamic model which includes plastic instability in the sub-crustal lithosphere (after Bassi et al., 1993). (b) Mid- to lower crustal necking and mantle boudinage in a physical model of 4-layer lithosphere extension, with a brittle upper mantle (after Beslier and Brun, 1991).

This interpretation is supported by dynamic models of continental extension which include a low-strength, ductile lower crust (e.g., Dunbar and Sawyer, 1989; Bassi et al., 1993). In this case, the weak lower crust allows differential thinning between crust and mantle, and an intra-crustal level appears to control the pattern of necking (Figure 6-3(a)). If the lower crustal and mantle strengths are large, a sub-crustal level of necking is predicted by dynamic models (Chéry et al., 1992; Boutilier and Keen, 1994). As such deep z_c levels appear incompatible with kinematic modelling studies of actual rifted basins, a detached upper crust and mantle lithosphere seems to be the norm for most tectonic settings (see also Allemand and Brun, 1991; Le Pichon and Chamot-Rooke, 1991; Burov and Diament, 1995).

An alternative approach was taken by Weissel and Karner (1989), who relate the kinematic reference level directly to a lower crustal detachment. An application of their model to the East African rifts (Ebinger et al., 1991) and the Brazilian Atlantic margin (Karner et al., 1992) assumes a detachment level at the base of the crust. However, from a mechanical point of view it is difficult to imagine why a low-strength layer, like the lower crust, would tend to remain horizontal. Most physical and dynamic modelling studies (e.g., Allemand et al., 1989; Dunbar and Sawyer, 1989; Beslier and Brun, 1991; Bassi et al., 1993) show that the lower crust is intensively deformed during extension (Figure 6-3). In Chapter 3, it was shown that the depth of the detachment level, required to fit the observations in the Baikal rift using a detachment model, is somewhat larger than the depth of necking inferred from a necking model. Thus, one could argue that mid-crustal necking levels are associated with lower

crustal detachments. This would imply that lower crustal weak zones have a strong rheological control on the kinematics of extension.

Spadini et al. (1995a) argue that an apparent lower crustal z_c level can arise from the interaction of two strong layers, a crustal and sub-crustal one. Such a scenario is consistent with 4-layer physical models of extension (Allemand et al., 1989; Beslier and Brun, 1991) which show the lower crust being 'squeezed' out between the two stronger layers above and below it (Figure 6-3(b)). However, this behaviour is possibly an artefact of the brittle character of the upper mantle layer adopted in these models. It still has to be demonstrated that brittle deformation of the upper mantle is a realistic mechanism. Models with a plastic rather than brittle upper mantle show more homogeneous lower crustal and upper mantle extension (Bassi et al., 1993; Boutilier and Keen, 1994). A plastic behaviour of the upper mantle is also suggested by the general absence of sub-crustal seismicity in areas where rheological models predict significant lithospheric strength (e.g., Cloetingh and Banda, 1992).

Cloetingh et al. (1995) compiled the parameters which best describe the kinematics of extension for a number of rifted basins in different tectonic settings, and discussed their correlation with pre-rift rheology (Figure 6-4). Although these plots show considerable scatter, resulting from varying data quality and the inherent non-uniqueness of kinematic modelling predictions, some interesting correlations do seem to exist. For Alpine-Mediterranean basins z_c seems to diminish with increasing crustal thickness. This is less clear for 'normal' and cratonic lithosphere, where crustal thickness does not vary so much (Figure 6-4(a)). However, for similar crustal thicknesses, basins in cratonic settings seem to be controlled by a deeper z_c level than the Alpine-Mediterranean basins, probably because the latter have, in general, higher geothermal gradients. This is also suggested by the (weak) positive correlation with lithospheric thickness (Figure 6-4(b)). These correlations, as well as the weak positive correlation with T_e (Figure 6-4(c)), suggest that there is a control of pre-rift lithospheric strength on the kinematics of extension, as expressed by z_c. If this conclusion is correct, it confirms the inferences from a dynamic modelling study by Chéry et al. (1992).

An intreresting correlation is suggested between extensional strain rates (calculated from the mean β factor across the rift zones and the duration of extension) and the level of necking. As strain rates and lithospheric strength mutually influence each other (e.g., England, 1983; Sawyer, 1985), the question of whether there is a strain rate control on the style of extension has remained somewhat of a 'chicken and egg' problem (cf. Bassi, 1995). The apparent positive correlation between estimated strain rates and z_c levels (Figure 6-4(d)) is in agreement with our current understanding of lithsopheric rheology, in that lithospheric strength increases with increasing strain rates. The Saudi Arabian Red Sea margin constitutes an intriguing anomaly in these plots: strain rates are very high and inferred z_c level anomalously low, compared to the lithospheric thickness and rigidity of the Arabian continent. In tectonic scenarios proposed for the evolution of the Red Sea margin, the last stages of extension and continental breakup occur by massive dyke intrusion (e.g., Bohannon, 1986; Bohannon and Eittreim, 1991; cf. Section 2.2.1). The associated magmatic weakening may play an important role in establishing the anomalous kinematics of the Red Sea margin.

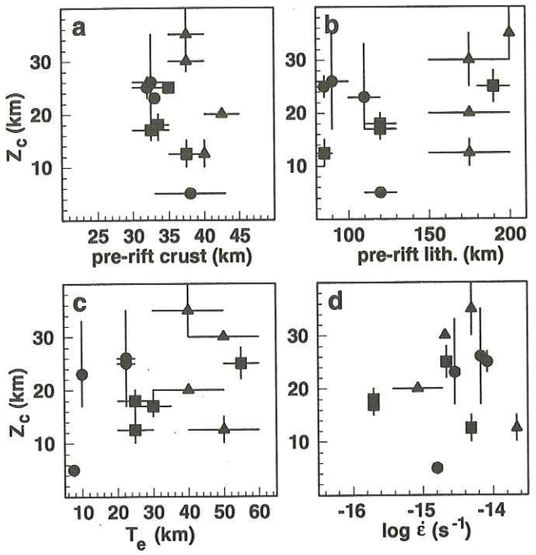

Figure 6-4. Correlation of (a) level of necking versus pre-rift crustal thickness; (b) level of necking versus pre-rift lithospheric thickness; (c) level of necking against effective elastic thickness; (d) level of necking against extensional strain rates, for the rifted basins and margins compiled in Figure 6-1 (after Cloetingh et al., 1995). Dots indicate basins formed in 'Alpine-Mediterranean' lithosphere; squares: 'normal' (Variscan-Caledonian) lithosphere; triangles: cratonic lithosphere. Error bars indicate uncertainties in modelling parameters and predictions.

Although, from the above, a general agreement seems to exist between inferences from dynamic and kinematic models of extension, there is a discrepancy between the vertical motions derived from fission track data and the predictions of kinematic models on one hand, and the motions predicted by dynamic models on the other. The latter predict a maximum tectonic uplift of rift flanks on the order of 2 km (e.g., Dunbar and Sawyer, 1989; Chéry et al., 1992; Bassi et al., 1993), which is a factor 2 lower than maximum flank uplift inferred for, for instance, the Transantarctic Mountains or the Saudi Arabian Red Sea margin (Section 2.3). One explanation for this discrepancy could be that, because of numerical stability limitations, dynamic models do not usually proceed further than a maximum value of $\beta \leq 3$ (e.g., Dunbar and Sawyer, 1989; Chéry et al., 1992; Boutilier and Keen, 1994), whereas maximum inferred β factors for, for instance, the west Antarctic rift system are larger than 5. Bassi (1991) noted that rift flank uplift is a late feature in dynamic models; thus, a large part of the uplift is possibly not modelled. Also, dynamic models tend to assume a relatively weak lithosphere, with thicknesses ≤120 km (e.g., Bassi et al., 1993) even for the 'strongest' models, in order to produce extension under reasonable plate boundary forces ($\leq 10^{13}$ Nm^{-2}). Such an initial lithospheric structure leads to relatively shallow necking levels (G. Bassi, pers. commun. 1994). Only the 'strongest' models of Chéry et al. (1992) show very deep levels of necking, but here flank uplift is limited by the very large predicted T_e (>100 km) resulting from coupling of crustal and upper mantle layers (e.g., Burov and Diament, 1995). This is a further argument to propose that cratonic lithosphere can be very strong, but the upper crust remains decoupled from the lithospheric mantle. Note, however,

that the width of the transition zone between unextended and highly extended crust exerts a strong control on the final amount of rift flank uplift (Figure 2-5); the Transantarctic Mountains and Red Sea margin may represent extreme cases in this respect. For lower amounts of extension, as observed at the Baikal and East African rifts, the amounts of rift flank uplift (~500-1000 m), as well as the final basin depth (5-8 km), are consistent with dynamic modelling predictions.

A major shortcoming of kinematic models, such as the ones applied here, is the separation between the kinematics of extension and the isostatic response of the lithosphere. It is highly questionable whether such an artificial separation of these two processes conforms to reality, given the non-linearity of the problems. Flexural bending stresses have a large effect on the strength distribution within continental lithosphere (e.g., Burov and Diament, 1995) and, therefore, isostasy should influence the kinematics of continued extension. The strength evolution during extension is also expected to influence the final style of rifting. One could speculate that slow extension, leading to increasing lithospheric strength (England, 1983), causes necking levels to deepen during rift basin evolution, whereas, on the other hand, rapid extension would lead to a shallowing z_c. Such effects could be incorporated in new kinematic models, in addition to variations in z_c levels due to initial conditions. This could be done by defining z_c as the depth to the brittle-ductile transition, by analogy with an isotherm-defined T_e.

6.2 What controls the (a)symmetry of rifting?

The question of whether continental rifting is a fundamentally symmetric (pure shear) or asymmetric (simple shear) process, has been a subject of debate since the concept of simple shear extension was presented a decade ago (Wernicke, 1985). The surface expression of continental rifts may be strongly asymmetric as a result of extension along a single border fault (Rosendahl, 1987), the location of which is often controlled by pre-existing structure (e.g., Daly et al., 1989; Versfelt and Rosendahl, 1989; Sherman, 1992; Landon, 1994; Theunissen et al., 1995). On a lithospheric scale, however, most continental rifts exhibit bulk pure shear behaviour. In Chapter 3, I showed that (largely) pure shear models of lithospheric extension can explain the first order characteristics of both the Baikal and Malawi rifts, despite the fact that the surface expressions of both these rifts are half grabens. These results are consistent with the dynamic modelling results of Boutilier and Keen (1994), which indicate that, even in the presence of a pre-existing crustal scale fault, the lithospheric deformation pattern can be generally described as pure shear. Simple shear extension depends on the possibility to activate faults or shear zones cutting across the entire lithosphere. Such faults have, as yet, not been clearly imaged by, for example, deep seismic reflection profiling. Available dynamic modelling studies suggest that lithospheric-scale faults can only be initiated in orogenically overthickened crust (e.g., Braun and Beaumont, 1989b,

Buck, 1991; Govers, 1993). In these settings, pre-existing structure, in the form of low-angle thrusts, may also favour the development of simple shear controlled extension.

Some of the examples presented in this thesis do show a certain degree of asymmetry between conjugate rifted margins. For instance, the topography and erosion patterns along the conjugate margins of the southern Atlantic suggest that more rift flank uplift has occurred on the Brazilian than on the Namibian margin (Section 2.5). An asymmetry also exists in the distribution of rift related flood basalts around the southern Atlantic, more than 90% of which occur in Brazil (Paraná) and only small amounts in Namibia (Etendeka). Asymmetry is also observed between the conjugate margins of the Red Sea (Section 2.5): the elevation of the Arabian continent is substantially higher than that of northeastern Africa, which has led to the development of a larger escarpment system on the Saudi Arabian side. Here as well, the asymmetry is accompanied by an asymmetric distribution of magmatism, which is concentrated in Saudi Arabia (Camp and Roobol, 1992). An extreme case of asymmetry is presented by the conjugate southeastern Australian / Lord Howe Rise margins of the Tasman Sea, the former having maximum elevations of over 1.5 km, whereas the latter is entirely submerged. These observations are not new; in fact, they constituted the basis for suggesting that simple shear may play a role in continental break-up (Lister et al., 1986; Ussami et al., 1986).

In some kinematic modelling studies, the need to adopt a lateral offset between crustal extension β and mantle extension δ suggests that intracrustal detachments were operating during extension (e.g., Karner et al., 1992). I have shown that, for the Transantarctic Mountains - west Antarctic rift system, mantle thinning should be concentrated under the rift flank, in order to explain the uplift/subsidence patterns while maintaining a reasonable crustal structure (Section 2.3.5). In the northern Baikal rift, the anomalously high flanks and shallow basin are possibly supported by non-uniform thinning, with mantle thinning concentrated below the northeastern side of the rift (Section 3.4). Both the Baikal and west Antarctic rifts developed on an old suture zone, with thick cratonic lithosphere bordering the rift zone on one side and thinner 'Caledonian' age lithosphere on the other.

In the case of southeastern Australia, not only was original rifting possibly asymmetric, but the margin also seems to have been reactivated during the Tertiary, as suggested by the anomalous elevation of the eastern highlands and recent magmatism (Sections 2.3.5, 2.4.3). Southern Norway is another case where thermal erosion of the lithosphere seems to affect the basin margin preferentially (Section 4.4.3). Thus, asymmetries may occur during the entire evolution of an extensional basin, from the intial rifting stage to continental break-up, and even during the post-rift evolution.

A number of explanations have been given for such asymmetric styles of extension. Bassi et al. (1993) showed that, for specific pre-rift rheologies, initially uniform thinning may lead to migration of the locus of maximum extension towards the side of the rift, resulting finally in asymmetric break-up with one very wide and one narrow margin. Such a style of break-up is observed, for instance, in the Tasman Sea (SE Australia / Lord Howe Rise) and the south Atlantic (Brazilian and Namibian conjugate margins) and is possibly developing

at present in the west Antarctic rift system. The effect of such a migration of the locus of lithospheric thinning on rift flank topography and magmatism has, however, not been investigated yet. The asymmetries in magmatic activity, as observed across the southern Atlantic and the Red Sea, suggest that the initial thermal structure of the lithosphere already differed from one side of the rift to the other. Dunbar and Sawyer (1989) propose that such asymmetries can result from extension of a lithosphere containing offset pre-existing crustal and mantle weaknesses. Whereas crustal weakness zones are relatively easy to identify and their control on rift evolution is generally accepted (cf. Landon, 1994), the existence of (thermally controlled?) mantle weakness zones is much more difficult to prove. The occurrence of continental flood basalt provinces at rifted continental margins, which were probably derived from a volatile-bearing and gravitationally instable 'lower lithosphere' (Gallagher and Hawkesworth, 1992; Anderson, 1994), does suggest an interplay between a small initial thermal disturbance and lithospheric extension. Initial thermal or mechanical weakening actually seems necessary to initiate rifting in strong cratonic lithosphere (e.g., England, 1983; Sawyer, 1985; cf discussion in Nicolas et al., 1994). In Chapter 5, it was shown that this is also the most probable scenario to explain the magmatism associated with the Oslo Graben. In this case, the loci of pre-existing crustal and mantle weaknesses probably overlapped, allowing the development of a highly magmatic symmetric rift, at probably rather low levels of extensional stress.

6.3 Some remarks on 'active' and 'passive' rifting

The 'active' versus 'passive' rifting debate (Şengör and Burke, 1978) has been vigorous since the role of rifting in plate tectonics was recognised. It has been accepted for more than a decade that most rifts display elements of both these idealised end member models (Morgan and Baker, 1983; Keen, 1985). For instance, White and McKenzie (1989) explain the generation of flood basalts and volcanic rifted margins as a result of independent passive rifting over mantle hot spots.

In recent years, it has been realised that excessive magmatism associated with rift zones may not unequivocally attest of the presence of a mantle plume. The presence of fluids in the lithosphere may be of similar importance (e.g., Gallagher and Hawkesworth, 1992). The timing of magmatism relative to extension and regional surface uplift, the chemical and isotopic signature of the magmas and the rate of melt production are important observations to take into account when discriminating between 'active' and 'passive' models for rift-related magmatism (e.g, Menzies et al., 1992; Hawkesworth and Gallagher, 1993; Wilson, 1993). For the Oslo Graben, it was shown in Chapter 5 that magmatism cannot be related to mantle plume activity, because of the evidence against pre-rift uplift, the lithospheric signature of the initial melts, the low magma production rates and the inferred low mantle temperature (see also Neumann, 1994). Oslo Graben magmatism was probably triggered by a small

thermal disturbance which affected a very fertile mantle. In the case of the Red Sea, the timing of magmatism and regional uplift with respect to rifting excludes the possibility that a mantle plume was present in the area prior to the onset of rifting (Bohannon et al., 1989; Menzies et al., 1992; cf. Section 2.2.1).

On the other hand, purely passive models of rifting, which ignore the contribution of active (non-extensional) thinning of the lithosphere, fail to reproduce some of the observations at continental rifts. The topography and gravity patterns along parts of the East African rift system (Ebinger et al., 1989; 1991) and the northern Baikal rift (Section 3.4) point to a deep source of buoyancy in the mantle, which is most easily explained by additional thermal thinning or dynamic support from upwelling asthenosphere. The high elevation of a number of rifted margins (e.g., Saudi Arabia, Brazil, southern Africa) also suggests support from either anomalously light mantle or underplated melts (Section 2.5). For the Oslo Graben, mantle thinning should have been substantially larger than crustal extension in order to explain the observed amounts of melt (Section 5.3).

Most modern and fossil rift systems show evidence of a certain degree of magmatic destabilisation of the Moho, by interaction with ascending melts (cf. Mohr, 1992; Ziegler, 1995): positive gravity anomalies over paleorifts point to the existence of lower crustal intrusions (e.g., Ramberg, 1976; Wessel and Husebye, 1987; Neumann et al., 1992); there is a correlation between the amount of surface volcanism and the seismic (P_n) velocity contrast at the Moho, in both modern and fossil rifts (Wendlandt et al., 1991). Deep seismic reflection profiles often show a pattern of lower crustal reflectivity associated with rifts, that can be interpreted as the result of lower crustal intrusion and metasomatism (Pinet et al., 1987; Ro and Faleide, 1992; Bois, 1993). Also, part of the often observed discrepancy between surfaceal extension and crustal thinning may result from non-extensional upward migration of the Moho (Bois, 1993; Stel et al., 1993; Ziegler, 1995).

These observations suggest that thermal thinning or erosion of the lithosphere is a real mechanism associated with rifting. A number of studies indicate that such a destabilisation occurs during the evolution of a rift system, thus suggesting a shift from 'passive' to 'active' mechanisms as rifting proceeds. In the case of the Baikal rift, paleostress data indicate that rifting was initiated in a transtensional regime, i.e. passively (Delvaux and Klerkx, 1994; Delvaux et al., 1995). Rapid rifting only started during the Pliocene (Logatchev and Zorin, 1992; Mats, 1992), coinciding with a change in stress patterns towards pure extension. Regional uplift of the Saudi Arabian continent did not take place until rifting was well underway (Bohannon et al., 1989; Menzies et al., 1992). Bois (1993) provides evidence that regional plateau uplift associated with the western European rift system (e.g. Rhenish Shield, Massif Central) only commenced 10-20 My after the onset of rifting, a feature that is also observed along the Mediterranean margin of Iberia (Cloetingh et al., 1992c; Janssen et al., 1993). A compilation of data which indicate that in many cases regional uplift post-dated rift initiation is given by Ziegler (1995).

Thermal destabilisation of the lithosphere-asthenosphere boundary can result from secondary convection related to passive rifting (Buck, 1986; Keen, 1987). However, whether

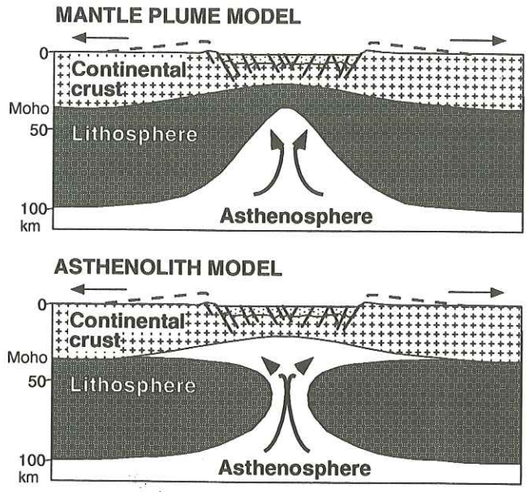

Figure 6-5. Cartoons of models of lithospheric extension including active destabilisation of the lithosphere - asthenosphere boundary. Modified from Ziegler (1988); after Turcotte and Emerman (1983).

such a mechanism can account for the observed large spatial and temporal scales of uplift and magmatism remains to be studied. A model that was presented more than a decade ago to account for an evolution from 'passive' to 'active' rifting is the so-called 'tensional failure' or 'asthenolith' model (Illies, 1981; Turcotte and Emerman, 1983; Neugebauer, 1987; Figure 6-5). In this model, which was originally proposed as an alternative for 'active' mantle plume models, the asthenosphere intrudes the continental lithosphere in a narrow rupture zone underlying a rift. Once the upwelling material reaches the Moho, it may interact with the continental crust and/or spread laterally because it cannot penetrate the less dense continental crust, thus forming an asthenospheric diapir or 'asthenolith'. An asthenolith model provides explanations for a range of geological observations, including the crust-mantle interaction and delayed regional uplift noted above. In the Baikal rift, both deep seismic refraction and petrological data point toward the existence of an asthenolith (cf. Section 3.2.1, Figure 3-4). Although non-flexural uplift of the northern Baikal region was modelled by depth-dependent lithospheric thinning (Section 3.4), it may be difficult to discriminate between the topographic and gravity effects of excess mantle thinning on one hand, and asthenolith intrusion on the other. In a recent review, Nicolas et al. (1994) compile evidence for lithospheric rupture and asthenospheric diapirism: field evidence from peridotite massifs associated with rifting (e.g., Zabargad Island in the Red Sea), xenoliths from the Massif Central, and seismic tomographic imaging of the Kenya rift indicate that upwelling occurred in a narrow and steep conduit. Continental break-up in the Red Sea area took place by massive dyke intrusion (Bohannon, 1986; Bohannon and Eittreim, 1991). Such rift related intrusions were probably caused by an asthenosphere intrusion through the lithosphere and lower crust (Nicolas et al., 1994).

The dynamic models of extension discussed above indicate that narrow lithospheric necking results from plastic instabilities in old, cold lithosphere which contains pre-existing weakness zones (Dunbar and Sawyer, 1989; Bassi et al., 1993; Boutilier and Keen, 1994). Some models have included predictions on the timing and amount of decompression melting (e.g., Dunbar and Sawyer, 1989; Arndt and Christensen, 1992; Pedersen, 1994). The effect of melt formation on bulk lithospheric strength has been discussed previously (Anders and Sleep, 1992; Karner et al., 1992), but the temporally and spatially localised weakening associated with decompression melting has never been included in dynamic models. One would expect that partial melting in an evolving neck or asthenosphere intrusion leads to further localisation of deformation and aids in propelling the intrusion upward. This would occur as a result of local heating and weakening, as well as the density difference between melt and lithosphere. In this manner, the process would be self-enhancing, although an initial thermal or mechanical instability would still be required to initiate rifting (cf. Nicolas et al., 1994).

25 AOUT 2003
Univ. J. Fourier - O.S.U.G.
MAISON DES GEOSCIENCES
DOCUMENTATION
B.P. 53
F. 38041 GRENOBLE CEDEX
Tél. 04 76 63 54 27 - Fax 04 76 51 40 58
Mail : ptalour@ujf-grenoble.fr

APPENDIX 1

THERMAL MODELLING OF APATITE FISSION TRACK DATA

Recent advances in our understanding of the kinetics of apatite fission track annealing permit the extraction of quantitative information on the thermal history of a sample from apatite fission track data. Annealing of fission tracks is a temperature-dependent diffusional process to which the (empirical) Arrhenius law can be applied (e.g., Green et al., 1985; Laslett et al., 1987). This law states that time (t) and Temperature (T) which lead to a specific degree of annealing r, are related as (Figure A1-1):

$$\ln(t_{(r)}) = A + B T_{(r)}^{-1} \qquad \text{(A1.1)}$$

A is a constant and B is usually interpreted in terms of an activation energy E and Boltzmann's constant k: $B \approx E / k$. However, no theoretical basis exists for the functional form of the Arrhenius equation for fission track annealing; for example, both A and E may be dependent on the degree of annealing. The 'fanning Arrhenius' model (A constant, $B = B(r)$) has been shown to describe laboratory experiments successfully (Laslett et al., 1987; Crowley et al., 1991). I will use parameterisations of the model from Laslett et al. (1987) for Durango apatite ([Cl] / [Cl + F] ≈ 0.2) and Crowley et al. (1991) for both Durango and Fluor-apatite ([Cl] / [Cl + F] ≈ 0.02). The Crowley et al. (1991) model for F-apatite leads to a larger degree of fanning in the Arrhenius plots than the Laslett et al. (1987) Durango model (i.e. B and consequently E are more strongly dependent on the amount of annealing r; c.f. Figure A1-1). As a result of this, on geological timescales, model F-apatites will anneal more quickly than Durango apatites at low temperatures (< 60°C) but slower at high temperatures.

A1.1 FORWARD MODEL

Annealing algorithm

The forward model calculates an apatite fission track age (FTA) and fission track length distribution (FTLD) from a given thermal history (i.e. a set of t,T points). The model is practically similar to that published by Lutz and Omar (1991); there are some minor differences in the parameters adopted. Track length reduction r is related to absolute temperature T (K) and annealing time t (s) by the function:

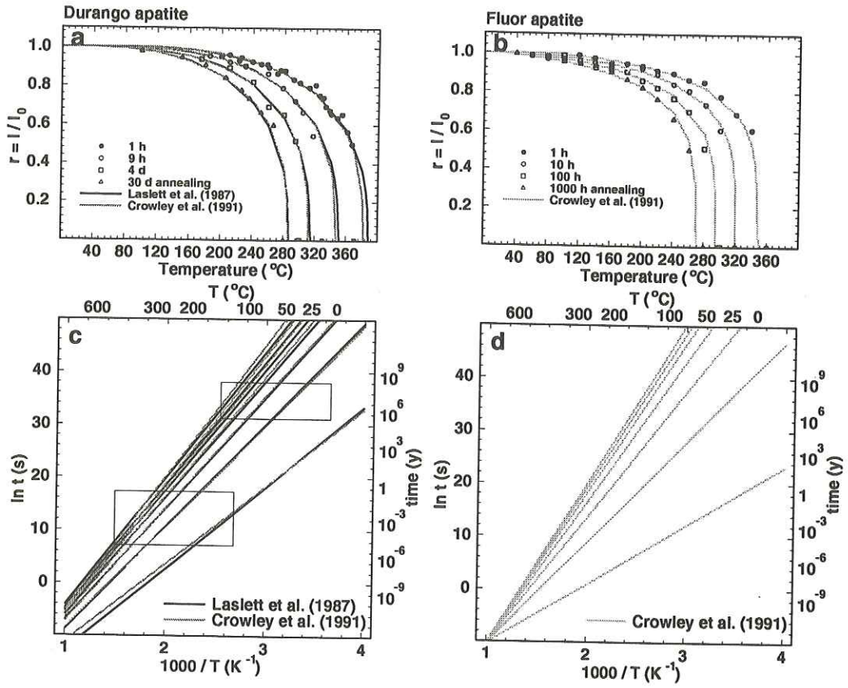

Figure A1-1. Annealing models of Laslett et al. (1987) and Crowley et al. (1991) fitted to laboratory data for Durango apatite (a) and Fluor apatite (b); Arrhenius plots for Durango apatite (c) and F-apatite (d). Laboratory data are from Green et al. (1986; a) and Crowley et al. (1991; b); lines in Arrhenius plots are for r = 0.99 (lower right), 0.90, 0.80, 0.70, 0.50, 0.10 and 0.01 (upper left). Boxes in (c) denote approximate t-T ranges for laboratory experiments (lower) and natural annealing (upper).

$$g(r;a,b) = C_0 + [C_1 \ln(t) + C_2] \,/\, [\left(\frac{1}{T}\right) - C_3] \qquad \text{(A1.2)}$$

with

$$g(r;a,b) = \{[(1 - r^b)/b]^a - 1\}/a \qquad \text{(A1.3)}$$

The track length reduction is defined as the ratio between the length (l) of an annealed track and the unannealed track length (l_0): $r = l \,/\, l_0$. The constants a, b, C_0, C_1, C_2 and C_3 were derived by fitting laboratory annealing data (Figure A1-1) and are given in Table A1-1. The parameter C_3 in the models of Crowley et al. (1991) is interpreted as the reciprocal 'critical

Table A1-1. Parameters for the annealing models used

model	parameter					
	a	*b*	C_0	C_1	C_2	C_3
Laslett et al. (1987) Durango	0.35	2.7	-4.87	0.000168	0.00472	0
Crowley et al. (1991) Durango	0.49	3.0	-3.202	0.0000937	0.001839	0.0004200
Crowley et al. (1991) F-apatite	0.76	4.16	-1.508	0.00002076	0.0002143	0.0009967

temperature' at which fission tracks anneal instantaneously. In the Laslett et al. (1987) model, $C_3 = 0$ and consequently $T_c \rightarrow \infty$.

The above equations define an isothermal annealing model; they can be applied to a variable temperature history by approximating this by a series of isothermal steps. The amount of annealing at the end of each step is calculated using the 'equivalent time' algorithm (Duddy et al., 1988):

$$g(r_j;a,b) = C_0 + [C_1 \ln(t_{eq} + \Delta t_j) + C_2] \,/\, [\left(\frac{1}{T_j}\right) - C_3] \qquad \text{(A1.4)}$$

where r_j is the reduced track length at the end of the jth isothermal step, Δt_j is the duration of the jth step and T_j is the temperature during the jth step. t_{eq} is the equivalent time, defined by:

$$\ln(t_{eq}) = \left(\frac{-C_2}{C_1}\right) + \left(\frac{[g(r_{j-1};a,b) - C_0]}{C_1}\right)\left[\left(\frac{1}{T_j}\right) - C_3\right] \qquad \text{(A1.5)}$$

Equations (A1.2) to (A1.4) are undefined over certain t-T intervals near $r = 0$ and $r = 1$ because of the exponents in (A1.3). The regions where this occurs are where:

$$\ln(t) \leq \left[\frac{(-aC_0 - 1)}{aC_1}\right]\left[\left(\frac{1}{T}\right) - C_3\right] - \left(\frac{C_2}{C_1}\right) \qquad \text{(A1.6)}$$

near $r = 1$ and

$$\ln(t) \geq \left[\frac{\left(\frac{1}{b}\right)^a - aC_0 - 1}{aC_1}\right]\left[\left(\frac{1}{T}\right) - C_3\right] - \left(\frac{C_2}{C_1}\right) \qquad \text{(A1.7)}$$

near $r = 0$.

This problem is circumvented by choosing a sufficiently large time step (1 My) to fall outside of range (A1.6) and stopping the calculations when $t_{eq}+\Delta t$ satisfies (A1.7). From there on, $r = 0$ is adopted.

The principle of equivalent time presumes that at any moment, a track which has been annealed to a certain degree behaves during further annealing independently of the conditions which caused the previous annealing. Further annealing depends only on the degree of annealing that has already occurred, and the prevailing *t-T* conditions. The order in which the isothermal steps occur is, therefore, not important.

The isothermal steps are chosen to be of equal length (1 My) and the associated temperature is gained by linear interpolation between input points of the thermal history. The annealing history is traced for a set of representative tracks, that are formed each at the beginning of a new time step. This procedure assumes that fission track production rate is constant through time. The half life for spontaneous fission of ^{238}U is sufficiently long (9.9×10^{15} y; Fleischer et al., 1975) to warrant this assumption, for time scales less than about 500 My. All newly formed tracks share a similar thermal history with existing tracks from their formation onward. Therefore, the principle of equivalent time allows all of the reduced track lengths to be calculated in a single pass through the isothermal steps in reverse order. In this manner the evolution of the track length reduction can not be traced but computing time is greatly reduced (e.g., a factor 595 for a 100 My history).

Calculation of FTLD

The calculated set of n reduced track lengths is transformed to a binned fission track length distribution (FTLD) using a probability density function $f(r)$. This procedure is required because a given amount of annealing does not lead to a single value of r but to a range in r, as a result of the anisotropy of annealing as well as the range in chemical composition and annealing properties of apatite in the sample (Green et al., 1986; Donelick et al., 1990). Following Lutz and Omar (1991), I use the function:

$$f(r) = (1/n)\sum_{j=1}^{n} K[(r-r_j)/\sigma]/\sigma \qquad \text{(A1.8)}$$

where σ is the standard deviation and $K[x]$ is a distribution function. A Gaussian distribution is most applicable (e.g., Crowley, 1985):

$$K[x] = \left(\frac{1}{2\pi}\right)^{\frac{1}{2}} e^{\left(-\frac{x^2}{2}\right)} \qquad \text{(A1.9)}$$

The standard deviation σ in (A1.8) is itself a function of r (Green et al., 1986). Different forms for this function have been suggested. Donelick (1988) uses a single second or third order (σ,r) relationship for the whole spectrum of r. This leads to very high values of σ for low r, which are not substantiated by measurements. Therefore, I follow Lutz and Omar (1991) in

using a 3-tier linear relationship with, however, slightly different parameter values (obtained from a linear regression of the data of Green et al. (1986); the values are not well constrained, with correlation coefficients well below 0.5):

$$\begin{aligned} \sigma &= 2.53 && r \le 0.43 \\ \sigma &= 5.08 - 5.93r && 0.43 < r \le 0.67 \\ \sigma &= 1.39 - 0.61r && 0.67 < r \end{aligned} \qquad \text{(A1.10)}$$

Note that this expression gives the real standard deviation (in µm) and not a normalized one. Therefore the term $(r - r_j)$ in (A1.8) should also be expressed in real values. A histogram of FTLD is now constructed by integration of (A1.8) over the range of r spanned by each histogram cell, and normalizing to 100%. The step size for evaluation and integration of (A1.8) is set to 0.01. This approach should be roughly similar to that of Green et al. (1989b), although they do not provide details on the algorithm used.

Calculation of FTA

Calculation of FTA is based on the observation of Green (1988), that the contribution to observed fission track density, and therefore FTA, of a particular track is dependent on the final length of that track. For n representative tracks produced, the contribution of each track to the total track density is calculated. The relationship between the reduced track density ($d = \rho / \rho_0$) and the reduced track length (r) has been estimated from the data of Green (1988) by Lutz and Omar (1991):

$$\begin{aligned} d &= 0 && r \le 0.35 \\ d &= 2.15r - 0.76 && 0.35 < r \le 0.66 \\ d &= r && 0.66 < r \end{aligned} \qquad \text{(A1.11)}$$

FTA is calculated by multiplying the mean reduced density by the modelled time span (t_a):

$$FTA = \frac{R_n t_a \left(\sum_{j=1}^{n} d(r_j)\right)}{n} \qquad \text{(A1.12)}$$

Since the number of representative tracks n is always equal to the modelled fission track age t_a, (A1.12) reduces to a simple summation of the reduced densities of the n tracks:

$$FTA = R_n \sum_{j=1}^{n} d(r_j) \qquad \text{(A1.13)}$$

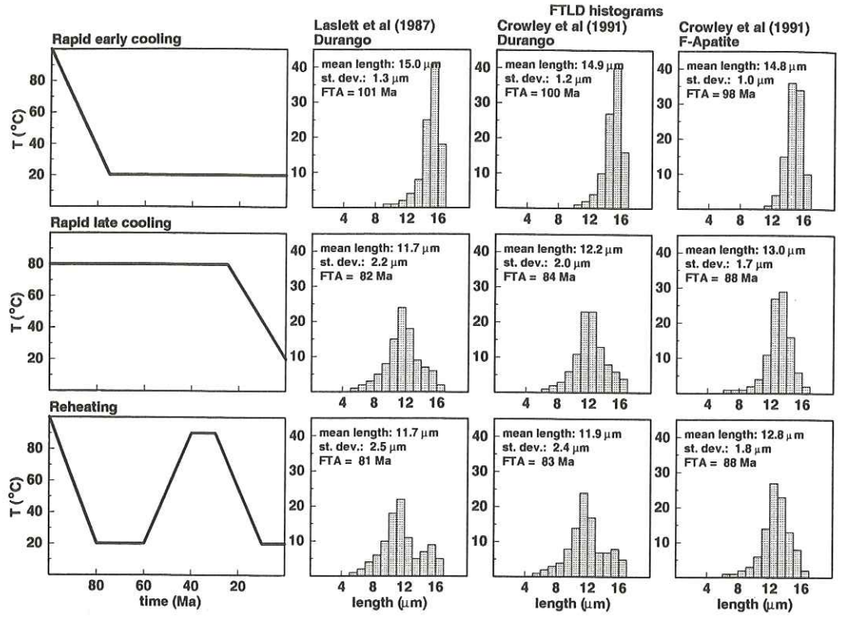

Figure A1-2. Forward modelling results for the three annealing models employed. FTA and FTLD are predicted for three representative thermal histories; l_0 = 16.5 µm and l_{STD} = 15.0 µm.

The factor R_n renormalises the calculated FTA to calibrate it against fission track age standards which have a mean length of spontaneous tracks (l_{std}) around 14.5-15 µm; $R_n = l_0 / l_{std}$.

Examples of the forward model output are given in Figure A1.2, for the three different annealing models adopted here.

Correcting for length bias

Optical measurements of track length distributions are biased against sampling short tracks, because these have a smaller probability of intersecting etching conduits. Laslett et al. (1982) proposed a geometrical correction to eliminate this length bias from observations:

$$f_{mi} = \frac{\frac{f_i}{r_i}}{\sum_{i=1}^{N} \frac{f_i}{r_i}} \qquad \text{(A1.14)}$$

where f_i is the observed frequency in the ith bin and f_{mi} is the corrected frequency in that bin. The forward model, as implemented here, optionally introduces length bias in the predicted track length distributions by numerically inverting (A1.14). The algorithm adopted to perform the inversion consists of calculating the unbiased length distribution (A1.14) from an iteratively adjusted biased distribution and comparing this with the predicted distribution, using a least squares goodness-of-fit criterion (cf. eq. A1.17, A1.18).

A1.2 INVERSE MODEL

Inversion of AFT data to a thermal history depends on a search routine and statistical goodness-of-fit criteria. Donelick (1988) calculates a best-fit *t-T* path by resolving the observed track length distribution into a best-fit sum of weighted component distributions. For each of these components, a best-fit *t-T̄* segment is calculated. The method is mathematically elegant and computationally simple, but is strictly applicable to cooling histories only. Lutz and Omar (1991) use an iterative approach (the multidimensional downhill simplex algorithm) to systematically modify a starting thermal history to achieve satisfactory statistical agreement between predicted and observed FTA and FTLD. This best-fit history is then used to yield a spectrum of thermal histories capable of fitting the data, using Monte Carlo simulations. Willet (1992) uses a similar Monte Carlo approach, but searches through the entire *t-T* space, keeping and updating a set of best-fitting thermal histories until these approach a predetermined fit. Gallagher (1994) also uses an adapted Monte Carlo approach known as genetic algorithms, but details on this method have not yet been published. Corrigan (1991) directly generates spectra of thermal histories using the technique of 'simulated annealing' (Metropolis algorithm).

The implementations of Corrigan (1991), Lutz and Omar (1991) and Willett (1992) all require significant computer time to arrive at a best-fit solution. In Corrigan's approach the thermal history is described by Chebichev polynomials, which has the disadvantage that additional geological information on the thermal history is not easily incorporated in the model. On the other hand, analytical and modelling uncertainties are as yet important enough to render the construction of a thermal history spectrum necessary, as putting too much emphasis on a single best-fit thermal history would be misleading. Therefore, I use the algorithm of Donelick (1988) to find a best-fit thermal history, and then use this to calculate a thermal history spectrum following Lutz and Omar (1991). Model testing, as well as an interlaboratory calibration at the 7th International fission track thermochronology workshop (Philadelphia, 13-17 July 1992), has shown that the performance of this approach is similar to that of other inversion techniques, while the computational effort required is kept well within reasonable limits.

Calculation of best-fit thermal history

Inversion of AFT data into a best-fit thermal history using the algorithm of Donelick (1988) is a four step procedure. First, the observed FTLD (optionally corrected for length bias using eq. A1.14) is resolved into a best-fit sum of weighted component distributions. Then the duration of the modelled time span is calculated, using the observed FTA and the component distributions. These are combined to assign time intervals for each of the components and, finally, average temperatures for each time interval are found, using an iterative procedure. Data input for the model comprises the measured FTA and its standard deviation, and the FTLD (distributed into 17 1µm-wide bins).

The concept of component distributions stems from the notion that natural fission track populations are characterized by a number of component populations of tracks, each of these having experienced a different part of the overall *t,T* history (Donelick, 1988). The inversion problem is to find the set of component distributions which, when summed with appropriate weighting factors, give the best fit to the observed FTLD. The weighting factor of a component distribution corresponds to the fraction of the total thermal history that is recorded by that component. The component distributions are represented by Gaussian distributions with means at the midpoints of the FTLD bins:

$$f_{i,j} = \frac{w_j}{\sqrt{2\pi}} e^{\left\{\frac{-(\bar{l}_j-\bar{l}_i)^2}{2\sigma_j^2}\right\}} \qquad \text{(A1.15)}$$

Each component distribution j is characterized by its mean length $\bar{l}_j$, a weighting factor w_j and a standard deviation σ_j. The standard deviation is again a function of mean length, and is given by (A1.10). The cumulative distribution f_{ci} is the normalized sum of the contributions from the N component distributions:

$$f_{ci} = \frac{\sum_{j=1}^{N} \frac{w_j}{\sqrt{2\pi}} e^{\left\{\frac{-(\bar{l}_j-\bar{l}_i)^2}{2\sigma_j^2}\right\}}}{\sum_{i=1}^{N}\sum_{j=1}^{N} \frac{w_j}{\sqrt{2\pi}} e^{\left\{\frac{-(\bar{l}_j-\bar{l}_i)^2}{2\sigma_j^2}\right\}}} \qquad \text{(A1.16)}$$

The goodness-of-fit of the cumulative distribution (f_{ci}) to the observed (corrected) distribution (f_i) is determined using a least-squares criterion:

$$e^2 = \sum_{i=1}^{N''} (f_i - f_{ci})^2 \qquad \text{(A1.17)}$$

where N'' is the number of bins for which f_i and f_{ci} are not simultaneously equal to 0. This fit can be improved by adjusting the N weighting factors w_j of the component distributions. A method that quickly converges towards a minimum proceeds as follows: bin h, with the largest positive error $e_h = (f_h - f_{ch})$, and bin k, with the largest negative error $e_k = (f_k - f_{ck})$, are identified, and these are assigned new weighting factors according to:

$$w_h^{new} = w_h^{old} - \Delta w$$

and (A1.18)

$$w_k^{new} = w_k^{old} + \Delta w$$

The cumulative distribution (A1.16) is recalculated and the mean squared deviation (A1.17) is compared to the previous one, until a best fit is obtained. To avoid being trapped in local minima, the procedure is then restarted until 40 successive attempts do not lead to a smaller mean squared deviation. A value of $\Delta w = 0.5\%$ is used, and generally leads to convergence within 100 iterations.

The time-span (t_a) to be modelled (which can be considered as the age of the oldest fission track present in the sample) is calculated from the inverse of (A1.12), modified to sum the contributions of the N' component distributions for which $w_j > 0$:

$$t_a = \frac{FTA}{R_n \sum_{j=1}^{N'} w_j d(\bar{r}_j)} \qquad \text{(A1.19)}$$

with $d(r)$ as in (A1.11). The fraction of the thermal history represented by component distribution i is now simply given by the weighting factor w_i:

$$\Delta t_i = w_i t_a \qquad \text{(A1.20)}$$

The thermal history is thus divided into N' segments with the time (t_i) at the end of each segment given by:

$$t_i = t_a - \sum_{j=1}^{i} \Delta t_j \qquad \text{(A1.21)}$$

The final problem is the determination of the mean temperature $\bar{T}$ during each time interval. This is found by iteration between $\bar{T} = T_{min}$ (0°C) and $\bar{T} = T_{max}$ (130° C), using equation (A1.2) for the N'^{th} interval. For the intervals j = 1 to (N' - 1), the iterative procedure first finds the appropriate equivalent time t_{eq} pertaining to $\bar{l}_{(j+1)}$ using (A1.5), and then applies equation (A1.4). The best-fit mean temperature $\bar{T}_j$ is that which gives the closest approximation to $\bar{l}_j$.

The best-fit thermal history is defined, by the above, as N' [Δt,$\bar{T}$] segments and has a staircase geometry. Examples of the application of this inverse procedure are given in Figure A1-3, for the three thermal histories that were used in the forward model, and the annealing model of Laslett et al. (1987). As shown by the figure, the inversion technique

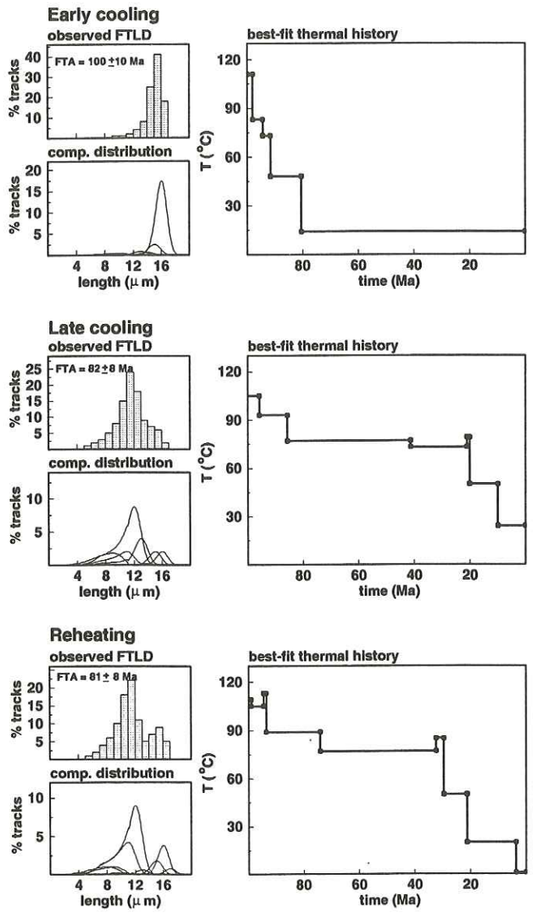

Figure A1-3. Best-fit thermal histories from inverse modelling of the synthetic AFT data of Figure A1-2, and the annealing model of Laslett et al. (1987).

performs well for relatively simple cooling histories. The method is, however, not capable of detecting a thermal peak; it 'smears out' the annealing effect of a peak over the previous thermal history. This phenomenon suggests that the observed FTA and FTLD permit a range of thermal histories and it is, therefore, necessary to construct thermal history spectra, in which such a thermal peak can be incorporated.

Calculation of thermal history spectra

If a thermal history that fits the observed FT data is defined by a set of time, temperature points $[t, T]$, then some thermal histories that are variants of these points, i.e. $[t \pm \delta t, T \pm \delta T]$, may also be statistically acceptable. The technique of calculating a spectrum of acceptable thermal histories comes down to defining the magnitudes of δt and δT. This is done by Monte Carlo simulation: regions $[t \pm \delta t, T \pm \delta T]$ (so called Monte Carlo boxes) are defined and random thermal histories which pass through these regions are generated. The sets of $[t, T]$ points that yield FTA and FTLD statistically indistinguishable from the observed FTA and FTLD then describe the spectrum.

Concerning the placement of Monte Carlo boxes, note that the spectrum of thermal histories that are statistically acceptable may be expected to lie around the best-fit history. Changes in slope in the best-fit thermal history can be readily detected, and these may be used as the midpoints of the $[t \pm \delta t, T \pm \delta T]$ boxes. On the other hand, as is clear in Figure A1-3(c) the 'real' thermal history may be quite different from the calculated best-fit history. Boxes which are placed around the changes in slope of the best-fit history will lead to a spectrum which does describe the data but is nevertheless erroneous. Therefore, geological criteria should, whenever possible, be incorporated in constraining the Monte Carlo spectrum.

In the implementation developed here, 5 Monte Carlo boxes may be placed to describe the thermal history. This may be considered as roughly the limit of complexity of a thermal history that can be detected by AFT thermochronology. One of the boxes may include a thermal peak. In the case where box j contains a thermal peak, only histories are considered for which $T_j > T_{(j-1)}$ and $T_j > T_{(j+1)}$. The present day sample temperature T_0 is also user-defined, as well as the range of starting times ($t_a \pm \delta t$). The starting temperature is kept fixed at 120-130° C, which is sufficient to erase all pre-existing tracks within 1 My. A maximum of 500 Monte Carlo thermal histories are then generated, and for each thermal history the resulting FTA and FTLD are calculated from the forward model (c.f. Section A1.1).

The degree of fit between FTA and FTLD calculated from a Monte Carlo history and the observed FTA and FTLD are expressed by an objective function G which consists of two independent terms:

$$G = g(\Delta FTA) + h(\Delta FTLD) \tag{A1.22}$$

Where $\Delta FTA = FTA_{obs} - FTA_{mod}$ and $\Delta FTLD = FTLD_{obs} - FTLD_{mod}$. For g the function

$$g(\Delta FTA) = \left(\frac{\Delta FTA}{\sigma_{FTA}}\right)^2 \tag{A1.23}$$

is used, with σ_{FTA} the standard error in measured FTA, and the test is passed when $g(\Delta FTA) \leq \delta^2$. The default significance level $\delta = 0.5$, i.e. histories are accepted which have $\Delta FTA \leq \frac{1}{2}\sigma_{FTA}$.

The function h is determined by a Kolmogorov-Smirnov criterion (e.g., Conover, 1980). Cumulative differences D_j are defined as:

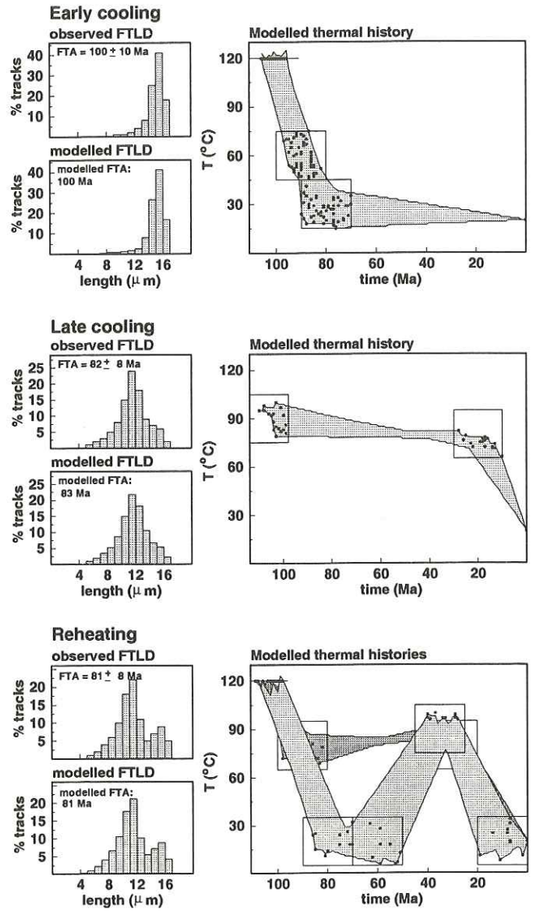

Figure A1-4. t-T spectra that fit the data using the given statistical rejectance level, constructed using a Monte-Carlo approach. Monte Carlo boxes and fitting t,T points are also shown. For the 'Reheating' case, thermal history spectra both in- and excluding a thermal peak were calculated. All spectra were generated by running 300 random thermal histories, rejectance levels were ±½σ for FTA and the Kolmogorov-Smirnov criterion with α = 0.20 for FTLD (see text).

$$D_j = \sum_{i=1}^{j} [FTLD_{i(obs)} - FTLD_{i(mod)}] \qquad \text{(A1.24)}$$

and the function is:

$$h(\Delta FTLD) = \frac{\max(|D_j|)}{n} \qquad \text{(A1.25)}$$

The K-S test is passed if h is smaller than a critical value, corresponding to the level of significance α with which the history can be rejected or accepted. These values are from Conover (1980), with α = 0.20, 0.10, 0.05, 0.02 or 0.01, and 16 degrees of freedom. Resulting thermal history spectra are given in Figure A1-4.

Geological Implementation

Quantitative analyses of apatite fission track data, such as presented above, are rapidly becoming more popular. Although extrapolation of the models, based on laboratory experiments, to geological time scales seems reasonable (Green et al., 1989a), some care should be taken. Both the Laslett et al. (1987) annealing model for Durango apatites and the Crowley et al. (1991) model for F-apatite may contain systematic errors as a result of the extrapolation. Vrolijk et al. (1992) and Ravenhurst et al. (1994) showed that the Laslett et al. (1987) model may underestimate annealing at low (<60°C) temperatures. On the other hand, the high temperature (>90°C) stability of tracks may be larger than that predicted by the Laslett et al. (1987) model (Naeser et al., 1990; Wagner et al., 1994). In a study of natural apatite annealing in differentially buried Oligocene strata in South Texas, Corrigan (1993) provides additional evidence for these inferences and also shows that the Crowley et al. (1991) model exhibits an opposite behaviour, i.e. overestimation of annealing at low temperatures and underestimation at high temperatures (Figure A1-5). Traditionally, F-apatites were believed to have a lower total annealing temperature (~110°C) than Cl-rich apatites (~125-130°C; e.g., Green et al., 1989a). The Crowley et al. (1991) parameterisation contradicts this inference but, surprisingly, seems to fit available data from sedimentary

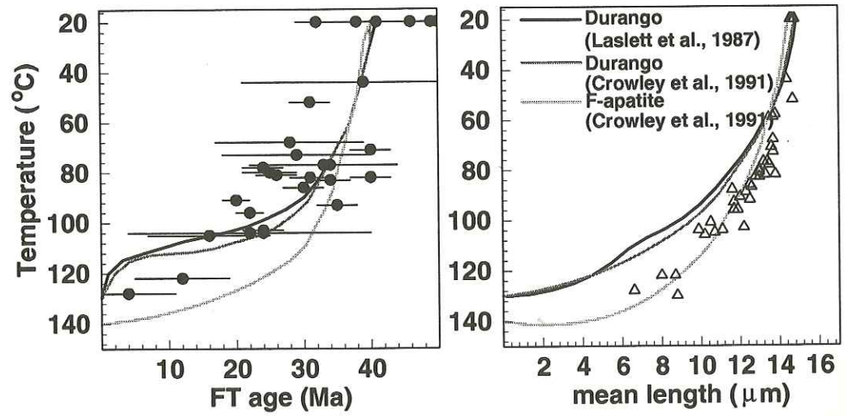

Figure A1-5. Age/temperature and mean length/temperature plots for apatites recovered from Oligocene strata of the Gulf Coast, South Texas (a sedimentary basin with a well known thermal history), compared with predictions of the Laslett et al. (1987) and the Crowley et al. (1991) annealing models (after Corrigan, 1993).

basins better than the Laslett et al. (1987) model (Corrigan, 1993; Rohrman et al., 1995b, J.-P. Stiberg, pers. commun. 1994).

Apart from possible systematic errors in the annealing models, observational errors also influence the applicability of quantitative inversion algorithms. For thermal histories which include a significant amount of time spent within the partial annealing zone, forward models predict strongly negatively skewed track length distributions, including tracks shorter than 4 µm. In practice however, tracks <7-8 µm are not observed. The length-bias algorithm of Laslett et al. (1982; eq. A1-14) does not correct for this discrepancy, because it only affects length bins which contain a finite number of measurements. Thus, annealing models systematically predict lower mean lengths and higher standard deviations than observed, for mean lengths <~12.5 µm. On the other hand, differential etching conditions and the compositional range of apatites studied may result in larger standard deviations than those predicted by the (mono-compositional) models.

The result of these uncertainties is that inversion of AFT data, especially when the Laslett et al. (1987) model is employed, often predicts thermal histories with a characteristic staircase geometry: rapid early and late cooling events are separated by a significant amount of time spent around ~60°C (cf. Figures 3-18, 4-10, 5-11). Care should be taken in interpreting these thermal histories, and the possibility that they are, at least partly, a model artefact should be taken into account.

APPENDIX 2

SAMPLE DETAILS

Table A2-1. Details for Baikal rift flank samples (Table 3-1).

sample	lab no.	location	latitude	longitude	elev.	lithology
ba 058	1184	Sarminski Gonets	N53:02:44	E106:42:23	1040	mylonitic gneiss
ba 060	1182	Sarminski Gonets	N53:03:17	E106:42:00	1180	sheared granite
ba 061	1183	Sarminski Gonets	N53:03:55	E106:39:51	1330	sheared granite
bai 1	1154	Sarma river mouth	N53:07:44	E106:50:00	500	mylonitic qz-fsp gneiss
bai 2	1155	Sarma river mouth	N53:08:00	E106:50:41	720	mylonitic qz-fsp gneiss
bai 3	1156	Sarma river mouth	N53:08:00	E106:50:55	960	qz-fsp-bi gneiss
bai 4	1157	Sarma river mouth	N53:08:32	E106:50:55	1050	felsic gneiss
bai 5	1158	Sarma river mouth	N53:08:32	E106:50:14	820	qz-fsp-bi gneiss
bai 6	1159	Muchar bay	N53:01:52	E106:45:14	455	amphibolite
bai 7	1160	"989 peak"	N52:57:41	E106:48:52	990	metagabbro
bai 8	1161	"989 peak"	N52:58:56	E106:48:25	830	gt bearing qz-fsp-bi gneiss
bai 9	1162	"989 peak"	N52:59:36	E106:47:03	625	amphibolite
bai 10	1163	Olkhon gate	N53:00:48	E106:54:33	455	qz-fsp-bi gneiss
bai 11	1164	"989 peak"	N52:56:32	E106:47:57	455	chl bearing quartzite
bai 14	1165	Tyrdan quarry	N52:44:36	E106:19:15	675	metagabbro
bai 15	1166	Kyret river	N52:48:16	E106:15:00	730	schistose rapakivi granite
bai 16	1167	Kodja Stej village	N52:50:56	E106:03:58	730	Vendian sandstone
bai 17	1168	Barguzin road	N51:56:14	E107:41:53	1020	granite
bai 18	1169	Barguzin road	N51:58:39	E107:42:04	1200	bi-fsp bearing meta-arkose
bai 19	1170	"1349 peak"	N52:01:05	E107:44:04	1300	granite
bai 20	1171	Irkilik valley	N52:07:00	E107:45:23	700	diorite
bai 21	1172	Ostrog village	N52:09:57	E107:26:37	500	leucocratic migmatite
bai 22	1173	road to Chergino	N52:12:23	E107:09:10	700	metagabbro
bai 27	1176	"1510 peak"	N51:23:02	E106:01:07	1250	quartzite
bai 30	1179	Sarmen Edzje mnt	N51:16:41	E106:10:19	1030	metadacite
bai 32	1180	Otsjurkovo quarry	N51:56:30	E107:26:42	640	ap bearing diorite

Table A2-2. Details for Malawi rift flank samples (Table 3-2).

sample	lab no.	location	latitude	longitude	elev.	lithology
DD013	942	Njombe	S09:32:07	E34:76:25	1890	granite
DD298	1086	Tanesco dam	S10:00:53	E34:35:12	1840	granite
DD486	941	Mlangali	S09:44:36	E34:36:55	1990	
DD115a	937	Livingstone Mts.	S09:59:37	E34:35:15	2200	granodioritic gneiss
DD478	938	Livingstone Mts.	S10:00:30	E34:35:40	2060	granodioritic gneiss
DD122	1083	Idofu, Luika	S10:00:18	E34:36:22	1530	dioritic gneiss
DD483	934	Livingstone scarp	S10:01:15	E34:33:48	1340	amphibolite
DD482	1089	Livingstone scarp	S10:01:18	E34:33:17	1110	amphibolite
DD484	1090	Mbuyura	S10:01:33	E34:33:04	905	amphibolitic gneiss
DD480	1088	Mbuyura	S10:01:30	E34:32:32	675	amphibolitic gneiss
DD485a	943	Lupingu	S10:03:49	E34:32:19	460	granitic gneiss
DD503	1091	Lufirio	S09:16:41	E33:51:51	890	
T92/22B	1085	Bulongwa	S09:18:51	E34:05:18	1280	feldspathic granite
T92/22A	1084	Bulongwa	S09:23:43	E34:01:43	1970	anorthosite
DD512	1092	Kashima hill	S09:27:06	E33:34:47	2020	
DD510	1098	Kitoye river	S09:30:48	E33:30:16	1250	
DD509	1093	Chija river	S09:29:52	E33:32:55	1120	
DD508	1097	Kyela - Itumba road	S09:30:11	E33:37:26	1000	
DD514a	1094	Mwalisi river	S09:30:13	E33:39:19	650	
DD329a	1087	Songwe coal mine	S09:28:30	E33:41:19	600	

Table A2-3. Details for samples from southern Norway (Table 4-1).

sample	lab no.	location	latitude	longitude	elev.	lithology
92-1	928	Rubbestadneset	N59:49:00	E5:17:25	0	granite
92-3	924	Markhus	N59:48:14	E6:13:09	35	metagabbro
92-4	933	Skare	N59:54:38	E6:37:18	525	augengneiss
92-5	906	Vlevavatnet	N59:51:22	E7:08:36	990	biotite granite
92-6	925	Haukelifjell	N59:45:13	E7:34:34	640	granite
92-9	918	Ånevatn	N60:23:52	E8:29:30	1020	hbl-granite
92-10	916	Ustevatn	N60:30:11	E8:02:06	1020	gabbro
92-14	932	Fjell	N60:19:56	E5:05:12	30	amphibolite
92-15	930	Espevik	N59:54:27	E5:39:21	0	lamprophyre
93-1	1015	Oppedahl	N61:03:56	E5:31:01	5	felsic gneiss
93-3	1017	Midgulen	N61:43:16	E5:15:09	0	Devonian sandstone
93-4	1018	Vestkappen	N62:11:45	E5:11:37	100	amphibolite
93-5	1019	Leknes	N62:12:30	E6:32:20	0	bi-gneiss
93-6	1020	Stryen	N61:53:48	E6:41:50	20	bi-amph gneiss
EID-11	913	Store Ishaug	N60:28:04	E7:13:03	1230	gneissic granite
EID-13	931	Smyttestolen	N60:27:01	E7:15:18	965	granitic gneiss
EID-15	909	Eidfjord	N60:25:54	E7:12:05	345	migmatitic gneiss
EID-16	914	Eidfjord	N60:25:21	E7:12:07	180	bi-gneiss
EID-17	908	Eidfjord	N60:28:27	E7:02:07	0	gneiss
JOT-1	920	Galdhøpiggen	N61:38:10	E8:19:14	2465	gabbroic gneiss
JOT-3	907	Galdhøpiggen	N61:38:10	E8:20:22	2150	metagabbro
JOT-5	917	Galdhøpiggen	N61:37:38	E8:22:29	1855	gneiss
JOT-9	921	Galdhøpiggen	N61:37:39	E8:23:47	1240	amphibolite
JOT-11	912	Krosbu pass	N61:34:16	E8:00:07	1430	diorite
JOT-12	915	Helgdalen	N61:30:25	E7:48:58	1010	amphibole schist
JOT-14	911	Bergsdalen	N61:29:59	E7:45:37	560	schistose quartzite
JOT-17	922	Skjolden	N61:29:45	E7:35:28	0	granitic gneiss
GAU-1	881	Gausta	N59:51:02	E8:39:39	1845	quartzite
GAU-3	926	Gausta	N59:50:30	E8:39:39	1670	metasandstone
GAU-5	867	Gausta	N59:50:30	E8:40:43	1590	gabbro
GAU-7	923	Gausta	N59:49:26	E8:41:48	1385	metawacke
GAU-9	871	Gausta	N59:48:53	E8:41:48	1250	amphibolite
GAU-11	929	Gausta	N59:51:35	E8:40:43	980	gabbro
GAU-12A	872	Gausta	N59:52:07	E8:41:47	870	amphibolite
GAU-15	919	Gausta	N59:53:12	E8:41:46	480	metarhyolite

Table A2-4. Details for samples from the Oslo Rift (Tables 5-1, 5-2).

sample	lab no.	location	latitude	longitude	elev.	lithology
B9	810	Slattas	N58:50:09	E09:25:00	30	amphibolite
DL129	814	Ringsjø	N58:57:40	E09:33:23		Cl-apatite vein
T3[A]	790	Haugsjasund	N58:57:08	E08:29:45	180	granodiorite
T3[B]	791[s]	Haugsjasund	N58:57:08	E08:29:45	180	pegmatite
T8	745	Amdal (Tinnsjø)	N59:55:23	E08:57:51	680	hornblendite
T14	796	Fossholt	N60:33:30	E09:47:03	400	Hedal granite
T15	797	Aurtjernasen	N60:38:58	E09:28:31	1000	Hedal granite
T17	873	Bromma river	N60:29:18	E09:14:12	200	amphibolite
T18	962[z]	Bruflat	N60:39:32	E10:35:30	400	hbl-gneiss
K1	799	Darbu	N59:41:46	E09:47:58	100	amphibolite
K5	857	Kongsberg mine	N59:38:36	E09:36:11	340	amphibolite
K9	743	Jonsknuten	N59:40:14	E09:30:53	900	amphibolite
K11	795	Kloftefoss	N60:05:28	E09:49:37		pegmatite
Ø2	747	Furuholmen	N59:07:08	E10:54:14	0	Bohus granite
Ø3	878	Nesodden	N59:49:23	E10:38:26	0	gabbroic sill
Ø6	792	Ski	N59:44:17	E10:56:20	140	garnet amphibolite
Ø7	874	lake Øyeren	N59:51:07	E11:07:27	100	amphibolite
Ø10	861	Bøensfjorden	N59:20:23	E11:38:14	120	amphibolite-pyroxenite
Ø12	882	Askim	N59:32:13	E11:10:30	70	amphibolite
Ø14	813	Moss	N59:27:45	E10:44:48	10	amphibolite
M1	860	Eidsvoll	N60:20:09	E11:12:35	200	amphibole skarn
M2	811/961[z]	Sorli	N60:22:06	E11:23:36	330	augengneiss
M5	876	Roverua	N60:16:04	E11:29:40	200	gabbro
M6	877	Jammerdal	N60:12:01	E11:43:26	320	gabbro
M7	869	Vestmarka	N59:56:05	E11:57:10	280	amphibole gneis
OR6	963[z]	Skjelsvik	N59:06:15	E09:38:45	0	SST (Langøyene Fm)
OR9	854	Engelstad	N59:22:20	E09:54:54	100	latite (RP26)
OR11	808/826[z]	Elvik	N60:06:17	E10:20:56	140	Ringerike SST
OR14	741	Ula	N59:01:43	E10:11:04	0	monzonite (larvikite)
OR15	816	Nes (Jeløya)	N59:28:54	E10:38:30	0	Ringerike SST
OR16	964[z]	Konglungen	N59:50:34	E10:29:56	0	SST (Langøyene fm)
OR20	807/825[z]	Grefsenåsen	N59:57:51	E10:50:41	340	rhyolitic tuff
OR22	748/832[z]	Holmestrand	N59:28:02	E10:20:28	0	quartzitic Ringerike SST
OR26	809/829[z]	Vien	N60:19:39	E10:31:16	500	gabbro (Oslo-essexite)
OR27	793	Amundrus	N60:27:08	E10:35:58	590	epidote skarn (Pre-€)
OR28	812/968[s]	Skimtesaeter	N60:27:33	E10:45:49	400	syenite
OR32	855	Sollihogda	N59:58:13	E10:19:32	250	latite (RP1)
OR33	856	Valaug	N60:16:06	E10:56:03	280	syenite (nordmarkite)
OR38	742	Brummundal	N60:55:54	E11:00:40	320	Brummundal SST
OR39	798	Brummundal	N60:55:54	E11:00:40	320	rhomb porphyry

Table A2-4 (continued)

OR45	862	Gullholmen	N59:26:16	E10:34:09	0	B1 basalt
OR46	863	Mellom Sletter Isl.	N59:17:33	E10:41:07	0	RP-lava boulder
OR47	864	Gyrihaugen	N60:05:43	E10:23:04	680	latite (RP11)
OR49	866	Skrukkelia	N60:28:02	E10:49:07	700	latite
OR52	870	SW point Jeløya	N59:25:09	E10:36:13	0	latite (RP2)
OR53	879	Horten	N59:25:51	E10:23:32	70	B1 basalt
OR54	868	Hillestad	N59:30:17	E10:09:57	40	latite (Hegg type RP)

Superscripts 's' and 'z' indicate sphene and zircon fission track samples, respectively.

Sample processing

Apatite, zircon and sphene separates were recovered from whole rock samples using standard magnetic techniques and a centrifuge for heavy liquid separation. Apatites were mounted in epoxy, polished and etched in 7% HNO_3 (1.6 M) at 20°C for 25 to 40 seconds to reveal spontaneous tracks. Zircons and sphenes were embedded in FEP teflon™. Zircons were etched in molten KOH-NaOH eutectic at 220°C for 3 to 8 hours. Sphene was etched in a HNO_3-HCl-HF-H_2O solution, at room temperature, for 6 to 25 minutes. All samples were dated by the external detector method, using a Zeta calibration factor for recommended age standards (Hurford and Green, 1983). Detailed descriptions of the procedure, as well as data for glass standards and Zeta calibration values will be given by Rohrman (manuscript in prep.).

Samples were irradiated in the LFR facility of the Dutch Energy Research Centre (ECN), with nominal fluxes in the range of 1 to 5 × 10^{15} neutrons/cm^2. Neutron fluences were monitored using NBS962, NBS963, CN1 and CN2 glasses. After irradiation, the micas covering the fluence monitors were etched in 48% HF at 20°C for 60 minutes and counted using a 80× dry objective (numerical aperture 0.95). The micas covering the apatite, zircon and sphene mounts were etched in 48% HF at 20°C for 15 minutes. The apatite mounts and detectors were counted using a 80× dry objective (numerical aperture 0.95) with drawing tube and digitising tablet. The zircon and sphene mounts and detectors were counted using a 100× oil immersion objective (numerical aperture 1.25). Track densities were measured only on crystals with sharp polishing scratches parallel to the c-axis for apatite; in all orientations for zircon and sphene.

Lengths of horizontal confined fission tracks in apatite were measured by digitising the track ends using a drawing tube. Durango and Fish Canyon apatite were used as standards for calibrating spontaneous track length determinations. Measured mean lengths are 14.27±0.14 and 14.68±0.11 µm, with standard deviations of 1.0 and 0.72 µm, respectively.

APPENDIX 3

FISSION TRACK ANALYTICAL DATA

Table A3-1. Analytical data for Baikal rift flank samples (Table 3-1).

sample	elev. (m)	number of grains	ρ_s (N_s) (x10^6 cm^{-2})	ρ_i (N_i) (x10^6 cm^{-2})	ρ_d (N_d) (x10^6 cm^{-2})	P(χ^2) (%)	age ±1σ (Ma)	D (%)
BA058	1040	18	0.193 (228)	0.632 (374)	0.025 (3111)	75	87± 9	12
BA060	1180	13	0.654 (58)	0.327 (145)	0.025 (3111)	75	57±10	9
BAI 1	500	16	0.455 (292)	0.838 (269)	2.690 (3314)	25	159±17	14
BAI 2	720	20	1.035 (668)	1.791 (578)	0.025 (3111)	25	165±14	13
BAI 3	960	19	0.204 (212)	0.505 (262)	2.690 (3314)	<1	132±22	57
BAI 4	1050	20	0.067 (85)	0.295 (187)	2.690 (3314)	2.5	74±12	30
BAI 5	820	20	0.130 (145)	0.166 (92)	0.025 (3111)	99	221±32	10
BAI 6	455	18	1.245 (719)	3.227 (932)	2.690 (3314)	50	116± 9	11
BAI 7	990	15	1.877(1162)	4.248 (1315)	2.690 (3314)	50	132± 9	10
BAI 8	830	16	1.547(1144)	3.065 (1133)	0.025 (3111)	10	142±11	13
BAI 9	625	17	0.670 (412)	1.634 (502)	2.690 (3314)	<1	130±14	30
BAI 10	455	20	1.642(1335)	3.910 (1590)	0.025 (3111)	25	120± 9	11
BAI 11	455	19	0.970 (490)	2.110 (533)	2.690 (3314)	2.5	133±14	24
BAI 14	675	20	1.018 (862)	2.189 (927)	2.690 (3314)	2.5	139±10	15
BAI 15	730	20	0.330 (299)	0.921 (417)	0.025 (3111)	25	101±10	12
BAI 16	730	20	0.823 (654)	1.258 (500)	2.690 (3314)	10	195±16	15
BAI 17	1020	20	2.954(1911)	8.252 (2669)	2.690 (3314)	1	107± 6	14
BAI 18	1200	20	1.578 (858)	4.069 (1106)	2.690 (3314)	<1	116± 9	22
BAI 19	1300	20	0.909 (739)	2.504 (1018)	2.690 (3314)	75	111± 8	9
BAI 20	700	20	2.378(1073)	6.502 (1467)	2.690 (3314)	75	112± 7	9
BAI 21	500	18	0.772 (897)	1.727 (1003)	2.690 (3314)	25	133± 9	12
BAI 22	700	20	1.155 (578)	1.526 (382)	2.690 (3314)	10	227±19	15
BAI 27	1250	15	0.653 (410)	0.201 (630)	0.025 (3111)	50	96± 9	12
BAI 32	640	14	0.173 (273)	0.377 (297)	0.025 (3111)	99	130±14	6

ρ_s = spontaneous track density; ρ_i = induced track density (includes 0.5 geometry factor); ρ_d = density of tracks in the glass dosimeter; N_s, N_i, N_d = number of tracks actually counted to determine the reported track densities. All ages are reported as central ages (Galbraith and Laslett, 1993); calculated with ζ = 113.6±3.8 for glass dosimeter CN2 ($\rho_d = 2.690 \times 10^6$) and ζ = 11493±522 for NBS963 ($\rho_d = 0.025 \times 10^6$). P($\chi^2$) = Chi-squared probability that the single grain ages represent one population; D = age dispersion.

Table A3-2. Analytical data for Malawi rift flank samples (Table 3-2).

sample	*elev.* (m)	*number of grains*	ρ_s (N_s) (x10^6 cm^{-2})	ρ_i (N_i) (x10^6 cm^{-2})	ρ_d (N_d) (x10^6 cm^{-2})	$P(\chi^2)$ (%)	age ±1σ (Ma)	D (%)
DD013	1890	16	3.578 (485)	4.707 (319)	2.551(13584)	10	217±20	15
DD298	1840	16	1.880 (973)	2.779 (719)	0.251 (3122)	10	192±15	13
DD486	1990	20	0.911 (216)	1.054 (125)	2.551(13584)	90	246±31	10
DD115a	2200	20	1.627(1080)	2.136 (709)	2.551(13584)	5	216±15	15
DD478	2060	15	1.260 (355)	1.646 (232)	2.551(13584)	75	214±22	10
DD122	1530	15	2.852(1296)	4.459(1013)	0.251 (3122)	75	178±14	9
DD483	1340	13	0.345 (78)	1.069 (121)	2.551(13584)	<1	30±15	145
DD482	1110	20	0.110 (102)	0.184 (85)	0.251 (3122)	99.5	170±27	5
DD484	905	15	0.905 (914)	3.951(1996)	0.251 (3122)	<1	66± 6	25
DD480	675	16	0.229 (165)	1.304 (470)	0.251 (3122)	75	50± 6	11
DD485a	460	15	0.289 (96)	0.643 (107)	2.551(13584)	90	128±20	7
DD503	890	15	0.051 (71)	0.430 (302)	0.251 (3122)	5	35± 6	36
T22B	1280	15	0.180 (55)	0.110 (169)	0.251 (3122)	<1	64±16	70
T22A	1970	12	0.075 (21)	0.653 (92)	0.251 (3122)	99.5	33± 8	3
DD512	2020	20	1.279(1034)	2.659(1075)	0.251 (3122)	10	135±10	14
DD510	1250	12	0.261 (124)	0.391 (93)	0.251 (3122)	75	188±29	9
DD509	1120	9	0.601 (211)	1.709 (300)	0.251 (3122)	50	100±12	12
DD508	1000	20	0.542 (343)	1.131 (358)	0.251 (3122)	50	137±13	13
DD514a	650	20	0.092 (94)	0.121 (62)	0.251 (3122)	99.5	214±37	4
DD329a	600	18	0.104 (90)	0.159 (69)	0.251 (3122)	99.5	186±33	4

All symbols and notations are as in Table A3-1. Ages were calculated with ζ = 113.6 ± 3.8 for glass dosimeter CN2 (ρ_d = 2.551 × 10^6) and ζ = 11493 ± 522 for NBS963 (ρ_d = 0.251 × 10^6).

Table A3-3. Analytical data for samples from southern Norway (Table 4-1).

sample	elev. (m)	number of grains	ρ_s (N_s) (x10^6 cm^{-2})	ρ_i (N_i) (x10^6 cm^{-2})	ρ_d (N_d) (x10^6 cm^{-2})	$P(\chi^2)$ (%)	age ±1σ (Ma)	D (%)
92-1	35	13	1.108 (239)	1.909 (206)	2.5509(13584)	10	181±22	15
92-3	35	20	1.825 (857)	3.191 (749)	0.0258 (1494)	<1	152±17	37
92-4	525	13	3.763 (346)	7.679 (353)	2.5509(13584)	<1	155±23	38
92-5	990	20	0.687 (186)	1.279 (173)	0.0258 (1494)	50	163±20	13
92-6	640	20	0.710 (483)	1.567 (533)	0.0258 (1494)	25	134±11	14
92-9	1020	20	1.075 (432)	2.125 (427)	0.0258 (1494)	25	154±14	12
92-10	1020	20	2.000 (773)	4.451 (860)	0.0258 (1494)	50	133±10	12
92-14	30	20	2.302 (540)	3.556 (417)	2.5509(13584)	2.5	200±20	22
92-15	0	17	2.937 (499)	4.913 (423)	2.5509(13584)	5	189±19	18
93-1	0	20	0.515 (414)	1.329 (534)	0.0272 (1574)	2.5	121±11	21
93-3	0	20	0.680 (305)	1.798 (403)	0.0272 (1574)	50	122±12	12
93-4	100	4	0.388 (75)	0.797 (77)	0.0272 (1574)	97.5	153±29	3
93-5	0	20	0.273 (241)	0.629 (278)	0.0272 (1574)	50	138±15	14
93-6	0	6	0.373 (72)	1.066 (103)	0.0272 (1574)	25	111±20	13
EID11	1230	20	1.510 (750)	2.993 (743)	0.0258 (1494)	25	152±12	13
EID13	965	18	0.687 (514)	1.180 (441)	2.5509(13584)	25	181±17	14
EID15	345	23	0.456 (451)	0.950 (470)	0.0258 (1494)	25	143±13	14
EID16	180	20	0.663 (382)	2.025 (583)	0.0258 (1494)	5	99± 9	15
EID17	0	20	1.250 (488)	3.305 (645)	0.0258 (1494)	<1	111±11	31
JOT1	2465	23	1.455 (745)	2.609 (668)	0.0258 (1494)	25	164±13	14
JOT3	2150	20	0.843 (420)	1.472 (367)	0.0258 (1494)	50	170±16	13
JOT5	1855	20	1.314 (640)	2.563 (615)	0.0258 (1494)	90	156±13	9
JOT9	1240	12	1.398 (370)	3.113 (412)	0.0258 (1494)	50	138+13	11
JOT11	1430	20	2.767(1283)	4.719(1094)	0.0258 (1494)	25	168±12	9
JOT12	1010	19	1.883 (484)	4.188 (538)	0.0258 (1494)	2.5	135±12	19
JOT14	560	20	1.136 (406)	2.305 (412)	0.0258 (1494)	50	146±13	14
JOT17	0	19	0.391 (151)	1.108 (214)	0.0258 (1494)	75	106±13	11
GAU1	1845	14	2.397 (609)	3.778 (480)	0.0261 (1517)	75	195±18	9
GAU3	1670	10	3.980 (407)	4.968 (254)	2.5509(13584)	10	243±28	13
GAU5	1590	19	0.210 (105)	0.372 (93)	0.0261 (1517)	97.5	171±26	10
GAU7	1385	19	0.569 (275)	1.023 (247)	0.0258 (1494)	25	159±17	17
GAU9	1250	20	0.171 (63)	0.260 (48)	0.0261 (1517)	99.5	199±40	7
GAU11	980	7	0.3577 (51)	0.617 (44)	2.5509(13584)	25	183±41	15
GAU12a	870	20	0.345 (132)	0.591 (113)	0.0261 (1517)	50	180±26	24
GAU15	480	18	3.462 (315)	5.827 (273)	0.0258 (1494)	10	174±18	15

All symbols and notations as in Table A3-1. Ages were calculated with ζ = 124±7 for glass dosimeter CN2 (ρ_d = 2.5509 × 10^6) and ζ = 111760±425 for NBS963 (ρ_d = 0.0258 - 0.0272 × 10^6).

Table A3-4. Apatite fission track analytical data for Oslo Rift samples (Table 5-1).

sample	elev. (m)	number of grains	ρ_s (N_s) (x10^6 cm^{-2})	ρ_i (N_i) (x10^6 cm^{-2})	ρ_d (N_d) (x10^6 cm^{-2})	P(χ^2) (%)	age ±1σ (Ma)	D (%)
B9	100	10	1.887 (237)	2.580 (162)	0.0256(1517)	75	218±27	11
DL129		15	0.471 (229)	0.578 (154)	0.0256(1517)	50	237±28	13
TN250		20	0.111 (644)	0.139 (403)	0.0258(1494)	75	240±21	10
T3	180	13	1.843 (456)	2.280 (282)	0.0255(1507)	25	238±23	13
T8	680	14	0.841 (321)	1.551 (296)	0.0256(1517)	2.5	160±19	27
T14	400	11	1.716 (640)	3.122 (582)	0.0256(1517)	0.5	163±15	18
T15[A]	1000	15	0.222 (134)	0.490 (148)	0.0256(1517)	10	132±20	32
T17	200	18	2.000 (649)	4.280 (695)	0.0261(1545)	10	141±11	14
K1	100	14	3.590 (570)	5.101 (405)	0.0256(1517)	25	208±19	12
K5	340	13	1.123 (229)	2.747 (280)	0.0242(1430)	<1	112±16	27
K9	900	15	0.287 (211)	0.433 (159)	0.0255(1507)	2.5	194±27	31
Ø2	0	23	0.668 (402)	1.229 (370)	0.0255(1507)	<1	165±20	40
Ø3	0	21	0.167 (124)	0.270 (85)	0.0261(1545)	75	219±33	12
Ø6	140	14	0.649 (194)	1.097 (164)	0.0256(1517)	50	177±22	13
Ø7	100	20	0.707 (187)	1.050 (139)	0.0261(1545)	50	204±26	14
Ø10	120	19	0.819 (313)	0.989 (189)	0.0242(1430)	10	215±24	14
Ø12	70	12	3.759 (915)	5.825 (709)	0.0261(1545)	25	194±16	11
M2[A]	330	19	0.226 (191)	0.222 (94)	0.0255(1507)	99	283±40	11
M5	200	20	0.350 (161)	0.474 (109)	0.0261(1545)	90	222±30	10
M6	320	20	1.226 (547)	2.088 (466)	0.0261(1545)	50	179±15	11
M7	280	20	1.215 (453)	1.931 (360)	0.0261(1545)	50	204±26	14
OR9	100	23	1.569 (782)	2.708 (675)	0.0242(1430)	50	162±12	12
OR11	140	11	3.741 (386)	5.349 (276)	2.55(13584)[§]	50	215±24	10
OR14	0	13	2.465(1005)	3.763 (767)	0.0255(1507)	5	192±15	14
OR15[A]	0	18	1.112 (428)	1.366 (263)	0.0256(1517)	95	225±23	11
OR20	340	13	0.761 (236)	1.264 (196)	0.0255(1507)	25	179±21	14
OR22	0	16	2.267 (749)	3.668 (606)	0.0255(1507)	10	186±15	14
OR26	500	23	0.457 (190)	0.722 (182)	0.0255(1507)	50	189±24	19
OR27[A]	590	12	0.392 (35)	0.851 (38)	0.0256(1517)	50	131±32	13
OR28	400	12	0.657 (222)	1.147 (194)	0.0255(1507)	50	170±20	13
OR32	250	18	1.122 (373)	1.721 (286)	0.0242(1430)	50	181±18	13
OR33	280	20	0.644 (285)	0.909 (201)	0.0242(1430)	5	201±24	24
OR38	320	23	1.004 (289)	2.272 (327)	0.0255(1507)	<1	136±14	32
OR39[A]	300	10	1.269 (432)	2.133 (363)	0.0256(1517)	10	169±16	15

Table 5-1 (continued)

sample	elev. (m)	number of grains	ρ_s (N_s) (x10^6 cm^{-2})	ρ_i (N_i) (x10^6 cm^{-2})	ρ_d (N_d) (x10^6 cm^{-2})	P(χ^2) (%)	age ±1σ (Ma)	D (%)
OR45	0	18	0.549 (246)	0.897 (201)	0.0261(1545)	25	185±20	15
OR46	0	16	1.125 (463)	1.910 (393)	0.0261(1545)	10	179±16	14
OR49	700	16	1.077 (206)	1.798 (172)	0.0261(1545)	25	182±21	12
OR52	0	20	0.943 (530)	1.551 (436)	0.0261(1545)	99	184±16	8
OR53	70	20	0.488 (233)	0.759 (181)	0.0261(1545)	75	194±22	12
OR54	40	14	1.241 (295)	2.002 (241)	0.0261(1545)	75	186±20	10

All symbols and notations as in Table A3-1. Age determinations by M. Rohrman, using ζ = 11760±425 for glass dosimeter NBS963, except § where ζ = 124±7 for CN2. [A] denotes samples dated by P. Andriessen using ζ = 11134±344 for NBS963.

Table A3-5. Zircon and sphene fission track analytical data for Oslo Rift samples (Table 5-2).

sample	elev. (m)	number of grains	ρ_s (N_s) (x10^6 cm^{-2})	ρ_i (N_i) (x10^6 cm^{-2})	ρ_d (N_d) (x10^6 cm^{-2})	P(χ^2) (%)	age ±1σ (Ma)	D (%)
Zircon								
T18	400	10	25.4 (782)	12.2 (188)	2.84 (1682)	50	600±65	10
M2	330	10	24.7 (666)	11.5 (154)	2.84 (1682)	90	634±72	9
OR6	0	14	12.0 (335)	15.9 (222)	2.84 (1682)	75	226±24	11
OR11[A]	140	15	24.3 (2281)	4.41 (207)	0.212(4277)	<1	378±62	52
OR16	0	12	22.0 (510)	12.4 (144)	2.84 (1682)	95	520±59	8
OR20[A]	340	10	14.7 (1090)	5.17 (191)	0.212(4277)	25	181±20	13
OR22[A]	0	10	18.6 (1033)	4.44 (123)	0.212(4277)	75	272±34	10
OR26[A]	500	11	16.8 (1240)	5.30 (196)	0.212(4277)	95	205±23	7
Sphene								
T3	180	5	34.2 (330)	18.0 (87)	2.84 (1682)	50	543±78	9
OR28	400	10	1.26 (359)	1.54 (220)	0.027(1574)	90	241±26	11

All symbols and notations as in Table A3-1. Age determinations labelled [A] are by P. Andriessen using ζ = 308±18 for glass dosimeter NBS962 (zircon); others by M. Rohrman, using ζ = 108±4 for CN1 (zircon), 105±3 for CN1 (sphene) and 11760±425 for NBS963 (sphene).

REFERENCES

Aldridge, R.J. 1984. Thermal metamorphism of the Silurian strata of the Oslo region, assessed by conodont colour. *Geol. Mag.* **121**, 347-349.

Allemand, P. and Brun, J.-P. 1991. Width of continental rifts and the rheological layering of the lithosphere. *Tectonophysics* **188**, 63-69.

Allemand, P., Brun, J.-P., Davy, Ph. and Van den Driessche, J. 1989. Symétrie et asymétrie des rifts et méchanismes d'amincissement de la lithosphère. *Bull. Soc. géol. France* **8**, 445-451.

Anders, M.H. and Sleep, N.H. 1992. Magmatism and extension: The thermal and mechanical effects of the Yellowstone hotspot. *J. Geophys. Res.* **97**, 15,379-15,393.

Andersen, T. and Taylor, P.N. 1988. Pb isotope chemistry of the Fen carbonatite comples, SE Norway: age and petrological implications. *Geochim. Cosmochim. Acta* **52**, 109-115.

Andersen, T.B., Jamtveit, B., Dewey, J.F. and Swensson, E. 1991. Subduction and eduction of continental crust: major mechanisms during continent-continent collision and orogenic extensional collapse, a model based on the south Norwegian Caledonides. *Terra Nova* **3**, 303-310.

Anderson, D.L. 1994. The sublithospheric mantle as the source of continental flood basalts; the case against the continental lithosphere and plume head reservoirs. *Earth Planet. Sci. Lett.* **123**, 269-280.

Anderson, D.L., Zhang, Y.-S. and Tanimoto, T. 1992. Plume heads, continental lithosphere, flood basalts and tomography. In: *Magmatism and the Causes of Continental Break-up* (edited by Storey, B.C., Alabaster, T. and Pankhurst, R.J.). Geol. Soc. Spec. Publ. **68**, pp. 99-124.

Andriessen, P.A.M. 1990. Anomalous fission track apatite ages of the Precambrian basement in the Hunnedalen region, south-western Norway. *Nucl. Tracks Radiat. Meas.* **17**, 285-291.

Andriessen, P.A.M. 1995. Fission-track analysis: principles, methodology and implications for tectono-thermal histories of sedimentary basins, orogenic belts and continental margins. *Geol. Mijnbouw*, in press.

Andriessen, P.A.M. and Bos, A. 1986. Post-Caledonian thermal evolution and crustal uplift in the Eidfjord area, western Norway. *Norsk Geol. Tidsskr.* **66**, 243-250.

Andriessen, P.A.M. and Verschure, R.H. 1988. Fission-track study of the rocks in and around the Siljan structure, Sweden. *Geol. Soc. Am. Abstracts* **20**(7), A25.

Arndt, N.T. and Christensen, U. 1992. The role of lithospheric mantle in continental flood volcanism: Thermal and geochemical constraints. *J. Geophys. Res.* **97**, 10,967-10,981.

Artemjev, M.E. and Artyushkov, E.V. 1971. Structure and isostasy of the Baikal Rift and mechanism of rifting. *J. Geophys. Res.* **76**, 1197-1211.

Baker, B.H., Mohr, P.A. and Williams, L.A.J. 1972. The geology of the Eastern Rift System of Africa. *Geol. Soc. Am. Spec. Paper*, 66 pp.

Balla, Z., Kuzmin, M. and Levi, K. 1991. Kinematics of the Baikal opening: results of modeling. *Annales Tectonicae* **5**, 18-31.

Balling, N. 1980. The land uplift in Fennoscandia, gravity field anomalies and isostasy. In: *Earth Rheology, Isostasy and Eustasy* (edited by Mörner, N.-A.). Wiley, Chichester, pp. 297-321.

Balling, N. 1990. Integrated geophysical investigations of the lithosphere beneath southern Scandinavia - objectives and first results. In: *Proc. sixth EGT Workshop* (edited by Freeman, R. and Mueller, St.). European Science Foundation, pp. 441-457.

Bally, A.W. 1982. Musings over sedimentary basin evolution. *Philos. Trans. Roy. Soc. London* **A305**, 325-338.

Bannister, S.C., Ruud, B.O. and Husebye, E.S. 1991. Tomographic estimates of sub-Moho seismic velocities in Fennoscandia and structural implications. *Tectonophysics* **189**, 37-53.

Barr, D. Lithospheric stretching, detached normal faulting and footwall uplift. In: *Continental Extensional Tectonics* (edited by M.P. Coward, J.F. Dewey and P.L. Hancock). Geol. Soc. Spec. Publ. **28**, pp. 75-94.

Barton, P. and Wood, R. 1984. Tectonic evolution of the North Sea Basin: crustal stretching and subsidence. *Geophys. J. Roy. astr. Soc.* **51**, 431-452.

Bassi, G. 1991. Factors controlling the style of continental rifting: insights from numerical modelling. *Earth Planet. Sci. Lett.* **105**, 430-452.

Bassi, G. 1995. Relative importance of strain-rate and rheology for the mode of continental extension. *Geophys. J. Int.*, in press.

Bassi, G., Keen, C.E. and Potter, P. 1993. Contrasting styles of rifting: Models and examples from the Eastern Canadian Margin. *Tectonics* **12**, 639-655.

Beaumont, C., Keen, C.E. and Boutilier, R. 1982. On the evolution of rifted continental margins: comparison of models and observations for the Nova Scotia margin. *Geophys. J. Roy. astron. Soc.* **70**, 667-715.

Beaumont, C., Fullsack, P. and Hamilton, J. 1992. Erosional control of active compressional orogens. In: *Thrust Tectonics* (Edited by McClay, K.R.), Chapman & Hall, London, pp. 1-18.

Beekman, W.W.W. 1994. Tectonic modelling of thick-skinned compressional intraplate deformation, *Ph.D. Thesis Vrije Universiteit Amsterdam*, 152 pp.

Behrendt, J.C. and Cooper, A. 1991. Evidence of rapid Cenozoic uplift of the shoulder escarpment of the Cenozoic West Antarctic rift system and a speculation on possible climate forcing. *Geology* **19**, 315-319.

Beslier, M.-O. and Brun, J.-P. 1991. Boudinage de la lithosphère et formation des marges passives. *C.R. Acad. Sci. Paris Série II* **313**, 951-958.

Bishop, P. 1988. The eastern highlands of Australia: the evolution of an intraplate highland belt. *Progr. Phys. Geogr.* **12**, 159-181.

Bjørlykke, K. 1983. Subsidence and tectonics in Late Precambrian and Paleozoic sedimentary basins of southern Norway. *Norges geol. Unders.* **380**, 159-12.

Bøe, R. and Bjerkli, K. 1989. Mesozoic sedimentary rocks in Edøyfjorden and Beitstadfjorden, central Norway: Implications for the structural history of the Møre-Trøndelag Fault Zone. *Mar. Geol.* **87**, 287-299.

Bohannon, R.G. 1986. Tectonic configuration of the western Arabian continental margin, southern Red Sea. *Tectonics 5*, 477-499.

Bohannon, R.G. and Eittreim, S.L. 1991. Tectonic development of passive continental margins of the southern and central Red Sea with a comparison to Wilkes Land, Antarctica. *Tectonophysics* **198**, 129-154.

Bohannon, R.G., Naeser, C.W., Schmidt, D.L. and Zimmerman, R.A. 1989. The timing of uplift, volcanism and rifting peripheral to the Red Sea: A case for passive rifting? *J. Geophys. Res.* **94**, 1683-1701.

Bois, C. 1993. Initiation and evolution of the Oligo-Miocene rift basins of southwestern Europe: contribution of deep seismic reflection profiling. *Tectonophysics* **226**, 227-252.

Bott, M.H.P. 1976. Formation of sedimentary basins of the graben type by extension of the continental crust. *Tectonophysics* **36**, 77-86.

Boutilier, R.R. and Keen, C.E. 1994. Geodynamic models of fault-controlled extension. *Tectonics* **13**, 439-454.

Braun, J. and Beaumont, C. 1989a. A physical explanation of the relation between flank uplifts and the breakup unconformity at rifted continental margins. *Geology* **17**, 760-764.

Braun, J. and Beaumont, C. 1989b. Contrasting styles of lithospheric extension: implications for differences between the Basin and Range Province and rifted continental margins. In: *Extensional Tectonics and Stratigraphy of the North Atlantic Margins* (edited by Tankard, A.J. and Balkwill, H.R.). Am. Assoc. Petrol. Geol. Mem. **46**, pp. 53-71.

Brekke, H. and Riis, F. 1987. Tectonics and basin evolution of the Norwegian shelf between 62°N and 72°N. *Norsk Geol. Tidsskr.* **67**, 295-322.

Brodie, J. and White, N. 1994. Sedimentary basin inversion caused by igneous underplating: Northwest Europe continental shelf. *Geology* **22**, 147-150.

Brooks, C.K. 1985. Vertical crustal movements in the Tertiary of central East Greenland: A continental margin at a hot-spot. *Zeitschr. Geomorph. Suppl.* **54**, 101-117.

Brown, R.W. 1991. Backstacking apatite fission-track "stratigraphy": A method for resolving the erosional and isostatic rebound components of tectonic uplift histories. *Geology* **19**, 74-77.

Brown, R.W., Rust, D.J., Summerfield, M.A., Gleadow, A.J.W. and De Wit, M.C.J. 1990. An Early Cretaceous phase of accelerated erosion on the south-western margin of Africa: Evidence from apatite fission track analysis and the offshore sedimentary record. *Nucl. Tracks Radiat. Meas.* **17**, 339-350.

Brown, R.W., Summerfield, M.A. and Gleadow, A.J.W. 1994. Apatite fission track analysis: Its potential for the estimation of denudation rates and implications for models of long-term landscape development. In: *Process Models and Theoretical Geomorphology* (edited by Kirkby, M.J.). Wiley, New York, pp. 24-53.

Brun, J.P., Wenzel, F. and EKORS-DEKORP team 1991. Crustal-scale structure of the southern Rhinegraben from ECORS-DEKORP seismic reflection data. *Geology* **19**, 758-762.

Bryhni, I. and Brahstad, K. 1980. Caledonian regional metamorphism in Norway. *J. Geol. Soc. London* **137**, 251-259.

Buchardt, B. and Lewan, M.D. 1990. Reflectance of vitrinite-like macerals as a thermal maturity index for Cambrian-Ordovician Alum Shale, southern Scandinavia. *Am. Assoc. Petrol. Geol. Bull.* **74**, 394-406.

Buck, W.R. 1986. Small-scale convection induced by passive rifting: The cause for uplift of rift shoulders. *Earth Planet. Sci. Lett.* **77**, 362-372.

Buck, W.R. 1991. Modes of continental lithospheric extension. *J. Geophys. Res.* **96**, 20,161-20,178.

Buck, W.R., Martinez, F., Steckler, M.S. and Cochran, J.R. 1988. Thermal consequences of lithospheric extension: Pure and simple. *Tectonics* **7**, 213-234.

Bullard, E.C. 1936. Gravity measurements in East Africa. *Philos. Trans. Roy. Soc. London* **A235**, 445-531.

Burke, K. and Dewey, J.F. 1973. Plume-generated triple junctions: Key indicators in applying plate tectonics to older rocks. *J. Geol.* **81**, 406-433.

Burov, E.B. and Diament, M. 1995. The effective elastic thickness (Te) of continental lithosphere: What does it really mean? (Constraints from rheology, topography and gravity). *J. Geophys. Res.*, in press.

Burov, E.B., Houdry, F., Diament, M. and Déverchère, J. 1994. A broken plate beneath the North Baikal rift zone revealed by gravity modelling. *Geophys. Res. Lett.* **21**, 129-132.

Burrus, J., Bessis, F. and Doligez, J. 1987. Heat flow, subsidence and crustal structure of the Gulf of Lions (NW Meditterranean): A quantitative discussion of the classic passive margin model. In: *Sedimentary Basins and Basin Forming Mechanisms* (edited by Beaumont, C. and Tankard, A.J.). Can. Soc. Petrol. Geol. Mem. **12**, pp. 1-15.

Camelbeeck, T. and Iranga, M.D. 1993. Focal depth of earthquakes and geometry of active faults along the Rukwa trough, East Africa. *Terra abstracts* 5(suppl. 1), 159-160.

Camp, V.E. and Roobol, M.J. 1992. Upwelling asthenosphere beneath Western Arabia and its regional implications. *J. Geophys. Res.* **97**, 15,255-15,271.

Carlson, W.D. 1990. Mechanisms and kinetics of apatite fission-track annealing. *Am. Mineralogist* **75**, 1120-1139.

Carson, M.A. and Kirkby, M.J. 1972. *Hillslope Form and Process*, Cambridge University Press, 475 pp.

Carter, N.L. and Tsenn, M.C. 1987. Flow properties of continental lithosphere. *Tectonophysics* **136**, 27-63.

Cassell, B.R., Mykkeltveit, S., Kanestrøm, R. and Husebye, E.S. 1983. A North Sea - southern Norway seismic crustal profile. *Geophys. J. Roy. astr. Soc.* **72**, 733-753.

Chéry, J., Lucazeau, F., Daignieres, M. and Vilotte, J.P. 1992. Large uplift of rift flanks: A genetic link with lithospheric rigidity? *Earth Planet. Sci. Lett.* **112**, 195-211.

Christiansen, F.G., Larsen, H.C., Marcussen, C., Hansen, K., Krabbe, H., Piasecki, S., Stemmerik, L. and Stuart Watt, W. 1992. Uplift study of the Jameson Land basin, East Greenland. *Norsk Geol. Tidsskr.* **72**, 291-294.

Cloetingh, S. and Banda, E. 1992. Europe's lithosphere: Mechanical structure. In: *The European Geotraverse, A Continent Revealed* (edited by Blundell, D., Freeman, R. and Mueller, St.). Cambridge University Press, pp. 80-91.

Cloetingh, S. and Kooi, H. 1992. Intraplate stresses and dynamical aspects of rifted basins. *Tectonophysics* **215**, 167-185.

Cloetingh, S. and Wortel, R. 1986. Stress in the Indo-Australian plate. *Tectonophysics* **132**, 49-67.

Cloetingh, S., Kooi, H. and Groenewoud, W. 1989. Intraplate stress and sedimentary basin evolution. In: *Origin and Evolution of Sedimentary Basins and their Energy and Mineral Resources* (edited by Price, R.A.). Am. Geophys. Union Geophys. Monogr. **48**, pp. 1-16

Cloetingh, S., Gradstein, F., Kooi, H., Grant, A.C. and Kaminski, M. 1990. Plate reorganisation: a cause of rapid late Neogene subsidence and sedimentation around the North Atlantic? *J. Geol. Soc. London* **147**, 495-506.

Cloetingh, S., Stein, C., Reemst, P.H.M., Gradstein, F., Williamson, P., Exon, N. and von Rad, U. 1992a. Continental margin stratigraphy, deformation and intraplate stresses for the Indo-Australian region. In: *Proc. Ocean Drilling Program, leg 123, Sci. Results* (edited by Gradstein, F.M., Ludden, J.N. et al.). College Station, TX, pp. 671-713.

Cloetingh, S., Reemst, P., Kooi, H. and Fanavoll, S. 1992b. Intraplate stresses and the post-Cretaceous uplift and subsidence in northern Atlantic basins. *Norsk Geol. Tidsskr.* **72**, 229-236.

Cloetingh, S., van der Beek, P.A., van Rees, D., Roep, Th. B., Biermann, C. and Stephenson, R.A. 1992c. Flexural interaction and the dynamics of Neogene extensional basin formation in the Alboran-Betic region. *Geo-Marine Lett.* **12**, 66-75.

Cloetingh, S., van Wees, J.D., van der Beek, P.A. and Spadini, G. 1995. Role of pre-rift rheology in kinematics of extensional basin formation: Constraints from thermomechanical models of meditterranean and intracratonic basins. submitted to *Mar. Petrol. Geol.*

Cloos, H. 1939. Hebung, Spaltung, Vulkanismus. *Geol. Rundschau* **30**, 403.

Cochran, J.R. 1983. Effects of finite extension times on the development of sedimentary basins. *Earth Planet. Sci. Lett.* **66**, 289-302.

Cochran, J.R. and Talwani, M. 1978. Gravity anomalies, regional elevation and the deep structure of the North Atlantic. *J. Geophys. Res.* **83**, 4907-4924.

Coney, P.J. 1987. The regional tectonic setting and possible causes of Cenozoic extension in the North American Cordillera. In: *Continental Extensional Tectonics* (edited by Coward, M.P., Dewey, J.F. and Hancock, P.L.). Geol. Soc. Spec. Publ. **28**, pp. 177-186.

Conover, W.J. 1980. *Practical Nonparametric Statistics* (2nd ed.), Wiley, New York, 493 pp.

Cooper, A.K., Davey, F.J. and Behrendt, J.C. 1991a. Structural and depositional controls on Cenozoic and (?) Mesozoic strata beneath the western Ross Sea. In: *Geological Evolution of Antarctica* (edited by Thomson, M.R.A., Crame, J.A. and Thomson, J.W.). Cambridge University Press, New York, pp. 279-283.

Cooper, A.K., Davey, F.J. and Hinz, K. 1991b. Crustal extension and origin of sedimentary basins beneath the Ross Sea and Ross Ice Shelf, Antarctica. In: *Geological Evolution of Antarctica* (edited by Thomson, M.R.A., Crame, J.A. and Thomson, J.W.). Cambridge University Press, New York, pp. 285-291.

Corrigan, J. 1991. Inversion of apatite fission track data for thermal history information. *J. Geophys. Res.* **96**, 10,347-10,360.

Corrigan, J. 1993. Apatite fission-track analysis of Oligocene strata in South Texas, U.S.A.: Testing annealing models. *Chem. Geol. (Isot. Geosci. Sect.)* **104**, 227-249.

Coussement, C., Rolet, J., Delvaux, D., Reynes, P., Lezzar, K.E., Richert, J.P., Rehault, J.P. and Tiercelin, J.J. 1993. Planation surfaces with basin facing dip in relation with surface flexion, flank uplift and subsidence in the East African Rift; with north-Tanganyika trough (Burundi, Zaire) and the Rukwa trough (Tanzania) cases as examples. *Terra abstracts* 5(suppl. 1), 160.

Coward, M.P., Dewey, J.F. and Hancock, P.L. (Editors) 1987. *Continental Extensional Tectonics*, Geol. Soc. Spec. Publ. **28**, 637 pp.

Cox, K.G. 1980. A model for flood basalt volcanism. *J. Petrol.* **21**, 629-650.

Cox, K.G. 1989. The role of mantle plumes in the development of continental drainage pattern. *Nature* **342**, 873-877.

Crane, K., Hecker, B. and Golubev, V. 1991. Heat flow and hydrothermal vents in Lake Baikal, U.S.S.R. *EOS Trans. Am. Geophys. Union* **72**, 585-589.

Crough, S.T. 1978. Thermal origin of mid-plate hot-spot swells. *Geophys. J. Roy. astron. Soc.* **55**, 451-459.

Crowley, K.D. 1985. Thermal significance of fission-track length distributions. *Nucl. Tracks Radiat. Meas.* **10**, 311-322.

Crowley, K.D., Cameron, M. and Schaefer, R.L. 1991. Experimental studies of annealing of etched fission tracks in fluorapatite. *Geochim. Cosmochim. Acta* **55**, 1449-1465.

Culling, W.E.H. 1960. Analytical theory of erosion. *J. Geol.* **68**, 336-344.

Daly, M.C., Chorowicz, J. and Fairhead, J.D. 1989. Rift basin evolution in Africa: the influence of reactivated steep basement shear zones. In: *Inversion Tectonics* (edited by Cooper, M.A. and Williams, G.D.). Geol. Soc. Spec. Publ. **44**, pp. 309-334.

de Beaumont, E. 1847. Note sur les systèmes de montagnes les plus anciens de l'Europe. *Bull. Soc. Geol. Fr. 2me Sér.* **4**, 864-991.

Delvaux, D. and Klerkx, J. 1994. Baikal rifting mechanism: from passive to active? *EOS Trans. Am. Geophys. Union* **75**(suppl. 44), 599.

Delvaux, D. and Wopfner, H. 1992. Some observations on the geomorphology and recent rift movements in the Livingstone Mountains, SW Tanzania. *UNESCO, Geol. Econ. Devel. Newsletter* **9**, 171-173.

Delvaux, D., Levi, K., Kajara, R. and Sarota, J. 1992. Cenozoic paleostress and kinematic evolution of the Rukwa - North Malawi rift valley (East African rift system). *Bull. Centr. Rech. Explor. Prod. Elf Aquitaine* **16**, 383-406.

Delvaux, D., Moeys, R., Stapel, G., Levi, K., Miroshnichenko, A., Rasskazov, S. and Sankov, V. 1995. Paleostress reconstructions and geodynamics of the Baikal region, Central Asia. Part II: Cenozoic rifting. submitted to *Tectonophysics*.

Déverchère, J., Houdry, F., Diament, M., Solonenko, N.V. and Solonenko, A.V. 1991. Evidence for a seismogenic upper mantle and lower crust in the Baikal Rift. *Geophys. Res. Lett.* **18**, 1099-1102.

Déverchère, J., Houdry, F., Solonenko, N.V., Solonenko, A.V. and Sankov, V.A. 1993. Seismicity, active faults and stress field of the North Muya Region, Baikal Rift: New insights on the rheology of extended continental lithosphere. *J. Geophys. Res.* **98**, 19,895-19,912.

Dewey, J.F. 1988. Extensional collapse of orogens. *Tectonics* **7**, 1123-1139.

Diament, M. and Kogan, M.G. 1990. Longwavelength gravity anomalies and the deep thermal structure of the Baikal rift. *Geophys. Res. Lett.* **17**, 1977-1980.

Dokka, R.K., Mahaffie, M.J. and Snoke, A.W. 1986. Thermochronologic evidence for major tectonic denudation associated with detachment faulting, northern Ruby Mountains-east Humboldt range, Nevada. *Tectonics* **5**, 995-1006.

Donelick, R.A. 1988. Etchable fission track length reduction in apatite: Experimental observations, theory and geological application, *Ph.D. Thesis Rensselaer Polytechnic Institute*, Troy, NY, 414 pp.

Donelick, R.A., Roden, M.K., Mooers, J., Carpenter, B.S. and Miller, D.S. 1990. Etchable length reduction of induced fission tracks in apatite at room temperature (23°C): crystallographic orientation effects and "initial" mean lengths. *Nucl. Tracks Radiat. Meas.* **17**, 261-266.

Doré, A.G. 1991. The structural foundation and evolution of Mesozoic seaways between Europe and the Arctic. *Paleogeogr., Paleoclimatol., Paleoecol.* **87**, 441-492.

Doré, A.G. 1992. The Base Tertiary surface of southern Norway and the northern North Sea. *Norsk Geol. Tidsskr.* **72**, 259-265.

Duddy, I.R., Green, P.F. and Laslett, G.M. 1988. Thermal annealing of fission tracks in apatite 3. Variable temperature behaviour. *Chem. Geol. (Isot. Geosci. Sect.)* **73**, 25-38.

Dumitru, T.A., Hill, K.C., Coyle, D.A., Duddy, I.R., Foster, D.A., Gleadow, A.J.W., Green, P.F., Kohn, B.P., Laslett, G.M. and O'Sullivan, A.J. 1991. Fission track thermochronology: Application to continental rifting of south-eastern Australia. *Austr. Petrol. Explor. Assoc. J.* **31**, 131-142.

Dunbar, J.A. and Sawyer, D.S. 1989. How preexisting weaknesses control the style of continental breakup. *J. Geophys. Res.* **94**, 7278-7292.

Dypvik, H., Nesteby, H., Ruden, F., Aagard, P., Johansson, T., Msindai, J. and Massay, C. 1990. Upper Paleozoic and Mesozoic sedimentation in the Rukwa-Tukuyu region, Tanzania. *J. Afr. Earth Sci.* **11**, 437-456.

Ebinger, C.J., Bechtel, T.D., Forsyth, D.W. and Bowin, C.O. 1989. Effective elastic plate thickness beneath the East African and Afar Plateaus and dynamic compensation of the uplifts. *J. Geophys. Res.* **94**, 2883-2901.

Ebinger, C.J., Karner, G.D. and Weissel, J.K. 1991. Mechanical strength of extended continental lithosphere: constraints from the Western rift system, Africa. *Tectonics* **10**, 1239-1256.

Ebinger, C.J., Deino, A.L., Tesha, A.L., Becker, T. and Ring, U. 1993. Tectonic controls on rift basin morphology: Evolution of the Northern Malawi (Nyasa) rift. *J. Geophys. Res.* **98**, 17,821-17,836.

England, P.C. 1983. Constraints on extension of continental lithosphere. *J. Geophys. Res.* **88**, 1145-1152.

England, P. and Molnar, P. 1990. Surface uplift, uplift of rocks and exhumation of rocks. *Geology* **18**, 1173-1177.

Ermikov, V.D. 1994. Mesozoic precursors of rift structures in Central Asia. *Bull. Centr. Rech. Explor. Prod. Elf Aquitaine* **18**, 123-134.

Etheridge, M.A., Symonds, P.A. and Lister, G.A. 1989. Application of the detachment model to reconstruction of conjugate passive margins. In: *Extensional Tectonics and Stratigraphy of the North Atlantic Margins* (edited by Tankard, A.J. and Balkwill, H.R.). Am. Assoc. Petrol. Geol. Mem. **46**, pp. 23-40.

Færseth, R.B., McIntyre, R.M. and Naterstad, J. 1976. Mesozoic alkaline dykes in the Sunnhordland region, western Norway: ages, geochemistry and regional significance. *Lithos* **9**, 332-345.

Fairhead, J.D. 1976. The structure of the lithosphere beneath the Eastern Rift, East Africa, deduced from gravity studies. *Tectonophysics* **30**, 269-298.

Fenner, J. 1988. Occurrences of pre-Quaternary diatoms in Scandinavia reconsidered. *Meyniana* **40**, 133-141.

Fitzgerald, P.G. 1992. The Transantarctic Mountains of Southern Victoria Land: the application of apatite fission track analysis to a rift shoulder uplift. *Tectonics* **11**, 634-662.

Fitzgerald, P.G. 1994. Thermochronologic constraints on post-Paleozoic tectonic evolution of the central Transantarctic Mountains, Antarctica. *Tectonics* **13**, 818-836.

Fitzgerald, P.G., Sandiford, M., Barrett, P.J. and Gleadow, A.J.W. 1987. Asymmetric extension associated with uplift and subsidence in the Transantarctic Mountains and Ross Embayment. *Earth Planet. Sci. Lett* **81**, 67-78.

Fjeldskaar, W. and Cathles, L. 1991. Rheology of mantle and lithosphere inferred from post-glacial uplift in Fennoscandia. In: *Glacial Isostasy, Sea-Level and Mantle Rheology* (edited by Sabadini, R. et al.). Kluwer Ac. Publ., Dordrecht, pp. 1-19.

Fleischer, R.L., Price, P.B. and Walker, R.M. 1975. *Nuclear Tracks in Solids - Principles and Applications*, Univ. California Press, Berkeley, 605 pp.

Fleitout, L., Froidevaux, C. and Yuen, D. 1986. Active lithospheric thinning. *Tectonophysics* **132**, 271-278.

Flemings, P.B. and Jordan, T.E. 1989. A synthetic stratigraphic model of foreland basin development. *J. Geophys. Res.* **94**, 3851-3866.

Forsyth, D.W. 1985. Subsurface loading and estimates of the flexural rigidity of continental lithosphere. *J. Geophys. Res.* **90**, 12,623-12,632.

Foster, D.A. and Gleadow, A.J.W. 1992. The morphotectonic evolution of rift-margin mountains in central Kenya: Constraints from apatite fission-track thermochronology. *Earth Planet. Sci. Lett.* **113**, 157-171.

Foster, D.A. and Gleadow, A.J.W. 1993. Episodic denudation in East Africa: A legacy of intracontinental tectonism. *Geophys. Res. Lett.* **20**, 2395-2398.

Foucher, J.-P., Le Pichon, X. and Sibuet, J.-C. 1982. The ocean-continent transition in the uniform lithospheric stretching model: role of partial melting in the mantle. *Phil. Trans. R. Soc. London* **A305**, 27-43.

Fowler, S. and McKenzie, D.P. 1989. Gravity studies of the Rockal and Exmouth Plateaux using SEASAT altimetry. *Basin Res.* **2**, 27-34.

Fyfe, W.S. 1992. Magma underplating of continental crust. *J. Volcanol. Geotherm. Res.* **50**, 33-40.

Gabrielsen, R.H. 1989. Reactivation of faults on the Norwegian continental shelf and its implications for earthquake occurrence. In: *Earthquakes at North-Atlantic Passive Margins: Neotectonics and Postglacial Rebound* (edited by Gregersen, S. and Basham, P.W.). Kluwer Ac. Publ., Dordrecht, pp. 67-90.

Gabrielsen, R.H., Færseth, R.B., Steel, R.J., Idil, S. and Kløvjan, O.S. 1990. Architectural styles of basin fill in the northern Viking Graben. In: *Tectonic Evolution of the North Sea Rifts* (edited by Blundell, D.J. and Gibbs, A.D.). Oxford Univ. Press, pp. 158-179.

Galbraith, R.F. 1990. The radial plot: Graphical assessment of spread in ages. *Nucl. Tracks Radiat. Meas.***17**, 207-214.

Galbraith, R.F. and Laslett, G.M. 1993. Statistical models for mixed fission track ages. *Nucl. Tracks Radiat. Meas.* **21**, 459-470.

Gallagher, K. 1994. Genetic algorithms: A powerful new method for modelling fission track data and thermal histories. In: *Proc. 8th Int. Conf. Geochronology, Cosmochronology and Isotope Geology* (edited by Lanphere, M.A., Dalrymple, G.B. and Turrin, B.D.). U.S. Geol. Survey Circ. **1107**, pp. 107.

Gallagher, K. and Hawkesworth, C. 1992. Dehydration melting and the generation of continental flood basalts. *Nature* **358**, 57-59.

Gallagher, K., Hawkesworth, C.J. and Mantovani, M.J.M. 1994a. The denudation history of the onshore continental margin of SE Brazil inferred from apatite fission track data. *J. Geophys. Res.* **99**, 18,117-18,145.

Gallagher, K., Dumitru, T.A. and Gleadow, A.J.W. 1994b. Constraints on the vertical motion of eastern Australia during the Mesozoic. *Basin Res.* **6**, 77-94.

Galloway, W.E., Garber, J.L., Liu, X. and Sloan, B.J. 1993. Sequence stratigraphic and depositional framework of the Cenozoic fill, Central and Northern North Sea basin. In: *Petroleum Geology of Northwestern Europe: Proc. 4th Conference* (edited by Parker, J.R.). Geol. Soc., London, pp. 299-315.

Gangi, A.F. (Editor) 1991. World Rift Systems. *Tectonophysics* **197**, 99-390.

Gao, S., Davis, P.M., Liu, H., Slack, P.D., Zorin, Yu. A., Logatchev, N.A., Kogan, M.G., Burkholder, P.D. and Meyer, R.P. 1994. Asymmetric upwarp of the asthenosphere beneath the Baikal rift zone, Siberia. *J. Geophys. Res.* **99**, 15,319-15,330.

Garfunkel, Z. 1988. Relation between continental rifting and uplifting: evidence from the Suez rift and northern Red Sea. *Tectonophysics* **150**, 33-49.

Gerrard, I. and Smith, G.C. 1982. Post-Paleozoic succession and structure of the Southwestern African continental margin. In: *Studies in Continental Margin Geology* (Edited by Watkins, J.S. and Drake, C.L.). Am. Assoc. Petrol. Geol. Mem. **34**, pp. 49-74.

Gettings, M.E., Blank, H.R., Jr., Mooney, W.D. and Healy, J.H. 1986. Crustal structure of southwestern Saudi Arabia. *J. Geophys. Res.* **91**, 6491-6512.

Gilchrist, A.R. and Summerfield, M.A. 1990. Differential denudation and flexural isostasy in formation of rifted-margin upwarps. *Nature* **346**, 739-742.

Gilchrist, A.R., Kooi, H. and Beaumont, C. 1994. The post-Gondwana geomorphic evolution of southwestern Africa: Implications for the controls on landscape development from observations and numerical experiments. *J. Geophys. Res.* **99**, 12,211-12,228.

Girdler, R.W., Fairhead, R.W., Searle, R.C. and Sowerbutts, W.T.C. 1969. Evolution of rifting in Africa. *Nature* 224, 1178-1182.

Gjessing, J. 1967. Norways Paleic Surface. *Norsk Geograf. Tidsskr.* **21**, 69-132.

Gleadow, A.J.W. and Brooks, C.K. 1979. Fission track dating, thermal histories and tectonics of igneous intrusions in East Greenland. *Contrib. Mineral. Petrol.* **71**, 45-60.

Gleadow, A.J.W. and Duddy, I.R. 1981. A natural long-term track annealing experiment for apatite. *Nucl. Tracks Radiat. Meas.* **5**, 169-174.

Gleadow, A.J.W. and Fitzgerald, P.G. 1987. Uplift history and structure of the Transantarctic Mountains: new evidence from fission track dating of basement apatites in the Dry Valleys area, southern Victoria Land. *Earth Planet. Sci. Lett.* **82**, 1-14.

Gleadow, A.J.W., Duddy, I.R., Green, P.F. and Lovering, J.F. 1986. Confined fission track lengths in apatite: a diagnostic tool for thermal history analysis. *Contrib. Mineral. Petrol.* **94**, 405-415.

Golubev, V.A., Klerkx, J. and Kipfer, R. 1993. Heat flow, hydrothermal vents and static stability of discharging thermal water in lake Baikal (southeastern Siberia). *Bull Centres Rech. Explor. Prod. Elf Aquitaine* **17**, 53-65.

Govers. R. 1993. Dynamics of lithospheric extension: a modeling study. *Ph.D. Thesis University Utrecht (Geologica Ultraiectina no. 105)*, 240 pp.

Green, P.F. 1986. On the thermo-tectonic evolution of Northern England: evidence from fission track analysis. *Geol. Mag.* **123**, 493-506.

Green, P.F. 1988. The relationship between track shortening and fission track age reduction in apatite: combined influences of inherent instability, annealing anisotropy, length bias and system calibration. *Earth Planet. Sci. Lett.* **89**, 335-352.

Green, P.F., Duddy, I.R., Gleadow, A.J.W. and Tingate, P.R. 1985. Fission-track annealing in apatite: Track length measurements and the form of the Arrhenius plot. *Nucl. Tracks Radiat. Meas.* **10**, 323-328.

Green, P.F., Duddy, I.R., Gleadow, A.J.W., Tingate, P.R. and Laslett, G.M. 1986. Thermal annealing of fission tracks in apatite 1. A qualitative description. *Chem. Geol. (Isot. Geosci. Sect.)* **59**, 237-253.

Green, P.F., Duddy, I.R., Gleadow, A.J.W. and Lovering, J.F. 1989a. Apatite fission-track analysis as a paleotemperature indicator for hydrocarbon exploration. In: *Thermal History of Sedimentary Basins* (edited by Naeser, N.D. and McCulloh, T.H.). Springer Verlag, New York, pp. 181-195.

Green, P.F., Duddy, I.R., Laslett, G.M., Hegarty, K.A., Gleadow, A.J.W. and Lovering, J.F. 1989b. Thermal annealing of fission tracks in apatite 4. Quantitative modelling techniques and extension to geological timescales. *Chem. Geol. (Isot. Geosci. Sect.)* **79**, 155-182.

Green, P.F., Duddy, I.R., Bray, R.J. and Lewis, C.L.E. 1993. Elevated paleotemperatures prior to Early Tertiary cooling throughout the UK region: Implications for hydrocarbon generation. In: *Petroleum Geology of NW Europe: Proceedings of the 4th Conference* (edited by Parker, J.R.). Geol. Soc., London, pp. 1067-1074.

Gregory, J.W. 1896. *The Great Rift Valley*, J. Murray, London, 424 pp.

Grønlie, A., Naeser, C.W., Naeser, N.D., Mitchell, J.G., Sturt, B.A. and Ineson, D. 1994. Fission-track and K-Ar dating of tectonic activity in a transect across the Møre-Trøndelag Fault Zone, central Norway. *Norsk Geol. Tidsskr.* **74**, 24-34.

Hanks, T.C., Bucknam, R.C., Lajoie, K.R. and Wallace, R.E. 1984. Modification of wave-cut and faulting-controlled landforms. *J. Geophys. Res.* **89**, 5771-5790.

Hansen, K. 1992. Post-orogenic tectonic and thermal history of a rifted continental margin: the Scoresby Sund area, East Greenland. *Tectonophysics* **216**, 309-326.

Hawkesworth, C. and Gallagher, K. 1993. Mantle hotspots, plumes and regional tectonics as causes of intraplate magmatism. *Terra Nova* **5**, 552-559.

Hellinger, S.J. and Sclater, J.G. 1983. Some remarks on two-layer extensional models for the evolution of sedimentary basins. *J. Geophys. Res.* **88**, 8251-8269.

Hendrie, D.B., Kusznir, N.J. and Hunter, R.H. 1993. Jurassic extension estimates for the North Sea 'triple junction' from flexural backstripping: implications for decompression melting models. *Earth Planet. Sci. Lett.* **116**, 113-127.

Hendrie, D.B., Kusznir, N.J., Morley, C.K. and Ebinger, C.J. 1994. Cenozoic extension in northern Kenya: a quantitative model of rift basin development in the Turkana region. *Tectonophysics* **236**, 409-438.

Henningsmoen, G. 1978. Sedimentary rocks associated with the Oslo region lavas. In: *The Oslo Paleorift: a review and guide to excursions* (edited by Dons, J.A. and Larsen, B.T.). Norges geol. Unders. **337**, pp. 17-24.

Holmes, A. 1965. *Principles of Physical Geology (2nd ed.)*, Nelson, London, 1288 pp.

Holtedahl, H. 1953. On the oblique uplift of some Northern lands. *Norsk Geogr. Tidsskr.* **14**, 132-139.

Horváth, F. and Berkhemer, H. 1982. Mediterranean back-arc basins. In: *Alpine-Mediterranean Geodynamics* (edited by Berkhemer, H. and Hsü, K.J.). Am. Geophys. Union/Geol. Soc. Am. Geodynamics Series **7**, pp. 141-173.

Houseman, G. and England, P. 1986. A dynamical model of lithosphere extension and sedimentary basin formation *J. Geophys. Res.* **91**, 719-729.

Hurford, A.J. 1990. International union of geological sciences subcommission on geochronology recommendation for the standardization of fission track dating calibration and data reporting. *Nucl. Tracks Radiat. Meas.* **17**, 233-236.

Hurford, A.J. 1991. Uplift and cooling pathways derived from fission track analysis and mica dating: a review. *Geol. Rundschau* **80**, 349-368.

Hurford, A.J. and Green, P.F. 1983. The zeta age calibration of fission-track dating. *Chem. Geol. (Isot. Geosci. Sect.)* **1**, 285-317.

Hutchinson, D.R., Golmshtok, A.J., Zonenshain, L.P., Moore, T.C., Scholz, C.A. and Klitgord, K.D. 1992. Depositional and tectonic framework of the rift basins of Lake Baikal from multichannel seismic data. *Geology* **20**, 589-592.

Ihlen, P.M. 1986. The geological evolution and metallogeny of the Oslo paleorift. In: *Metallogeny associated with the Oslo paleorift* (edited by Olerud, S. and Ihlen, P.M.). Sver. Geol. Unders. Ser. Ca., No. 59, Uppsala, pp. 6-17.

Ihlen, P.M., Ineson, P.R. and Mitchell, J.G. 1978. K/Ar dating of clay-mineral alteration associated with ore deposition in the northern part of the Oslo Region. In: *Petrology and Geochemistry of Continental Rifts* (edited by Neumann, E.-R. and Ramberg, I.B.). Reidel, Dordrecht, pp. 255-264.

Illies, J.H. (Editor) 1981. Mechanisms of Graben Formation. *Tectonophysics* **73**, 1-266.

Ineson, P.R., Mitchell, J.G. and Vokes, F.M. 1978. Further K/Ar dating on clay-mineral alteration associated with fluorite deposition in southern Norway. In: *Petrology and Geochemistry of Continental Rifts* (edited by Neumann, E.-R. and Ramberg, I.B.). Reidel, Dordrecht, pp. 265-275

Ingersoll, R.V. 1988. Tectonics of sedimentary basins. *Geol. Soc. Am. Bull.* **100**, 1704-1719.

Issler, D.R. and Beaumont, C. 1989. A finite element model of the subsidence and thermal evolution of extensional basins: Application to the Labrador Continental Margin. In: *Thermal History of Sedimentary Basins* (edited by Naeser, N.D. and McCulloh, T.H.). Springer Verlag, New York, pp. 239-267.

Izzeldin, A.Y. 1987. Seismic, gravity and magnetic surveys in the central part of the Red Sea: their interpretation and implications for the structure and development of the Red Sea. *Tectonophysics* **143**, 269-306.

Jackson, J.A. 1987. Active normal faulting and crustal extension. In: *Continental Extensional Tectonics* (edited by M.P. Coward, J.F. Dewey and P.L. Hancock). Geol. Soc. Spec. Publ. **28**, pp. 3-17.

Jackson, J. and Blenkinsop, T.G. 1993. The Malawi earthquake of March 10, 1989: Deep faulting within the East African Rift System. *Tectonics* **12**, 1131-1139.

Jacobs, J., Hejl, E., Van den haute, P. and Wagner, G.A. 1993. A preliminary tectono-thermal model for the KTB deduced from apatite, zircon and sphene fission-track analysis. *KTB Report no. 93-2*, pp. 125-128.

Jansen, E. and Sjøholm, J. 1991. Reconstruction of glaciation over the past 6 Myr from ice-borne deposits in the Norwegian Sea. *Nature* **349**, 600-603.

Janssen, M.E., Torné, M., Cloetingh, S. and Banda, E. 1993. Pliocene uplift of the eastern Iberian margin: Inferences from quantitative modelling of the Valencia Trough. *Earth Planet. Sci. Lett.* **119**.

Janssen, M.E., Stephenson, R.A. and Cloetingh, S. 1995. Temporal and spatial correlations between changes in plate motions and the evolution of rifted basins in Africa. submitted to *Geol. Soc. Am. Bull.*

Jarvis, G.T. and McKenzie, D.P. 1980. Sedimentary basin formation with finite extension rates. *Earth Planet. Sci. Lett.* **48**, 42-52.

Jensen, L.N. and Schmidt, B.J. 1993. Neogene uplift and erosion in the northeastern North Sea; magnitude and consequences for hydrocarbon exploration in the Farsund Basin. In: *Generation, Accumulation and Production of Europe's Hydrocarbons* (edited by Spencer, A.M.). Eur. Assoc. Petrol. Geol. Special Publ **3**, pp. 79-88.

Jordt, H., Faleide, J.I. and Bjørlykke, K. 1995. Cenozoic sequence development in the central and northern North Sea: Implications on outbuilding and tectonic development. submitted to *Mar. Petrol. Geol.*

Kamp, P.J.J. and Tippett, J.M. 1993. Dynamics of Pacific plate crust in the South Island (New Zealand) zone of oblique continent-continent convergence. *J. Geophys. Res.* **98**, 16,105-16,118.

Karner, G.D., Egan, S.S. and Weissel, J.K. 1992. Modeling the tectonic development of the Tucano and Sergipe-Alagoas rift basins, Brazil. *Tectonophysics* **215**, 133-160.

Kashik, S.A. and Mazilov, V.N. 1994. Main stages and palaeogeography of Cenozoic sedimentation in the Baikal rift system (eastern Siberia). *Bull. Centr. Rech. Explor. Prod. Elf Aquitaine* **18**, 453-462.

Keen, C.E. 1985. The dynamics of rifting: Deformation of the lithosphere by active and passive driving forces. *Geophys. J. Roy. astron. Soc.* **80**, 95-120.

Keen, C.E. 1987. Some important consequences of lithospheric extension. In: *Continental Extensional Tectonics* (edited by M.P. Coward, J.F. Dewey and P.L. Hancock). Geol. Soc. Spec. Publ. **28**, pp. 67-73

Keen, C.E. and Beaumont, C. 1990. Geodynamics of rifted continental margins. In: *Geology of the Continental Margin of Eastern Canada* (edited by Keen, M.J. and Williams, G.L.). Geol. Surv. Can., Geology of Canada no. 2, pp. 391-472. (also: Geol. Soc. Am. The Geology of North America, v. I-1).

Keen, C.E. and Dehler, S.A. 1993. Stretching and subsidence: Rifting of conjugate margins in the North Atlantic region. *Tectonics* **12**, 1209-1229.

Kenyon, P.M. and Turcotte, D.L. 1985. Morphology of a delta prograding by bulk sediment transport. *Geol. Soc. Am. Bull.* **96**, 1457-1465.

Khain, V.E. 1990. Origin of the Central Asian Mountain Belt: Collision or mantle diapirism? *J. Geodynamics* **11**, 389-394.

Kinck, J.J., Husebye, E.S. and Lund, C.-E. 1991. The South Scandinavian crust: Structural complexities from seismic reflection and refraction profiling. *Tectonophysics* **189**, 117-133.

King, L.C. 1955. Pediplanation and isostasy: an example from South Africa. *Q. J. Geol. Soc. London* **111**, 353-359.

King, L.C. 1963. *South African Scenery*, Oliver & Boyd, Edinburgh/London, 699 pp.

Kirkby, M.J. 1971. Hillslope process response models based on the continuity equation. *Inst. British Geographers Spec. Publ.* **3**, 15-30.

Kiselev, A.I. and Popov, A.M. 1992. Asthenospheric diapir beneath the Baikal rift: petrological constraints. *Tectonophysics* **208**, 287-296.

Klemperer, S.M. 1988. Crustal thinning and nature of extension in the northern North Sea from deep seismic reflection profiling. *Tectonics* **7**, 803-821.

Kooi, H. 1991. Tectonic modelling of extensional basins: the role of lithospheric flexure, intraplate stress and relative sea-level change. *Ph.D. Thesis Vrije Universiteit Amsterdam*, 183 pp.

Kooi, H. and Beaumont, C. 1994. Escarpment evolution on high-elevation rifted margins; insights derived from a surface processes model that combines diffusion, advection and reaction. *J. Geophys. Res.* **99**, 12,191-12,210.

Kooi, H. and Beaumont, C. 1995. Large-scale geomorphology: Classical concepts reconciled and integrated with contemporary ideas via a surface-processes model. *J. Geophys. Res.*, in press.

Kooi, H. and Cloetingh, S. 1989. Intraplate stresses and the tectono-stratigraphic evolution of the central North Sea. In: *Extensional Tectonics and Stratigraphy of the North Atlantic Margins* (edited by Tankard, A.J. and Balkwill, H.R.). Am. Assoc. Petrol. Geol. Mem. **46**, pp. 541-558.

Kooi, H., Hettema, M. and Cloetingh, S. 1991. Lithospheric dynamics and the rapid Pliocene-Quaternary subsidence phase in the southern North Sea basin. *Tectonophysics* **192**, 245-259.

Kooi, H., Cloetingh, S. and Burrus, J. 1992. Lithospheric necking and regional isostasy at extensional basins 1, subsidence and gravity modeling with an application to the Gulf of Lions margin (SE France). *J. Geophys. Res.* **97**, 17,553-17,571.

Krylov, S.V., Mandelbaum, M.M. and Mishenkin, B.P. 1981. *The interior of Baikal from seismic data.* Nauka, Novosibirsk, 173 pp. (in Russian).

Kusznir, N.J. and Ziegler, P.A. 1992. The mechanics of continental extension and sedimentary basin formation: A simple-shear/pure-shear flexural cantilever model. *Tectonophysics* **215**, 117-131.

Kusznir, N.J., Karner, G.D. and Egan, S.S. 1987. Geometric, thermal and isostatic consequences of detachments in continental lithsophere extension and basin formation. In: *Sedimentary Basins and Basin Forming Mechanisms* (edited by Beaumont, C. and Tankard, A.J.). Can. Soc. Petrol. Geol. Memoir **12**, pp. 185-203.

Kusznir, N.J., Marsden, G. and Egan, S.S. 1991. A flexural-cantilever simple-shear/pure-shear model of continental lithosphere extension: application to the Jeanne d'Arc Basin, Grand Banks and Viking Graben, North Sea. In: *The Geometry of Normal Faults* (edited by Roberts, A.M., Yielding, G. and Freeman, B.). Geol. Soc. Spec. Publ. **56**, pp. 41-60.

Lambeck, K. and Stephenson, R. 1986. The post-Paleozoic uplift history of south-eastern Australia. *Austr. J. Earth Sci.* **33**, 253-270.

Landon, S.M. (Editor) 1994. *Interior Cratonic Basins*, Am. Assoc. Petrol. Geol. Mem. **59**, 276 pp.

Larsen, H.C. 1990. The East Greenland Shelf. In: *The Geology of North America: The Arctic Ocean region* (edited by Grantz, A., Johnson, L. and Sweeney, J.F.). Geol. Soc. Am., Boulder, pp. 185-210.

Larsson, F.R. and Husebye, E.S. 1991. Crustal reflectivity in the Skagerrak area. *Tectonophysics* **189**, 135-148.

Laslett, G.M., Kendall, W.S., Gleadow, A.J.W. and Duddy, I.R. 1982. Bias in measurement of fission-track length distributions. *Nucl. Tracks Radiat. Meas.* **6**, 79-85.

Laslett, G.M., Green, P.F., Duddy, I.R. and Gleadow, A.J.W. 1987. Thermal annealing of fission tracks in apatite 2. A quantitative analysis. *Chem. Geol. (Isot. Geosci. Sect.)* **65**, 1-13.

Latin, D.M., Dixon, J.E. and Fitton, J.G. 1990. Rift-related magmatism in the North Sea basin. In: *Tectonic Evolution of the North Sea Rifts* (edited by Blundell, D.J. and Gibbs, A.D.). Oxford Sci. Publ., pp. 101-144.

Latin, D.M., Norrey, M.J. and Tarzey, R.J.E. 1993. Magmatism in the Gregory Rift, East Africa: Evidence for melt generation by a plume. *J. Petrol.* **34**, 1007-1027.

Lawver, L.A. and Muller, R.D. 1994. Iceland hotspot track. *Geology* **22**, 311-314.

Leeder, M.R. 1991. Denudation, vertical crustal movements and sedimentary basin infill. *Geol. Rundschau* **80**, 441-458.

Le Pichon, X. and Sibuet, J.C. 1981. Passive margins: A model of formation. *J. Geophys. Res.* **86**, 3708-3720.

Le Pichon, X. and Chamot-Rooke, N. 1991. Extension of continental crust. In: *Controversies in Modern Geology* (edited by Müller, D.W., McKenzie, J.A. and Weissert, H.). Academic Press, London, pp. 313-338.

Lewis, C.L.E., Green, P.F., Carter, A. and Hurford, A.J. 1992. Elevated K/T palaeotemperatures throughout Northwest England: three kilometres of Tertiary erosion? *Earth Planet. Sci. Lett.* **112**, 131-145.

Lie, J.E. and Husebye, E.S. 1994. Simple-shear deformation of the Skagerrak lithosphere during the formation of the Oslo rift. *Tectonophysics* **232**, 133-141.

Lister, G.A., Etheridge, M.A. and Symonds, P.A. 1986. Detachment faulting and the evolution of passive continental margins. *Geology* **14**, 246-250.

Lister, G.A., Etheridge, M.A. and Symonds, P.A. 1991. Detachment models for the formation of passive continental margins. *Tectonics* **10**, 1038-1064.

Logatchev, N.A. 1993. History and geodynamics of the Baikal Rift (East Siberia): A review. *Bull. Centr. Rech. Explor. Prod. Elf Aquitaine* **17**, 353-370.

Logatchev, N.A. and Zorin, Yu. A. 1987. Evidence and causes of the two-stage evolution of the Baikal rift. *Tectonophysics* **143**, 225-234.

Logatchev, N.A. and Zorin, Yu. A. 1992. Baikal rift zone: structure and geodynamics. *Tectonophysics* **208**, 273-286.

Logatchev, N.A., Zorin, Yu. A. and Rogozhina, V.A. 1983. Baikal rift: active or passive? - Comparison of the Baikal and Kenya rift zones. *Tectonophysics* **94**, 223-240.

Lutz, T.M. and Omar, G.I. 1991. An inverse method of modeling thermal histories from apatite fission-track data. *Earth Planet. Sci. Lett.* **104**, 181-195.

Lysak, S.V. 1992. Heat flow variations in continental rifts. *Tectonophysics* **208**, 309-323.

Magnavita, L.P., Davison, I. and Kusznir, N.J. 1994. Rifting, erosion and uplift history of the Recôncavo-Tucano-Jatobá Rift, northeast Brazil. *Tectonics* **13**, 367-388.

Marsden, G., Yielding, G., Roberts, A.M. and Kusznir, N.J. 1990. Application of a flexural cantilever simple-shear/pure-shear model of continental extension to the formation of the northern North Sea basin. In: *Tectonic Evolution of the North Sea Rifts* (edited by Blundell, D.J. and Gibbs A.D.). Oxford Sci. Publ., pp. 240-261.

Mats, V.D. 1992. The structure and development of the Baikal rift depression. *Baikal International Centre for Ecological Research. Preprint no. 1*, 69 pp. (also: *Earth Sci. Rev.* **34**, 81-118, 1993).

Mbede, E.I. 1993. Tectonic Development of the Rukwa Rift Basin in SW Tanzania. *Ph.D. Thesis TU Berlin (Berliner Geowiss. Abh. A152)*, 92 pp.

Mbede, E.I., Hurford, A., Ebinger, C.J. and Schandelmeier, H. 1993. A constraint on the uplift history of the Rukwa rift, SW Tanzania: A reconnaissance apatite fission track analysis. *Ann. Rep. Roy. Mus. Centr. Africa Tervuren*, 99-108.

McCulloch, A.A. 1993. Apatite fission track results from Ireland and the Porcupine basin and their significance for the evolution of the North Atlantic. *Mar. Petrol. Geol.* **10**, 572-590.

McKenzie, D.P. 1978. Some remarks on the development of sedimentary basins. *Earth Planet. Sci. Lett.* **40**, 25-31.

McKenzie, D.P. 1984. A possible mechanism of epeirogenetic uplift. *Nature* **307**, 616-619.

McKenzie, D.P. and Bickle, M.J. 1988. The volume and composition of melts generated by extension of the lithosphere. *J. Petrol.* **29**, 625-679.

McKenzie, D.P. and O'Nions, R.K. 1991. Partial melt distributions from inversion of rare earth element concentrations. *J. Petrol.* **32**, 1021-1091.

Melnikov, A.I., Mazubakov, A.M., Sklyarov, E.V. and Vasiljev, E.P. 1994. Baikal rift basement: structure and tectonic evolution. *Bull. Centr. Rech. Explor. Prod. Elf Aquitaine* **18**, 99-122.

Menzies, M.A., Baker, J., Bosence, D., Dart, C., Davison, I., Hurford, A., Al'Kadasi, M., McClay, K., Al'Subbary, A. and Yelland, A. 1992. The timing of magmatism, uplift and crustal extension: preliminary observations from Yemen. In: *Magmatism and the Causes of Continental Break-up* (edited by Storey, B.C., Alabaster, T. and Pankhurst, R.J.). Geol. Soc. Spec. Publ. **68**, pp. 293-304.

Miller, D.S. and Duddy, I.R. 1989. Early Cretaceous uplift and erosion of the northern Appalachian Basin, New York, based on apatite fission track analysis. *Earth Planet. Sci. Lett.* **93**, 35-49.

Mohr, P. 1992. Nature of the crust beneath magmatically active continental rifts. *Tectonophysics* **213**, 269-284.

Mokhtari, M. and Pegrum, R.M. 1992. Structure and evolution of the Lofoten continental margin, offshore Norway. *Norsk Geol. Tidsskr.* **72**, 339-355.

Molnar, P. and England, P. 1990. Late Cenozoic uplift of mountain ranges and global climate change: Chicken or egg? *Nature* **346**, 29-34.

Molnar, P. and Tapponier, P. 1975. Cenozoic tectonics of Asia: Effects of a continental collision. *Science* **189**, 419-426.

Moore, M.E., Gleadow, A.J.W. and Lovering, J.F. 1986. Thermal evolution of rifted continental margins: New evidence from fission tracks in basement apatites from southeastern Australia. *Earth Planet. Sci. Lett.* **78**, 255-270.

Morgan, P. 1983. Constraints on rift thermal processes from heat flow and uplift. *Tectonophysics* **94**, 277-298.

Morgan, P. and Baker, B.H. (Editors) 1983. Processes of continental rifting. *Tectonophysics* **94**, 1-210.

Müller, B., Zoback, M.L., Fuchs, K., Mastin, K., Gregersen, S., Pavoni, N., Stephansson, O. and Ljungren, C. 1992. Regional patterns of tectonic stress in Europe. *J. Geophys. Res.* **97**, 11,783-11,804.

Mutter, J.G., Buck, W.R. and Zehnder, C.M. 1988. Convective partial melting 1. A model for the formation of thick basaltic sequences during the initiation of spreading. *J. Geophys. Res.* **93**, 1031-1048.

Naeser, C.W. 1979. Thermal history of sedimentary basins: Fission-track dating of subsurface rocks. In: *Aspects of Diagenesis* (edited by Scholle, P.A. and Schluger, P.R.). Soc. Econ. Paleont. Mineral. Spec. Publ. **26**, pp. 109-112.

Naeser, C.W. 1981. The fading of fission tracks in the geologic environment: Data from deep drill holes. *Nucl. Tracks Radiat. Meas.* **5**, 248-250.

Naeser, N.D., Naeser, C.W. and McCulloh, T.H. 1990. Thermal history of rocks in the southern San Joaquin Valley, California: Evidence from fission-track analysis. *Am. Assoc. Petrol. Geol. Bull.* **74**, 13-29.

Nesje, A. and Whillans, I.M. 1994. Erosion of the Sognefjord, Norway. *Geomorphology* **9**, 33-45.

Neugebauer, H.J. 1987. Models of lithospheric thinning. *Ann. Rev. Earth Planet. Sci.* **15**, 421-443.

Neumann, E.-R. 1994. The Oslo Rift: P-T relations and lithospheric structure. *Tectonophysics* **240**, 159-172.

Neumann, E.-R., Pallesen, S. and Andresen, P. 1986. Mass estimates of cumulates and residues after anatexis in the Oslo Graben. *J. Geophys. Res.* **91**, 11,629-11,640.

Neumann, E.-R., Tilton, G.R. and Tuen, E. 1988. Sr, Nd and Pb isotope geochemistry of the Oslo rift igneous province, southeast Norway. *Geochim. Cosmochim. Acta* **52**, 1997-2007.

Neumann, E.-R., Sundvoll, B. and Øverli, P.E. 1990. A mildly depleted upper mantle beneath southeast Norway: Evidence from basalts in the Permo-Carboniferous Oslo Rift. *Tectonophysics* **178**, 89-107.

Neumann, E.-R., Olsen, K.H., Baldridge, W.S. and Sundvoll, B. 1992. The Oslo rift: A review. *Tectonophysics* **208**, 1-18.

Newman, W.I. and Turcotte, D.L. 1990. Cascade model for fluvial geomorphology. *Geophys. J. Int.* **100**, 433-439.

Nicolas, A., Achauer, U. and Daignieres, M. 1994. Rift initiation by lithospheric rupture. *Earth Planet. Sci. Lett.* **123**, 281-298.

Nyblade, A.A., Pollack, H.N., Jones, D.L., Podmore, F. and Musjayandebvu, M. 1990. Terrestrial heat flow in East and Southern Africa. *J. Geophys. Res.* **95**, 17,371-17,384.

Olaussen, S. 1981. Marine incursion in Upper Paleozoic sedimentary rocks of the Oslo Region, southern Norway. *Geol. Mag.* **118**, 281-288.

Olaussen, S., Larsen, B.T. and Steel, R.J. 1995. The Upper Carboniferous-Permian Oslo Rift; basin fill in relation to tectonic development. In: *Proc. Pangea Conference* (edited by Embry, A.), Can. Soc. Petrol. Geol. Mem., in press.

Ollier, C.D. 1982. The Great Escarpment of eastern Australia: tectonic and geomorphic significance. *J. Geol. Soc. Australia* **29**, 13-23.

Ollier, C.D. (Editor) 1985. Morphotectonics of passive continental margins. *Zeitschr. Geomorph. Suppl.* **54**, 120 pp.

Olsen, K.I. and Griffin, W.L. 1984. Fluid inclusion studies of the Drammen Granite, Oslo paleorift, Norway. *Contrib. Mineral. Petrol.* **87**, 1-23.

Omar, G.I., Steckler, M.S., Buck, W.R. and Kohn, B.P. 1989. Fission-track analysis of basement apatites at the western margin of the Gulf of Suez rift, Egypt: Evidence for synchroneity of uplift and subsidence. *Earth Planet. Sci. Lett.* **94**, 316-328.

Owen, A.W., Bruton, D.L., Bockelie, J.F. and Bockelie, T.G. 1990. The Ordovician successions of the Oslo Region, Norway. *Nor. Geol. Unders. Spec. Publ.* **4**, 54 pp.

Pallesen, S. 1993. Crustal extension in the Oslo Graben, SE Norway: a method incorporating magmatism and erosion. *Tectonophysics* **221**, 155-172.

Pazzaglia, J. and Gardner, T.W. 1994. Late Cenozoic flexural deformation of the middle U.S. Atlantic passive margin. *J. Geophys. Res* **99**, 12,143-12,157.

Pedersen, T. 1994. Some remarks on lithospheric forces and decompression magmatism. *Tectonophysics* **240**, 11-20.

Pedersen, T. and Ro, H.E. 1992. Finite duration extension and decompression melting. *Earth Planet. Sci. Lett.* 113, 15-22.

Pedersen, T. and van der Beek, P.A. 1994. Extension and magmatism in the Oslo Rift, SE Norway: No sign of a mantle plume. *Earth Planet. Sci. Lett.* **123**, 317-329.

Pedersen, T., Petterson, S.E. and Husebye, E.S. 1991. Skagerrak evolution derived from tectonic subsidence. *Tectonophysics* **189**, 149-163.

Peulvast, J.-P. 1985. Post-orogenic morphotectonic evolution of the Scandinavian Caledonides during the Mesozoic and Cenozoic. In: *The Caledonide Orogen - Scandinavia and Related Areas* (edited by Gee, D.G. and Sturt, B.A.). Wiley, Chichester, pp. 979-995.

Pinet, B., Montadert, L., Mascle, A., Cazes, M. and Bois, C. 1987. New insights on the structure and the formation of sedimentary basins from deep seismic profiling in Western Europe. In: *Petroleum Geology of North West Europe* (edited by Brooks, J. and Glennie, K.). Graham & Trotman, London, pp. 11-31.

Popova, S.M., Mats, V.D. and 13 others 1989. *Paleolimnological reconstructions, the Baikal rift zone*, Nauka, Novosibirsk., 111 pp. (in Russian).

Ramberg, I.B. 1976. Gravimetry interpretation of the Oslo Graben and associated igneous rocks. *Nor. Geol. Unders.* **325**, 1-194.

Ramberg, I.B. and Larsen, B.T. 1978. Tectonomagmatic evolution. In: *The Oslo Paleorift: a review and guide to excursions* (edited by Dons, J.A. and Larsen, B.T.). Norges geol. Unders. **337**, pp. 55-73.

Ramberg, I.B. and Neumann, E.-R. (Editors) 1978. *Tectonics and Geophysics of Continental Rifts*, Reidel, Dordrecht.

Ramberg, I.B., Milanovsky, E.E. and Qvale, G. (Editors). 1987 Continental rifts - principal and regional characteristics. *Tectonophysics* **143**, 1-252.

Rasskazov, S.V. 1994. Magmatism related to the eastern Siberian rift system and geodynamics. *Bull. Centr. Rech. Explor. Prod. Elf Aquitaine* **18**, 437-452.

Ravenhurst, C.E. and Donelick, R.A. 1992. Fission track thermochronology. In: *Short course Handbook on Low Temperature Geochronology* (edited by Zentilli, M. and Reynolds, P.H.). Mineral. Assoc. Canada, Wolfville, NS, pp. 21-42.

Ravenhurst, C.E., Willett, S.D., Donelick, R.A. and Beaumont, C. 1994. Apatite fission track thermochronometry from central Alberta: Implications for the thermal history of the Western Canada Sedimentary Basin. *J. Geophys. Res.* **99**, 20,023-20,042.

Raymo, M.E. and Ruddiman, W.F. 1992. Tectonic forcing of late Cenozoic climate. *Nature* **359**, 117-122.

Reading, H.G. 1982. Sedimentary basins and global tectonics. *Proc. Geol. Assoc.* **93**, 321-350.

Reemst, P.H.M., Cloetingh, S. and Fanavoll, S. 1994. Tectono-stratigraphic modelling of Cenozoic uplift and erosion in the SW Barents Sea. *Mar. Petrol. Geol.* **11**, 478-490.

Riis, F. 1995. Quantification of Cenozoic vertical movements of Scandinavia by correlation of morphological surfaces with offshore data. submitted to *Global Change*.

Riis, F. and Fjeldskaar, W. 1992. On the magnitude of the Late Tertiary and Quaternary erosion and its significance for the uplift of Scandinavia and the Barents Sea. In: *Structural and Tectonic Modelling and its Application to Petroleum Geology* (edited by Larsen, R.M., Brekke,

H., Larsen, B.T. and Talleraas, E.). Norsk Petrol. Føren. Spec. Publ. **1**. Elsevier, Amsterdam, pp. 163-185.

Ring, U., Betzler, C. and Delvaux, D. 1992. Normal vs. strike-slip faulting during rift development in East Africa: The Malawi rift. *Geology* **20**, 1015-1018.

Ro, H.E. and Faleide, J.I. 1992. A stretching model for the Oslo Rift. *Tectonophysics* **208**, 19-36.

Ro, H.E., Larsson, F.R., Kinck, J.J. and Husebye, E.S. 1990a. The Oslo Rift - its evolution on the basis of geological and geophysical observations. *Tectonophysics* **178**, 11-28.

Ro, H.E., Stuevold, L.M., Faleide, J.I. and Myhre, A.M. 1990b. Skagerrak Graben - the offshore continuation of the Oslo Graben. *Tectonophysics* **178**, 1-10.

Roberts, D. and Gee, D.G. 1985. An introduction to the structure of the Scandinavian Caledonides. In: *The Caledonide Orogen - Scandinavia and Related Areas* (edited by Gee, D.G. and Sturt, B.A.). Wiley, Chichester, pp. 55-61.

Rohrman, M., van der Beek, P.A. and Andriessen, P.A.M. 1994. Syn-rift thermal structure and post-rift evolution of the Oslo Rift (SE Norway): new constraints from fission-track thermochronology. *Earth Planet. Sci. Lett.* **127**, 39-54.

Rohrman, M., van der Beek, P.A., Andriessen, P.A.M. and Cloetingh, S. 1995a. Meso-Cenozoic morphotectonic evolution of southern Norway: Neogene domal uplift inferred from apatite fission-track thermochronology. *Tectonics*, in press.

Rohrman, M., Andriessen, P.A.M. and van der Beek, P.A. 1995b. The relationship between basin and margin thermal evolution assessed by fission track thermochronology: an application to offshore southern Norway. submitted to *Basin Res.*

Rosendahl, B.R. 1987. Architecture of continental rifts with special reference to East Africa. *Ann. Rev. Earth Planet. Sci.* **15**, 445-503.

Rosendahl, B.R., Kilembe, E. and Kaczmarick, K. 1992. Comparison of the Tanganyika, Malawi, Rukwa and Turkana Rift zones from analyses of seismic reflection data. *Tectonophysics* **213**, 235-256.

Rowley, D.B. and Sahagian, D. 1986. Depth-dependent stretching: A different approach. *Geology* **14**, 32-35.

Royden, L. and Keen, C.E. 1980. Rifting process and thermal evolution of the continental margin of Eastern Canada determined from subsidence curves. *Earth Planet. Sci. Lett.* **51**, 343-361.

Rundberg, Y. and Smalley, P.C. 1989. High-resolution dating of Cenozoic sediments from northern North Sea using $^{87}Sr/^{86}Sr$ stratigraphy. *Am. Assoc. Petrol. Geol. Bull.* **73**, 298-308.

Ruppel, C., Kogan, M.G. and McNutt, M.K. 1993. Implications of new gravity data for Baikal Rift zone structure. *Geophys. Res. Lett.* **20**, 1635-1638.

Sales, J.K. 1992. Uplift and subsidence in Northwestern Europe: causes and influence on hydrocarbon entrapment. *Norsk Geol. Tidsskr.* **72**, 253-258.

Salveson, J.O. 1978. Variations in the geology of rift basins - A tectonic model. *Proc. International Symposium on the Rio Grande Rift.* Los Alamos Sci. Lab. LA-7487-C, pp. 82-86.

Sawyer, D.S. 1985. Brittle failure in the upper mantle during extension of continental lithosphere. *J. Geophys. Res.* **90**, 3021-3025.

Sawyer, D.S. and Harry, D.L. 1991. Dynamic modeling of divergent margin formation: application to the U.S. Atlantic margin. *Mar. Geol.* **102**, 29-42.

Scholz, C.A., Klitgord, K.D., Hutchinson, D.R., Ten Brink, U.S., Zonenshain, L.P., Golmshtok, A.J. and Moore, T.C. 1993. Results of 1992 seismic reflection experiment in Lake Baikal. *EOS Trans. Am. Geophys. Union* **74**, 465-470.

Sclater, J.G. and Célerier, B. 1987. Extensional models for the formation of sedimentary basins and continental margins. *Norsk Geol. Tidsskr.* **67**, 253-268.

Sclater, J.G. and Christie, P.A.F. 1980. Continental stretching: An explanation of the post-mid-Cretaceous subsidence of the Central North Sea basin. *J. Geophys. Res.* **85**, 3711-3739.

Şengör, A.M.C. and Burke, K. 1978. Relative timing of rifting and volcanism on Earth and its tectonic implications. *Geophys. Res. Lett.* **5**, 419-421.

SGU (Sveriges Geol. Unders.) 1985. Scandinavian Caledonides Gravity Anomaly Map. In: *The Caledonide Orogen - Scandinavia and Related Areas* (edited by Gee, D.G. and Sturt, B.A.). Wiley, Chichester.

Sherman, S.I. 1992. Faults and tectonic stresses of the Baikal rift zone. *Tectonophysics* **208**, 287-296.

Shudofsky, G.N., Cloetingh, S., Stein, S. and Wortel, R. 1987. Unusually deep earthquakes in East Africa: constraints on the thermo-mechanical structure of a continental rift system. *Geophys. Res. Lett.* **14**, 741-744.

Skogseid, J., Pedersen, T., Eldholm, O. and Larsen, B.T. 1992. Tectonism and magmatism during NE Atlantic continental break-up: the Vøring margin. In: *Magmatism and the Causes of Continental Break-up* (edited by Storey, B., Alabaster, T. and Pankhurst, R.J.). Geol. Soc. Spec. Publ. **68**, pp. 305-320.

Spadini, G., Cloetingh, S. and Bertotti, G. 1995a. Thermo-mechanical modelling of the Tyrrhenian Sea: lithospheric necking and kinematics of rifting. *Tectonics*, in press.

Spadini, G., Bertotti, G. and Cloetingh, S. 1995b. Tectono-stratigraphic modelling of the Sardinian margin of the Tyrrhenian Sea. submitted to *Tectonophysics*.

Spadini, G., Robinson, A. and Cloetingh, S. 1995c. Western versus Eastern Black Sea tectonic evolution: Pre-rift lithospheric controls on basin formation. submitted to *Earth Planet. Sci. Lett.*

Specht, T.D. and Rosendahl, B.R. 1989. Architecture of the Lake Malawi rift, East Africa. *J. Afr. Earth Sci.* **8**, 355-382.

Srivastava, S.P. and Tapscott, C.R. 1986. Plate kinematics of the North Atlantic. In: *The Geology of North America: The western North Atlantic region* (edited by Vogt, P.R. and Tucholke, B.E.). Geol. Soc. Am., Boulder, pp. 379-401.

Starmer, I. 1993. The Sveconorwegian orogeny in southern Norway, relative to deep crustal structures and events in the North Atlantic Proterozoic supercontinent. *Norsk Geol. Tidsskr.* **73**, 109-132.

Steckler, M.S. 1985. Uplift and extension at the Gulf of Suez: Indications of induced mantle convection. *Nature* **317**, 135-139.

Steckler, M.S. and Omar, G.I. 1994. Controls on erosional retreat of the uplifted rift flanks at the Gulf of Suez and northern Red Sea. *J. Geophys. Res.* **99**, 12,159-12,173.

Steckler, M.S. and Watts, A.B. 1978. Subsidence of the Atlantic-type continental margin off New York. *Earth Planet. Sci. Lett.* **41**, 1-13.

Steckler, M.S., Watts, A.B. and Thorne, J.A. 1988. Subsidence and basin modelling at the U.S. Atlantic passive margin. In: *The Geology of North America: The Atlantic Continental Margin, U.S.* (edited by Sheridan, R.E. and Grow, J.A.). Geol. Soc. Am., Boulder, pp. 399-416.

Steckler, M.S., Omar, G.I., Karner, G.D. and Kohn, B.P. 1993. Pattern of hydrothermal circulation within the Newark basin from fission-track analysis. *Geology* **21**, 735-738.

Steel, R.J. 1993. Triassic-Jurassic megasequence stratigraphy in the Northern North Sea: rift to post-rift evolution. In: *Petroleum Geology of Northwestern Europe: Proc. 4th Conference* (edited by Parker, J.R.). Geol. Soc., London, pp. 299-315.

Stel, H., Cloetingh, S., Heeremans, M.M.H. and van der Beek, P.A. 1993. Anorogenic granites, magmatic underplating and the origin of intracratonic basins in a non-extensional setting. *Tectonophysics* **226**, 285-299.

Stephenson, R.A. 1981. Continental Topography and Gravity, *Ph.D. Thesis Dalhousie University*, Halifax, 341 pp.

Stephenson, R. and Lambeck, K. 1985. Erosion-isostatic rebound models for uplift: an application to south-eastern Australia. *Geophys. J. Roy. astr. Soc.* **82**, 31-55.

Stephenson, R., Nakiboglu, S.M. and Kelly, M.A. 1989. Effects of asthenosphere melting, regional thermoisostasy and sediment loading on the thermomechanical evolution of extensional sedimentary basins. In: *Origin and Evolution of Sedimentary Basins and their Energy and Mineral Resources* (edited by Price, R.A.). Am. Geophys. Union Geophys. Monogr. **48**, pp. 17-27.

Stern, T. and Ten Brink, U. 1989. Flexural uplift of the Transantarctic Mountains. *J. Geophys. Res.* **94**, 10,315-10,330.

Stern, T., Davey, F.J. and Delisle, G. 1991. Lithospheric flexure induced by the load of the Ross Archipelago, southern Victoria Land, Antarctica. In: *Geological Evolution of Antarctica* (edited by Thomson, M.R.A., Crame, J.A. and Thomson, J.W.). Cambridge University Press, New York, pp. 323-328.

Stiberg, J.-P. 1993. Apatite fission track analysis from the Western Gneiss Region, preliminary results: Constraints to the Cenozoic uplift of the Norwegian passive margin. *Geonytt* **1**, 46.

Stuevold, L.M., Skogseid, J. and Eldholm, O. 1992. Post-Cretaceous uplift events on the Vøring continental margin. *Geology* **20**, 919-922.

Stüwe, K., White, L. and Brown, R.W. 1994. The influence of eroding topography on steady-state isotherms. Application to fission track analysis. *Earth Planet. Sci. Lett.* **124**, 63-74.

Suess, E. 1880. Ueber die vermeintlichen Schwankungen einzelner Theile der Erdoberflaeche. *Verh. K. Geol. Reichsanst. Wien*, 180 pp.

Suess, E. 1909. *The Face of the Earth* (Vol. 3), F. Tempsky, Vienna, 316 pp.

Summerfield, M.A. 1991a. *Global Geomorphology: An Introduction to the Study of Landforms*, Wiley, New York, 537 pp.

Summerfield, M.A. 1991b. Sub-aerial denudation of passive margins: Regional elevation versus local relief models. *Earth Planet. Sci. Lett.* **102**, 460-469.

Sundvoll, B. and Larsen, B.T. 1994. Architecture and early evolution of the Oslo rift. *Tectonophysics* **240**, 173-189.

Sundvoll, B., Neumann, E.-R., Larsen, B.T. and Tuen, E. 1990. Age relations among Oslo rift magmatic rocks: implications for tectonic and magmatic modelling. *Tectonophysics* **178**, 67-87.

Sundvoll, B., Larsen, B.T. and Wandaas, B. 1992. The age of the incipient magmatic phase in the Oslo rift and its related stress regime. *Tectonophysics* **208**, 37-54.

Tapponier, P. and Molnar, P. 1979. Active faulting and Cenozoic tectonics of the Tien Shan, Mongolia and Baykal regions. *J. Geophys. Res.* **84**, 3425-3456.

Ten Brink, U. and Stern, T. 1992. Rift flank uplifts and hinterland basins: Comparison of the Transantarctic Mountains with the Great Escarpment of southern Africa. *J. Geophys. Res.* **97**, 569-585.

ter Voorde, M. and Bertotti, G. 1994. Thermal effects of normal faulting during rifted basin formation, 1. A finite difference model. *Tectonophysics* **240**, 133-144.

ter Voorde, M. and Cloetingh. S. 1995. Numerical modelling of extension in the faulted crust: effects of localised and regional deformation on basin stratigraphy. submitted to *Modern Developments in Structural Interpretation, Validation and Modelling*, Geol. Soc. Spec. Publ.

Theilen, Fr. and Meissner, R. 1979. A comparison of crustal and upper mantle features in Fennoscandia and the Rhenish Shield, two areas of recent uplift. *Tectonophysics* **61**, 227-242.

Theunissen, K., Klerkx, J., Melnikov, A. and Mruma, A. 1995. Mechanisms of inheritance of rift faulting (Tanganyika-Malawi rift) in the Western Branch of the East African Rift. *Tectonics*, in press.

Thorne, A.J. and Watts, A.B. 1989. Quantitative analysis of North Sea subsidence. *Am. Assoc. Petrol. Geol. Bull.* **73**, 88-116.

Torske, T. 1972. Tertiary oblique uplift of western Fennoscandia; crustal warping in connection with rifting and break-up of the Laurasian continent. *Nor. Geol. Unders.* **273**, 43-48.

Tryti, J. and Sellevoll, M.A. 1977. Seismic crustal study of the Oslo Rift. *Pure Appl. Geophys.* **115**, 1061-1085.

Tucker, G.E. and Slingerland, R.L. 1994. Erosional dynamics, flexural isostasy and long-lived escarpments: a numerical modeling study. *J. Geophys. Res.* **99**, 12,229-12,243.

Turcotte, D.L. and Emerman, S.H. 1983. Mechanisms of active and passive rifting. *Tectonophysics* **94**, 39-50.

Turcotte, D.L. and Oxburgh, E.R. 1973. Mid-plate tectonics. *Nature* **244**, 337-339.

Ufimtsev, G.F. 1991. Morphotectonics of the Baikal rift valley, Eastern Siberia, USSR. *Geojournal* **23**, 197-206.

Ussami, N., Karner, G.D. and Bott, M.H.P. 1986. Crustal detachment during South Atlantic rifting and formation of Tucano-Gabon basin system. *Nature* **322**, 629-632.

Vågnes, E. and Amundsen, H.E.F. 1993. Late Cenozoic uplift and volcanism on Spitsbergen; caused by mantle convection? *Geology* **21**, 251-254.

van Balen, R.T. and Cloetingh, S. 1994. Tectonic control of the sedimentary record and stress-induced fluid flow: constraints from basin modelling. In: *Geofluids: Migration and Evolution of Fluids in Sedimentary Basins* (edited by Parnell, J.). Geol. Soc. Spec. Publ. **78**, 9-26.

van Balen, R.T., Lenkey, L., Cloetingh, S. and Horváth, F. 1995. Two-dimensional modelling of stratigraphy and fluid flow in the Pannonian Basin. submitted to *Mar. Petrol. Geol.*

Van den haute, P. 1977. Apatite fission track dating of Precambrian intrusive rocks from southern Rogaland (south-western Norway). *Bull. Soc. Belge Géol.* **86**, 97-110.

Van den haute, P. 1984. Fission-track ages of apatites from the Precambrian of Rwanda and Burundi: relationship to East African rift tectonics. *Earth Planet. Sci. Lett.* **71**, 129-140.

van Haren, J. and Rohrman, M. 1988. Fission track ouderdommen van apatiet in het Bamble gebied (ZW Noorwegen), *Internal Report ZWO lab. Isotope Geology*, Amsterdam, 33 pp. (in Dutch).

van Wees, J.D. 1994. Tectonic Modelling of Basin Deformation and Inversion Dynamics: the role of pre-existing faults and continental lithosphere rheology in basin evolution. *Ph.D. Thesis Vrije Universiteit Amsterdam*, 164 pp.

van Wees, J.D. and Cloetingh, S. 1994. A finite-difference technique to incorporate spatial variations in rigidity and planar faults into 3-D models for lithospheric flexure. *Geophys. J. Int.* **117**, 179-195.

Veevers, J.J. 1984. *Phanerozoic Earth History of Australia*, Clarendon Press, Oxford.

Vejbæk, O.V. 1990. The Horn Graben and its relationship to the Oslo Graben and the Danish Basin. *Tectonophysics* **178**, 29-49.

Vening-Meinesz, F.A. 1950. Les Graben Africains, resultat de compression ou de tension dans la croûte terrestre? *Bull. Inst. Roy. Col. Belge* **21**, 539-552.

Verschure, R.H. 1985. Geochronological framework for the Late-Proterozoic evolution of the Baltic Shield in South Scandinavia. In: *The Deep Proterozoic Crust in the North Atlantic Provinces* (edited by Tobi, A.C. and Touret, J.L.R.). NATO ASI Series C **158**. Reidel, Dordrecht, pp. 381-410.

Versfelt, J. and Rosendahl, B.R. 1989. Relationships between pre-rift structure and rift architecture in Lakes Tanganyika and Malawi, East Africa. *Nature* **337**, 354-357.

Vrolijk, P., Donelick, R.A., Queng, J. and Cloos, M. 1992. Testing models of fission track annealing in apatite in a simple thermal setting: Site 800, ODP Leg 129. *Proc. Ocean Drilling Program, Leg 129, Scientific Results*. College Station, TX, pp. 169-176.

Wagner, G.A. 1979. Correction and interpretation of fission track ages. In: *Lectures in Isotope Geology* (edited by Jäger, E. and Hunziker, J.C.). Springer Verlag, Berlin, pp. 170-177.

Wagner, G.A. and Reimer, G.M. 1972. Fission track tectonics: the tectonic interpretation of fission track apatite ages. *Earth Planet. Sci. Lett.* **14**, 263-268.

Wagner, G.A. and Van den haute, P. 1992. *Fission Track Dating*, Kluwer Ac. Publ., Dordrecht.

Wagner, G.A., Hejl, E. and Van den haute, P. 1994. The KTB fission-track project: methodical aspects and geological implications. *Nucl. Tracks Radiat. Meas.* **23**, 95-101.

Wagner, M., Altherr, R. and Van den haute, P. 1992. Apatite fission-track analysis of Kenyan basement rocks: constraints on the thermotectonic evolution of the Kenya dome. A reconnaissance study. *Tectonophysics* **204**, 93-110.

Waltham, D. 1992. Mathematical modelling of sedimentary basin processes. *Mar. Petrol. Geol.* **9**, 265-273.

Watts, A.B., Karner, G.D. and Steckler, M.S. 1982. Lithosphere flexure and the evolution of sedimentary basins. *Philos. Trans. Roy. Soc. London* **A305**, 249-281.

Wegener, A. 1912. Die Entstehung der Kontinente. *Geol. Rundschau* **3**, 276-292.

Weissel, J.K. 1990. Long-term erosional development of rifted continental margins: Toward a quantitative understanding. *Proc. Pacific Rim Congress '90*. Australasian Inst. Mining Metallurgy, Parkville, Vic., pp. 63-70.

Weissel, J.K. and Karner, G.D. 1989. Flexural uplift of rift flanks due to mechanical unloading of the lithosphere during extension. *J. Geophys. Res.* **94**, 13,919-13,950.

Wellman, P. 1987. Eastern Highlands of Australia: Their uplift and erosion. *BMR J. Geol. Geophys.* **10**, 277-286.

Wendlandt, R.F., Baldridge, W.S. and E.-R Neumann 1991. Modification of lower crust by continental rift magmatism. *Geophys. Res. Lett.* **18**, 1759-1762.

Wernicke, B. 1985. Uniform-sense normal simple shear of the continental lithosphere. *Can. J. Earth Sci.* **22**, 108-125.

Wessel, P. and Husebye, E.S. 1987. The Oslo Graben gravity high and taphrogenesis. *Tectonophysics* **142**, 15-26.

Westaway, R. 1993. Forces associated with mantle plumes. *Earth Planet. Sci. Lett.* **119**, 331-348.

White, R.S. and McKenzie, D.P. 1989. Magmatism at rift zones: The generation of volcanic continental margins and flood basalts. *J. Geophys. Res.* **94**, 7685-7729.

White, R.S., McKenzie, D.P. and O'Nions, R.K. 1992. Oceanic crustal thickness from seismic measurements and rare earth element inversions. *J. Geophys. Res.* **97**, 19,683-19,715.

Wilch, T.I., Lux, D.R., Denton, G.R. and McIntosh, W.C. 1993. Minimal Pliocene-Pleistocene uplift of the Dry Valleys sector of the Transantarctic Mountains: A key parameter in ice-sheet reconstructions. *Geology* **21**, 841-844.

Willett, S.D. 1992. Modelling thermal annealing of fission tracks in apatite. In: *Short course Handbook on Low Temperature Geochronology* (edited by Zentilli, M. and Reynolds, P.H.). Mineral. Assoc. Canada, Wolfville, NS, pp. 43-74.

Wilson, J.T. 1966. Did the Atlantic close and then reopen? *Nature* **211**, 676-681.

Wilson, M. 1993. Magmatism and the geodynamics of basin formation. *Sed. Geol.* **86**, 5-29.

Windley, B.F. and Allen, M.B. 1993. Mongolian Plateau: Evidence for a late Cenozoic mantle plume under central Asia. *Geology* **21**, 295-298.

Wood, R.J., Edrich, S.P. and Hutchison, I. 1989. Influence of North Atlantic tectonics on the large-scale uplift of the Stappen High and Loppa high, Western Barents Shelf. In: *Extensional Tectonics and Stratigraphy of the North Atlantic Margins* (edited by Tankard, A.J. and Balkwill, H.R.). Am. Assoc. Petrol. Geol. Mem. **46**, pp. 559-566.

Worsley, D., Aarhus, N., Bassett, M.G., Howe, M.P.A., Mørk, A. and Olaussen, S. 1983. The Silurian succession of the Oslo Region. *Nor. Geol. Unders.* **384**, 1-57.

Zaun, P. and Wagner, G.A. 1985. Fission-track stability in zircons under geological conditions. *Nucl. Tracks Radiat. Meas.* **10**, 303-307.

Zeck, H.P., Andriessen, P.A.M., Hansen, K., Jensen, P.K. and Rasmussen, B.L. 1988. Paleozoic paleo-cover of the southern part of the Fennoscandian Shield - fission track constraints. *Tectonophysics* **149**, 61-66.

Ziegler, P.A. 1988. *Evolution of the Arctic-North Atlantic and the Western Tethys*, Am. Assoc. Petrol. Geol. Mem. **43**, 198 pp.

Ziegler, P. 1990. *Geological Atlas of Western and Central Europe (2nd ed.)*, Shell Int. Petrol. Maatsch., Den Haag, 239 pp.

Ziegler, P.A. (Editor) 1992. Geodynamics of rifting (vols. 1-3). *Tectonophysics* **208, 213, 215**, 1-364, 1-284, 1-253.

Ziegler, P.A. 1995. Geodynamic processes governing development of rifted basins. In: *Proc. Symp. Geodynamic Evolution of Sedimentary Basins* (edited by Roure, F., Shein, V.S. Ellouz, N. and Skvortsov, L.). Éditions Technip, Moscow, Paris, in press.

Zoback, M.L., Zoback, M.D. and World Stress Map Team 1989. Global patterns of tectonic stress. *Nature* **341**, 291-298.

Zoetemeijer, R. 1993. Tectonic Modelling of Foreland Basins; thin skinned thrusting, syntectonic sedimentation and lithospheric flexure. *Ph.D. Thesis Vrije Universiteit Amsterdam*, 148 pp.

Zonenshain, L.P. and Savostin, L.A. 1981. Geodynamics of the Baikal Rift Zone and plate tectonics of Asia. *Tectonophysics* **76**, 1-45.

Zorin, Yu. A. 1981. The Baikal rift: An example of the intrusion of asthenospheric material into the lithosphere as the cause of disruption of lithospheric plates. *Tectonophysics* **73**, 91-104.

Zorin, Yu. A. and Cordell, L. 1991. Crustal extension in the Baikal rift zone. *Tectonophysics* **198**, 117-121.

Zorin, Yu. A., Kozhevnikov, V.M., Novoselova, M.R. and Turutanov, E.K. 1989. Thickness of the lithosphere beneath the Baikal rift zone and adjacent regions. *Tectonophysics* **168**, 327-337.